ENVIRONMENTAL RADIOACTIVITY STUDIES RELEVANT TO THERMOLUMINESCENCE DATING

ANDREW SEAN MURRAY

LINACRE COLLEGE

This thesis is submitted in partial fulfilment of the requirements for the degree of Doctor of Philosophy in the University of Oxford

Hilary Term
1981

ABSTRACT

ENVIRONMENTAL RADIOACTIVITY STUDIES RELEVANT TO THERMOLUMINESCENCE DATING

A. S. Murray, Linacre College. D.Phil. thesis, submitted Hilary term, 1981.

This thesis critically examines assumptions commonly used in determining dose rates to material suitable for dating by thermoluminescence (TL); in particular, the influence of radioactive disequilibria and ion exchange effects is investigated. In obtaining absolute dates for Peruvian pottery used in studies of geomagnetic field magnitude variations over the past 2000 years, the existing laboratory beta source calibration for fine grains of pottery was found to be 15% high. Revised beta source dose rates are used to evaluate the doses absorbed by variously encapsulated TL phosphors exposed in a 1 m cube of concrete doped with uranium ore. Calculated dosimeter (TLD) responses are compared with those observed and it is shown that observed doses in the preferred combination of calcium fluoride surrounded by 1.5 mm of copper must be multiplied by 1.19 to give the infinite matrix dose rate, indicating that capsule wall attenuation is more important than anticipated. A portable NaI scintillometer is also developed. Using additional concrete cubes, the count rate above 0.43 MeV is found to be independent of whether the gamma rays are from uranium, thorium or potassium, within 1%. Field tests in Peru show that for dry sites there is generally good agreement with TLD results; empirical corrections are needed for wet sites.

Activity analyses of the natural decay series, and K-40, using 7 g samples in an intrinsic germanium well detector, the calibration of which is detailed, reveals that series disequilibrium is commonplace. It is also demonstrated for the first time that up to 50% of some isotope activities may be held on ion exchange sites. Such activity must be considered potentially mobile, rendering dosimetry calculations suspect. These analyses also show the hitherto well established techniques of thick source alpha counting and flame photometry to be unreliable, whereas beta TLD is found to be accurate and precise.

CONTENTS

ABSTRACT. i

ACKNOWLEDGEMENTS. xi

CHAPTER I

THE ANNUAL DOSE RATE TO BURIED MATERIAL 1.1

1.1 THE DATING OF FIRED MATERIAL BY THERMOLUMINESCENCE 1.1

1.2 EVALUATING THE ARCHAEOLOGICAL DOSE 1.3

1.3 THE ANNUAL DOSE RATE TERM. 1.5

1.4 SCOPE OF THIS THESIS 1.6

CHAPTER II

BETA SOURCE CALIBRATION 2.1

2.1 INTRODUCTION 2.1

2.1.1 Previous work. 2.2
2.1.2 Reproducibility of the 'on/off' dose rate ratio. 2.4
2.1.3 Dependence of dose rate on backing material. 2.5
2.1.4 Variation of dose rate with thickness of backscattering medium. 2.6
2.1.5 Discussion 2.7
2.1.6 A new method of sample preparation for 100 μm grains . . 2.8

2.2 THE PROBLEMS ASSOCIATED WITH THE USE OF QUARTZ AS A CALIBRATION PHOSPHOR 2.8

2.2.1 TL and dosimetry characteristics of obsidian 2.9
2.2.2 Comparison of the dosimetry response of the 110°C peak in quartz with that of the 305°C peak in obsidian . 2.11
2.2.3 The dosimetry of the high temperature region in the quartz glow curve. 2.13

2.3 ABSOLUTE CALIBRATION 2.14

2.3.1 Attenuation in capsule wall. 2.16
2.3.2 Phosphor irradiations. 2.16
2.3.3 Systematic errors in the evaluation of the gamma dose 2.18

2.3.4 Discussion. 2.18

2.4 SUMMARY 2.20

CHAPTER III

ENVIRONMENTAL DOSIMETRY USING TL DOSIMETERS. 3.1

3.1 CONSTRUCTION OF A QUASI-INFINITE MATRIX OF KNOWN ACTIVITY 3.2

3.1.1 Minimum size for a quasi-infinite uranium doped concrete matrix 3.3

3.1.2 Description of uranium ore used, and activity required 3.5

3.1.3 Homogeneity of activity in concrete mix 3.6

3.1.4 Homogeneity measurements on casting samples 3.7

3.1.5 Calculated and observed activity of the concrete. . . . 3.7

3.1.6 Activity of Rn-222 in solid concrete. 3.8

3.1.7 Annual dose rate at the centre of the quasi-infinite block. 3.9

3.1.8 The doped concrete as a radiological hazard 3.9

3.2 EXPERIMENTALLY OBSERVED DOSE RATES IN THE URANIUM BLOCK . 3.10

3.2.1 Phosphors and encapsulating materials used as TL dosimeters 3.10

3.2.2 Fading corrections. 3.13

3.2.3 Weight of phosphor used 3.14

3.2.4 Experimentally observed quasi-infinite matrix dose rates. 3.15

3.3 CALCULATION OF DOSE ABSORBED IN A TL DOSIMETER PLACED IN AN INFINITE GAMMA EMITTING MEDIUM. 3.15

3.3.1 The infinite matrix spectrum. 3.16

3.3.2 Attenuation and absorption of energy by a capsule . . . 3.17

3.3.3 Calculation of the dose rate recorded by TL capsules. . 3.20

3.3.4 Discussion. 3.22

3.3.5 Variation of relative response of capsules with energy compared with a small unencapsulated shale absorber . . 3.25

3.3.6 Calculated average response of capsules exposed to a composite infinite matrix spectrum. 3.25

3.4 CONCLUSION 3.26

CHAPTER IV

DIRECT MEASUREMENT OF GAMMA DOSE RATES USING A SODIUM IODIDE DETECTOR 4.1

4.1 INTRODUCTION 4.1

4.1.1 Conversion of detector count rate to phosphor dose rate. 4.1
4.1.2 Experimental determination of threshold position . . . 4.4
4.1.3 Description of detector and associated electronics . . 4.4
4.1.4 The calibration facilities 4.5
4.1.5 Spectra of calibration blocks. 4.6
4.1.6 Threshold stability. 4.8

4.2 FIELD USE OF CALIBRATED DETECTOR 4.9

4.2.1 The capsule results. 4.9
4.2.2 Effects of variations in the cosmic ray intensity on the calibration of the sodium iodide detector . . . 4.10
4.2.3 Comparison of the dose rates measured by the sodium iodide detector with those from calcium fluoride in copper capsules. 4.12

4.3 CONCLUSION 4.14

CHAPTER V

PERUVIAN SHERDS: A DATING PROGRAMME 5.1

5.1 DESCRIPTION OF SAMPLES 5.1

5.2 DATING TECHNIQUE 5.2

5.3 MODIFICATIONS TO THE FINE GRAIN TECHNIQUE. 5.2

5.4 DESCRIPTION OF THE TL MEASURING EQUIPMENT. 5.4

5.5 TL DATA. 5.4

5.6 ERRORS 5.6

5.7 DISCUSSION 5.7

5.8 CONCLUSION 5.8

CHAPTER VI

DESIGN AND CALIBRATION OF A HIGH RESOLUTION, HIGH SENSITIVITY GAMMA SPECTROMETER FOR THE ANALYSIS OF NATURAL RADIOISOTOPES . 6.1

6.1 INTRODUCTION. 6.1

6.1.1 Sources of disequilibrium 6.1
6.1.2 Uranium series. 6.2
6.1.3 Thorium series. 6.3
6.1.4 Stability of disequilibria patterns 6.4
6.1.5 Existing measurements of chain disequilibria in archaeological contexts 6.5
6.1.6 Uncertainties in dose rate due to disequilibria. . . . 6.6

6.2 GAMMA SPECTROMETRY AS A MEANS OF QUANTITATIVE RADIOISOTOPE DETERMINATION. 6.7

6.2.1 High resolution spectrometry. 6.7
6.2.2 Uranium series. 6.8
6.2.3 Thorium series. 6.10
6.2.4 Potassium analysis. 6.10
6.2.5 Summary of the potential of high resolution spectrometry. 6.10

6.3 SPECTROMETER DESIGN 6.11

6.3.1 Spectrometer resolution 6.11
6.3.2 Efficiency. 6.12
6.3.3 Background. 6.15
6.3.4 Anti-Compton shield 6.19
6.3.5 Encapsulation of the anti-Compton guard crystals. . . . 6.21
6.3.6 Electronics 6.22
6.3.7 Reduction of data 6.23
6.3.8 Sample geometry 6.23

6.4 SPECTROMETER PERFORMANCE. 6.24

6.4.1 Resolution. 6.24
6.4.2 Efficiency. 6.24
6.4.3 Compton suppression 6.25
6.4.4 Background. 6.25
6.4.5 Summary 6.26

6.5 SAMPLE NORMALISATION PROCEDURES 6.26

6.5.1 Sample self attenuation 6.27
6.5.2 Typical elemental composition of pottery and soils. . . 6.27
6.5.3 Mass attenuation coefficients of pottery and soils. . . 6.29
6.5.4 Evaluation of variations in sample self attenuation with sample weight, using a range of elemental compositions. 6.30
6.5.5 Treatment of experimental data. 6.31
6.5.6 Summary 6.34

6.6 CALIBRATION. 6.34

6.6.1 Dispersion procedure for standards. 6.35
6.6.2 Group 1: U-238 and U-235 standards 6.36
6.6.3 Groups 2 and 3: U-234, Th-230, Pa-231 standards. . . . 6.37
6.6.4 Group 4: Ra-226 standard 6.37
6.6.5 Group 5: Rn-222 standard 6.37
6.6.6 Group 6: Pb-210 standard 6.39
6.6.7 Group 7: Th-232 standard 6.39
6.6.8 Group 8: Rn-220 standard 6.39
6.6.9 Potassium standard. 6.40
6.6.10 Thorium series interference with the Th-234 peak at 63 keV 6.40
6.6.11 Summary of calibration standards. 6.41
6.6.12 Effect of sealing on determining levels of radon escape in unsealed samples. 6.42

6.7 COMPARISON OF CALIBRATION DATA WITH OTHER WELL KNOWN STANDARDS. 6.44

6.7.1 Uranium series. 6.44
6.7.2 Thorium series. 6.45
6.7.3 Uranium series equilibrium. 6.45
6.7.4 Conclusions 6.45

6.8 ANALYSIS OF LOW ACTIVITY SAMPLES. 6.45

6.8.1 Comparison of observed reproducibility with the errors from the peak fitting routine 6.46
6.8.2 Systematic errors in the peak fitting of low intensity peaks 6.46
6.8.3 Discussion. 6.48
6.8.4 Conclusion. 6.48

CHAPTER VII

LOW LEVEL RADIOISOTOPE ANALYSIS OF SAMPLES OF ARCHAEOLOGICAL INTEREST 7.1

7.1 MEASURED ACTIVITIES IN A RANGE OF POTTERY SAMPLES. 7.1

7.2 VARIATIONS OF ACTIVITY WITH GRAIN SIZE IN A POTTERY SAMPLE BEFORE AND AFTER FIRING 7.2

7.2.1 Discussion 7.3
7.2.2 Conclusion 7.5

7.3 STABILITY OF RADIOISOTOPE CONCENTRATIONS 7.6

7.3.1 Experimental technique 7.6
7.3.2 Discussion 7.7
7.3.3 Conclusion 7.9

7.4 SITES SHOWING LITTLE U-238/Ra-226 DISEQUILIBRIUM 7.9

7.4.0 Huaca Gallinazo, Viru Valley, Peru 7.9
7.4.1 Samples analysed 7.9
7.4.2 Discussion 7.10
7.4.3 Potential isotope mobility 7.11
7.4.4 Effect of the spectrometer data on age evaluation. . . . 7.12
7.4.5 Huari, Ayacucho, Peru. 7.13
7.4.6 Samples analysed 7.13
7.4.7 Discussion 7.14
7.4.8 Potential isotope mobility 7.14
7.4.9 Effect of spectrometer data on age evaluation. 7.15

7.5 SITES SHOWING CONSIDERABLE U-238/Ra-226 DISEQUILIBRIUM . . 7.16

7.5.0 Sham Wan, Lamma Island, Hong Kong. 7.16
7.5.1 Samples studied. 7.16
7.5.2 Discussion 7.17
7.5.3 Potential isotope mobility 7.17
7.5.4 Effects of spectrometer data on age evaluation 7.18
7.5.5 Discussion 7.21
7.5.6 Cheung Chan, Hong Kong 7.21
7.5.7 Samples measured 7.22
7.5.8 Discussion 7.22
7.5.9 Potential radioisotope mobility. 7.23
7.5.10 Effect of spectrometer data on age evaluation. 7.23

7.5.11 Discussion 7.25
7.5.12 Alpha spectrometry analyses. 7.26

7.6 SAMPLE SELECTION USING RADIOISOTOPE ANALYSIS 7.28

7.6.0 La Cotte, Guernsey 7.28
7.6.1 Material studied 7.28
7.6.2 Discussion 7.28
7.6.3 Potential radioisotope mobility. 7.29
7.6.4 Conclusion 7.30

7.7 PATTERNS AND TRENDS IN THE DATA ALREADY PRESENTED. 7.30

7.7.1 Laboratory escape of Rn-222, and Ra-226 excess 7.31
7.7.2 Deductions from ion exchange behaviour 7.31
7.7.3 Radon migration before and after burial. 7.34

7.8 CONCLUSION 7.35

CHAPTER VIII

THE PERFORMANCE OF ROUTINE DOSIMETRY TECHNIQUES WHEN COMPARED WITH GAMMA SPECTROMETRY 8.1

8.1 THICK SOURCE ALPHA COUNTING. 8.1

8.1.1 Comparison of observed and predicted count rates 8.2
8.1.2 Likely sources of count rate discrepancy 8.3
8.1.3 Empirical approach to the problem of overcounting of alpha activity. 8.4
8.1.4 Effect of resin on alpha ranges. 8.5
8.1.5 Count rate build up in a sealed sample 8.6
8.1.6 Conclusion 8.7

8.2 GAS CELL ANALYSIS. 8.7

8.2.1 Gas cell measurements compared with spectrometer predictions 8.8
8.2.2 Conclusion 8.9

8.3 BETA DOSE RATE ESTIMATION USING TL DOSIMETRY 8.9

8.3.1 Beta dose rates from TL dosimetry compared with those calculated from gamma spectrometry 8.9

8.4 GAMMA DOSE RATE ESTIMATION USING GAMMA TL DOSIMETRY. . . . 8.10

8.4.1 Gamma TLD measurements compared with spectrometry predictions 8.10

8.5 FLAME PHOTOMETRY 8.11

8.5.1 Comparison with gamma spectrometry 8.11

8.6 ALPHA SPECTROMETRY ANALYSIS OF Po-210. . . . . 8.12

8.6.1 Comparisons with gamma spectrometry. 8.12

8.7 SUMMARY. 8.12

APPENDICES

APPENDIX A

'SAMPO', A FORTRAN PROGRAM FOR COMPUTER ANALYSIS OF GAMMA SPECTRA FROM SOLID STATE DETECTORS. A.1

APPENDIX B

STANDARDISED RADIOACTIVE SOLUTIONS. B.1

B.1 ARTIFICIAL RADIONUCLIDES B.1

B.2 Ra-226 SOLUTION. B.1

B.3 Pb-210 SOLUTION. B.2

B.4 THORIUM NITRATE. B.2

APPENDIX C

DERIVATION OF THE MAXIMUM LIKLEY Rn-222 ESCAPE FROM THE USNBS URANIUM STANDARD NBL 74-A C.1

APPENDIX D

PERUVIAN SITE NOTES REPRODUCED FROM GUNN (1980) D.1

APPENDIX E

CONVERSION FROM ISOTOPE ACTIVITIES TO ALPHA COUNT RATE AND DOSE RATES. E.1

E.1 ALPHA COUNT RATE E.1

E.2 DOSE RATE DATA E.2

APPENDIX F

AGE CALCULATIONS FOR SITE 164: SHAM WAN, LAMMA ISLAND, HONG KONG F.1

F.1 SUPPORTED Ra-226 EXCESS. F.1
F.2 UNSUPPORTED Ra-226 EXCESS. F.2

APPENDIX G
CALCULATION OF AVERAGE EFFECTIVE SIZE OF AN EMANATING GRAIN FROM A KNOWLEDGE OF THE ACTIVITY RATIO OF FIXED Pb-210 to FIXED Ra-226. . . . . G.1

REFERENCES. R.1

ERRATA. . . . . inside back cover

-o-

ACKNOWLEDGEMENTS

My thanks go first to Dr Martin Aitken, for encouraging and supervising the work described in this thesis, and I would also like to express my gratitude to all the academic and technical staff of the Laboratory, past and present, whose tolerance and willingness to help and criticize contributed to a very enjoyable and memorable period in my life.

I am indebted to Mrs J. MacAulay, Ms Patricia MacKintosh and Ms Kim Parfitt for typing the manuscript, and to the many others who have assisted with advice and practical help over the years.

Finacial support by the Natural Environment Research Council, grant numbers GR3/2396(A) and GR4/74/GS/142, by the Science Research Council, grant number GR/A/4555.5, and by The Research Laboratory for Archaeology is gratefully acknowledged.

Old Aberdeen,
February, 1981

CHAPTER I

THE ANNUAL DOSE RATE TO BURIED MATERIAL

INTRODUCTION

The techniques of thermoluminescence (TL) dating have been available to archaeologists for some years now. In the course of the development of these techniques many assumptions have of necessity been made, and as the approach to the problems involved becomes more sophisticated, the validity of these assumptions must be re-examined from both a theoretical and an experimental point of view. This thesis is concerned with such re-examination of the methods of determining the annual dose rate to buried material, with particular reference to pottery fragments.

1.1 THE DATING OF FIRED MATERIAL BY THERMOLUMINESCENCE

When minerals are heated they give out light, usually in the visible region of the spectrum, the intensity of which is related to the amount of energy stored in the lattice structure by electrons displaced into meta-stable states as a result of exposure to ionizing radiation. This is the phenomenon of thermoluminescence. After such a heating process, the crystal lattice again commences to store energy, as a result of interactions with the natural environmental radiation field. Over geological periods of time this storage of energy eventually saturates, but over shorter periods, such as are of interest to archaeologists, the growth of TL with the dose absorbed from the environment is often linear, or nearly so. This growth of TL with time can be expressed as

$$T = \frac{N}{\chi_\alpha D_\alpha + \chi(D_\beta + D_{\gamma,c})} \qquad - - - - - - - - 1$$

where T is the time elapsed since the last heating which was sufficient to release all the stored energy,

N is the TL light output from the sample,

χ_α is the sensitivity of the growth of TL to irradiation by alpha particles,

χ is the sensitivity of the growth of TL to irradiation by beta or gamma rays,

D_α is the alpha particle dose rate,

D_β is the beta ray dose rate,

$D_{\gamma,c}$ is the gamma and cosmic ray dose rate.

This equation can be rewritten as

$$T = \frac{AD}{kD_\alpha + D_\beta + D_{\gamma,c}} \qquad \text{- - - - - - - - 2}$$

where AD is known as the archaeological dose = $\frac{N}{\chi}$,

and k is the ratio of the TL sensitivity to alpha particles to that to beta and gamma rays, i.e. $\frac{\chi_\alpha}{\chi}$. This usually takes values of about 0.1.

This equation is known as the age equation for fine grains, because it contains the assumption that the sample has been uniformly irradiated by each of the three important forms of ionizing radiation, in particular alpha particles, and it was first employed by ZIMMERMAN (1970, 1971).

FLEMING (1969) has developed a similar expression which restricts itself to those grains which have received a negligible alpha dose. The age equation for this approach, known as the quartz inclusion technique, is simply

$$T = \frac{AD}{D_\beta + D_{\gamma,c}} \qquad \text{- - - - - - - - 3}$$

The assumptions involved in this equation are most nearly satisfied in the case of sand sized grains of quartz (about 100 μm in diameter), which contain very little internal radioactivity. However the outer 10 μm of such grains will usually have received a significant alpha dose from the surrounding clay minerals and also from surface impurities, and so this outer shell must be removed by etching in hydrofluoric acid. In addition there will be some attenuation of the beta dose across the grain, which must be allowed for. (FLEMING, 1978; BELL, 1979a; MEJDAHL, 1979). FLEMING (1969, 1979) and others have also developed a technique based on the sensitivity changes in

the low temperature quartz peak at 110°C with dose history. However, this approach is not considered as well established as the fine grain and quartz inclusion techniques, and as the dosimetry is identical with that of the inclusion technique it will not be considered further. A review of the application of TL dating to materials other than ceramics has been given by WINTLE (1980).

1.2 EVALUATING THE ARCHAEOLOGICAL DOSE

We shall consider the fine grain technique as illustrative, as this is the approach actually employed in chapter 5 of this thesis. Since Zimmerman's initial work, considerable effort has been expended in refining this technique, particularly in its application to pottery.

The first stage in sample preparation is to remove the outer 2 mm of the sherd, to ensure that the beta dose rate to the sherd is entirely from the fabric of the ceramic. This removes uncertainties in the beta dose rate arising from differences in the activities of the sherd and surrounding soil. The interior of the sample is crushed in a vice and the grain size fraction 2 to 8 μm deposited from suspension in acetone onto 1 cm diameter aluminium discs 0.45 mm thick. Some of these discs are then exposed to various additional beta irradiations using a calibrated beta source. These laboratory irradiated discs, along with 4 or 5 which have received only their natural dose, are then heated to about 500°C at a linear heating rate of, say, 10° sec^{-1} in an oxygen free nitrogen atmosphere, and the TL observed with a photomultiplier tube. The experimental apparatus used is described by AITKEN et al (1968). The resulting graph of TL output against temperature is known as a glow curve. Figure 1.1 shows two illustrative fine grain glow curve shapes, one arising from a natural dose only, and one from a subsequent laboratory beta dose. The TL output at selected temperatures is then plotted against dose, yielding the first glow growth curves for these temperatures. The intercepts, $\underline{Q}$, obtained by extrapolating these growth curves back to the dose axis are then plotted against temperature, and the resulting curve examined for a plateau region, usually from about 350° to 450°C, across which the value of $\underline{Q}$ is constant within experimental error. (It should be

Figure 1.1

Illustrative glow curves following a natural and a laboratory irradiation of a fine grain sample

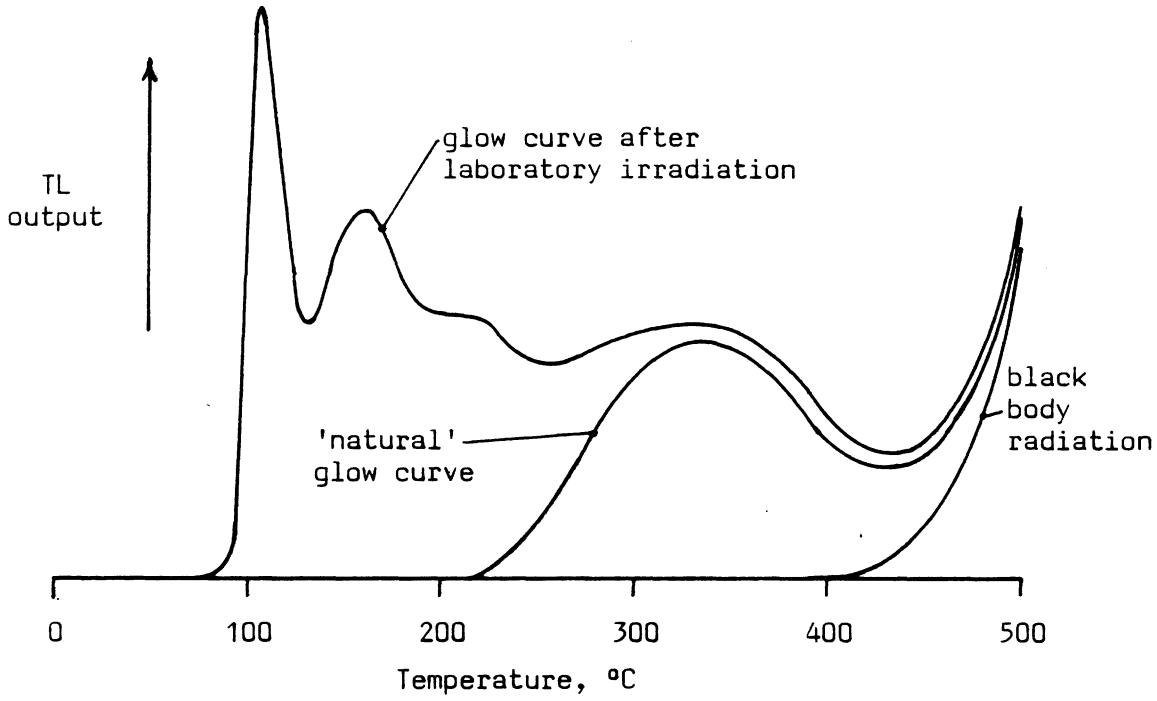

Figure 1.2

Illustrative first and second glow growth curves

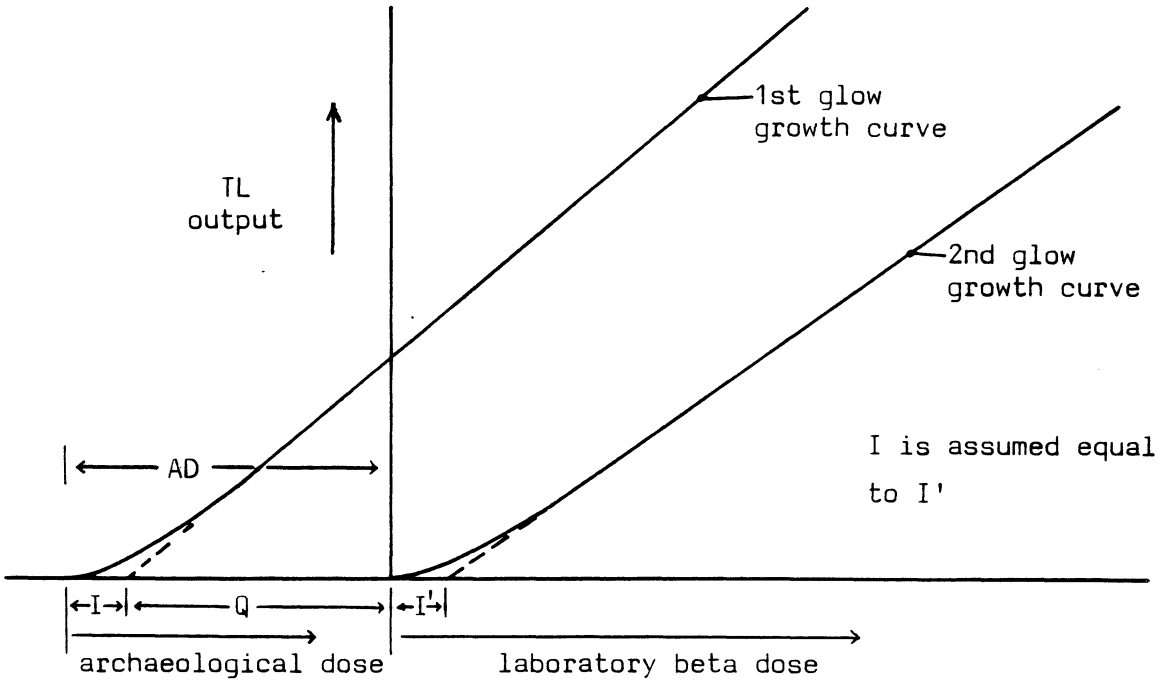

noted that Q is sometimes referred to as equivalent dose, ED). This is then the temperature region from which the date is eventually calculated. This additive dose procedure is then repeated using those 4 or 5 discs which had contained only their natural dose before they were read out for the first glow growth curve. This second dose and heating cycle gives rise to the second glow growth curves. Such idealised first and second glow growth curves for a particular temperature are shown in figure 1.2. By combining the intercepts Q and I' obtained from these two curves it is then possible to evaluate the archaeological dose, AD, that the sherd has received. The assumptions implicit in this approach are discussed by THOMPSON (1970), FLEMING (1975) and BOWMAN (1975). The quartz inclusion technique adopts a similar approach to evaluating the archaeological dose, except that in this case the samples are in the form of aliquots of quartz grains about 100 μm in diameter that have been etched in hydrofluoric acid, as already discussed.

Returning to the fine grain technique, an alpha growth curve is produced in a similar manner to that used to produce the first glow beta growth curve, by exposing a series of previously unheated discs to various alpha particle irradiations in order to determine the number of minutes, y, of alpha source irradiation required to increase the level of TL to twice that of the natural TL across the plateau region. As expected theoretically, this has been found to be linear and pass through the origin, and so no second glow growth curve is necessary. This alpha growth curve is then used to evaluate the ratio of the alpha to beta TL sensitivity as described in the next section.

Finally, mention should be made of the phenomenon of anomalous fading (WINTLE, 1973, 1978). Although the plateau test deals adequately with the thermal fading of low temperature TL peaks, it is known that in some materials even high temperature TL, which on kinetic grounds should be stable for millions of years at room temperature, may fade by as much as 50% after only a few days' storage following a laboratory irradiation. Fortunately it appears that such simple storage tests are sufficient to identify the worst cases at least, although it is difficult to establish the reliability of these tests.

1.3 THE ANNUAL DOSE RATE TERM

The annual dose rate to a buried sherd originates mainly from the decay of the various naturally occurring radionuclides, with a small contribution from the cosmic ray flux reaching the earth's surface. The important isotopes in this context are those of the U-238 (and U-235) decay series, the Th-232 series, and K-40. Rb-87 also contributes typically less than 1% to the total dose rate. Table 1.1 gives a breakdown of the contributions of these different sources of dose rate to a buried sherd assuming the radioactive and major element composition of the sherd and surrounding soil are identical and homogeneous. This subdivision of dose rate has been calculated assuming secular equilibrium in the uranium and thorium decay chains, and the 'typical' isotope activities given in the table.

The most commonly used technique for evaluating the alpha component of the annual dose rate, which arises entirely from the uranium and thorium decay chains, is thick source alpha counting with gas cell analysis (AITKEN and BOWMAN, 1975 ; AITKEN, 1978 b). The effective alpha dose rate $\underline{D'_\alpha}$, (equal to $\underline{kD_\alpha}$ in equation (2)) is then calculated from

$$\underline{D'_\alpha} = 0.128\ a\ \alpha \qquad \text{- - - - - - - - - 4}$$

where $\underline{\alpha}$ is the alpha count rate $ksec^{-1}$ from a thick source, 42 mm in diameter, with an electronic threshold set to reject 15% of the pulses from a Th-232 source in secular equilibrium (see Appendix E). The $\underline{a}$ value (AITKEN and BOWMAN, 1975) is calculated from

$$a = \frac{Q}{1300\ Sy} \qquad \text{- - - - - - - - - 5}$$

where $\underline{S}$ is the source strength of the alpha source, in $\mu m^{-2}\ min^{-1}$, used to determine the number of minutes, $\underline{y}$, of irradiation needed to match the natural TL light level (see section 1.2).

The usual technique for evaluating the beta dose, D_β, is beta TL dosimetry (BAILIFF, 1976; MEJDAHL, 1978b; BAILIFF and AITKEN, 1980), and for evaluating the gamma and cosmic dose, $D_{\gamma,c}$, is gamma TL dosimetry (AITKEN, 1968; MEJDAHL, 1970, 1972, 1978a), although other

Table 1.1 Breakdown of the effective annual dose rate to a 'typical' buried sherd containing 1 pCi g^{-1} U-238 (+U-235), 1 pCi g^{-1} Th-232 and 15 pCi g^{-1} K-40

	Alpha % of total	Beta % of total	Gamma % of total
U-238 series	15.5	8.4	6.6
U-235 series	0.8	0.2	-
Th-232 series	13.5	5.2	9.1
K-40	-	28.9	8.8
cosmic ray dose	-	-	3.0
Totals	29.8	42.7	27.5
Total dose rate, mrad yr^{-1}	151	216	139

Note: 1) the decay chains are taken to be in equilibrium.

2) the U-235 contribution was calculated assuming an atomic ratio of 0.00726; this and other nuclear data are given in more detail in Appendix E.

3) the effective alpha contribution is calculated assuming an alpha efficiency at producing TL of 0.1 compared with beta and gamma rays.

4) dose rates are calculated assuming that the energy released per gram is equal to the energy absorbed per gram.

5) the activities given above correspond to 2.9 ppm natural uranium, 9.1 ppm thorium, and 2.1% K_2O.

analytical techniques such as flame photometry (for potassium analysis), neutron activation and fission track analysis are used by some workers.

1.4 SCOPE OF THIS THESIS

The impetus for the first half of this thesis arose during the fine grain dating programme described in chapter 5, in which dates were required for material which had been analysed using archaeomagnetic techniques, in order to derive a curve of variation of the earth's magnetic field magnitude against time. The field work for this programme was undertaken in Peru, and so it became necessary to develop some rapid method of determining the gamma dose rate contribution 'on site', because the existing approach of gamma dosimetry could only be applied in a limited number of cases, as revisiting the majority of these sites was impractical. For the remainder a portable gamma counter was developed, and calibrated to give a direct conversion to dose rate. The calibration of this counter, and the field use in Peru is described in chapter 4.

This gamma counter had been calibrated in terms of dose rate to a buried TL phosphor; the relationship between this dose rate and that to a fine grain of pottery or a quartz inclusion had previously been assumed, and it was decided to investigate this relationship in some detail to provide a sounder interpretation of the measured gamma dose rates obtained from both TL dosimetry and from the gamma counter. This problem is considered from an experimental and a theoretical point of view in chapter 3, where the results obtained from exposing a variety of encapsulated TL phosphors in a concrete matrix of known uranium series activity are described, and compared with prediction.

The dosimetry work of chapter 3 required an accurately calibrated and repeatable laboratory irradiation facility for phosphor grains of about 100 μm diameter. In addition, earlier work by WINTLE and AITKEN (1977) had cast doubt on the existing fine grain beta source dose rate, and this discrepancy had to be resolved before the dating programme of chapter 5 was undertaken. These problems are considered in chapter 2, where revised beta source dose rates to both grain sizes of calcium fluoride and obsidian (a phosphor with energy

absorption characteristics similar to those of quartz) are derived.

In the second half of this thesis disequilibrium in the natural decay chains, particularly that of U-238, is examined in samples of pottery and soils and the long term stability of such disequilibrium patterns considered. The effect of disequilibrium on TL dates is then discussed.

Chapter 6 considers, briefly, the causes of disequilibrium, and its possible effects on TL dates. Gamma spectrometry is proposed as a convenient method of analysing radioisotope concentrations in small samples, and the design and calibration of a sensitive spectrometer is described. The problems of sample self attenuation are considered, and the spectrometer calibrations are confirmed by the analysis of a variety of counting standards, each of well known activity. Further tests are carried out to confirm the reliability of the analysis of low activity samples.

Chapter 7 presents results of such low level analyses. A series of sherds from around the world is analysed to give an overall picture of the likely range of sample activities and degrees of disequilibrium. Preliminary measurement of the degree of grain size dependence on radioisotope concentrations, and also of the proportion of activity held on ion exchange sites in both a clay and a pottery sample are also presented. This latter measurement procedure is then incorporated in the analysis of samples from 5 archaeological sites, two from Peru, two from Hong Kong, and one from Guernsey. The effect of these measurements on derived TL ages is considered. Finally in chapter 7 all the analyses are collected together to permit general conclusions to be drawn about the mechanisms which give rise to the observed disequilibria, particularly escape of Rn-222 in the uranium decay chain.

In chapter 8, the analyses reported in chapter 7 are used to calculate the values of the various parameters that should have been observed for the samples under discussion using the existing techniques of alpha counting and gas cell analysis, beta and gamma TLD, flame photometry and Po-210 alpha spectrometry. These predictions are then compared with the experimental results actually obtained using these methods, and those analytical techniques which appear to be the most reliable are identified.

The results presented in the first half of this thesis have contributed to new knowledge of the history of variations in the geomagnetic field. Furthermore, the measurement of the infinite matrix gamma dose rate by gamma TL dosimetry has been put on a sound basis, and the assumptions previously employed have been shown to be inaccurate by about 20%. This is of considerable importance to those dating techniques which depend heavily on the gamma dose rate contribution, such as the dating of palaeolithic flints and calcite deposits.

The detailed analysis of radioisotope concentrations by gamma spectrometry described in the second half of this thesis has established that disequilibrium in the natural decay series in both pottery and soil samples is commonplace. In addition it has been demonstrated for the first time that a significant fraction of this activity may be held on ion exchange sites, and therefore must be considered potentially mobile.

These analyses have also revealed that the hitherto well established dosimetry techniques of thick source alpha counting and flame photometry can no longer be considered reliable, in contrast to beta TL dosimetry which has been found to be an accurate and precise technique.

CHAPTER II

BETA SOURCE CALIBRATION

2.1 INTRODUCTION

In making absolute dosimetry measurements with TL phosphors, an accurate knowledge of the TL sensitivity is required. This is usually measured by means of a known dose delivered from a beta irradiation using a Sr-90/Y-90 source, and it is important to ensure that the irradiation conditions are sufficiently well defined that the amount of energy absorbed by the phosphor can be accurately reproduced. The dose rate from the source obtained under these conditions is derived from a calibration experiment in which comparison is made with the TL acquired by the phosphor during an accurately known exposure from a gamma source.

It was decided to investigate the existing beta source calibrations in some detail, as the work described in chapters 3 and 5 is very dependent on the accuracy with which doses delivered by laboratory irradiations are known. The problems associated with such irradiations are discussed in sections 2.1 and 2.2, and absolute dose rates from the new laboratory sub-standard beta source (laboratory code $\beta(44)$) to both obsidian and calcium fluoride are derived in section 2.3 for the two ranges of grain size most commonly encountered in TL dating, i.e. 100 μm diameter grains and fine grains of 2 to 8 μm diameter. The validity of equating quartz dose rates with those to obsidian is also discussed.

The existing calibration for fine grains was derived by ZIMMERMAN (1970). However, after investigating the way in which a beta dose builds up with penetration depth, WINTLE and AITKEN (1977) predicted that Zimmerman's calibration ought to be in error by 16%. The work reported in section 2.3 confirms this.

In addition Zimmerman had made a theoretical calculation which predicted that the dose rate to quartz from a beta source would be

1.05 times higher than that to calcium fluoride, for a given set of irradiation conditions. This ratio is important since it is both more convenient and precise to carry out calibrations using the latter. Ratios derived from the absolute dose rates discussed above confirm this value for 100 μm grains of obsidian, but show that for fine grains deposited on an aluminium disc, the ratio is 1.10 ± 0.015. A possible explanation is suggested.

2.1.1 Previous work

It has been customary in this laboratory to refer all dose rates to irradiations by a particular 5 mCi Sr-90/Y-90 plaque beta source (type SIP from the Radiochemical Centre, Amersham; laboratory reference β(5)) at a fixed height of 15.7 mm (0.620 inch) above a phosphor sample of diameter less than 10 mm, resting on a perspex block. These irradiations are usually referred to as 'off plate', while irradiations performed with the sample spread directly on the nichrome heater plate (still constrained to a diameter of less than 10 mm) are referred to as 'on plate'. Both these irradiation geometries are illustrated in figure 2.1.1.

The 'off plate' facility was originally calibrated by AITKEN (private communication) using natural calcium fluoride grains of about 100 μm in diameter which had been given a known exposure in a Co-60 gamma beam at the Churchill Hospital, Oxford. The TL of these grains was read out in the usual way, and the light level matched with that from an 'on plate' irradiation using the beta source. Then the ratio of 'on plate' to 'off plate' dose rates was determined by giving the samples an 'off plate' beta irradiation, transferring the grains to the heater plate for measurement, and then irradiating 'on plate' and measuring again. This ratio of dose rates is known as the 'on/off' ratio and was used to give the absolute value of the 'off plate' dose rate to 100 μm grains of calcium fluoride which was then adopted as the laboratory standard. ZIMMERMAN (1970) converted from this calibration to dose rates in other phosphors (in particular, quartz) using calculated values of the appropriate stopping powers. The calculations behind this conversion were not given in detail, but presumably were based on a knowledge of the primary beta spectrum from the source, and

Figure 2.1.1 'On plate' and 'off plate' irradiation geometries

'Off plate'

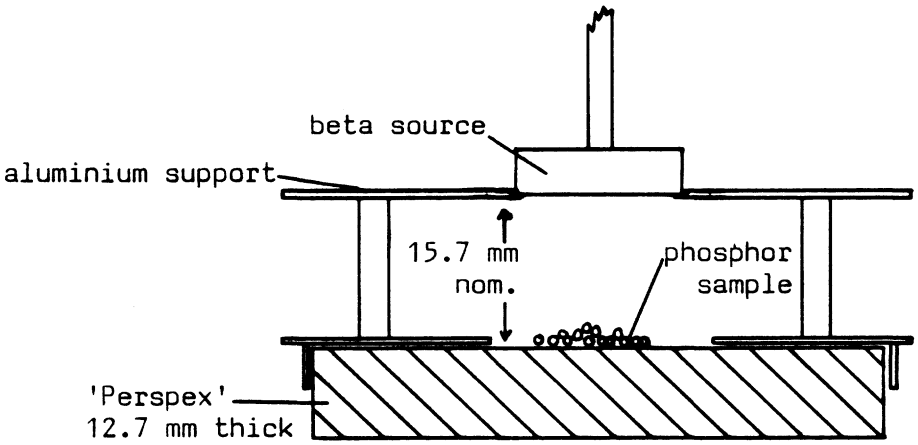

'On plate'

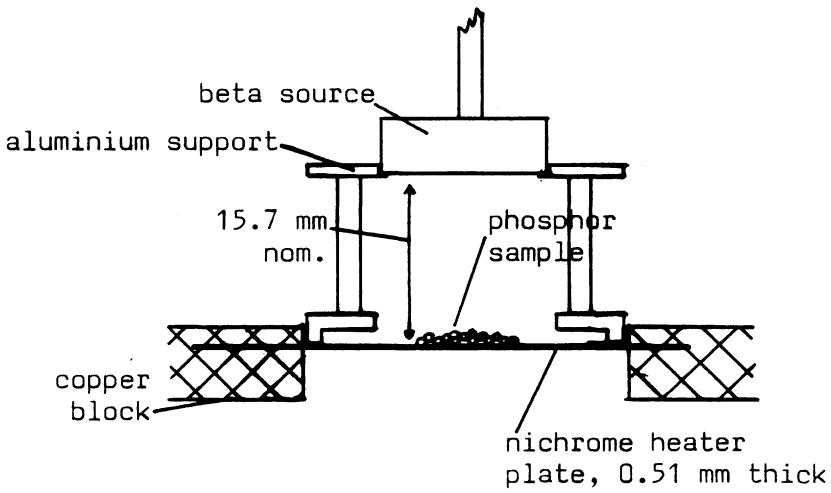

calculated values of the electronic stopping powers. However, as there is a considerable contribution from the backscattered flux, (the dose rate to 100 μm grains is about 40% more 'on plate' than on perspex) and as the ratio of the stopping powers is not independent of energy, it is not clear that this assumption is justified. Nor is it obvious that the value applicable to 100 μm grains will also apply to fine grains, which will be more uniformly irradiated by the low energy backscattered flux, making any variation in response at low energies more important.

In addition, of the various factors likely to affect the reproducibility of laboratory irradiations, only the uniformity of dose rate across the sample and the effect of the size of the phosphor grains, were investigated in any detail. The factors likely to affect this reproducibility are:

(a) the phosphor used,
(b) the source to sample distance,
(c) the backing material on which the sample is spread,
(d) the uniformity of dose rate across the sample,
(e) the sample thickness,
(f) the size and shape of the phosphor grains.

ZIMMERMAN (1970) found that the dose rate to a TL phosphor located in the inner 10% of a 10 mm diameter area is about 9% higher than that to the outer 10%, for a source to sample distance of 15.7 mm. He also deduced from experiment that the beta dose rate to fine grains is the same as that to 100 μm grains (to better than 1%) when both are irradiated on the same backscattering material, aluminium. As this conclusion has been questioned by WINTLE and AITKEN (1977) and proved erroneous by work presented in this chapter, his experimental procedure will now be described.

He first established that the beta dose rate to 100 μm grains of natural calcium fluoride irradiated on aluminium was 1.18 times that to the same grains on perspex. This increase was attributed to enhanced backscattering. He then irradiated 100 μm grains on perspex, crushed them in an agate mortar and deposited the fine grain fraction (2 to 8 μm) onto aluminium discs in the usual manner. The TL from these grains was then read out and matched with that from a subsequent

beta irradiation. From these observations he calculated that the dose rate to fine grains on aluminium was 18% higher than that to 100 μm grains on perspex.

However, WINTLE and AITKEN (1977), in a study of beta dose variation with depth, showed that the dose rate at first increased with depth in a 300 μm slice of TL phosphor. This increasing dose rate was attributed to build up of an isotropic electron flux as the beta rays penetrated the absorbing material. From this they calculated that the average dose rate to 100 μm grains, when irradiated on aluminium, should be 1.16 times that to fine grains on aluminium i.e. 16% more than indicated by Zimmerman's experiments.

This discrepancy clearly had to be resolved before any further TL dates based on fine grain dose rates were to be attempted. However, before considering the calibration procedure directly, additional problems in the reproducibility of the 100 μm grain laboratory dose rates must be described.

2.1.2 Reproducibility of the 'on/off' dose rate ratio

The reproducibility of the 'on/off' ratio for fine grains on aluminium discs has been found to be excellent (typically better than 1%). Unfortunately the reproducibility of this ratio for loose 100 μm grains is only about ± 4%. This is clearly unacceptable, bearing in mind that this ratio is used initially to derive the standard 'off plate' dose rate, and again subsequently to derive the 'on plate' dose rate for other TL sets.

In examining the causes of this spread, it was decided to investigate the reproducibility of the 'on plate' dose rates directly using two phosphors, calcium fluoride and obsidian. The relevant characteristics of obsidian are described in section 2.2.1, those of calcium fluoride are given in AITKEN (1968). Approximately 500 mg of each was exposed in glass capsules (3 mm wall thickness) in a Cs-137 gamma beam and given doses of about 100 rads. These two phosphors were then measured on three different TL sets and the number of minutes of 'on plate' beta irradiation (known as 'equivalent time') needed to match the gamma induced TL noted. The usual 'on/off' ratios were measured at the same time, using the appropriate phosphor.

These results are listed in table 2.1.1. Note that the spread in irradiation time for each phosphor when the gamma induced TL was matched with an 'on plate' irradiation is much less than for the time needed 'off plate' derived using the measured 'on/off' ratios. The ratio of irradiation time 'on plate' for calcium fluoride to that for obsidian, given in table 2.1.1, is also seen to be constant. As some spread in the 'on plate' dose rates is to be expected as a result of slight variations in the 'on plate' irradiation distance (the heater plates tend to warp by as much as 0.5 mm with use) this ratio is a better indicator of the true spread in dose rates for 'on plate' irradiation at a fixed height. Thus it seems from these data that the poor reproducibility in the 'on/off' ratios lies in the 'off plate' irradiations.

It seemed likely that variations in sample thickness 'off plate' could cause variations in dose rate and so the 'on/off' ratios were remeasured using 300 μm thick slices of both CaF_2:Dy and obsidian. These ratios are listed in table 2.1.2. Note that in this case both aluminium and perspex were used as a backing material for the 'off plate' facility. It can be seen that the results are consistent for a given backing material, reinforcing the suggestion that the reason for the poor reproducibility lies in variations in the 'off plate' sample thickness. Note that there is no evidence that the 'on/off' ratio varies between the two phosphors used.

2.1.3 Dependence of dose rate on backing material

To determine the importance of changes in the effective backing material, the relative dose rates to 100 μm grains of calcium fluoride were measured on four different backscattering materials, perspex, aluminium, nichrome and lead, all of which were sufficiently thick to completely absorb the incident beta particles except for nichrome, which was a standard glow oven heater plate, 0.51 mm (0.02 inch) thick. (The incident beta rays would be stopped by about 3 mm of nichrome). Approximately 5 mg of 90 to 125 μm grains of calcium fluoride was spread in the usual manner on the various backscattering materials for irradiation and then transferred to the heater plate for measurement of the TL. The observed dose rates, normalised to that on perspex, are plotted against the atomic number of the back-

Table 2.1.1

Direct investigation of the reproducibility of 'on plate' dose rates

Set	Beta irradiation time: Calcium fluoride min	Obsidian min	Calcium fluoride / Obsidian
3.6	1.41	1.35	1.04
3.7	1.46	1.41	1.04
3.9	1.44	1.38	1.04
'on/off' ratios measured simultaneously with above:			
3.6	1.30	1.27	
3.7	1.28	1.32	
3.9	1.40	1.31	
Derived beta irradiation time for 'off plate' irradiation:			
	min	min	
3.6	1.83	1.71	
3.7	1.87	1.87	
3.9	2.02	1.81	

Note: standard errors derived from at least four individual measurements of each figure were typically $\pm$ 1%

Table 2.1.2

'On plate' to 'off plate' dose rate ratios for 300 μm slices of calcium fluoride:Dy and obsidian

Set	'Off plate' medium	Calcium fluoride:Dy	Obsidian
3.6	aluminium	1.137	-
	'Perspex'	1.250	-
3.7	aluminium	1.139	1.131
	'Perspex'	1.260	1.258

Note: standard errors based on at least four measurements of each ratio were typically less than ± 1%.

scattering medium in figure 2.1.2. Note that as already discussed there will be experimental errors of about ± 4% in these dose rates.

It can be seen that even when irradiated on aluminium a considerable fraction (more than 20%) of the total dose absorbed by the phosphor comes from backscattered flux. As the electronic stopping powers of calcium fluoride are very close to those of aluminium, it is important to determine the depth in the backing material from which this flux originates; if a sample was to be irradiated on perspex, but not as a single layer of grains, it is possible that some grains would be irradiated by a different backscattered flux from others and thus absorb a different dose.

2.1.4 Variation of dose rate with thickness of backscattering medium

The 'on/off' ratio was measured with calcium fluoride grains, 90 to 150 μm in diameter using the perspex 'off plate' facility. This ratio was then remeasured using various thicknesses of aluminium foil between the sample and the perspex plate. These data are presented in figure 2.1.3 as the variation of dose rate with the thickness of aluminium foil, normalised to the dose rate on perspex. This ratio was also measured using a thick aluminium plate (12.7 mm) which gave a dose rate 20% higher than that on perspex alone, as would be expected from figure 2.1.2. The errors on each measurement again will be about ± 4%.

The smooth curve shown in figure 2.1.3 is a best fit to the equation

$$D = F\,(1 - e^{-\lambda x}) + 1 \qquad \text{- - - - - - - - 1}$$

where x is the foil thickness in microns,

F is the fractional increase in dose rate going from perspex to a thick aluminium plate,

and D is the observed dose rate normalised to that on perspex alone.

Taking F as 0.2, gives

$$\lambda = 0.006\ \mu m^{-1}$$

Figure 2.1.2

Ratio of beta dose rates to loose 100 μm grains of calcium fluoride, irradiated on various materials

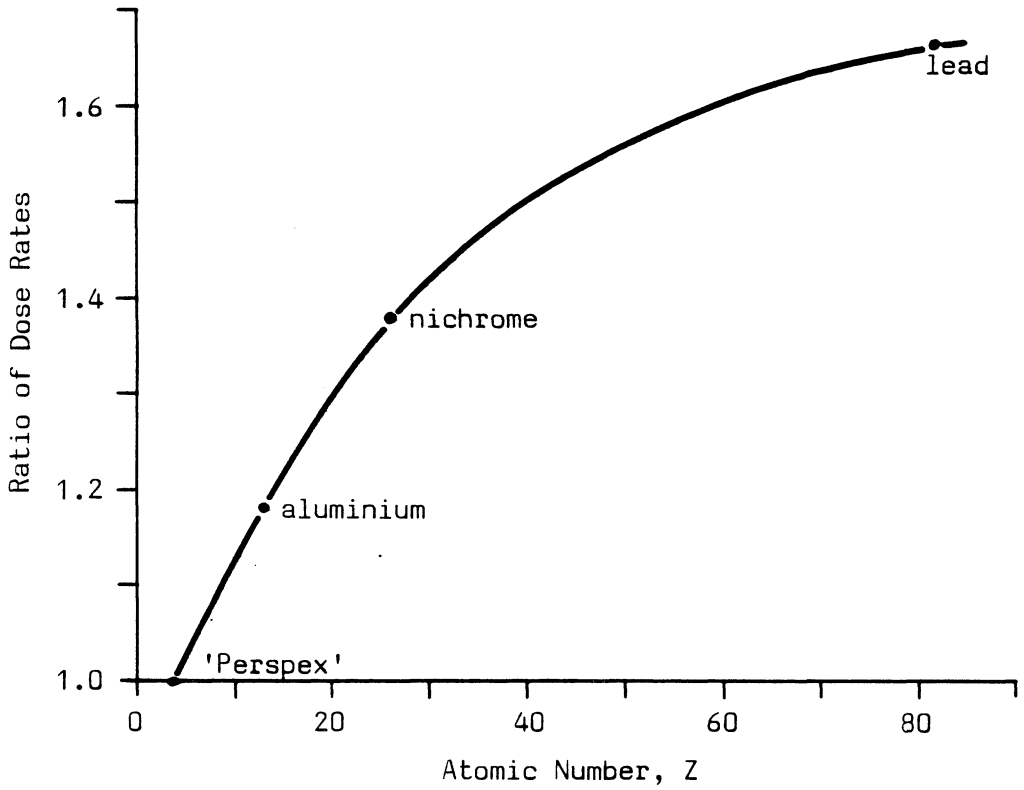

Figure 2.1.3 Variation of total dose rate to loose 100 μm grains of calcium fluoride with thickness of aluminium supported by 'Perspex'

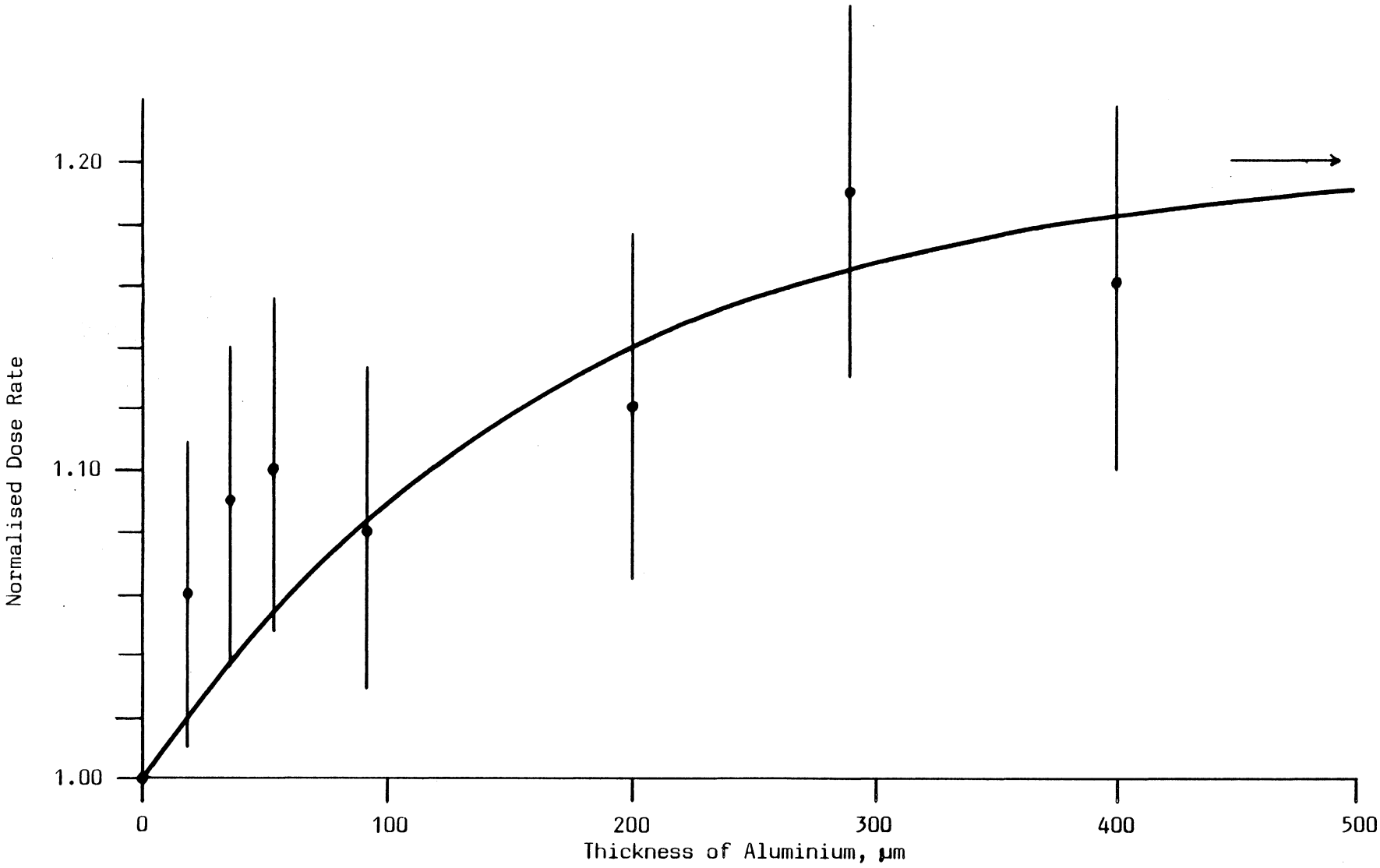

which in turn gives a characteristic backscattering depth of about 115 μm of aluminium, i.e. 30 mg cm^{-2}.

2.1.5 Discussion

From the results presented in section 2.1.2 it was concluded that the poor reproducibility in the 'on/off' ratios was likely to be because of variations in the spreading of samples 'off plate', giving grains piling on top of one another to varying degrees. This will affect the dose rate in three ways. Firstly, there will be a simple height dependent variation; if the sample is, say four grains thick, then the top layer will absorb about 2.5% more than the bottom layer, simply because it is closer to the source. (This neglects any attenuation of the beam passing through the sample).

In addition, there will be a variation due to the build up of the isotropic electron flux within the phosphor. According to WINTLE and AITKEN (1977) the dose delivered to a 300 μm thick sample is 6% higher because of this mechanism than that to a 100 μm thick sample.

Finally there will be a dose rate variation with sample thickness because of the change in the effective backscattering medium going from the bottom grains in a pile, in contact with perspex, to those at the top of a pile, which rest on other calcium fluoride grains. From data presented in BERGER and SELTZER (1964) it is known that the stopping powers of aluminium and calcium fluoride will be very similar, within one percent from 10 keV to 1 MeV, and within 3% to 3 MeV (see figure 3.3.6, chapter 3) and so the degree of backscattering of the incident particle beam is likely to be similar for these two materials. Thus we can consider the results presented in section 2.1.4 for aluminium as applicable to calcium fluoride as a backscattering material. This suggests that the dose rate to a 100 μm grain resting on top of a layer of such grains supported on perspex, would be about 10% higher than the dose rate to the bottom layer.

This potential dependence of dose rate on sample spreading is clearly unsatisfactory and before attempting an accurate absolute source calibration, the 100 μm grain irradiation geometry must be more precisely defined.

2.1.6 A new method of sample preparation for 100 μm grains

The excellent reproducibility of the fine grain samples deposited on aluminium discs suggested an improved irradiation geometry for larger grain sizes. It proved possible to make a satisfactory form of coarse grain disc by giving a light spray of silicone oil to an aluminium disc, spreading a 100 μm grain sample as evenly as possible across the surface, and then inverting and tapping to remove any surplus not adhering to the silicone oil. This approach was seen to give a mono-layer of grains stuck to the disc when viewed under a microscope, i.e. a reproducible thickness. As well as giving good reproducibility in the measurement of 'on/off' ratios, this technique also offers the advantage that the sample is now in a form suitable for long term storage after irradiation or measurement, which was not readily achieved with grains placed directly on the heater plate.

Unfortunately the combination of aluminium and silicone oil was also shown to give rise to spurious (non radiation induced) TL, at any rate after storage in the dark exposed to the atmosphere. This spurious light level was shown to increase with storage time and although the intensity was too low to affect the type of work described here, it would be sufficient to interfere significantly with the lower light levels usually found in archaeological quartz; in one case the spurious signal was found to be as much as four times the light level from a quartz sample with an archaeological dose of about 400 rads.

Accordingly, similar 10 mm diameter discs were prepared from 0.61 mm (0.024 inch) stainless steel. When samples were prepared on these discs similar excellent reproducibility in the 'on/off' ratios was obtained, as can be seen from table 2.1.3, and furthermore, there was no measurable spurious signal after a storage of one week in air (under red light only). This sample geometry is now employed for routine irradiation and measurement of archaeological quartz in this laboratory.

2.2 THE PROBLEMS ASSOCIATED WITH THE USE OF QUARTZ AS A CALIBRATION PHOSPHOR

Before considering the absolute calibration procedure, it is

Table 2.1.3

'On plate' to 'off plate' dose rate ratios for 100 μm grains of calcium fluoride and obsidian on 0.61 mm thick stainless steel discs

Date	Phosphor	'on/off' ratio
August 1977	calcium fluoride	1.022_{6}
Sept. 1977	obsidian	1.022_{6}
June 1978	calcium fluoride	1.003_{6}
June 1978	obsidian	1.024_{6}

Note: errors shown are standard errors derived from at least four measurements and are in the least significant figures.

necessary to consider the suitability of the phosphors to be used. Clearly it is desirable to calibrate a beta source with the phosphor to be subsequently studied. With phosphors such as calcium fluoride this is straightforward, but not with quartz. It is well known that the high temperature region of the quartz glow curve may show undesirable characteristics such as low sensitivity, non-linearity with dose, and dose dependent sensitivity changes on heating (pre-dose) which make it difficult to reliably evaluate the dose in a sample to an accuracy of better than about 5%. However, it is possible to make accurate measurements using the 110°C peak if certain precautions are taken. Although the sensitivity of this peak is also dependent on its irradiation history, FLEMING (1969) has shown that it is possible to saturate the sensitivity change mechanism. If the material is given a large dose (Fleming used 10^6 rads), and is heated to about 500°C, the sensitivity of this peak then remains unchanged by further dose and heating cycles. In addition, this peak is considerably more sensitive than the high temperature region, permitting dose measurements of only a few rads.

Unfortunately, the half life of this peak is about 145 minutes at 19°C, which is reduced to 75 minutes if heavily irradiated before use. FLEMING (1969) observed a change in trap depth after heavy irradiation and postulated increasing localisation of luminescence centres and traps as the changing physical process. This half life is a severe restriction as the calibrated gamma source used for accurate exposures is located several miles from the laboratory. It was in fact considered impractical to make any attempt to calibrate directly using quartz as a phosphor, although relative measurements are reported in section 2.2.2. Instead attention was turned to the use of obsidian as a quartz substitute.

2.2.1 TL and dosimetry characteristics of obsidian

A typical major element composition of obsidian may be taken as 10% Al_2O_3, 84% SiO_2 with the remainder Na, K and Ca (TAYLOR,1976). The mass energy absorption characteristics have been calculated for such a mixture of elements and found to be indistinguishable from those of pure SiO_2 (quartz) at 0.662 MeV (Cs-137). Thus obsidian and quartz will absorb the same amount of energy from an exposure

in a Cs-137 gamma beam. Similarly the ratio of the stopping powers of obsidian to quartz are within 0.4% from 25 keV to 2.5 MeV, and so these two materials will absorb the same amount of energy when exposed to a beta source.

The material described in the following section is an obsidian from Obsidian Creek, British Columbia. It has been used in three forms, as 300 μm thick slices, as 90 to 125 μm grains and as fine grains (2 to 8 μm). The solid material was crushed in a steel mortar and sieved to separate the 90 to 125 μm grain fraction, which was then washed in acetone to remove any residual dust and dried. Fine grains 2 to 8 μm were deposited in the usual manner from the fraction below 90 μm. The slices were cut using a diamond impregnated wire saw. The TL characteristics described here were obtained from 90 to 125 μm grains, usually handled directly 'on plate'.

The glow curve, with the black body radiation subtracted, of a 5 mg sample heated at 10°C sec^{-1} after annealing at 550°C and beta irradiating, is shown in figure 2.2.1. All the behaviour reported here refers to that of the area of peak III at 305°C integrated from 250°C to 350°C. The emission bands of peaks I, II, and III have been measured by BAILIFF (private communication) and all three show an increase of intensity around 480 nm and 580 nm, the limit of Bailiff's measurements.

It was found that the reproducibility and sensitivity were dependent on the time spent at the maximum annealing temperature; the sensitivity decreased by a factor of four when heated at 10°C sec^{-1} to 700°C rather than 550°C. On the other hand when the sample was irradiated, read out to 550°C, cooled, and then the cycle repeated, the light output decreased by 6%. The annealing condition finally adopted involved heating to 550°C, maintaining this temperature for 1 minute, and then cooling to room temperature, all in an atmosphere of oxygen free nitrogen. The subsequent maximum heating temperature was 500°C. After this treatment the sensitivity decreased by less than 1% for each heating through to 500°C independent of dose given (up to at least 300 rads).

The linearity of response of this phosphor has not been investigated explicitly because the method used to evaluate a dose in a

Figure 2.2.1 Tl glow curve of 90 to 125 μm grains of obsidian, after a beta dose of about 150 rads

Note: heating rate 10°C sec^{-1}, 7-59 and HA3 filters

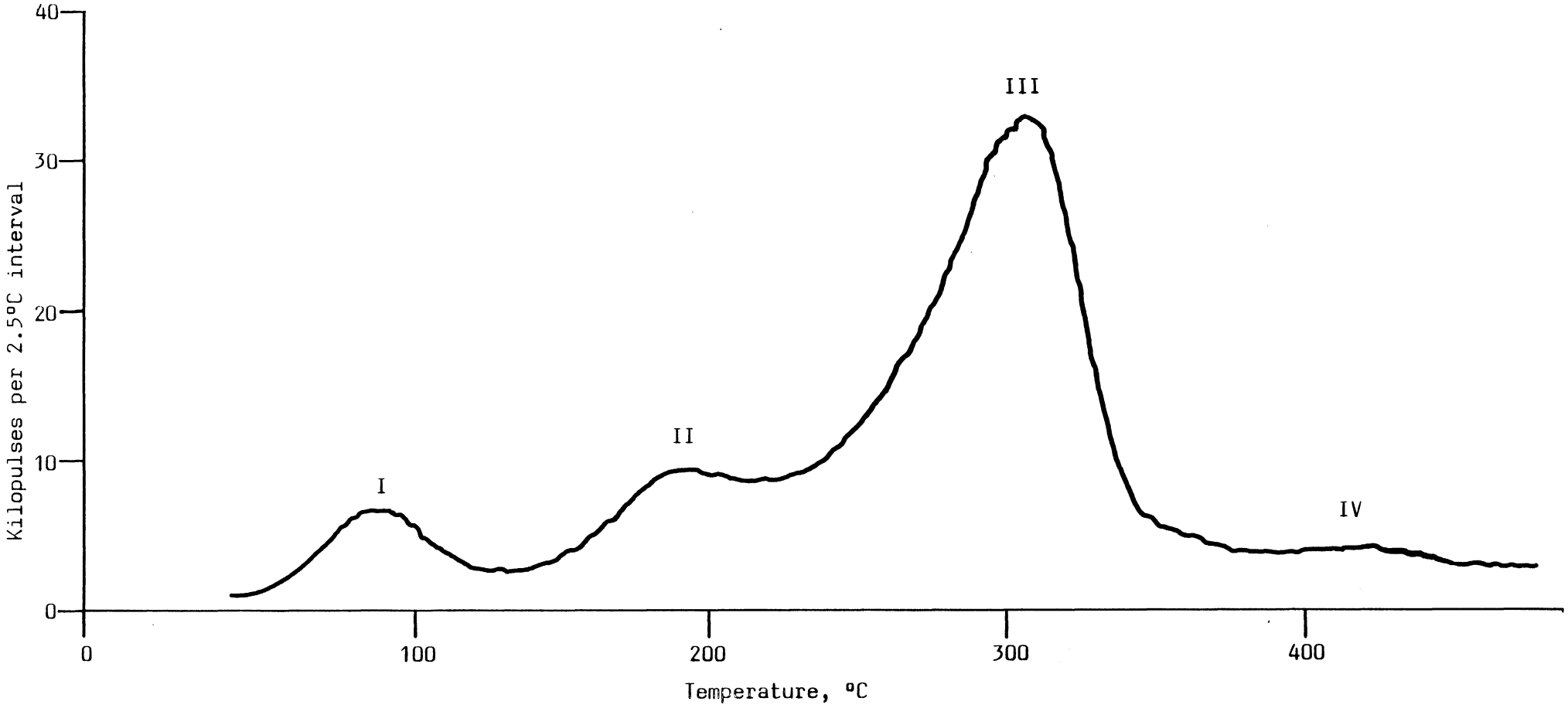

sample, i.e. matching the light level with that from a subsequent beta irradiation, is not dependent on linearity of response, but only on an absence of significant sensitivity changes. However, the response has been measured for one sample at two different levels covering the dose range of interest, namely 151 rads and one rad. The light levels observed in each case for a 3 mg sample were 7.11×10^3 rad^{-1} ($\pm$ 0.05) and 7.50×10^3 rad^{-1} ($\pm$ 0.06) respectively.

Of more importance in this context is the presence of non radiation induced TL, including that induced by visible light. The TL induced when the phosphor was exposed to a 60 watt light bulb at a distance of 30 cm for one minute was approximately equal to that from a one rad dose. However, when exposed to the red fluorescent light used routinely for TL work, the induced TL was not measurable (i.e. less than 1% of that induced by a dose of one rad). In addition there was no measurable TL induced when the sample was scratched across the heater plate with a spatula.

Finally, the fading characteristics of the material were investigated by irradiating samples and storing for various periods of time. They were then read out, irradiated again and read out immediately. The results of several such measurements are listed in table 2.2.1. Little or no correlation with storage time or dose can be seen, although the phenomenon was found to be reproducible within one set of measurements. Although table 2.2.1 suggests a fading of (6 $\pm$ 1)% in the first half hour and none thereafter, it has been routine practice to monitor the fading appropriate to each experiment, as described in the next section.

2.2.2 Comparison of the dosimetry response of the 110°C peak in quartz with that of the 305°C peak in obsidian

As discussed in section 2.2, it is possible to saturate the predose effect in the 110°C peak in quartz with a large dose. Thus if the problem of the short half life can be overcome, it is possible to compare the dosimetry response of quartz and obsidian directly.

A previously annealed sample of quartz grains (90 to 150 μm) prepared from material supplied by British Drug Houses as 'native quartz' was given a beta dose of approximately 35 krads, heated up to 550°C and allowed to cool. The reproducibility of the response

Table 2.2.1

Fading of peak III in the obsidian glow curve

Storage time	Initial dose rads	Ratio of 'faded' to 'prompt' TL
0.1 hr	50	1.01 $_{2}$
0.5 hr	1	0.93 $_{3}$
1 hr	1	0.88 $_{3}$
2 hr	1	0.94 $_{2}$
16 hr	150	0.96 $_{1}$
7 days	50	0.94 $_{3}$
42 days	50	0.98 $_{2}$
42 days	50	0.97 $_{2}$

Note: 1) errors are standard errors from at least four measurements on each sample, are are in the least significant figures.

2) the two 42 day measurements were taken at different times.

of this material to doses of about 60 rads was found to be better than 2% to one standard deviation, with no sign of systematic changes in sensitivity. About 200 mg of this material was then packed into glass tubes of 3 mm wall thickness, 3 mm internal diameter and about 15 mm long. A portion of 90 to 125 μm grains of recently annealed obsidian was similarly packed and both capsules were exposed simultaneously for 30 seconds in a Cs-137 gamma beam (0.662 MeV). The dose absorbed (about 60 rads) by both materials from this exposure should be the same, as discussed in section 2.2.1.

Fading of the obsidian was monitored by giving a sample of the annealed grains an 'on plate' beta dose. This sample was then packed into a separate but identical glass capsule about 20 minutes before the gamma irradiation. The two obsidian capsules were then kept together (except of course during the irradiation itself) until the obsidian grains were read out. The TL from the 'faded' grains was then compared with that from a subsequent beta dose, read out immediately, to give a fading correction of (5 $\pm$ 1)% after about 28 hours. Employing this correction gave an 'equivalent time' of 0.759 minutes $\pm$ 0.009 for the obsidian irradiation.

The quartz grains were measured as soon as possible after the gamma irradiation; the 'equivalent times' measured at various times are shown in figure 2.2.2. These data can be represented by an equation of the form

$$M = M_o e^{-\lambda t} \qquad - - - - - - - \quad 2$$

where M is the 'equivalent time' observed at time t,

M_o is the 'equivalent time' at $t = 0$,

and λ is a decay constant.

A best fit to these data gives

$M_o = 0.767$ min $\pm$ 0.010

and $\lambda = 0.01255\ \text{min}^{-1} \pm 0.00018$

which corresponds to a half life of 55.0 min $\pm$ 0.8. This is significantly shorter than the figure of 75 minutes obtained by FLEMING (1969)

Figure 2.2.2

Decay of TL from the 110°C peak in quartz after gamma irradiation

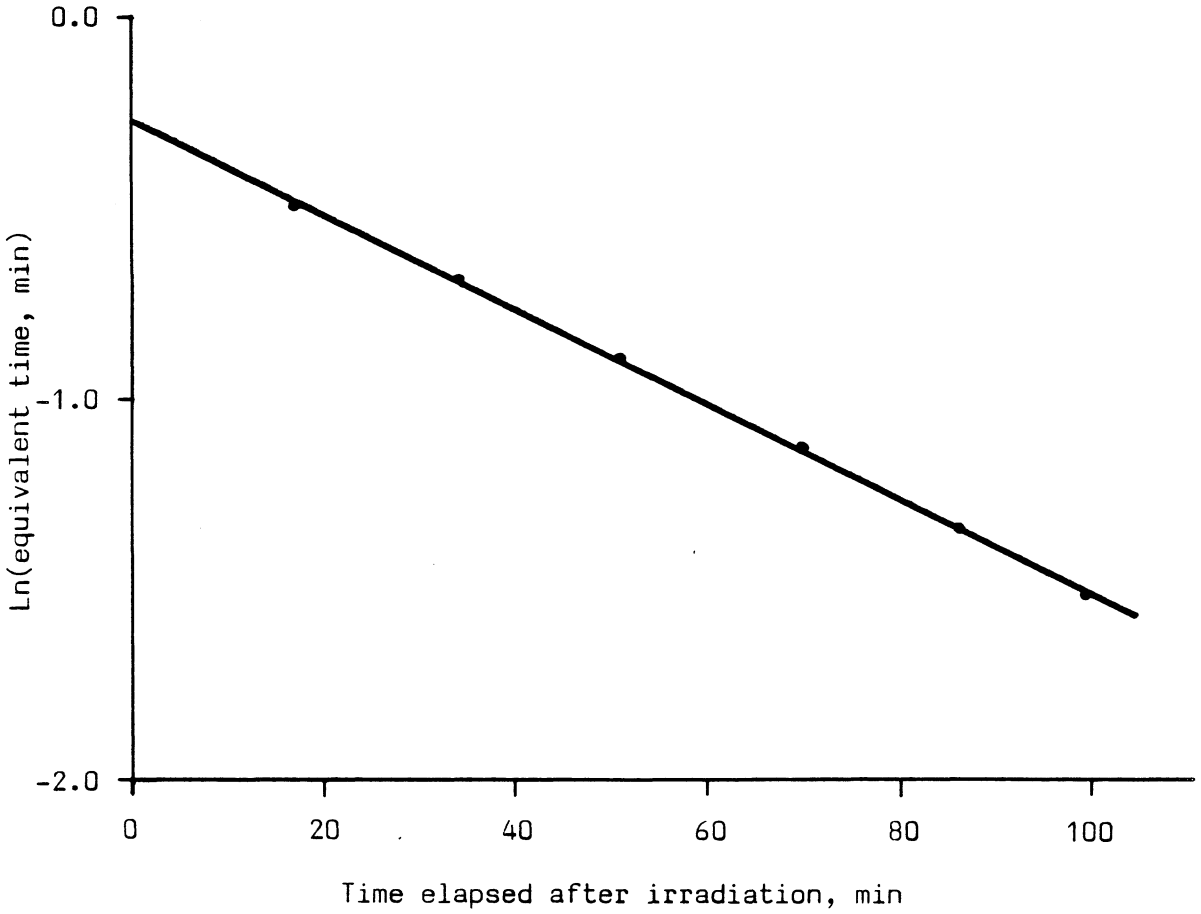

and is probably due to the higher ambient temperature (estimated at 22°C, rather than Fleming's 19°C).

The beta irradiation times for the two materials, quartz and obsidian, are the same to within the experimental error of less than 2%. This result confirms that the effective dose delivered by the beta source is the same for both the 110°C peak in quartz and the 305°C peak in obsidian.

2.2.3 The dosimetry of the high temperature region in the quartz glow curve

It has been shown that the dosimetry response of the 305°C peak in the obsidian glow curve is indistinguishable from that of the 110°C quartz peak, and this suggests that the same will apply to the high temperature quartz peaks around 350°C. This assumption is supported by measurements made on a quartz which had been given a known dose using a gamma beam by PERNICKA and WAGNER (1979). HUXTABLE (private communication) has analysed this material using the beta dose rate to 100 μm grains of obsidian derived in the next section, and she found that the ratio of the measured dose to that given by the gamma irradiation was 0.96, with an estimated total uncertainty in this ratio of 5%.

Nevertheless, the reliability of this assumption can be questioned because of the transparency effects found in quartz by BELL (1980 a,b) and BELL and MEJDAHL (1980). As quartz and obsidian are very different in transparency, and in view of the results of the previous section, it seems unlikely that this effect is interfering in the present work, and it should be noted that Bell uses 20 mg samples in platinum cups without making any attempt to ensure either a monolayer of grains or a uniform sample thickness from one batch of twenty-four samples to the next. However, it must also be acknowledged that BELL and MEJDAHL (1980) have observed marked correlation between apparent beta dose rate and quartz firing temperature which can be accounted for most readily in terms of grain transparency changes, and it must be concluded that the importance of grain transparency in the dosimetry of the high temperature peaks in quartz is far from understood, and further investigation is needed before the beta dose rate to obsidian grains is extended to cover the high temperature quartz glow curve.

2.3 ABSOLUTE CALIBRATION

The absolute calibration of the beta source was undertaken by comparing the TL induced by a known exposure to gamma rays with that induced by the beta source. The preceding sections have been solely concerned with relative dose rates, and it has not been necessary to discuss in any detail the gamma doses absorbed by the various materials. However, for the absolute calibration of the laboratory beta source, the mechanism of dose absorption from gamma rays must be considered, to allow accurate calculation of the dose delivered to a phosphor.

Gamma rays interact with matter mainly by the Compton or photo-electric processes, at least at the energies of interest here. These interactions produce fast secondary electrons, which then go on to dissipate their kinetic energy by multiple interactions with other electrons. The amount of energy transferred per unit mass from the gamma rays to these secondary electrons, the kerma, $\underline{K}$ is given by

$$K = F\,(^{\mu}K/\rho) \qquad \text{- - - - - - - - - - 3}$$

where $\underline{F}$ is the gamma ray fluence,

and $\underline{(^{\mu}K/\rho)}$ is the mass energy transfer coefficient, a characteristic dependent on the gamma ray energy and the atomic number of the material in which the energy is deposited.

If the energy imparted to secondary electrons at a point in the material of interest, i.e. the kerma, is equal to energy absorbed from charged particles at that point, then charged particle equilibrium (CPE) is said to exist, and the dose absorbed can be readily calculated. This is seldom rigorously true, and care must be taken to ensure that it is at least closely approximated. For instance some of this energy will be radiated as Bremsstrahlung photons and thus will escape from small dosimeter materials; this loss can be taken into account by replacing the mass energy transfer coefficient with the mass energy absorption coefficient $\underline{(^{\mu}en/\rho)}$. At the energies of interest this is a negligibly small change (< 1%).

In practice, gamma ray irradiations are usually calibrated in terms of exposure rather than fluence. The exposure is a property of X or gamma radiation at a point and is a measure of the potential ability of the radiation to produce ionization in air at that point. As an exposure of one Roentgen delivers a dose of 0.869 rads in dry air (assuming CPE), if the exposure, $\underline{X}$, at a point is known then the dose, $\underline{D}$, in some other material placed at that point, such as a TL phosphor, can be calculated from

$$D = 0.869 \frac{(\mu_{en}/\rho)_{phosphor}}{(\mu_{en}/\rho)_{air}} X \quad - - - - - - 4$$

where $\underline{(\mu_{en}/\rho)_{phosphor,\ air}}$ are the mass energy absorption coefficients.

This relationship again assumes CPE, and also that the gamma flux throughout the phosphor is identical with that at the point at which the exposure would have been measured.

In order to ensure CPE throughout the volume of the irradiated phosphor, it is usually surrounded by a buffer material, which must be at least as thick as the range of the most energetic secondary electrons produced by the gamma flux; this is about 1 mm in materials such as glass or aluminium, at 0.662 MeV. Only if the atomic constituents of this buffer are identical with, or at least very similar to, those of the phosphor (e.g. a glass capsule containing quartz) will equation 4 still strictly apply.

For the purposes of source calibration, it was decided to irradiate both calcium fluoride and obsidian in glass capsules of 3 mm wall thickness, 3 mm internal diameter and length 15 mm; the capsules were completely filled. As the major constituents of obsidian are very similar to those of glass, these two materials may be considered perfectly matched. For calcium fluoride the match is still considered good; the ratio of the electronic stopping powers and the mass energy absorption coefficients of calcium fluoride to glass are 0.95 and 1.02, respectively, at 0.662 MeV. The stopping power ratio does not vary significantly with energy. These small differences, coupled with the large effective path length to secondary electrons of the

phosphor itself should ensure that errors arising from the use of equation 4 are negligible if appropriate allowance for the photon attenuation through the wall material is made.

2.3.1 Attenuation in capsule wall

ROESCH (1958) showed that the dose deposited at a point in aluminium irradiated by 0.6 MeV photons is equal to the kerma produced about 0.3 mm closer to the gamma source, once CPE has been established. Thus when allowing for attenuation of the gamma beam in the buffer material surrounding the phosphor, this must be subtracted to give the attenuating thickness of material. This gives an effective thickness for the glass walled capsule (measured density 2.66 g cm^{-3}) of about 2.7 mm, which will attenuate the 0.662 MeV gamma beam by 5.5%.

It must also be recognised that the phosphor itself is of finite thickness. The internal diameter of the glass capsule is 3 mm, and so the average gamma path length through the phosphor if irradiated normal to the cylindrical axis will be about 2 mm. If the exposure is known at the point in air replaced by the centre of the phosphor, then the average attenuation will be that through 1 mm of phosphor grains.

The packing density of such grains is dependent on the capsule internal diameter; an effective density of about 2 g cm^{-3} has been measured for these capsules. Thus the effective phosphor attenuation is about 1.5%, which gives a total gamma beam attenuation of about 7%.

2.3.2 Phosphor irradiations

Both calcium fluoride and obsidian 100 μm grains were annealed and packed into capsules as described above which were then covered with a light-tight layer of black plastic tape. The obsidian fading was monitored by giving an 'on plate' beta irradiation to obsidian grains on stainless steel discs. These grains were then removed and packed into an identical glass capsule which was stored with the annealed grains at all times, except during the actual gamma irradiation, when the fading capsule was placed in the same room, but remote from the gamma beam. The fading was measured in the usual way, at

the same time as the gamma irradiated samples, as 5% and 2% for two separate irradiations.

The fine grain calibration was also undertaken using samples of calcium fluoride and obsidian, crushed in an agate mortar and then annealed. This dust was then packed into capsules, again sealed with a single layer of black tape. After being gamma irradiated, the 2 to 8 μm grains were deposited on aluminium discs in the usual way. The obsidian fading was monitored in this case using predeposited obsidian discs, again given an 'on plate' beta dose, as 2.5% and < 1% for two separate irradiations.

The gamma irradiations were given at the National Radiological Protection Board, Harwell, using a Cs-137 source in scatter free geometry which had been standardised by the National Physical Laboratory. The experiment was performed on two occasions, six months apart, and the doses absorbed were about 50 rads and 100 rads. The calcium fluoride fine grain calibration was also performed a third time. The 'on/off' dose rate ratios were measured each time to give the 'off plate' dose rates given in table 2.3.1, and the errors shown are standard errors on the mean of at least four measurements from each capsule. Note that a new standard source, β(44), has been adopted. It was felt that the use of a stronger source than β(5) was desirable, as this made direct irradiation of less sensitive materials such as obsidian and quartz practical. The dose rate ratio between these two sources is 7.74 (standard error 0.09).

It is appropriate here to mention the experiment described in MURRAY and WINTLE (1979), where the dose rates derived from the above were compared with those derived using fine grains deposited before gamma irradiation. It was concluded that a significant difference existed. This is not now considered to be the case, as no allowance for the slightly differing electronic stopping powers between aluminium and obsidian or calcium fluoride was made. The uncertainties associated with such corrections are such that it is no longer possible to say a discrepancy exists.

The ratio of the beta dose rate to 100 μm grains of calcium fluoride on stainless steel 'on plate' to the dose rate directly 'on plate' has also been measured as 1.047 $\pm$ 0.010. Combining this

Table 2.3.1

Calibration of laboratory beta source β(44), 'off plate' dose rates

100 μm grains on stainless steel discs		Fine grains on aluminium discs	
Calcium fluoride rads min^{-1}	Obsidian rads min^{-1}	Calcium fluoride rads min^{-1}	Obsidian rads min^{-1}
65.3_{7}	67.8_{7}	46.9_{8}	50.7_{7}
66.0_{4}	69.1_{5}	46.0_{5}	51.0_{9}
		46.0_{4}	
Weighted average:			
65.8_{3}	68.7_{4}	46.1_{3}	50.8_{6}
(69)	(72)	(57)	(60)

Note: 1) all dose rates are corrected to the 15th June 1978 using the Sr-90 half life of 28.0 years.

2) errors shown are in the least significant figures, and are standard errors derived from at least four measurements.

3) figures in parentheses are the dose rates derived from the original calibration.

4) the source was 15.7 mm above the base of the sample disc.

figure with the best estimate of the 'on/off' ratio for loose grains of 1.37 ± 0.05, and for fine grains of 1.01 ± 0.01, permits the derivation of the dose rates given in parentheses from the original calibration of the β(5) dose rate to loose grains of calcium fluoride 'off plate'.

2.3.3 Systematic errors in the evaluation of the gamma dose

In addition to the experimental errors of table 2.3.1, there are various sources of systematic error to be considered. It is assumed that an uncertainty of less than 1% will arise from the assumption that there is no significant dose deposited by photons previously scattered within the wall material of the phosphor, i.e. that the attenuation of the gamma flux is indeed described by the mass attenuation coefficients.

In calculating the absorbed dose knowing the exposure, a ratio of mass absorption coefficients is taken (equation 4). Although the errors in the individual values can be as much as 5% (STORM and ISRAEL, 1970), the relative errors between values of (μ_{en}/ρ) for individual elements will be small; typical relative uncertainties in the average values for compounds are taken to be ± 2%. There is also a negligibly small error in the slight corrections to beta source strength between the two calibrations six months apart, arising from the uncertainties in the 28.0 year half life of Sr-90.

Finally, the estimated total uncertainty in the exposure used was 2% (BURGESS, private communication). This gives a total systematic uncertainty in the absorbed gamma dose of about 3% (errors added in quadrature). When this is added to the experimental errors given in table 2.3.1, typical total uncertainties in source calibrations are 3.5%.

2.3.4 Discussion

Consider first the dose rate to 100 μm grains of calcium fluoride on stainless steel discs. Bearing in mind that the error in the existing calibration is given as ± 5% the revised calibration is consistent with the earlier work, but the associated error, now of about 3.5%, is reduced. The corresponding dose rate to 100 μm grains of obsidian is also consistent with the earlier quartz dose rate, which

in that case was not derived directly, but was the product of the calcium fluoride dose rate with an averaged electronic stopping power ratio of quartz to calcium fluoride of 1.05 (ZIMMERMAN, 1970). The corresponding experimentally derived ratio from table 2.3.1 is 1.044 ± 0.008.

Now consider the fine grain dose rates. There is a large difference (24%) between the existing calcium fluoride fine grain dose rate and the revised figure. As was discussed in section 2.1.1, Zimmerman deduced a ratio of 1.00 between the dose rate to fine grains of calcium fluoride on an aluminium disc and that to 100 μm grains on an aluminium disc. From figure 2.1.2, the dose rate to 100 μm grains on nichrome is 1.17 times the dose rate to 100 μm grains on aluminium. Combining these two ratios, it is to be expected that when 100 μm grains are irradiated on nichrome, i.e. 'on plate', they will absorb 1.17 times the dose that a fine grain sample on an aluminium disc would absorb if it was also irradiated 'on plate'. From section 2.3.2 the ratio of the dose rate to 100 μm grains irradiated on stainless steel discs to that to 100 μm grains directly 'on plate' is 1.047. Thus the predicted ratio between the dose rate to 100 μm grains on stainless steel 'on plate' and fine grains on an aluminium disc 'on plate' using Zimmerman's ratio of 1.00 mentioned at the beginning of the paragraph, is 1.22.

Now consider the same calculation using Wintle and Aitken's ratio of 1.16 between the dose rate to 100 μm grains of calcium fluoride on aluminium and that to fine grains on aluminium. Here the derived ratio of the dose rate to 100 μm grains on stainless steel 'on plate' to that to fine grains on an aluminium disc 'on plate' is now 1.42. The observed ratio for calcium fluoride from table 2.3.1 is 1.43 ± 0.01. (The 'on/off' ratio for both grain sizes on disc is 1.01). This confirms the predictions of Wintle and Aitken and shows that Zimmerman's original derivation was at fault. It is presumed that the disagreement with the earlier calibration derives from the fact that in the Zimmerman process, it was necessary to obtain fine grains from the irradiated 100 μm grains (see section 2.1.1). This had to be by grinding and it is now known that such a procedure can induce TL in unirradiated samples.

Finally let us consider the ratio between the fine grain obsidian

and calcium fluoride dose rates. Zimmerman assumed that the appropriate ratio was again 1.05. However, the observed value is 1.102 $\pm$ 0.015, and reasons why the former ratio should not be expected to apply can be found by considering the dose deposition process. If the curve of increasing dose rate to 100 μm grains plotted against the atomic number of the backscattering medium, shown in figure 2.1.2 is extrapolated back to give that dose rate when no backscattered flux is present (i.e. Z = 0), it can be deduced that the backscattered spectrum deposits approximately 25% of the total dose to these grain sizes. SNYMAN and CLAYTON (1963) give the backscattered spectrum for a Sr-90/Y-90 beta spectrum incident on a thick aluminium absorber; a strong increase in intensity with decreasing energy down to about 100 keV can be seen. Thus, for fine grains the backscattered contribution will be even greater than for 100 μm grains, as a significant proportion of the low energy electrons will be completely stopped within the larger grain sizes. (a 100 keV electron has a range of less than 70 μm in quartz). In contrast to the dose absorbed from high electron energies, this dose contribution will not at first decrease in proportion to grain size. At these low energies the ratio of the electronic stopping powers of quartz to calcium fluoride increases above the value of 1.05. It can be calculated from data presented in BERGER and SELTZER (1964) that this ratio is 1.06 at 200 keV (electrons of this energy would have a range of less than 140 μm in quartz) rising to 1.07 and 1.08 at 100 and 33 keV (ranges of less than 70 μm and 10 μm respectively in quartz).

It can be seen from the above discussion that the dosimetry of fine grains on aluminium is a complex subject, and it would be unwise to place too much emphasis on the numerical values of the stopping power ratio given above. On the other hand it is clear that the ratio of 1.05, derived for the primary spectrum, is not applicable to fine grains and so the experimental result is certainly not inconsistent with theory, which seems to suggest a ratio of between 1.05 and 1.08. The experimentally observed value is used throughout the remainder of this thesis.

2.4 SUMMARY

It has been shown that when considering laboratory beta

irradiations of phosphors, any uncertainties in the backscattering material such as are found when a phosphor grain is not in contact with the substrate, but in fact is supported by other phosphor grains, will give rise to uncertainties in the dose rate to the sample. A new method of sample preparation for 100 μm grains was devised to avoid these uncertainties. The problems of using quartz as a dosimeter were discussed and the TL characteristics of a new phosphor, obsidian, described. It was shown that the response of the 305°C peak in the glow curve of this phosphor to beta and gamma irradiation was the same to within 2% as that of the 110°C peak in quartz. However, it was acknowledged that extending results obtained using obsidian to include the high temperature region in quartz was an assumption.

The problems of accurately calculating the dose absorbed in a gamma irradiation were considered and an irradiation procedure presented which enabled absolute beta dose rates to 100 μm grains on stainless steel discs and to fine grains on aluminium discs to be calculated for two phosphors, calcium fluoride and obsidian. This experiment was repeated twice and the total error associated with the average figures proved significantly less than that of the previous calibration. These results have resolved two major uncertainties in source calibration. Firstly, it was demonstrated that the existing fine grain calibration was in error by 16% and secondly, it was shown that the dose rate ratio between the two phosphors was not independent of grain size, as had previously been supposed, but that in this case the ratio was 5% larger between fine grains of obsidian and calcium fluoride than between 100 μm grains of the two phosphors, for which the existing ratio of 1.05 was confirmed.

The absolute dose rates derived in this chapter give a firm foundation for the dosimetry work of chapter 3, and the fine grain dating programme of chapter 5.

C H A P T E R III

ENVIRONMENTAL GAMMA DOSIMETRY USING TL DOSIMETERS

INTRODUCTION

One of the more difficult problems in TL dating is the reliable estimation of the environmental gamma dose rate. Because of difficulties arising from inhomogeneity, changes in radon escape, and changes in water content, it is not usually sufficiently reliable to employ laboratory analysis of soil samples. If practical, the preferred approach is to bury a sensitive TL phosphor, appropriately encapsulated, in the same or similar surroundings to those from which the pottery fragments were removed. This 'capsule' is then left in place for some months, preferably a full year, to average out seasonal effects, such as changes in water content and radon emanation. This long time period also permits the assumption that the disturbance of the soil layers by excavation of the sherds and subsequent burial of the capsule has had a negligible effect on the gamma field. This approach has been described in some detail by several workers, in particular AITKEN (1968, 1969) and MEJDAHL (1970, 1972, 1978). However, none of these have attempted to test the absolute response of a particular dosimeter, although comparisons with alpha counting of associated soil samples have been made (e.g. HUXTABLE and AITKEN, 1978, described in chapter 7). However, BOWMAN (1976) did attempt such absolute comparisons using 20 inch cubes of concrete doped respectively with uranium and thorium ores, a potassium salt and a solution of Zn-65. She found that the observed dose rates at the centres of these blocks, measured using calcium fluoride in nylon, aluminium and copper capsules, were much lower than expected. These results appeared to cast considerable doubt on the conversion from a known concentration of a gamma emitter to dose rate, and it was felt necessary to examine this problem afresh.

Accordingly, section 3.1 reports the construction of a larger (1 metre cube) uranium doped concrete block having about 15 times the activity of that used by Bowman. The results of measurements of the state of radioactive equilibrium of the concrete mix are also described, and these measurements are used to calculate an annual dose rate to concrete at the centre of the block.

Section 3.2 discusses the phosphors and encapsulation materials used to measure the dose rate in this block, and gives the results of such measurements. Section 3.3 considers the problem of calculating the response of the phosphor/wall combinations used and derives calculated calibration factors to be compared with those found experimentally. Some discrepancies are found, and these are discussed.

Finally, the calculated calibration factors for these capsules are derived when exposed to a 'typical' soil containing uranium, thorium and potassium. The most suitable combination for routine use is discussed.

3.1 CONSTRUCTION OF A QUASI-INFINITE MATRIX OF KNOWN ACTIVITY

In order to make absolute dosimetry measurements which simulate those made on archaeological sites, there are two main requirements:-

i) the dose rate to a particular material at a given point should be well known, and

ii) the gamma ray field from which this dose is absorbed should simulate as closely as possible that found in soil.

Now in the real case, the dose rate to be determined is that to a 100 μm grain of quartz, or a fine grain of indeterminate composition, but which may be taken as similar to that of bulk pottery (given in section 6.5.3). Neglecting the perturbing effect of the pottery matrix on the gamma field, the dose to such small grains is given by the Bragg-Gray cavity theory, which implies that the ratio of the dose to a quartz or fine grain, to the dose rate in the surrounding soil matrix is given by the ratio of the electronic stopping powers. Even for pure quartz this ratio is within 3% of unity in the energy region of interest, for pottery the agreement is better still. Thus this aspect of the problem of measuring the archaeological gamma dose rate reduces to measuring the dose rate to soil in an infinite soil matrix. This can be calculated from a knowledge of the radioisotope concentrations present, their half lives and decay schemes. Then the gamma energy released by radioactive decay per unit mass of soil may be calculated; for an infinite (or effectively infinite) matrix, this must be identically equal to the dose rate.

Probably the most convenient approach to this problem is that attempted by BOWMAN (1976) using concrete to simulate the soil medium. The constituents of concrete are given in table 3.1.1 with those of a 'typical' soil (taken from section 6.5.3), and it can be seen that they are very similar. The ratio of the mass attenuation coefficients of these two mixtures varies by less than 1.5% from unity from 25 keV to 3 MeV. These similarities should ensure that the degraded photon spectrum resulting from inelastic scattering of primary photons emitted from within a concrete absorbing medium will be very similar to that found in a soil matrix. Thus a large concrete matrix uniformly doped with appropriate radioisotopes should fulfil both the requirements, although there remains the question of the minimum size. Ideally, the block would be of global dimensions, although it is recognized that a more practical size will give a good approximation to this 'infinite' matrix spectrum - this is the quasi-infinite approximation.

For purely practical reasons it was decided to consider the minimum size of matrix required if the radioisotopes were to be those of the uranium series (a large quantity of refined uranium ore was already available).

3.1.1 Minimum size for a quasi-infinite uranium doped concrete matrix

In calculating the gamma dose rate at the centre of a 20 inch cube of uranium doped concrete Bowman initially assumed a density of 2.35 g cm^{-3}, which to a first order allowed the assumption that the effective attenuation path length from the centre of the block to each of the six faces was great enough to absorb most of the energy of the highest energy photon emitted from the uranium series. Thus the dose rate at the centre was assumed to be that found in an infinite medium of the same specific activity, and was calculated assuming conservation of energy, as described in the previous section. However, it was subsequently found that the density of concrete achieved was only 1.93 g cm^{-3}, and therefore this assumption was shown to be unjustified at high energies (above 1.5 MeV). The integrated primary photon spectrum of the U-238 series is given in figure 3.1.1, and it can be seen that a negligible fraction of the total energy is carried above 2.2 MeV. However, 5% of U-238 decays

Table 3.1.1

Constituents of 'typical' soil and concrete

Element	Soil %	Concrete %
H	1.0	0.6
O	52.6	49.8
Na	1.3	1.7
Al	8.3	4.8
Si	28.2	31.7
K	1.5	1.9
Ca	2.5	8.3
Fe	4.6	1.2

Note: 1) percentages are by weight.

2) the data for concrete are taken from EVANS (1968b); 0.2 % Mg has been included with Al, and 0.1 % S with Si.

3) the data for soil is taken from section 6.5.3; again the Mg is included with Al in the above, and Ti with Fe.

Figure 3.1.1

Proportion of total spectral energy carried by photons above a given energy, derived from the uranium series primary spectrum

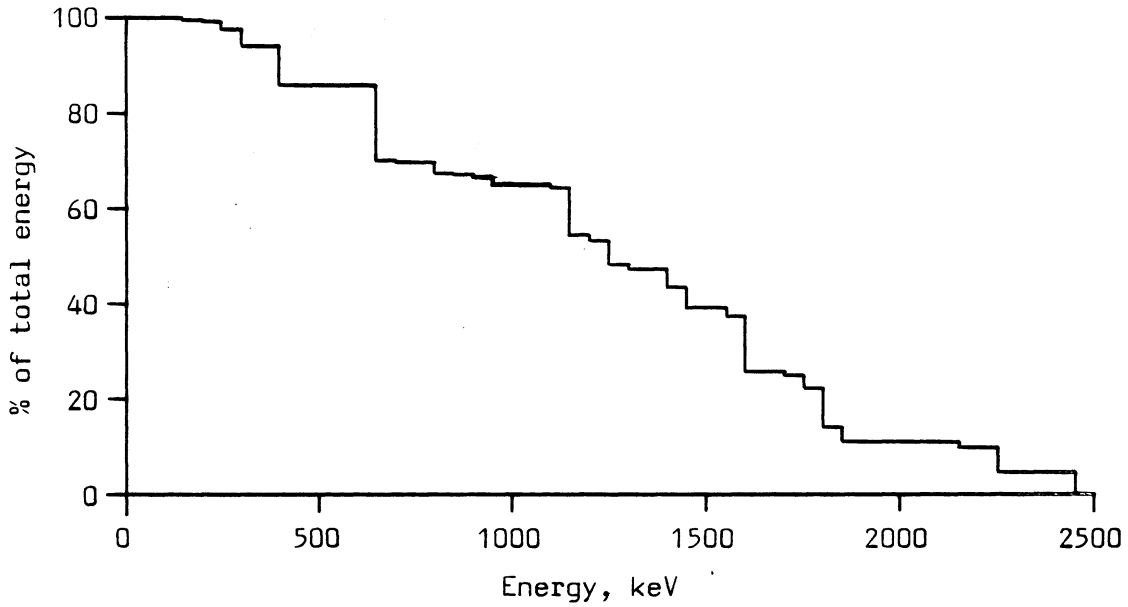

Figure 3.1.2

Build up to infinite matrix dose rate at the centre of a sphere

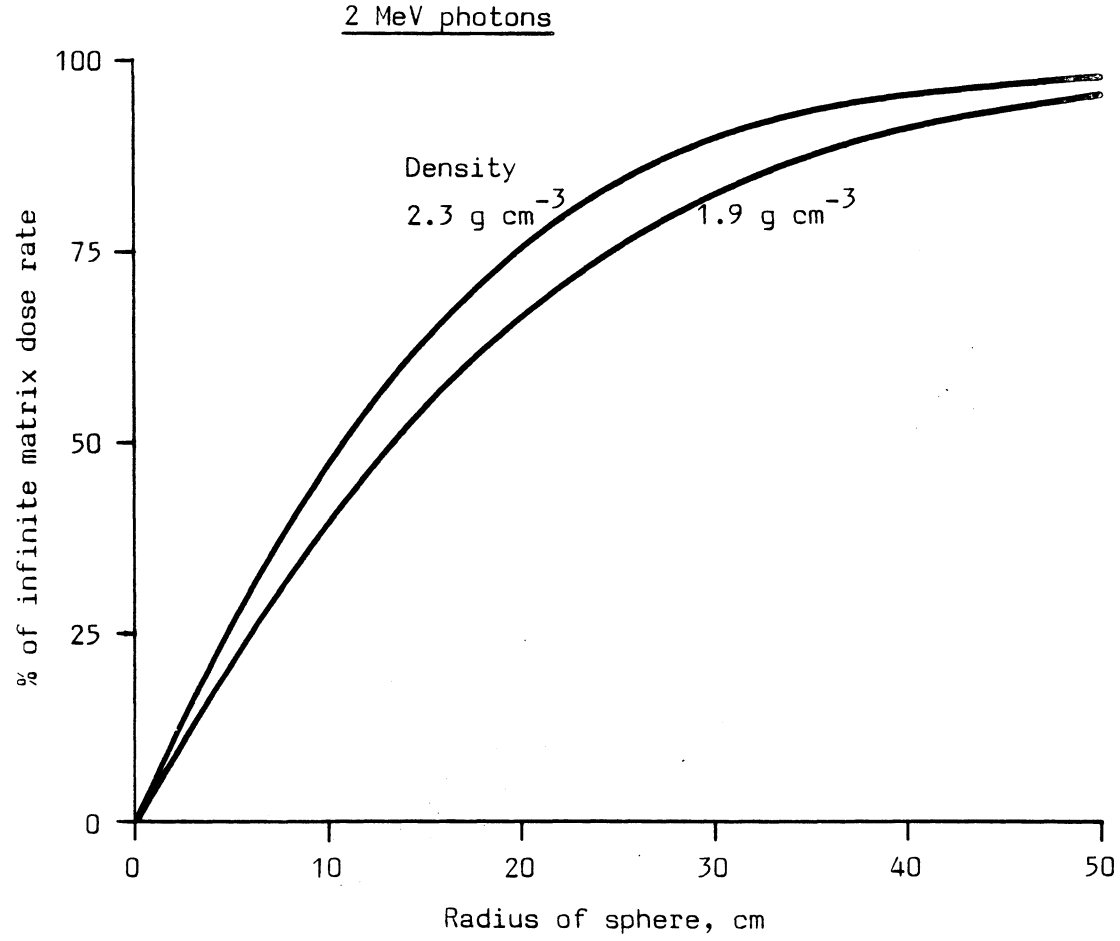

will eventually result in 2.20 MeV photons (from the decay of Bi-214) and it is thus this energy that determines the size of the infinite matrix.

EVANS (1968a) gives an approximate expression for the dose rate $\dot{D}_{primary}$, due to interactions with primary photons at the centre of a sphere of homogeneously distributed activity of radius r cm as

$$\dot{D}_{primary} = n_1 E_p \frac{\mu_a}{\mu} (1 - e^{-\mu r}) \qquad ---- 1$$

and the corresponding expression for the dose rate, $\dot{D}_{secondary}$, from secondary (i.e. scattered) photons as

$$\dot{D}_{secondary} = n_1 E_p \frac{\sigma_s}{\mu} (1 - e^{-\mu r}(1 + \mu r)) \; - - \; 2$$

where n_1 is the number of decays per second which give rise to photons of energy E_p MeV, in a gram of material,

μ_a is the linear energy absorption coefficient, cm^{-1},

μ is the linear attenuation coefficient, cm^{-1}

and σ_s is the total linear Compton scattering coefficient, cm^{-1}.

Note that these coefficients all refer to the same medium, in this case concrete.

Now the infinite matrix dose rate, $\dot{D}_\infty$, calculated as described earlier is

$$\dot{D}_\infty = n_1 E_p \qquad ---------- 3$$

As $r \to \infty$, the sum of equations (1) and (2) becomes

$$\dot{D}_{primary} + \dot{D}_{secondary} = n_1 E_p \frac{1}{\mu} (\mu_a + \sigma_s)$$

$$\simeq n_1 E_p, \quad \text{i.e. } \dot{D}_\infty$$

Combining equations (1), (2) and (3) gives

$$\frac{\dot{D}_{primary} + \dot{D}_{secondary}}{\dot{D}_\infty} = \frac{\mu_a}{\mu} (1 - e^{-\mu r}) + \frac{\sigma_s}{\mu} (1 - e^{-\mu r}(1 + \mu r)) \; - - \; 4$$

Figure 3.1.2 gives the fraction of the infinite matrix dose rate derived from equation 4, plotted against $\underline{r}$, the radius of the sphere, for two densities, 1.9 g cm^{-3} and 2.35 g cm^{-3}, at 2 MeV. For $\underline{r}$ = 50 cm, the dose rate at the centre is within 4% of the infinite matrix dose rate even for the lower density of 1.9 g cm^{-3}. As the 2.2 MeV photon carries only 7% of the gamma energy of the uranium series decay, a cube of side 1 metre should be a good approximation to an infinite matrix, even if the density achieved is low.

3.1.2 Description of uranium ore used, and activity required

In order to increase the range of phosphor sensitivities that could be usefully exposed in such a matrix, it was decided to use a considerably higher specific activity than had been employed before. This has the added advantage of making background corrections negligible, which is of great practical importance, as otherwise an inert concrete matrix of similar dimensions would be required.

Fortunately about 15 kg of high grade uranium ore was made available to us by the University Museum; this had been collected in Katanga by the late Professor Soddy of the Geology department at the University of Oxford. His chemical analysis (of unknown date) is given in table 3.1.2. The UO_3 concentration of 63.8% corresponds to an activity of 185.5 nCi g^{-1} (see Appendix E). It was decided to plan a cube of nominal activity 1 nCi g^{-1} (about 1000 times natural levels) which would require about 11 kg of ore added to a cube of concrete of side one metre, and density about 2 g cm^{-3}. The dose rate at the centre would be 33 rad yr^{-1}, assuming no disequilibrium in the uranium chain. This would permit measurements using insensitive phosphors such as the obsidian described in the previous chapter.

The geometry adopted was to build the cube from 125 separate blocks each of side 20 cm, with 5 of these blocks cast with an 8 cm hole through the centre of two opposing faces. When assembled, this gives an access channel passing through the centre of the one metre cube. Cylindrical plugs were also cast which could then be used to fill this hole. To increase the flexibility of the design, it was also decided to manufacture a further 50 smaller blocks of 10 by 10

Table 3.1.2

Chemical analysis of uranium ore

	% by weight
UO_3	63.81
PbO	11.17
CuO	0.03
SnO_2	0.37
Fe_2O_3 / Al_2O_3	0.73
P_2O_5	0.64
H_2O	5.87
CO_2	1.24
insoluble	14.28
Total	98.14

Note: the above analysis was performed at the instigation of the late Professor Soddy, but the date is unkown.

by 20 cm. These permit the assembly of a sequence of geometries, ranging from a 20 cm cube up to a one metre cube, in 20 cm steps. In addition, a selection of undoped blocks of each of the two sizes was cast, to permit the effects of inhomogeneity within the matrix to be examined.

3.1.3 Homogeneity of activity in concrete mix

BOWMAN (1976) was concerned that at least part of her anomaly lay with inhomogeneous distribution of the uranium ore added during mixing, and she was obliged to conduct lengthy tests in retrospect to test this. In order to forestall some of these problems, the components of the new block were cast in batches of 6 (for the 20 cm cubes) and 12 (for the 10 by 10 by 20 cm blocks). Samples of about 200 g were taken from each of these mixes, and allowed to set in polystyrene petri dishes, which were then coded by number. In order to ensure optimum mixing of the finely powdered uranium ore within each batch, it was dry mixed for 15 minutes with the cement only (in a cement mixer); sharp sand (screened to less than 5 mm) was then added and mixed for a further 15 minutes. The mix was also colour coded at this stage, using a cement based colouring agent, yellow for the active batches, and black for the undoped, to avoid later confusion. Finally sufficient water was added to make a thick mix, and this was transferred to wooden moulds and rammed thoroughly before being allowed to set. The actual quantities of material used for each batch of 20 cm cubes are given in table 3.1.3, along with the estimated uncertainties. The measured density of the resulting blocks after curing was 2.25 ± 0.05 g cm^{-3}. Each set of blocks was number coded before removal from the mould, so that blocks from a particular mix could be identified later if necessary.

After about 2 weeks storage the individual blocks were given a coat of masonry sealer (a polyurethane based varnish) to stabilise the surface and to reduce fluctuations in the water content, and two coats of emulsion paint, yellow for the active blocks and grey for the inert blocks. The number coding of each block was transferred to the painted surface. It should be noted that no aggregate was used in mixing the concrete, and that the cement content is about

Table 3.1.3

Weights of components used in each batch of six 20 cm cubes of active concrete

	kg
sand (<5 mm grain size)	73.9_{5}
cement	37.0_{5}
colour	0.72_{2}
uranium ore	0.7310_{5}
water	17.5_{22}

Note: errors are in the least significant figures.

28% of the total. This was done to improve the uniformity of the uranium ore distribution, and to reduce the friability of the finished blocks. However, the resulting major element concentrations will be different from those given in table 3.1.1. The effect of this change will be considered further in section 3.3.

3.1.4 Homogeneity measurements on casting samples

The 24 samples taken in petri dishes during the mixing and casting of the active blocks were weighed and then counted on a 3 inch by 3 inch sodium iodide crystal operating in total counting mode. The counts above a threshold of about 0.25 MeV were recorded for 1000 seconds and a background count subtracted. The standard deviation of the resulting 24 count rates after weight normalisation was 2.8%. As every effort was made at the time of mixing to ensure that these casting samples were representative, it is felt that this spread accurately reflects the variation in activity in the completely assembled block.

3.1.5 Calculated and observed activity of the concrete

From the data presented in tables 3.1.2 and 3.1.3, the concentration of uranium in the wet mix can be calculated as 2990 $\pm$ 50 ppm (1045 pCi g^{-1}), where the uncertainty is derived only from the uncertainties in weighing the components. However, the final concentration will be slightly higher than this, because of water losses in the casting and curing of the concrete and subsequent drying out during storage. The water content of the wet mix was 13.4% but the observed water content of the concrete some weeks after curing was 8.0%. A fraction of this difference will have been chemically bound by the curing process, so not all has been lost. If the amount lost is assumed to be (2.7 $\pm$ 2.7)% i.e. half the difference, then the calculated concentration rises to 3079 $\pm$ 90 ppm uranium. This corresponds to an activity of 1070 $\pm$ 30 pCi g^{-1} natural uranium.

Unfortunately it is unlikely that the U-238 chain is in equilibrium. Some fraction of the Rn-222 activity is almost certain to be able to escape from the uranium ore, and most probably also from the concrete. Thus the calculated uranium activity cannot be converted directly into dose rate with any degree of confidence, especially since about 95% of the dose rate is carried by Rn-222

daughter products. Accordingly one of the casting samples was broken up, crushed to less than 500 μm and analysed by high resolution gamma spectrometry, as described in chapter 6. The results of this analysis are given in table 3.1.4. As this sample gave a total gamma count (section 3.1.5) of 1.022 times the average, the activities shown should be corrected appropriately to give the best estimate of the average activities. However, these results could not be relied on to give a good estimate of the Rn-222 activity in the block, as it seemed unlikely that the level of escape from a sample crushed to less than 500 μm would be the same as that from a solid 20 cm cube, and so attempts were made to estimate the Rn-222 activity in the solid discs of concrete taken as casting samples. Nevertheless, it should be noted that the observed uranium activity is within experimental error of that calculated earlier.

3.1.6 Activity of Rn-222 in solid concrete

It was decided to determine the Rn-222 activity in the solid concrete discs by total gamma counting a standard of known Rn-222 activity and comparing. This is straightforward because all the intense gamma emissions above 0.25 MeV originate with Rn-222 daughters.

An accurately known weight of the U.S. National Bureau of Standards' uranium ore NBL 42-1 was mixed with cement, sand and water to produce a wet concrete mix containing 0.9073% of the standard ore. This mix was allowed to cure in a polystyrene petri dish, the weight before and after curing being noted, and the uranium activity of the concrete disc was calculated as equivalent to 131.0 pCi g^{-1}, normalised to the same weight as was used in section 3.1.4. This disc was then sealed in the petri dish with polyester resin. However, spectrometer analysis (see section 6.7) also revealed that this ore was not in secular equilibrium. The activity of Ra-226, the Rn-222 parent, is 1.046 times that of U-238, and as a loose powder, the activity of Rn-222 is 0.955 times that of Ra-226. Thus the activity ratio of Rn-222 to U-238 in the sealed concrete disc could be between 0.998 and 1.046; a value of 1.022 $\pm$ 0.022 is assumed. This implies a Rn-222 activity of 133.9 $\pm$ 3.3 pCi g^{-1}. This sample was then counted using the total gamma counting system outlined in section 3.1.5 and an average Rn-222 activity of 945 $\pm$ 35 pCi g^{-1} calculated for the

Table 3.1.4

Isotope activities of casting sample $A10_2$

Isotope	Activity pCi g^{-1}
U-238	1068_{20}
Th-230	1065_{120}
Ra-226	1191_{25}
Rn-222	986_{20}
Pb-210	912_{20}

From total gamma counting:

$$\text{Activity ratio } \frac{A10_2}{\text{Average of 24 samples}} = 1.022$$

Note: errors are in the least significant figures.

24 casting samples. This is within experimental error of the 965 ± 33 pCi g^{-1} derived for the average activity from table 3.1.4, where the sample was crushed to less than 500 μm. Thus there is no evidence to suggest that the Rn-222 escape from the solid is different from that of a crushed sample. Nevertheless, it must be acknowledged that the emanation from a 20 cm cube could be different from that of an 8 cm diameter by 1.5 cm thick disc, and accordingly the calculated error limits of ± 3% are rounded up to 5% when the average Rn-222 activity of 955 pCi g^{-1} is used to derive the annual dose rate.

3.1.7 Annual dose rate at the centre of the quasi-infinite block

Using the average Rn-222 activity derived from the previous section, and the activities of the other members of the decay chain derived from table 3.1.4, the annual gamma dose rate was calculated from the dose rate data given in Appendix E, as 31.7 ± 1.6 rads yr^{-1}.

The errors in the dose rate arise almost entirely from the uncertainties in the level of Rn-222 escape from the solid concrete.

3.1.8 The doped concrete as a radiological hazard

It is appropriate here to give some consideration to the health hazard posed by the assembled block. For security reasons, and for protection from the weather, the finished concrete bricks were assembled in a small basement room approximately 2m by 2m by 2m. Thus the equilibrium activity of Rn-222 in the atmosphere, assuming no air movement, would be about 5×10^4 pCi l^{-1}. The maximum recommended level is 30 pCi l^{-1} for a 2000 hour working year (ICRP 24, Radiation protection in uranium and other mines, 1977). Although there is no need, in this case, for this level of occupancy, it is clear that the completed blocks pose a considerable health hazard. In addition, there is the gamma dose rate at the surface of the block to be considered. At about 3.5 mrad hr^{-1}, this is also slightly above the maximum permissible dose rate for a 2000 hour working year.

After consultation with the University Radiation Protection Officer, a ventilation fan was fitted to the room before the blocks were installed. This vents outside the building, and it is conservatively calculated that it should give about seven air changes every hour. Thus the equilibrium concentration of Rn-222 is now expected to be about 50 pCi l^{-1}, which is considered acceptable,

provided the room is not normally occupied.

3.2 EXPERIMENTALLY OBSERVED DOSE RATES IN THE URANIUM BLOCK

In this section the experimentally observed dose rates in various phosphor and encapsulating material combinations, exposed at the centre of the uranium doped concrete block, are compared with the calculated infinite matrix dose rate, and experimental calibration factors for each combination determined.

3.2.1 Phosphors and encapsulating materials used as TL dosimeters

The TL phosphors used were chosen for a variety of reasons:

i) Calcium fluoride (natural)

This is the phosphor most commonly used in the past in this laboratory for environmental work, and it is thus important to determine its absolute response if earlier measurements are to be interpreted correctly. It also has considerable advantages, in that, unlike most other phosphors, the TL peak III at about 270°C has no detectable (i.e. less than 3%) fading over a five year period (AITKEN, 1968). It is also very sensitive (with appropriate care, doses of less than 1 mrad can be measured with a sample of less than 10 mg). However, it has some disadvantages, in particular it has an internal dose rate of 10 mrad yr^{-1} (AITKEN, 1968), which is a limitation when very low dose rates are being measured. In addition the mass energy absorption coefficients at low energies are about 3 times those of quartz, which suggests that a calcium fluoride dosimeter is likely to be more sensitive to the low energy end of the spectrum than quartz. These relative absorption coefficients are shown in figure 3.2.1. They have been calculated from data given by STORM and ISRAEL (1970), assuming the Bragg additivity rule applies,

i.e. assuming

$$\overline{(\mu/\rho)} = \sum_i (\mu/\rho)_i \, w_i \qquad - - - - - - - - 5$$

where $\overline{(\mu/\rho)}$ is the average mass energy absorption coefficient, $(\mu/\rho)_i$ are the mass energy absorption coefficients of the

Figure 3.2.1 Ratios of the mass absorption coefficients of various absorbers to those of quartz

Note: values of the ratio at 1 MeV are given in parentheses

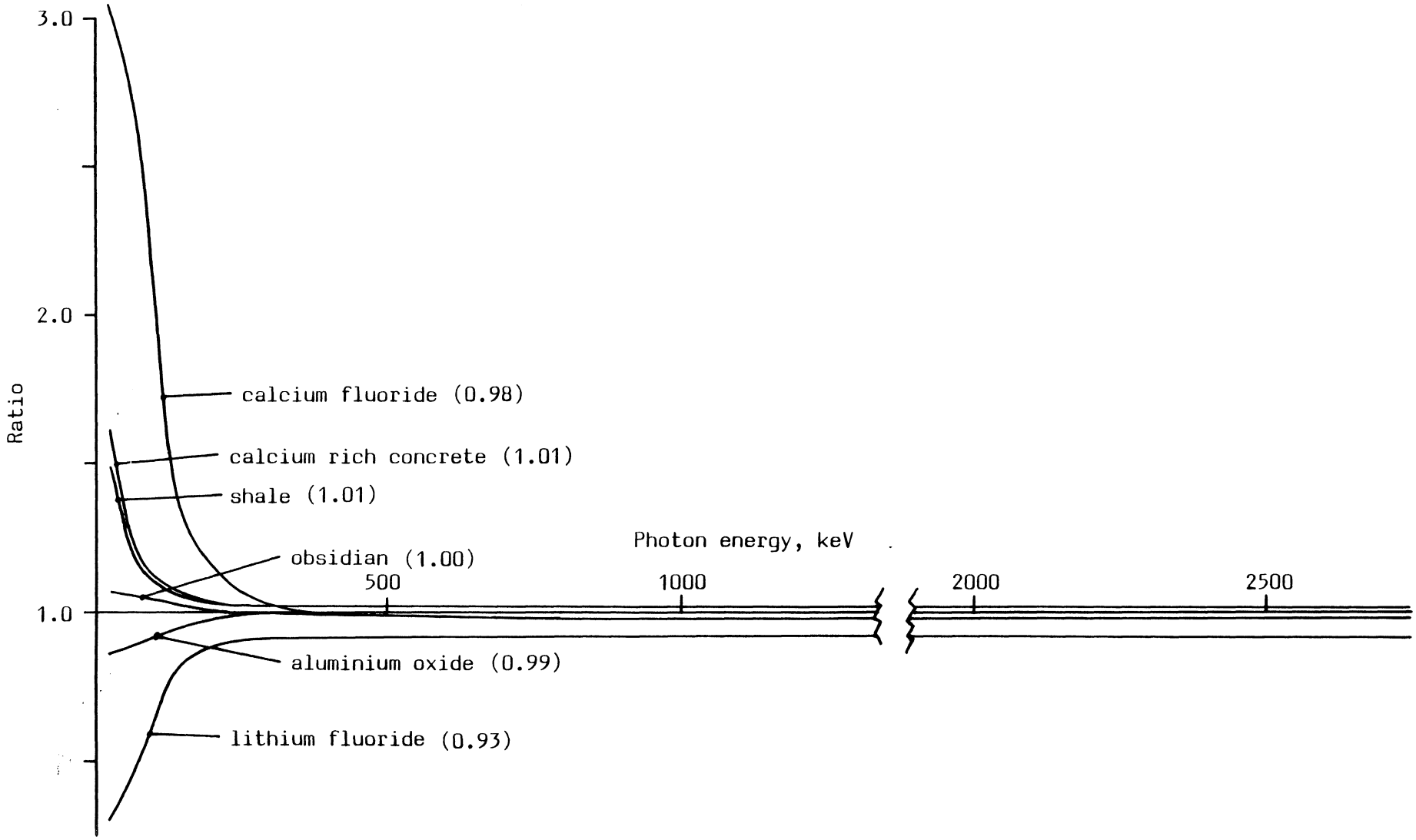

individual components,

and $\underline{w}_i$ are the fractions by weight of the individual components, which are listed in table 3.2.1.

The supplier of the phosphor used, type Super S, was MBLE, Brussels, (see SCHAYES et al, 1963).

ii) Obsidian

This phosphor was described in some detail in the last chapter. Its principal advantage is that it has an almost identical response to that of quartz (figure 3.2.1). However, it is insensitive (about 10^{-3} times natural calcium fluoride), and the fading must be monitored (section 3.2.2).

iii) Aluminium oxide (doped with Si and/or Na)

Aluminium oxide shows the same advantages as obsidian, in that the absorption characteristics are very similar to those of quartz, (figure 3.2.1) but it has much greater sensitivity (about 0.2 of that of natural calcium fluoride) and on kinetic grounds, it is not expected to show any thermal fading. However, the sample used did show some short term fading (about 5% in 24 hours), which is assumed to be 'anomalous' (WINTLE, 1973, 1978), and thus fading corrections had to be made as described in section 3.2.2. This material was kindly supplied by G.Portal, CEA, Fontenay-sur-Rose, France.

iv) Lithium fluoride

Lithium fluoride is perhaps the best known TL phosphor in common use, because of its medical significance. From the point of view of a quartz like dosimeter it is not very satisfactory because its absorption coefficients are significantly different, as can be seen from figure 3.2.1. In addition it is only about 0.02 times as sensitive as calcium fluoride, and it also shows short term fading. The material used was Harshaw type TLD 100.

With these four different phosphors, four different encapsulations have been used.

i) Nylon

Prior to the work described in this thesis, nylon was the routine encapsulation material used in this laboratory. It is used here because it has a low atomic number which 'matches'

Table 3.2.1 Assumed composition of phosphors and encapsulation materials

Element	CaF_2 %	Al_2O_3 %	Obsidian %	LiF %	Nylon %	Aluminium %	Glass %	Copper %
H	-	-	-	-	8.9	-	-	-
Li	-	-	-	26.8	-	-	-	-
C	-	-	-	-	58.6	-	-	-
O	-	47.1	50.8	-	32.5	-	49.3	-
F	48.7	-	-	73.2	-	-	-	-
Na	-	-	2.2	-	-	-	11.0	-
Al	-	52.9	5.3	-	-	100	-	-
Si	-	-	39.3	-	-	-	39.7	-
K	-	-	1.7	-	-	-	-	-
Ca	51.3	-	0.7	-	-	-	-	-
Cu	-	-	-	-	-	-	-	100
Density, $g\ cm^{-3}$	3.18	3.5	2.7	2.64	1.14	2.7	2.65	8.9

Note: 1) 12% nitrogen has been included with the oxygen component in Nylon, $C_{12}\ H_{22}\ O_3\ N_2$

2) the percentages shown are by weight.

lithium fluoride. In addition, the results obtained allow reinterpretation of earlier work, if necessary. The capsules were cylindrical in shape, with a 4 mm wall thickness and an internal cavity 5.1 mm diameter by 4.0 mm long.

ii) Aluminium

This was chosen because it has an atomic number close to the average of that of calcium fluoride, obsidian and aluminium oxide, and thus will have similar energy attenuation and absorption characteristics to these materials. It has also been used as a routine encapsulation. However, most sources of aluminium have considerable radioactive impurities (see chapter 6) which increases the minimum detectable dose rate to unsatisfactory levels. The capsules were cylindrical in shape, with a 1.5 mm wall thickness, and an internal cavity 4.8 mm diameter by 4.0 mm.

iii) Glass

This was selected because it also provides an excellent 'match' to both aluminium oxide and obsidian. It was used in the form of a glass tube of wall thickness 3 mm, about 20 mm long. The internal diameter was 3 mm, and the ends of the tube were blocked with 'Blu-Tak', an adhesive putty that does not set. The end effects introduced by this material are reduced by the fact that a layer of grains adhere to the putty and so they are not analysed. These are the grains most likely to be affected by the secondary electron spectrum produced by the photon flux in the putty; such end effects will be further reduced by the capsule geometry.

iv) Copper

Copper has been used more recently because of its practical convenience, as it is possible to anneal the phosphor 'on site' by heating a preloaded capsule in a portable oven. It also has the big advantage of being corrosion resistant and can be made moisture tight by silver soldering. Compared with other encapsulating materials, it has a high atomic number and so a relatively large photoelectric coefficient. Thus it can be used as an energy filter to selectively attenuate low energy photons.

The capsules were about 20 mm long, made from copper tube 3 mm internal diameter and 1.5 mm wall thickness. The ends were pinched flat and silver soldered.

It is obviously important that the beta dose rate to a phosphor contained in one of these materials should be a negligible fraction of the gamma dose rate. Of the four described above, 1.5 mm of aluminium was calculated to attenuate the beta flux from the U-238 decay chain by more than 97% (EVANS, 1968a); all the others were more effective than this. The beta dose rate is 1.4 times the gamma dose rate (for 20% Rn-222 escape) and so about 4% of the phosphor dose will be from beta particles (neglecting gamma attenuation effects). However, the beta flux will be further attenuated by passing through the phosphor, and so a 2% contribution is probably generous. The other materials, glass, nylon and copper, are predicted to have a 0%, 1% and 0% beta contribution respectively.

All the phosphors were used as grains sieved to 90 to 150 μm diameter. Measurement was by direct comparison of light levels induced by exposure in the concrete block with those induced by the beta source described in chapter 2, as sensitivity changes were found to be negligible in all cases. All the phosphors were beta irradiated as monolayers on stainless steel discs. The calibration of the beta source for calcium fluoride and obsidian was described in detail in chapter 2; the approach used to calibrate for aluminium oxide and lithium fluoride was identical in all respects, except that lithium fluoride was gamma irradiated in perspex.

3.2.2 Fading corrections

Fading corrections proved necessary when using obsidian, aluminium oxide and lithium fluoride. In all cases they were determined by giving a portion of the phosphor a known beta dose at least two orders of magnitude greater than the anticipated dose from the concrete block. This portion was packed into a capsule identical with those used to determine the block dose rate, placed in the block a few centimetres from the unirradiated capsule and left throughout the exposure. All the capsules were withdrawn from the block 24 hours before measurement, and in the case of the dosed capsules, the loss of TL evaluated by repeating the known beta dose after measurement of the 'faded' TL.

Initially this regime was more complex in that the fading was monitored after 24 hours, and then at the end of the exposure, and it was found that the observed fading after these two periods was the same, within experimental error, in every case. Thereafter the simplified procedure was used.

In the case of obsidian it was shown experimentally that this fading measurement did indeed measure the true fading. A portion of obsidian 100 μm grains was given a known beta dose and then part was measured after 24 hours, and part after 6 days. The 'faded' to 'prompt' ratio was 0.959 and 0.964 after 24 hours using two discs and 0.963 and 0.970 after 6 days on a further two discs. An additional disc was exposed continuously over a five day period to a weak beta source, so that the total dose given was about 13% of the single known dose used to monitor fading. This disc was then stored for 24 hours before measurement of the TL. The dose was then repeated, this time over 57 seconds, and the 'faded' to 'prompt' ratio calculated to be 0.964. (These ratios include corrections for the slight (1%) change in sensitivity after every heating cycle discussed in chapter 2). Thus for obsidian at least, the fading measured after the total storage time agrees well with the true fading.

3.2.3 Weight of phosphor used

If the dimensions of the phosphor are comparable with the path length of the secondary electrons produced in the encapsulating material by the photon flux, then the dose in the phosphor may be dependent on the mass of phosphor used. However, if a large enough mass is irradiated, the contribution from the dose delivered by wall secondary electrons to the average dose will be negligible. From a consideration of the ratios of mass absorption coefficients and electronic stopping powers given in section 3.3.3, this will not be an important effect for aluminium and glass capsules, but it will be significant for nylon and copper.

This effect should be most obvious in copper, and so this has been investigated experimentally using calcium fluoride. Five copper capsules were packed with different amounts of calcium fluoride, ranging from 20 mg to 500 mg. The observed doses after an exposure of about five days in the block are shown in figure 3.2.2. It is

Figure 3.2.2 Variation of dose rate with mass of calcium fluoride in copper capsule

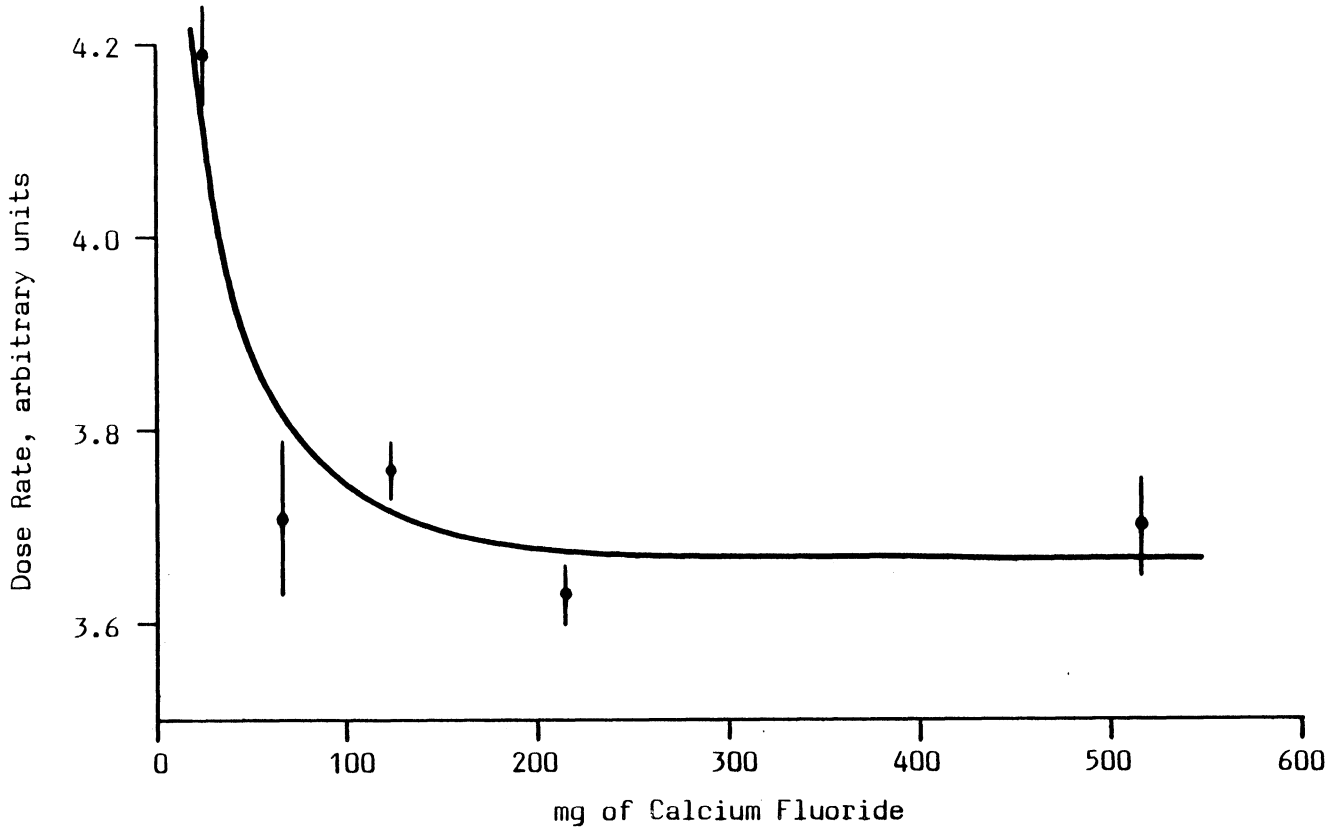

clear that for more than about 80 mg of calcium fluoride, the effective dose rate will be within 3% of that to 500 mg. In routine use, more than 100 mg of each phosphor was used in all capsules. This should ensure that small variations in phosphor weight do not affect the reproducibility from one capsule to another.

3.2.4 Experimentally observed quasi-infinite matrix dose rates

The dose rate at the centre of the assembled uranium block has been measured over a period of about two years, using most of the possible combinations of phosphors and wall materials. The observed dose rates are shown in table 3.2.2.

Typically the fading correction applied to the lithium fluoride and aluminium oxide results was 4% and 6% respectively. That applied to obsidian varied between 0% and 9%. Irradiation times varied between about 2 and 50 days. The errors shown are the standard errors on at least four determinations from each capsule, combined with the experimental error in the beta source calibration. The average dose rates derived from table 3.2.2, after removal of the beta dose contribution (section 3.2.1) and expressed as fractions of the infinite matrix dose rate derived in section 3.1.7, are given in table 3.2.3. Here the errors include experimental scatter in the observed dose rates (or an estimate thereof) and also the 3% systematic beta source error (see chapter 2) and the 5% uncertainty in the infinite matrix dose rate (section 3.1.6).

Discussion of these results will be postponed until the end of section 3.3. It is sufficient here to observe that the routine combinations of calcium fluoride in nylon, aluminium and copper all appear to underestimate the infinite matrix dose rate, and thus the gamma dose rate to quartz, by between 10 and 15%.

3.3 CALCULATION OF DOSE ABSORBED BY A TL DOSIMETER PLACED IN AN INFINITE GAMMA EMITTING MEDIUM

In this section data are presented which permit the calculation of the dose absorbed by a capsule (i.e. an encapsulated TL dosimeter) from the infinite matrix gamma spectra derived from a uranium series

Table 3.2.2

Observed dose rates in a 1 m cube of concrete doped with 1 nCi g^{-1} (nom.) uranium, in mrad yr^{-1}

	calcium fluoride	aluminium oxide	obsidian	lithium fluoride
Nylon	27.5 $_2$ 28.6 $_6$ 27.4 $_6$	28.3 $_7$	-	27.8 $_9$ 24.9 $_{10}$
aluminium	27.8 $_3$	25.7 $_5$	29.1 $_9$	-
glass	25.9 $_3$	26.0 $_7$	26.5 $_6$ 28.4 $_9$	-
copper	27.2 $_5$ 26.3 $_3$ 27.6 $_3$ 27.3 $_3$ 27.9 $_3$	27.1 $_6$	32.6 $_{14}$ 36.0 $_4$ 35.3 $_6$ 32.5 $_5$	33.3 $_{10}$

Note: errors are in the least significant figures, and are standard errors derived from at least four measurements from each capsule.

Table 3.2.3

Observed ratios of capsule dose rates to the infinite matrix dose rate in the uranium block

	calcium fluoride	aluminium oxide	obsidian	lithium fluoride
Nylon	0.87_{5}	0.88_{6}	-	0.82_{6}
aluminium	0.86_{5}	0.79_{5}	0.90_{6}	-
glass	0.82_{5}	0.82_{6}	0.87_{6}	-
copper	0.86_{6}	0.85_{6}	1.08_{8}	1.05_{8}

Note: errors are in the least significant figures, and are total errors (see text)

source, a thorium series source and a potassium source. In the case of the uranium spectrum, the calculated dose rates are compared with the experimental results of the last section, and finally the calculated dose rates for all three spectra are used to derive correction factors to enable routine measurements to be made of infinite matrix soil dose rates using encapsulated TL dosimeters.

3.3.1 The infinite matrix spectrum

The photon energies and intensities present in an infinite matrix gamma spectrum result from a combination of degradation of the primary photons, mainly by inelastic (Compton) scattering, and absorption of energy by both Compton scattering and the photoelectric process. In an infinite absorbing matrix containing a homogeneously distributed gamma emitter these processes result in an equilibrium spectral distribution being set up throughout the matrix. It is this equilibrium secondary spectrum which deposits energy in a TL capsule inserted in such a medium, and thus a knowledge of this spectral distribution is essential if any attempt is to be made to calculate the dose in the phosphor. BOWMAN (1976) presents no such information, and until recently only MEJDAHL (1970) had considered this problem in any detail. From a consideration of work published by GUSTAFSON and BRAR (1964), and from his own experimental data, he suggested that between 2% and 4% of the total energy was carried by photons of energy less than 150 keV in a composite uranium, thorium and potassium infinite matrix spectrum. He also examined the response of calcium sulphate (doped with dysprosium) in steel tubes when externally irradiated with gamma and X rays, and concluded that such a dosimeter would over-respond by less than 2% compared with quartz grains in a clay tablet exposed to a typical soil spectrum. However, he neglected consideration of overall attenuation effects. Although there will clearly have been some attenuation of the external flux before it interacted with the quartz grains in the clay tablet, in the real case of a buried sherd the sherd matrix is also radioactive, and is often similar in activity to the surrounding matrix. Thus the nett effect is only a second order correction to the secondary gamma flux, and so the attenuation through an inactive capsule wall will give rise to an underestimate of the true dose rate to a small absorbing grain.

More recently JAIN et al (1979) have considered the problem of

calculating the infinite matrix secondary spectrum in some detail, and have performed these calculations for two media, sandstone and shale, with a variety of porosities and water contents, assuming an equilibrium uranium series source homogeneously distributed throughout the medium, and also an equilibrium thorium source, and a potassium source. They approached the problem by solving the general transport equation using the discrete ordinates method, and as a check on their technique compared the results for a single gamma emitter with those obtained from a Monte Carlo calculation using the Los Alamos Monte Carlo code MCP (CASHWELL et al, 1973). The results were in excellent agreement.

Figure 3.3.1 reproduces the calculated infinite matrix spectra derived from the three sources in a non porous shale matrix. The components of this shale are given in table 3.3.1, as are those of concrete, corrected for the increased calcium content which arose because the proportion of cement used in the construction of the quasi-infinite matrix was 28% instead of the typical 15% used in table 3.1.1. The ratio of the mass attenuation coefficients of shale and of the calcium rich concrete, to those of the 'typical' soil given in table 3.1.1 are shown in figure 3.3.2. It can be seen that the characteristics of shale and soil are very similar. Thus the calculated spectra of figure 3.3.1 should be very close to those found in soil.

For comparison, the primary uranium, thorium and potassium spectra used by Jain et al are shown in figure 3.3.3. Figures 3.3.4 and 3.3.5 show the energy spectra and integrated energy spectra respectively. These were derived directly from the data of figure 3.3.1.

3.3.2 Attenuation and absorption of energy by a capsule

If the material surrounding the phosphor (the capsule wall) is sufficiently thick to ensure that charged particle equilibrium is set up within the wall, then in principle the problem is covered by the general cavity theory developed by BURLIN (1966). However, his approach is not immediately relevant here, because he assumed that the gamma flux was homogeneous throughout the dosimeter, a condition closely approximated at the energies considered by Burlin and later workers in testing the general theory. However, in the case of an

Figure 3.3.1

Infinite matrix spectra for shale

Note: derived from Jain et al, (1979)

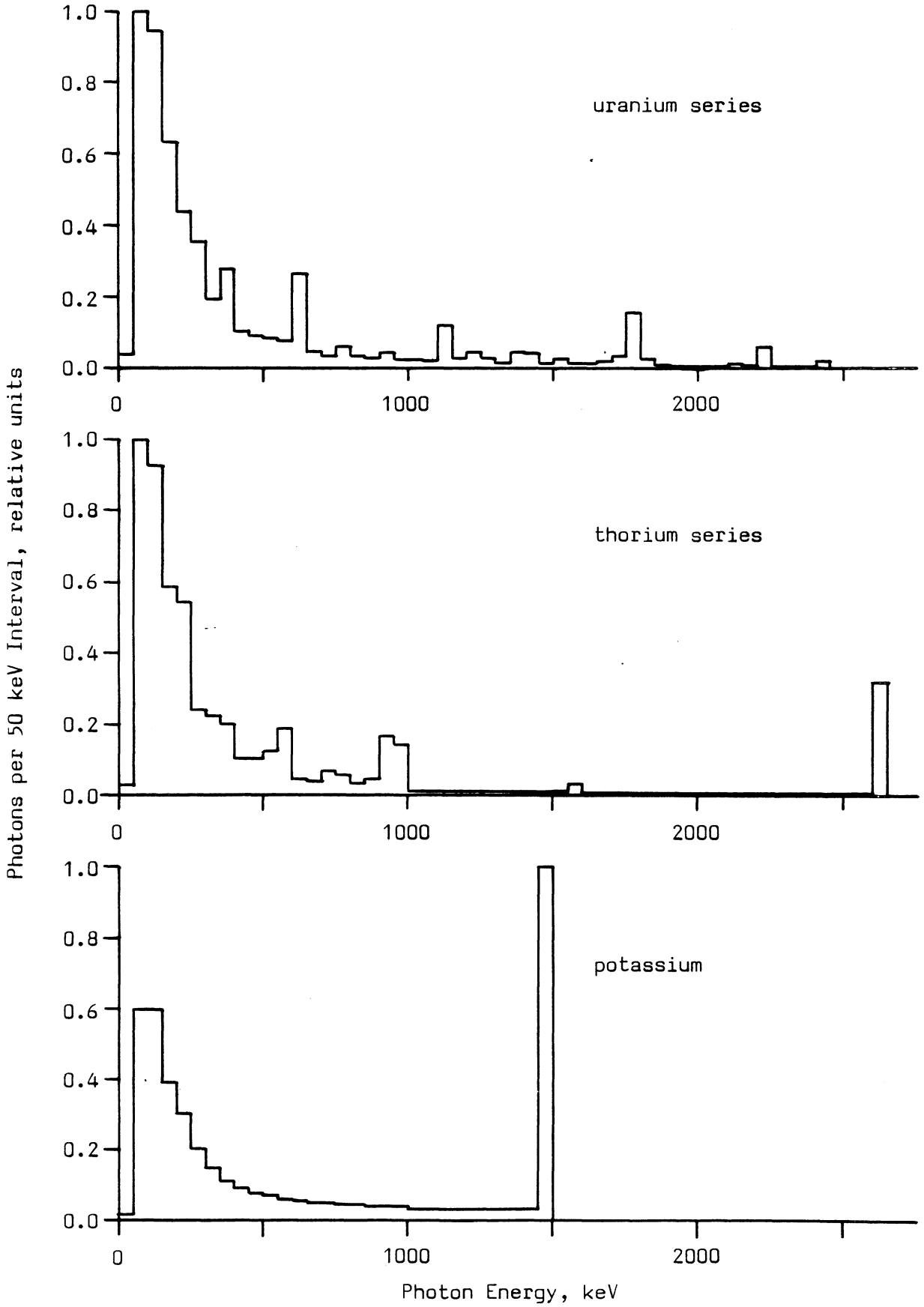

Table 3.3.1

Components of shale and calcium rich concrete

Element	Shale %	Concrete %
H	1.34	0.8
C	1.55	-
O	49.77	49.0
Na	-	1.5
Al	9.79	4.2
Si	27.76	27.6
K	2.74	1.7
Ca	2.26	14.1
Fe	4.79	1.1

Note: 1) the components of concrete are those from table 3.1.1, but with the cement fraction increased from about 15% to 28% of the total.

2) the components of shale are taken from JAIN et al (1979). 1.5% Mg has been included with Al.

Figure 3.3.2

Ratio of mass attenuation coefficients of shale and calcium rich concrete to 'typical' soil

Note: calculated assuming the concentrations given in table 3.3.1

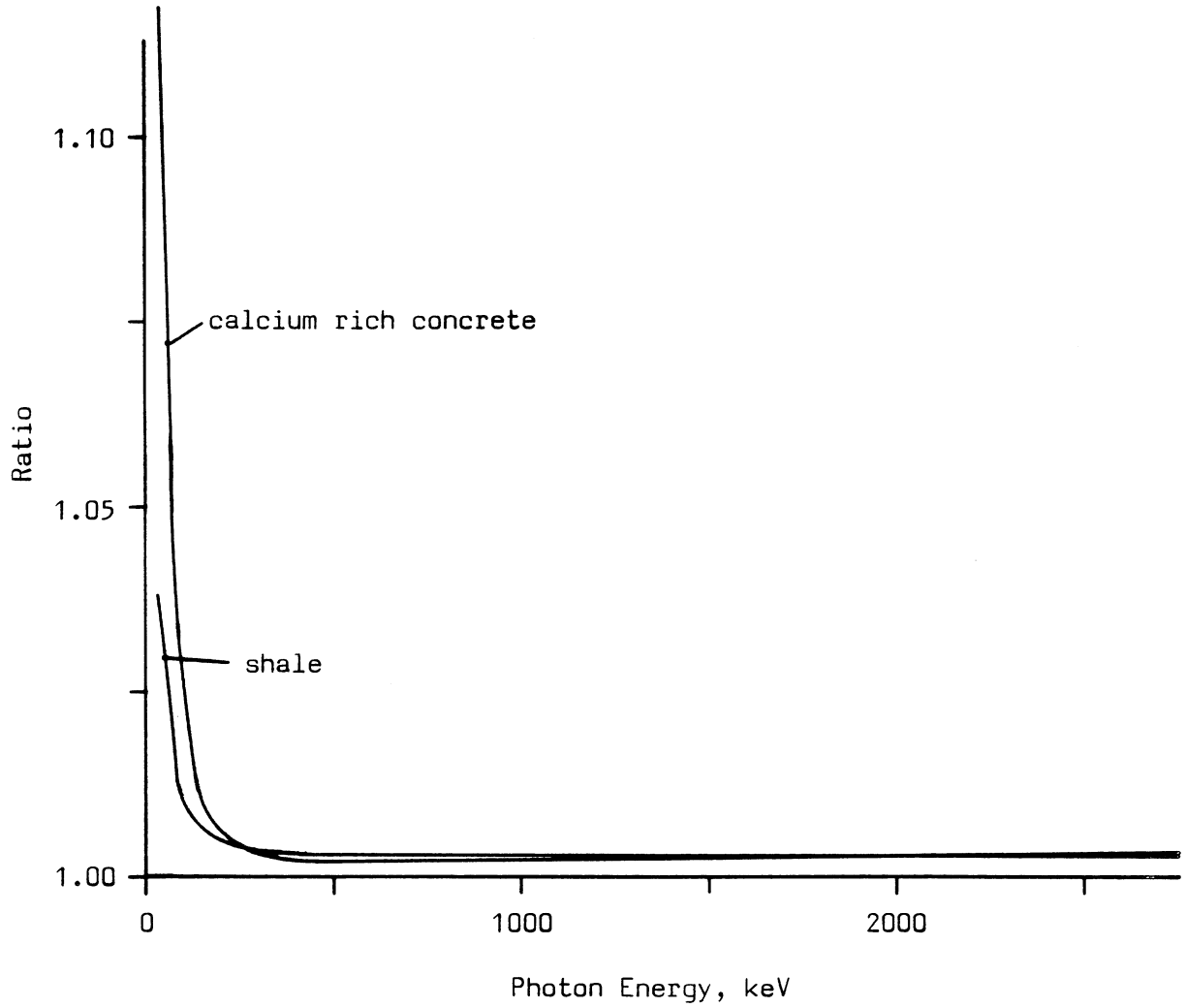

Figure 3.3.3

Primary spectra used to calculate the infinite matrix spectra of figure 3.3.1

Note: derived from Jain et al, (1979)

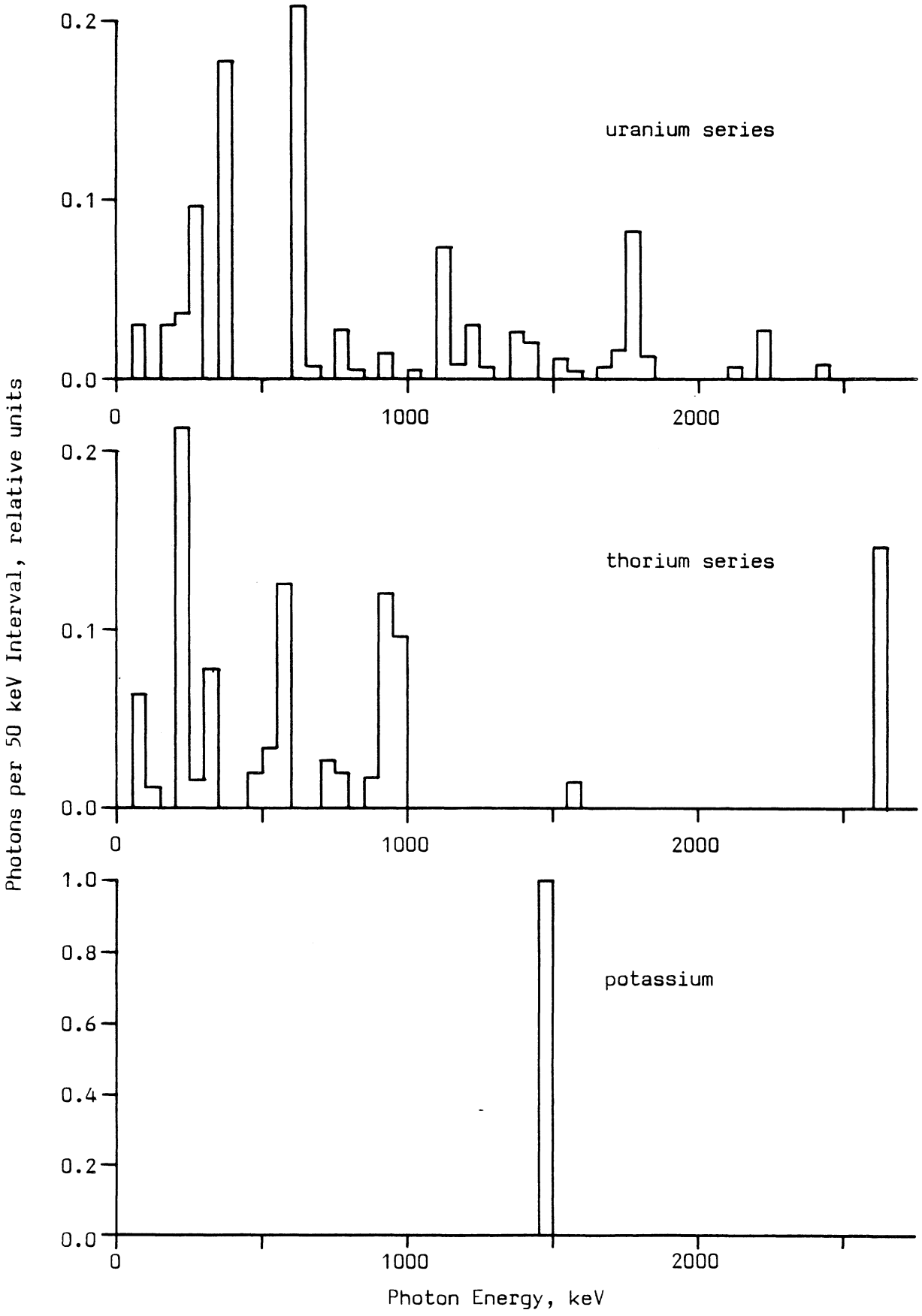

Figure 3.3.4

Infinite matrix energy spectra for shale

Note: calculated from the data of figure 3.3.1

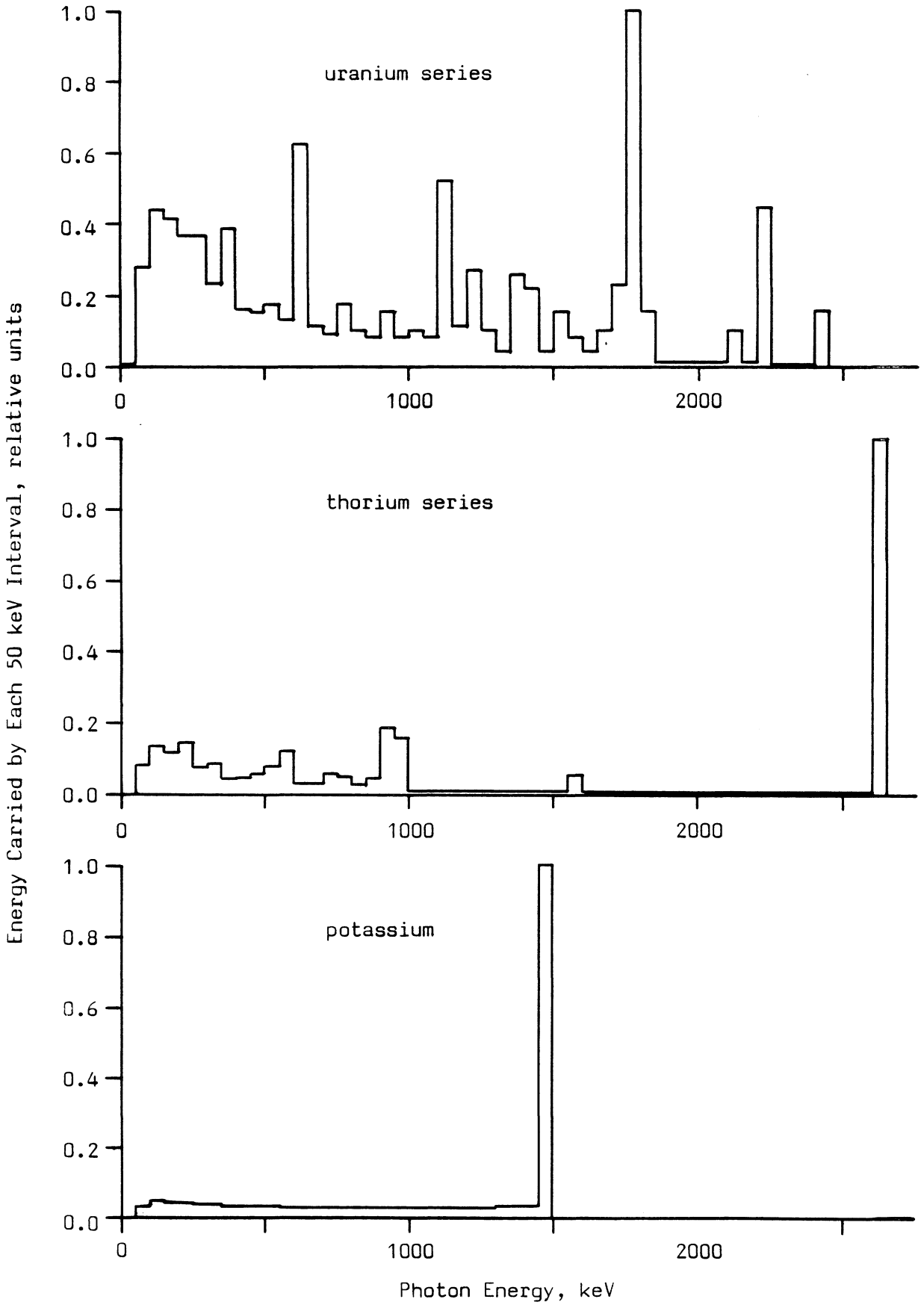

Figure 3.3.5

Proportion of the integrated spectral energy carried by photons above a given energy, for the infinite shale matrix spectra

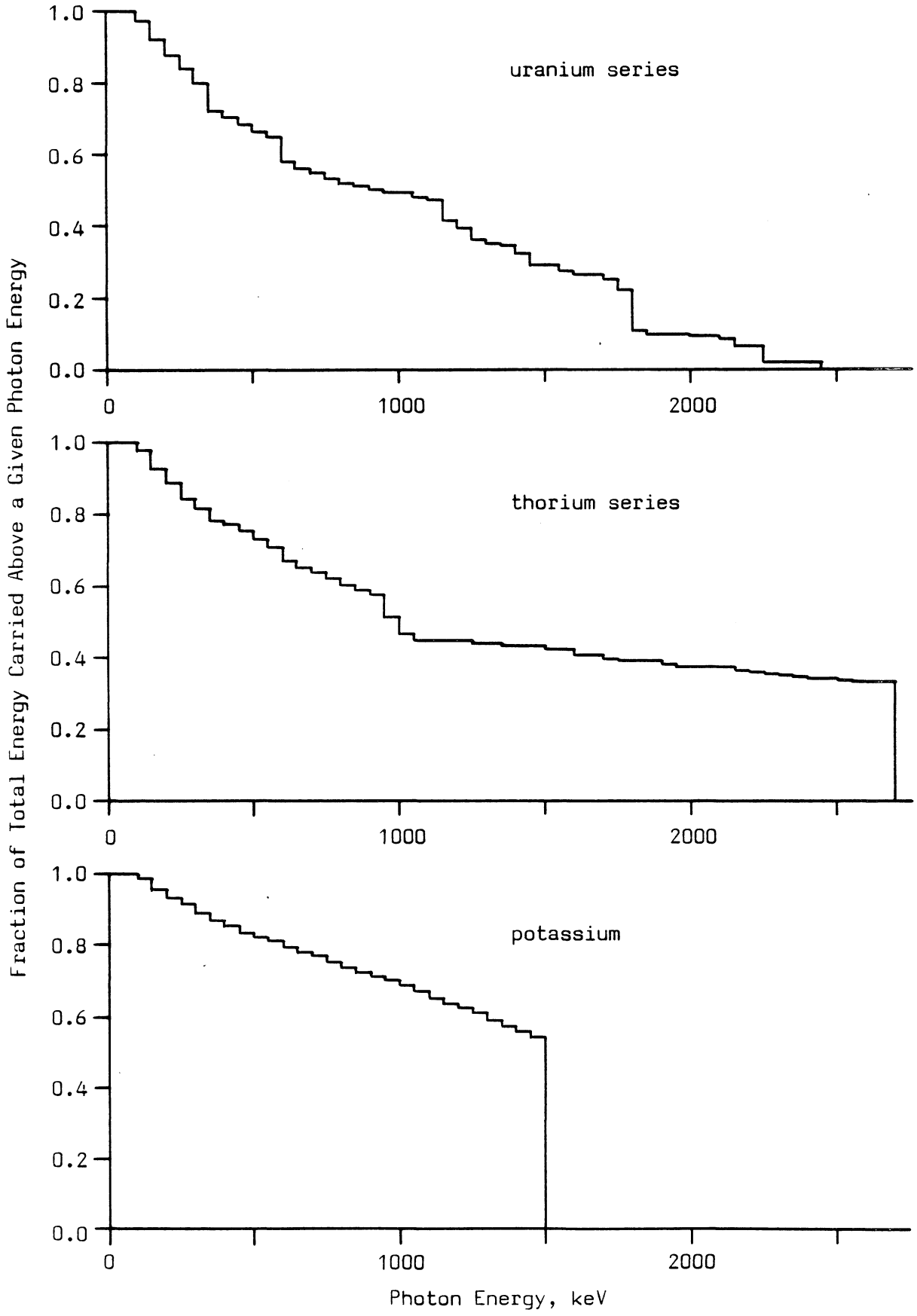

infinite matrix spectrum it is likely that a significant fraction of the total energy absorbed by a phosphor is carried by photons that will be noticeably attenuated by practical phosphor dimensions (e.g. photon energies of less than 200 keV, see figure 3.3.8) and so this assumption is not necessarily valid. Although it should be possible to modify the general theory to remove this limitation, the simpler approach adopted here is to assume charged particle equilibrium (CPE) across the phosphor/wall interface, and to calculate the attenuation due to the wall material using the appropriate mass attenuation coefficients. The degree to which this assumption is satisfied by the phosphor/wall combinations used in the preceding sections will be discussed in section 3.3.3. The rate of energy absorption from this attenuated photon spectrum by the phosphor can then be calculated for each energy interval, and the total dose rate obtained by summation. Consider first the attenuation of the infinite matrix spectrum by the capsule wall, such that

$$I(E) = I_o(E) \exp(- (\mu/\rho)^{w}_{att} \rho^{w} g^{w}) \qquad ------ 6$$

where $\underline{I(E)}$ is the attenuated photon flux in the energy interval $\underline{E}$,

$\underline{I_o(E)}$ is the incident photon flux in the energy interval $\underline{E}$,

$\underline{(\mu/\rho)_{att}}$ is the mass attenuation coefficient at that energy,

$\underline{\rho}$ is the bulk density,

$\underline{g}$ is the average path length,

and the superscript $\underline{w}$ indicates the wall material. This assumes of course that any photons scattered by the wall are unlikely to undergo further interactions with the phosphor. The other extreme would be to use the mass energy absorption coefficients to give the attenuation; this would assume that all scattered photons are subsequently available to interact with the phosphor. The true situation will clearly lie somewhere in between, but from a consideration of the likely geometries, and of the angular dependence of Compton scattering, it can be concluded that the mass attenuation coefficients are the better choice. The resulting attenuated spectrum, $\underline{I(E)}$, then interacts with the phosphor, and the energy absorbed is calculated using the mass energy absorption coefficients. This assumes that the

probability of a photon inelastically scattered in the phosphor subsequently interacting with the phosphor is negligibly small, and also that the TL response per rad of the phosphor is independent of the photon energy, (see section 3.3.4). Thus the energy absorbed per second, $\dot{E}_a^P(E)$, in the phosphor from the attenuated gamma flux $I(E)$ is given by

$$\dot{E}_a^P(E) = I(E)\left[1 - e^{-(\mu/\rho)_{en}^P \rho^P g^P}\right]\frac{V}{g^P} \quad \text{- - - - - - 7}$$

where $(\mu/\rho)_{en}$ are the mass energy absorption coefficients, and the superscript P stands for the phosphor. The effective path length through the wall, g^W, in equation (6) is taken to be the radial wall thickness; that through the phosphor, g^P, in equation (7) is taken to be the average length of randomly oriented chords in a convex body, given by ICRU 33 (1980) as

$$g = \frac{4V}{S} \quad \text{- - - - - - - - - - - - 8}$$

where V is the volume of a convex body of surface area S. It should also be noted that ρ is the bulk density which may be dependent on grain size and packing density in the case of the phosphor. Note that using the radial wall thickness for g^W will tend to underestimate the true value, because it neglects oblique photon incidence. It is thought that this simplification is justified because the degree of obliquity is constrained by the condition that the photon must pass through the phosphor, and also because the dose at a point is absorbed from the kerma produced some distance 'upstream' of that point (see chapter 2). Therefore the geometric path length will always tend to give rise to an overestimate of the true attenuation.

The absorbed energy per second in equation (7) may then be expressed as dose rate in the phosphor, $\dot{D}^P(E)$, by dividing by the phosphor mass, $\rho^P V^P$, i.e.

$$\dot{D}^P(E) = \frac{\dot{E}_a^P(E)}{\rho^P V^P} \quad \text{- - - - - - - - - - - - 9}$$

Thus the energy absorbed from the photon flux in a single energy

interval may be calculated using equations (6) to (9). In this case. where a broad spectrum of energies is involved, equation (9) must then be summed with respect to energy. This has been done for the phosphors and encapsulations described in section 3.2.1, and is detailed in the next section.

3.3.3 Calculation of the dose rate recorded by TL capsules

This section sets out the results of the calculations described above, with the capsules exposed to the infinite matrix spectra discussed in section 3.3.1. However, the sources of the remaining input data must first be given, and the degree to which the assumptions set out in section 3.3.2 are met must be considered further.

The most important assumption was that of charged particle equilibrium across the phosphor/wall interface. This will only be the case if the two materials are perfectly matched, i.e. if both the ratios of the electronic stopping powers and of the mass energy absorption coefficients of the phosphor to the wall material are close to unity across the energy range of interest. Figure 3.3.6 a,b,c,d gives the ratio of the electronic stopping powers of the four phosphors used to those of copper, of glass, of aluminium and of nylon respectively. These curves have been calculated from data presented in BERGER and SELTZER (1964) assuming the compositions given in table 3.2.1, and that the Bragg additivity rule applies, i.e. that the average stopping power for a compound is given by

$$\overline{S} = \sum_i S_i w_i \qquad \text{- - - - - - - - - - 10}$$

where $\overline{S}$ is the average stopping power,

S_i is the stopping power of the 'i'th element,

w_i is the fraction by weight of that element.

Similarly figure 3.3.7 a,b,c,d gives the same ratios of the mass energy absorption coefficients, calculated from data given by STORM and ISRAEL (1970), using equation (5). Note that here the vertical scale is logarithmic.

Clearly the best agreement is between aluminium oxide, obsidian

Figure 3.3.6

Ratio of phosphor stopping powers to those of the encapsulating material

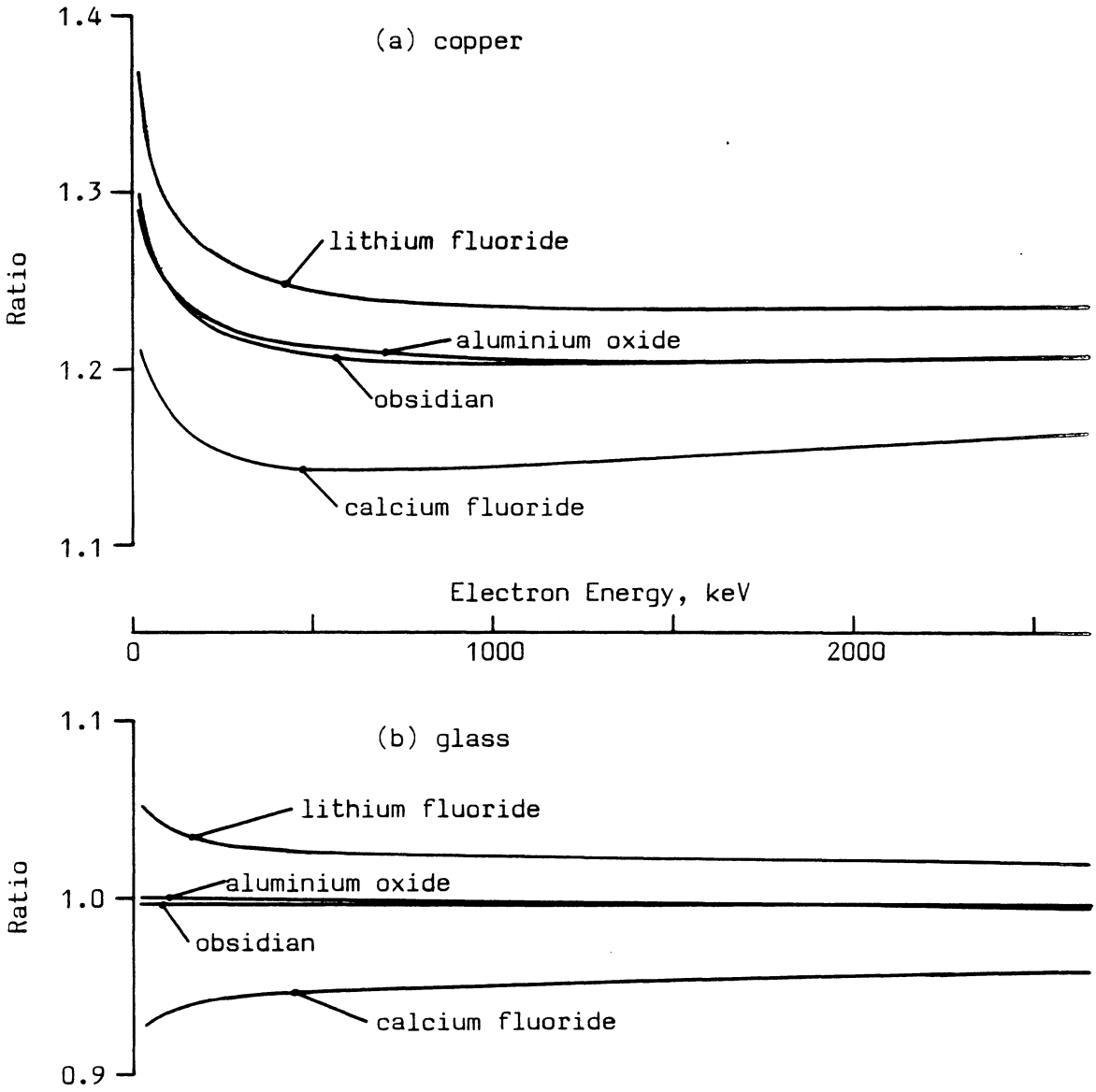

Figure 3.3.6 (continued)

Ratio of phosphor stopping powers to those of the encapsulating material

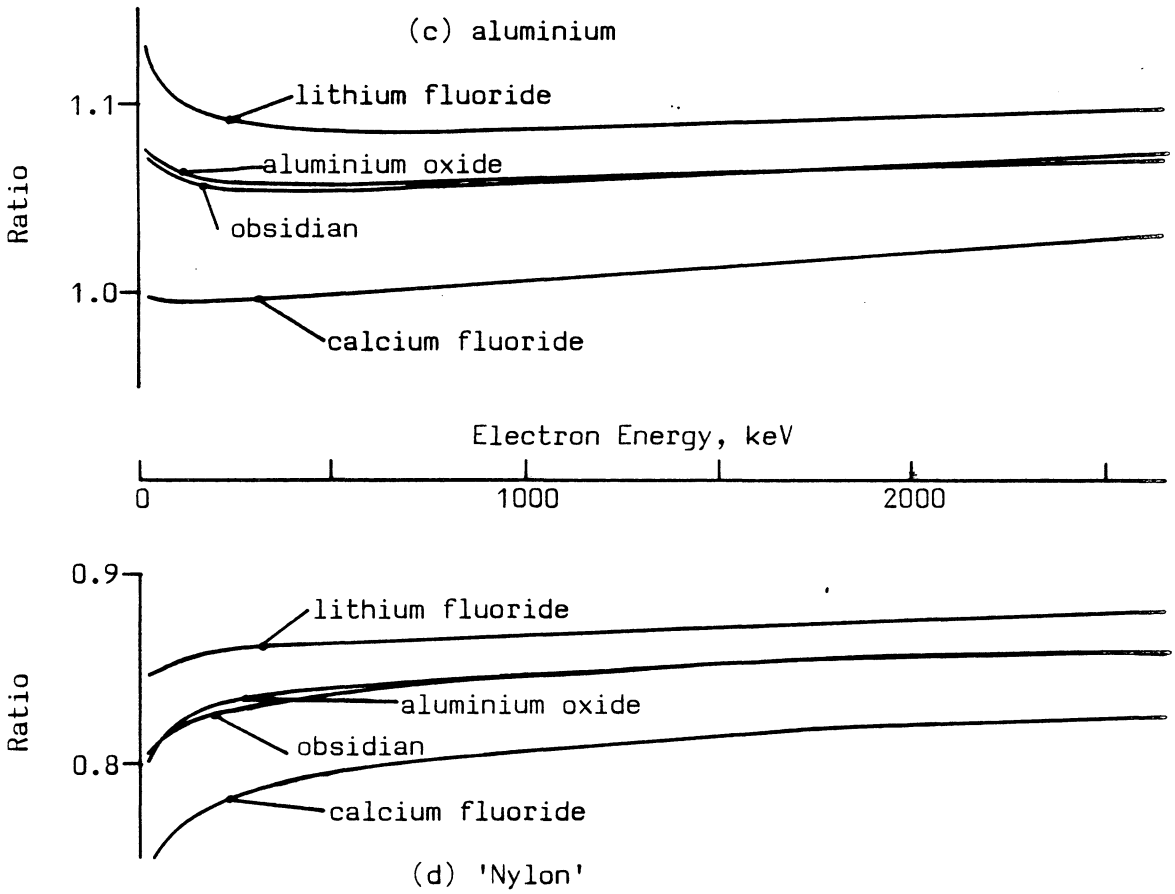

Figure 3.3.7

Ratio of phosphor mass absorption coefficients to those of the encapsulating material

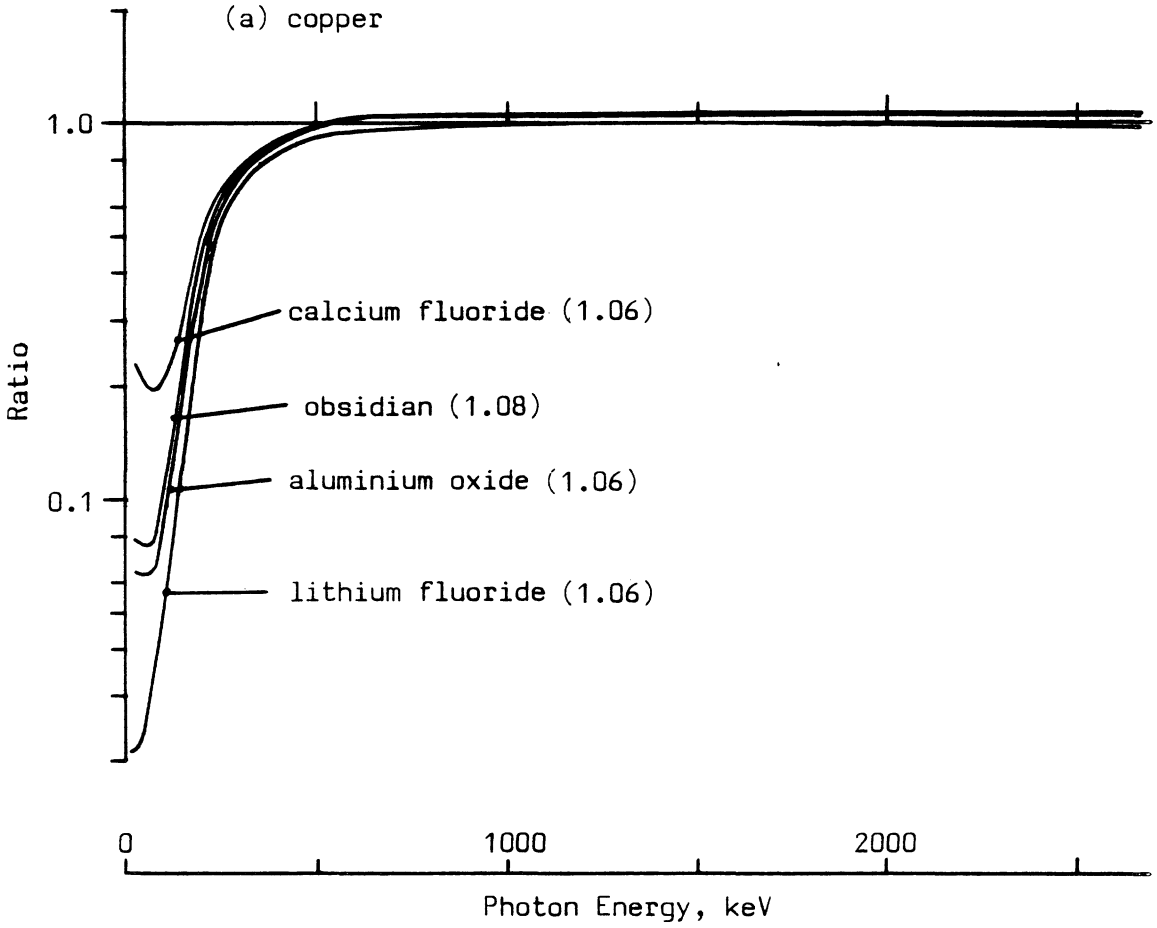

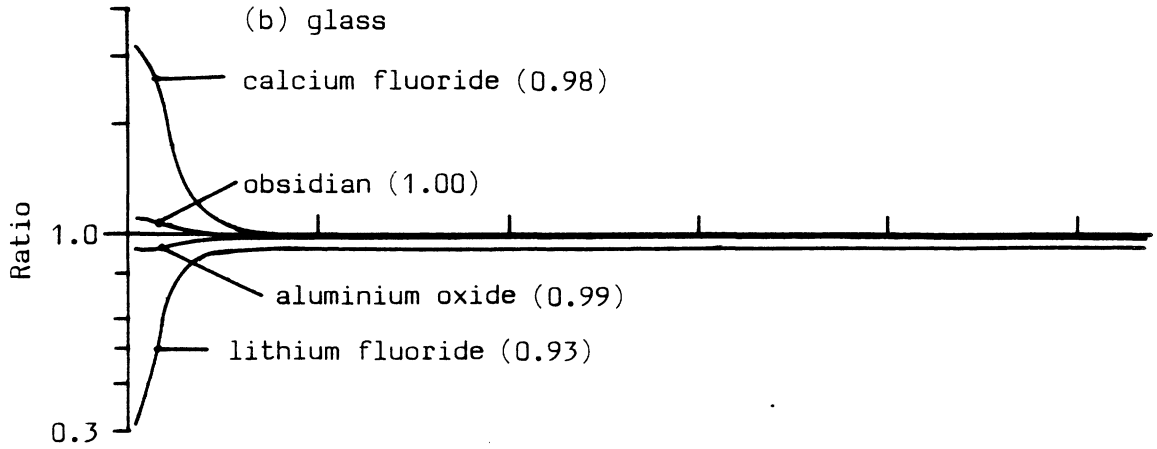

Note: values of the ratio at 1 MeV are given in parentheses

Figure 3.3.7 (continued)

Ratio of phosphor mass absorption coefficients to those of the encapsulating material

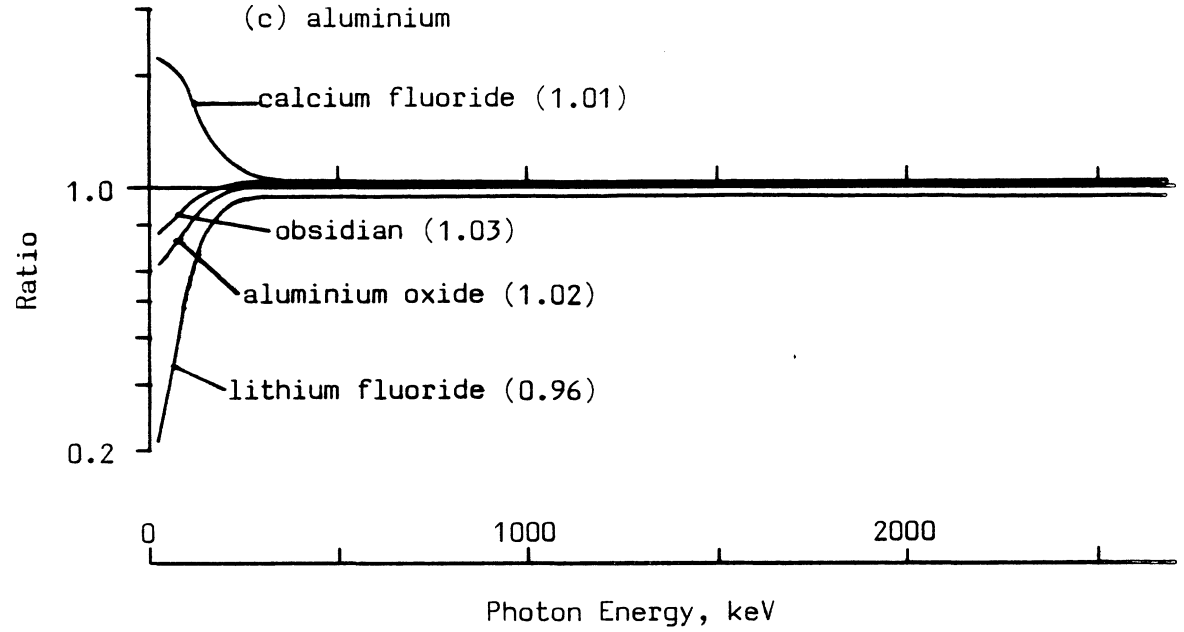

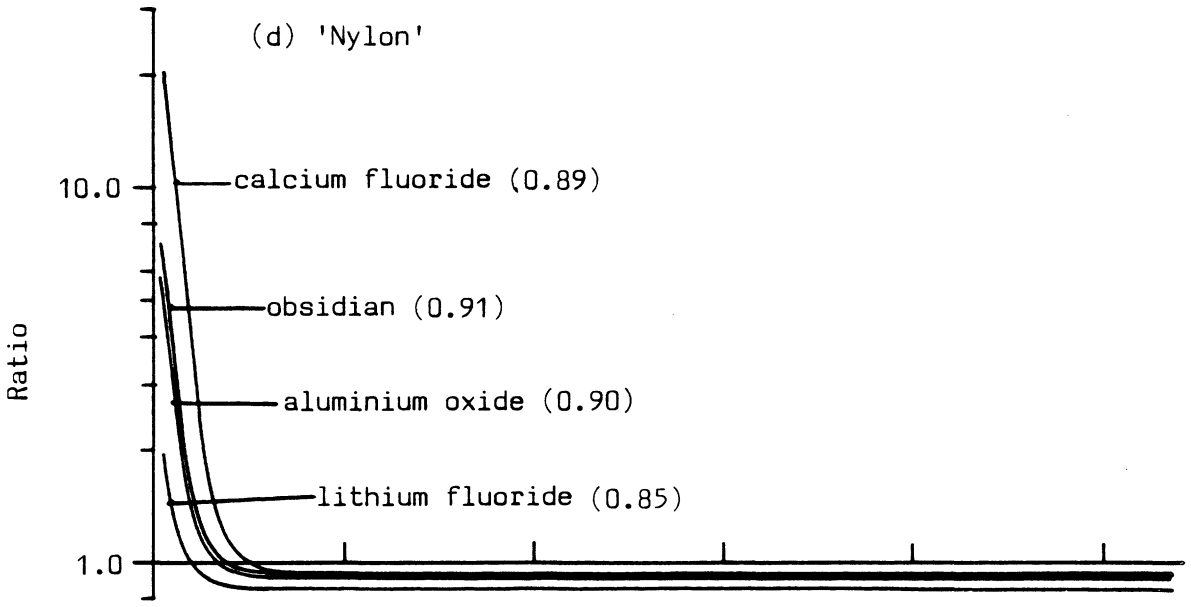

Note: values of the ratio at 1 MeV are given in parentheses

and glass, and it is for these two combinations that equation (9) should most closely approximate to the experimental situation, no matter how little phosphor was used in the capsule. The best match to calcium fluoride is aluminium, and to lithium fluoride, nylon, although these combinations are not as satisfactory. In practice however, it is expected that in view of the minimum quantity of 100 mg used, equation (9) should provide reasonably accurate predictions of the dose rate in all the phosphors encapsulated in aluminium and glass, and also of that of lithium fluoride in nylon. Furthermore, it was shown in section 3.2.3 that, at least for calcium fluoride in copper, sufficient phosphor was used to ensure that the dose rate was independent of phosphor mass, up to about 500 mg. This implies that the effect of any changes in the secondary electron flux across the phosphor/wall boundary on the average dose rate was small, and so it is likely that equation (9) will apply in this case. It is less certain that this should also be true of the remaining combinations, as the fractional differences in stopping powers and mass absorption coefficients for these phosphor/wall combinations are greater than those between calcium fluoride and copper.

It must also be noted here that only the copper capsules are sufficiently thick to guarantee that all the secondary electron flux in the wall is generated within the wall material. For instance, an electron of energy about 0.8 MeV would just penetrate 1.5 mm of aluminium, the corresponding figure for 3 mm of glass is about 1.6 MeV, and for 4 mm of nylon, about 0.9 MeV. Nevertheless, in view of the similarities in photon absorption characteristics and stopping powers of concrete, soil, glass and aluminium this will introduce a negligible error in these cases. Even for nylon capsules the error is not thought to be significant as it is that material closest to or in contact with the phosphor that will be the most important factor in determining the electron spectrum entering the phosphor (BURLIN and CHAN, 1969).

The effective density of the phosphors must now be considered. All of the phosphors were of the same grain size fraction, and so it is assumed that the same packing fraction for loosely piled grains applies to each. This fraction has been investigated for calcium fluoride directly; for volumes greater than 0.02 cm^3 it was found to

be constant at 0.63 $\pm$ 0.03. This is the coefficient used to derive the bulk density, $\underline{\rho^p}$, from the density of the solid phosphor, to be used in equations (8) and (9).

Finally we must reconsider the spectral data. The emitted photon intensities used by JAIN et al (1979) for the primary spectra were relative, and so comparison with the dose rate per unit activity figures given in Appendix E cannot readily be made. However, the infinite matrix dose rate for the 'unit source' used by these authors can be calculated, in two ways. (The 'unit source' is defined as that concentration of K-40, or of emitters from the uranium or thorium series, that would give rise to 1 photon sec^{-1} cm^{-3} in the infinite medium.) The first method is to derive the average energy per photon for each of the primary spectra, calculated to be 797.4 keV, 843.0 keV and 1461 keV for the uranium, thorium and potassium spectrum respectively, and then knowing the density of shale (2.6117 g cm^{-3}) calculate the infinite matrix dose rate assuming that the energy absorbed per unit mass equals that emitted. The second approach is to allow the calculated infinite matrix spectra to interact with a small unencapsulated shale absorber, using equations (7) to (9). This calculation has been performed for a variety of absorber sizes (all with no wall attenuation) and the dose rate has been found to be constant to within 0.1% for spherical grain sizes less than 10 μm in diameter. Both methods give results within 3% of each other for each spectrum. It is thought that these small differences arise as a result of the approximations made in computing the infinite matrix spectra, as well as from systematic errors in mass energy absorption coefficients, and so the latter approach of interacting with a shale absorber is used here when expressing the calculated dose rates as fractions of the appropriate infinite matrix dose rates.

Equation (9) has been summed with respect to energy for each of the phosphor/wall combinations discussed, using each of the three source spectra, uranium, thorium and potassium, as input data, and the results are given in table 3.3.2, with the dose rates expressed as fractions of the appropriate infinite matrix dose rate.

3.3.4 Discussion

Before considering the calculated results for the thorium and

Table 3.3.2

Calculated ratios of capsule dose rates to the infinite matrix dose rates

	calcium fluoride	aluminium oxide	obsidian	lithium fluoride
Uranium spectrum:				
Nylon	1.01	0.86	0.89	0.79
aluminium	1.01	0.87	0.90	0.79
glass	0.97	0.84	0.87	0.76
copper	0.83	0.76	0.78	0.71
Thorium spectrum:				
Nylon	1.01	0.87	0.90	0.79
aluminium	1.01	0.87	0.90	0.79
glass	0.98	0.84	0.87	0.77
copper	0.84	0.77	0.79	0.72
Potassium spectrum:				
Nylon	0.98	0.90	0.92	0.83
aluminium	0.98	0.88	0.93	0.84
glass	0.95	0.88	0.90	0.81
copper	0.86	0.83	0.84	0.77

Note: calculated as described in text using infinite matrix spectra given by JAIN et al (1979).

and potassium spectra, the experimental calibration factors taken from section 3.2 must be compared with the calculated values derived using the uranium spectrum. This is done in table 3.3.3. As expected obsidian and aluminium oxide in both aluminium and glass capsules give good agreement with the calculated response, as does lithium fluoride in nylon. However, the calcium fluoride results for these three encapsulations appear significantly discrepant. This is unexpected, at least in the case of calcium fluoride in aluminium, and it is thought that two effects combine to produce this discrepancy. The first arises from the differences between the composition of shale and the calcium rich concrete in the block. Figure 3.3.2 shows that at low energies the mass attenuation coefficients of the block are greater than those of shale, which implies that the actual photon flux at these low energies will be less than that calculated for shale. Aluminium oxide, obsidian and lithium fluoride are not expected to be sensitive to such low energy discrepancies; as can be seen in figure 3.3.8(a) less than 6% of the total dose to aluminium oxide in glass is delivered by photons of energy less than 100 keV, whereas calcium fluoride in nylon, aluminium and glass (figure 3.3.8(b))absorbs about 14% of the total dose from such low energy photons. Calcium fluoride in copper (figure 3.3.8(c)) again absorbs less than 5% from this region because of the large attenuation coefficient of copper at low energies. Clearly calcium fluoride in nylon, aluminium and glass will be much more sensitive to discrepancies between the calculated and true low energy flux than any of the other combinations. Secondly it is possible, although unlikely, that insufficient phosphor was used to ensure that the effects arising from the failure of charged particle equilibrium across the phosphor/wall boundary were reduced to negligible proportions.

It is worth noting at this point that another possible explanation for these discrepancies would arise if the TL response per rad was not independent of energy, i.e. if the variation of TL response with energy was not given by the mass energy absorption coefficients. However, ALMOND et al (1968) have measured the relative response of calcium fluoride and found that it agrees well with the calculated response in the energy range of interest here.

Table 3.3.3

Ratio of observed capsule response in uranium concrete block to calculated response

	calcium fluoride	aluminium oxide	obsidian	lithium fluoride
Nylon	0.86_{5}	1.02_{7}	-	1.04_{8}
aluminium	0.85_{5}	0.91_{6}	1.00_{7}	-
glass	0.85_{5}	0.98_{7}	1.00_{7}	-
copper	1.04_{7}	1.12_{8}	1.38_{10}	1.49_{11}

Note: errors are in the least significant figures, and arise from errors in the observed results only. They include the total error in beta source calibration and in the block dose rate. Note that the beta source was calibrated for each phosphor used. When comparing the results from different phosphors a large fraction of the normally systematic error in this calibration will in this case no longer be necessarily systematic in the same direction, and in general separation of the total errors given into systematic and random components is complex. However it is estimated that on average these two components contribute approximately equally to the total error.

Figure 3.3.8

Absorbed dose plotted against photon energy for three phosphor/wall combinations when exposed to the infinite matrix uranium spectrum

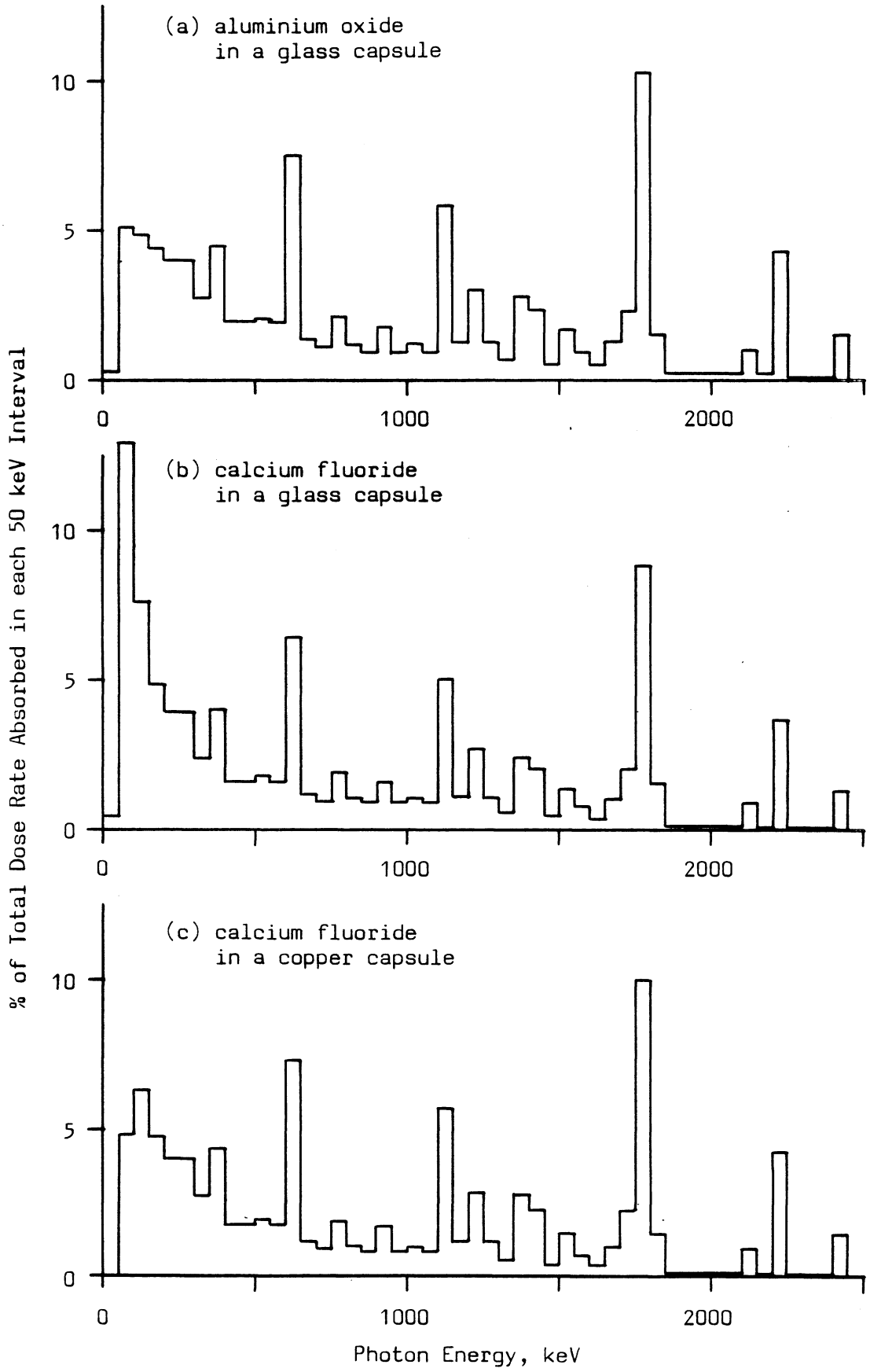

We shall now consider the other major discrepancies between the calculated and observed responses, those of lithium fluoride and obsidian in copper. The most likely cause of this disagreement is that a significant proportion of the total dose to these phosphors is in fact derived from the secondary electron flux generated in the wall material. This is possible in these cases, because the fractional differences between the mass energy absorption coefficients and stopping powers of, say, obsidian and those of copper are greater than the differences between those of calcium fluoride and of copper. Thus the results of section 3.2.3, where the variation of dose rate with mass of calcium fluoride in copper was investigated, would not necessarily apply to these combinations. However, it must be acknowledged that this explanation does not account for the observed difference in the response of aluminium oxide and obsidian in copper. Both the mass energy absorption characteristics and the electronic stopping powers of these two phosphors are very similar, and so it is thought that the difference found is an experimental artefact. (The aluminium oxide result is based on only one measurement). Another important contribution in these circumstances is likely to arise from electron backscattering effects at the phosphor/wall interface such as have been observed, albeit in planar geometry, by DUTREIX and BERNARD (1966) and by OGUNLEYE et al (1980).

Despite the discrepancies discussed above, it is felt that the results of table 3.3.3 show that for those phosphor/wall combinations where the assumption of charged particle equilibrium is valid the calculations of section 3.3.3 do provide good estimates of the true response. Furthermore, this conclusion can be extended to those cases where we can be sure that any discontinuity that does exist contributes little to the average dose rate. The particular example of importance here is that of calcium fluoride in copper for which it has been experimentally demonstrated that sufficient phosphor was used to ensure that this condition was fulfilled. It is now considered valid to use the calculated response of the combinations discussed above, when allowed to interact with the thorium and potassium spectra, to calculate average calibration factors for use when exposed to a typical composite spectrum.

3.3.5 Variation of relative response of capsules with energy compared with a small unencapsulated shale absorber

It is instructive to consider variations in the relative response of some of the phosphor/wall combinations with energy, when compared with the response of the infinite matrix medium. This has been done for aluminium oxide in glass, and calcium fluoride in glass and copper, by dividing the proportion of energy absorbed from the incident photon flux by these capsules, by that absorbed by a small (<10 μm diameter) unencapsulated shale absorber for each energy interval. This variation in response is shown in figure 3.3.9(a). The dose absorbed from each energy interval by the shale absorber from the uranium spectrum is also shown (figure 3.3.9(b)) as is the integrated dose absorbed above each energy interval (figure 3.3.9(c)).

The response of the combination of calcium fluoride in copper is seen to be constant within ± 3% from about 100 keV to 2.5 MeV, in contrast to that of calcium fluoride and aluminium oxide in glass, which varies rapidly below about 250 keV. This relatively flat response of calcium fluoride in copper is the combined result of the large increase in energy absorption at low energies of calcium fluoride, with the correspondingly large attenuation of low energy photons by the copper capsule. Over the higher energy range of the spectrum calcium fluoride in copper under-responds by about 11% on average, the other two combinations by about 8%. Unfortunately, about 25% of the infinite matrix dose is absorbed from photons of energy less than 250 keV, only 10% from photons less than 100 keV. Clearly calcium fluoride in copper will be much less sensitive to variations in spectral shape when the relative response compared with that of the infinite matrix is considered. Thus the calibration factor of (1/0.83) derived from table 3.3.2 is likely to be less dependent on small variations in the composition of the infinite matrix, for instance due to water content fluctuations, than are the calibration factors appropriate to other potentially useful combinations.

3.3.6 Calculated average response of capsules exposed to a composite infinite matrix spectrum

Table 3.3.4 gives the averaged response of these various phosphor/wall combinations when exposed to a composite spectrum

Figure 3.3.9

(a) Relative response of various phosphor/wall combinations to a small unencapsulated shale grain

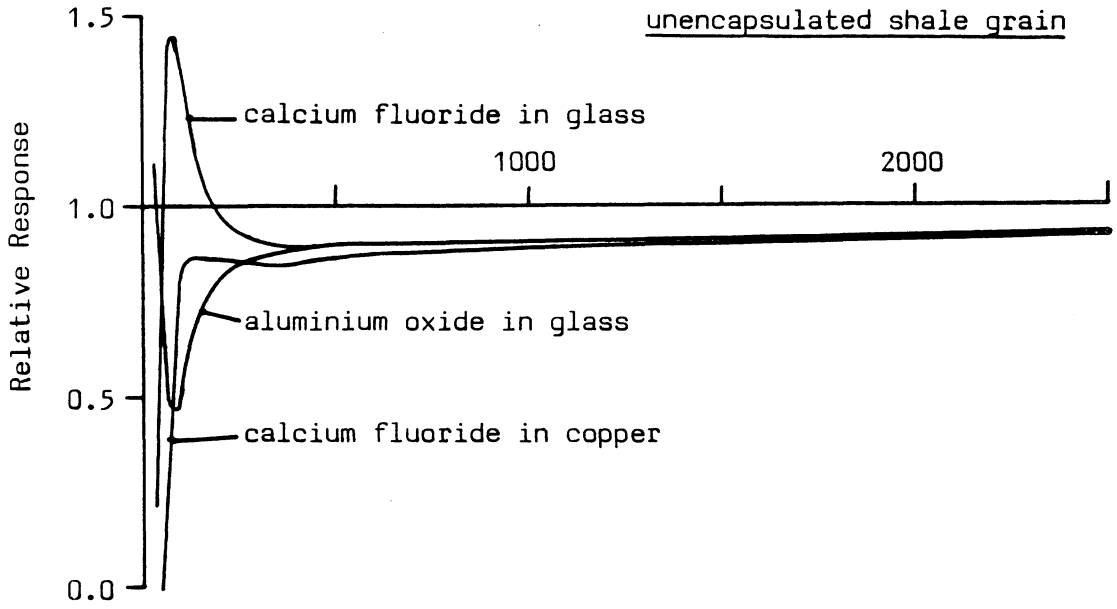

(b) Absorbed dose in an unencapsulated shale grain plotted against energy, uranium spectrum

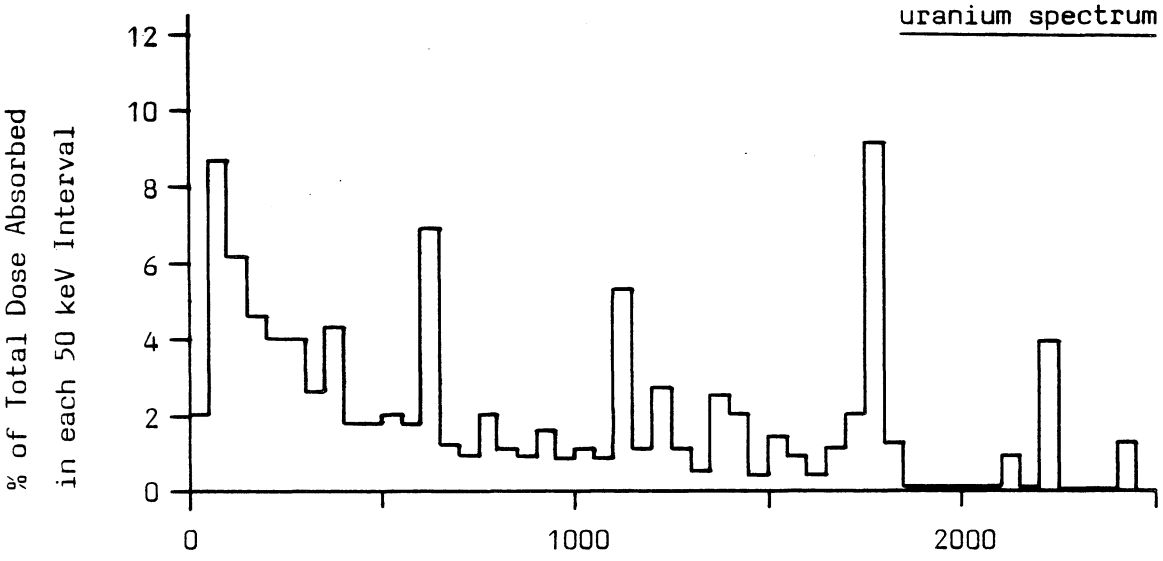

(c) Total dose absorbed from photons above a given energy in a small unencapsulated shale grain plotted against energy, uranium spectrum

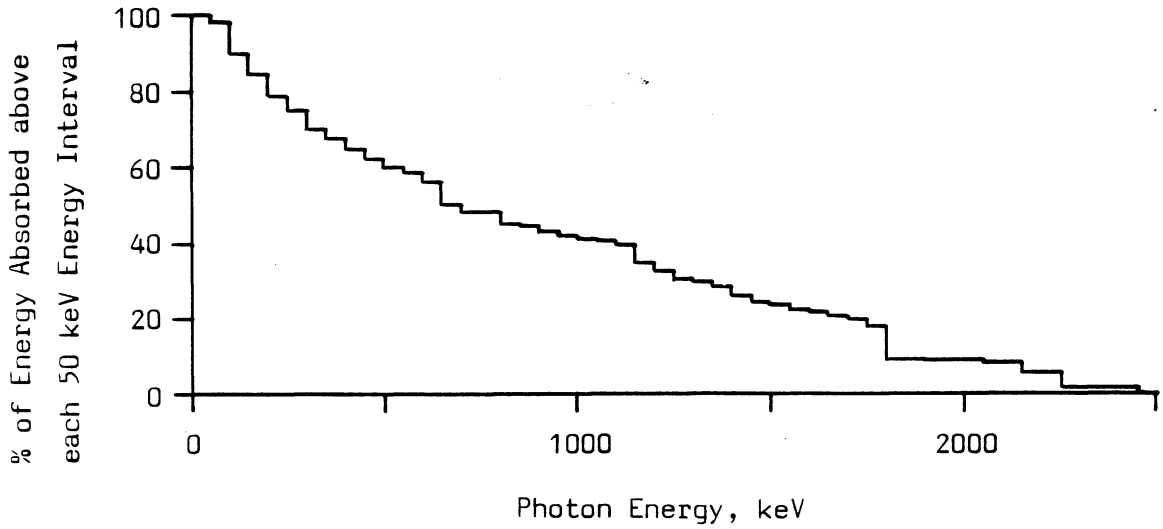

Table 3.3.4

Calculated average ratio of capsule dose rates to a composite infinite matrix dose rate

	calcium fluoride	aluminium oxide	obsidian	lithium fluoride
Nylon	1.01 $_{1}$	0.89 $_{3}$	0.92 $_{2}$	0.82 $_{3}$
aluminium	1.03 $_{2}$	0.90 $_{3}$	0.94 $_{3}$	0.83 $_{5}$
glass	0.97 $_{2}$	0.85 $_{2}$	0.88 $_{2}$	0.78 $_{3}$
copper	0.84 $_{2}$	0.79 $_{4}$	0.81 $_{3}$	0.74 $_{3}$

Note: 1) the above ratios have been calculated assuming a contribution of 27%, 37.2% and 35.8% from uranium, thorium and potassium respectively. These are the ratios that would arise from 'typical' activities of 1 pCi g^{-1} U-238 (+ U-235), 1 pCi g^{-1} Th-232 and 15 pCi g^{-1} of K-40.

2) an average correction of 3.4% and 1.5% for the beta dose contribution, in the aluminium and nylon capsules respectively, is also included.

3) the uncertainties given, in the least significant figures, are estimates of the degree of isotope dependence (see text)

4) the dose rate to quartz inclusions or pottery fine grains is expected to be within 3% of the infinite matrix soil dose rate.

corresponding to that from 1 pCi g^{-1} of uranium and thorium in secular equilibrium with their daughter products, and 15 pCi g^{-1} of K-40, i.e. 'typical' soil concentrations. The possible errors that might result if the true activity was entirely from one source are also given. The recommended combination for routine field use is calcium fluoride in copper. This has been shown to be insensitive to variations in the amount of material in the capsule, and as discussed in section 3.2.3, this phosphor is sensitive, fading is negligible, the measurement procedure is straightforward and the encapsulation is robust; all of these characteristics are important in a routine field dosimeter. As the attenuation characteristics of 'typical' soil are almost identical with those of shale, the ratio derived in this section should be directly applicable to environmental measurements 'on site' Furthermore, it was shown in the preceding section that this ratio should be insensitive to variations in spectral quality and thus to variations in soil composition.

Finally, the uncertainties on the correction factor of 1.19 derived from table 3.3.4 for the recommended combination of calcium fluoride in copper must be considered. Firstly there is a contribution of about 2.5% to allow for variation in the proportion of the three contributing sources to the composite spectrum. However, this figure covers the extreme possibilities of only one such source being in fact present; this is very unlikely in practice, and an uncertainty of about 1.5% is considered more realistic. Secondly, there is a component arising from the conversion from the infinite matrix dose rate to the dose rate in a 100 μm quartz grain or pottery fine grain. As discussed in section 3.1, this is likely to be less than 3%. There is also uncertainty arising from the variation in the infinite matrix spectral shape due to the range of soil compositions likely to be encountered. This is difficult to quantify, but it is not expected to be larger than the errors already discussed, and so total uncertainties of $\pm$ 5% are considered realistic.

3.4 CONCLUSION

The first part of this chapter described the design and construction of a 1 m cube of uranium doped concrete, built up from individual 20 cm cubes. The observed density was 2.25 g cm^{-3} $\pm$ 0.05,

and it is calculated that this is sufficient to allow the assumption that the energy absorbed per gram equals the energy released per gram (to better than 2%) to be used to calculate the dose rate at the centre of the block. Homogeneity tests suggest that the activity is uniform from one batch of approximately six 20 cm cubes to another, with a standard deviation of 2.8%. Gamma spectrometry measurements confirm the calculated uranium activity, but indicate that Ra-226 is in excess by 12%, and that there is 17% escape of Rn-222, at least from a sample crushed to less than 500 μm, and from a 1.5 cm thick solid disc. From these activities a dose rate to concrete at the centre of the 1 m concrete cube of 31.7 $\pm$ 1.6 rads yr^{-1} has been calculated.

Using this block it has been possible for the first time to make accurate absolute dosimetry measurements using a variety of phosphors and encapsulations. The dose rates in these various combinations were then predicted using published calculations of the infinite matrix uranium spectrum in shale, and when compared with the experimental results, these calculated responses gave agreement within experimental error for most of the combinations used. In particular, the ratio of the experimentally observed response of calcium fluoride in copper to that calculated is 1.04 $\pm$ 0.07, and this gives confidence that the approach used to calculate the phosphor/wall response is valid. In the course of these calculations it has become clear that the attenuation of the infinite matrix spectrum through a few millimetres of glass is not trivial; the calculated response of aluminium oxide or obsidian, both shale-like absorbers, in a glass capsule of 3 mm wall thickness, is about 13% below the infinite matrix dose rate. This suggests that care must be taken when estimating gamma dose rates to sherds of very different activity to that of the surrounding soil, especially when it is remembered that the outer 2 mm of a sherd is routinely removed to simplify the beta dosimetry.

Similar dosimeter response calculations have been performed using published infinite shale matrix thorium and potassium spectra, and the average response of a calcium fluoride in copper dosimeter to a 'typical' composite uranium, thorium and potassium spectrum evaluated. For this dosimeter combination, a correction factor of

1.19 must be applied to the observed dose rate to give the true infinite matrix dose rate, and thus the dose rate to a quartz inclusion or a pottery fine grain. Estimated uncertainties of 5% are associated with this figure, which has been previously assumed to be unity in the literature. This correction has been applied to all gamma TL dosimetry results described in subsequent chapters.

CHAPTER IV

DIRECT MEASUREMENT OF GAMMA DOSE RATES USING A SODIUM IODIDE DETECTOR

4.1 INTRODUCTION

On many occasions it is impractical to leave a dosimeter buried 'on site' for even a few weeks, and so a rapid means of measuring the gamma dose rate becomes a necessity. Such a technique has the further advantage of giving a means of surveying a site for radioactive inhomogeneity without having to wait for perhaps several months, as is necessary with a TL dosimeter, thus reducing the risk of misdirected effort.

This approach has been developed using a NaI(Tl) detector with portable scaler, and field tested against the standard TL dosimeter, calcium fluoride in copper capsules. It is found that for dry sites (soil water contents less than about 10%) the agreement is good, but that for wet sites there is a systematic discrepancy which shows some increase with increasing soil water content.

4.1.1 Conversion of detector count rate to phosphor dose rate

There are three possible approaches to the measurement of the environmental gamma dose rate using a sodium iodide crystal as detector. Two of these (see, for example, DEANS, 1964; ADAMS, 1964) involve some form of spectral analysis and often complex calculations to reduce the data to isotope concentrations and thus to dose rates. The third approach is the most readily applied to field studies. It assumes that there is an energy threshold above which the number of photons counted by the detector is proportional to the dose rate in the appropriate medium. Such a system is briefly described by WOLLENBERG and SMITH (1964), where a threshold position of about 0.11 MeV is used with a 3 inch by 3 inch crystal to determine the exposure rate above geological formations. A more complete description of a similar detector using a threshold of 0.37 MeV is given by LØVBORG and KIRKEGAARD (1974).

In this case the detector is to be buried in the ground, i.e. placed in an effectively infinite matrix of gamma emitters, and the spectral quality (the proportion of energy carried at high energies compared with low energies) is not necessarily similar to the two

cases mentioned above. It is thus useful to consider the conditions under which such a threshold position could exist, and then to examine the problem of conversion of the count rate above threshold to the dose rate in, say, calcium fluoride encapsulated in copper.

Consider first dose absorption by the capsule. Infinite matrix spectra calculated by JAIN et al (1979) were presented in chapter 3, and the similarities to soil spectra were discussed there. It was also shown that the calculated dose rate to calcium fluoride in a copper capsule was in good agreement with that observed. Figure 4.1.1 gives these photon spectra, integrated to give the total number of photons above a given energy, and each normalised to the dose rate calculated when the appropriate spectrum was allowed to interact with the standard copper capsule containing calcium fluoride, as described in section 3.3. It can be seen that there is an energy region between 100 keV and 500 keV where the number of photons above a given energy is independent, to a good approximation, of the emitter present when normalised to unit dose rate.

Now consider the interaction of the same photon flux with the sodium iodide crystal. The probability of an incident photon undergoing some interaction with the crystal is given by

$$1 - e^{-\mu g} \qquad \text{- - - - 1}$$

where μ is the linear attenuation coefficient of sodium iodide, and g is the average path length through the crystal.

ICRU 33 (1980) states that the average path length, g, for isotropic radiation through any convex volume is given by

$$g = \frac{4V}{S} \qquad \text{- - - - - 2}$$

where S is the surface area enclosing the volume V. For instance, for a typical 1 inch radius by 2 inch high right cylindrical crystal,

$$g = 3.39 \text{ cm}$$

If the detector was operated with a zero energy threshold, the probability of an interaction would give the probability of counting

Figure 4.1.1

Calculated integrated infinite matrix spectra, normalised to unit dose rate in calcium fluoride in copper

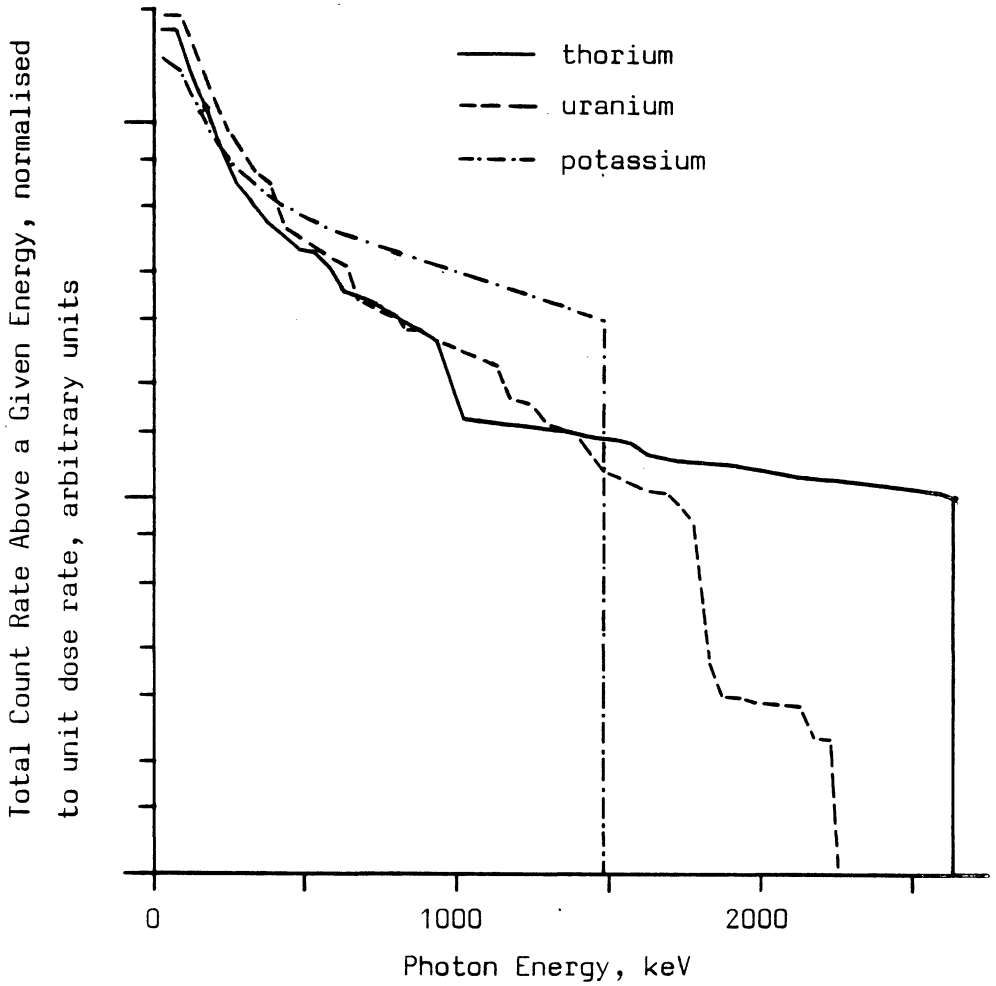

Note: spectral data derived from Jain et al (1979), see chapter 3.

the event, and hence the count rate, directly (neglecting coherent scattering). However, when an energy threshold, E_T, is used, the interaction probability must be multiplied by the fraction of interactions, f, that will deposit more energy in the crystal than the threshold value, i.e. the probability, P, of observing a photon is given by

$$P = f\,(1 - e^{-\mu g}) \qquad \text{- - - - - - - - - -} \quad 3$$

At the energies of interest (up to 3 MeV) these interactions will be dominated by Compton scattering and the photoelectric effect. However the proportion of interactions that take place by each of these two mechanisms is not simply given by the ratio of the incoherent scattering attenuation coefficient to the photoelectric coefficient, because multiple scattering events within the detector in which all the incident energy is eventually absorbed will not be resolved in time, and may appear as a single full energy release event, indistinguishable from a photoelectric absorption. MILLER et al (1958) have evaluated the fraction of all interactions that give rise to full energy release events (i.e. contribute to the photopeak) using the Monte Carlo method. The remaining fraction of interactions can be assumed to be entirely Compton scattering, with the energy of the Compton edge, E_c, given by

$$E_c = \frac{E}{1 + \frac{1}{2a}} \qquad \text{- - - - - - - - - - - - -} \quad 4$$

where

$a = \frac{E}{m_o c^2}$

E is the incident photon energy,

m_o is the electron rest mass, and

c is the velocity of light.

The average distribution of deposited energy by such inelastic scattering can be approximated by a uniform continuum up to the energy of the Compton edge, E_c. Figure 4.1.2 shows the relationship of this simplified continuum to the photopeak and threshold position. Combining the value of the photofraction f_p from MILLER et al (1958) and the fraction of scattering events, $(1 - f_p)$, we obtain an expression for the

Figure 4.1.2

Diagram of the relationship between a photopeak, Compton edge, Compton continuum and threshold, E_T, in the spectrum seen by the detector

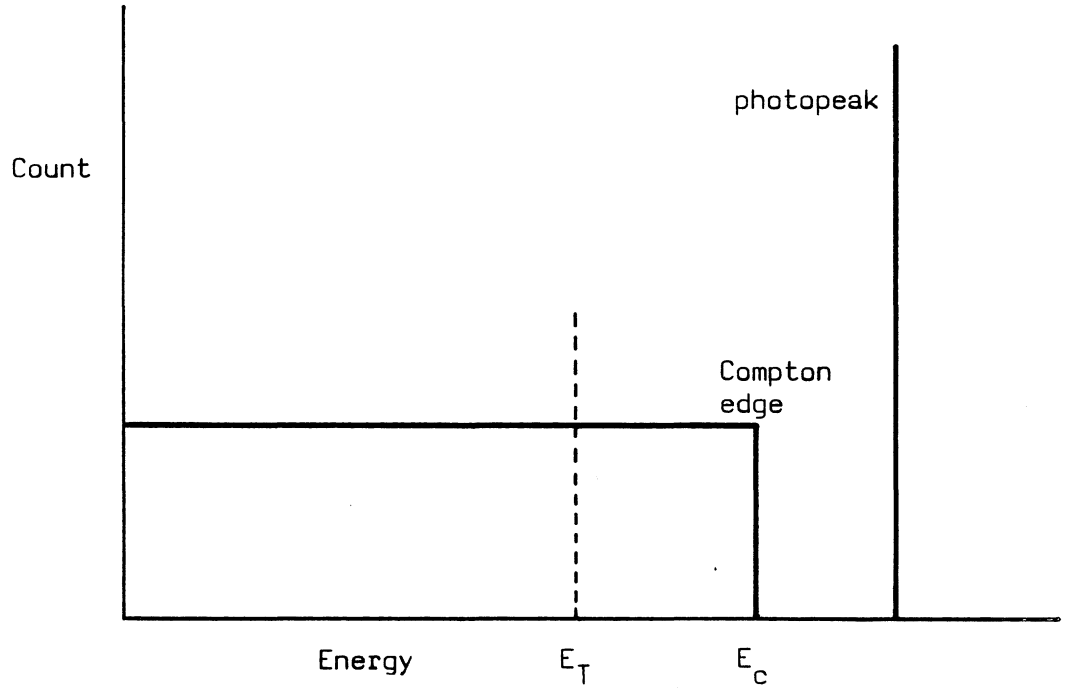

Figure 4.1.3

Probability, P, of observing an incident photon, energy E, for various threshold values, E_T

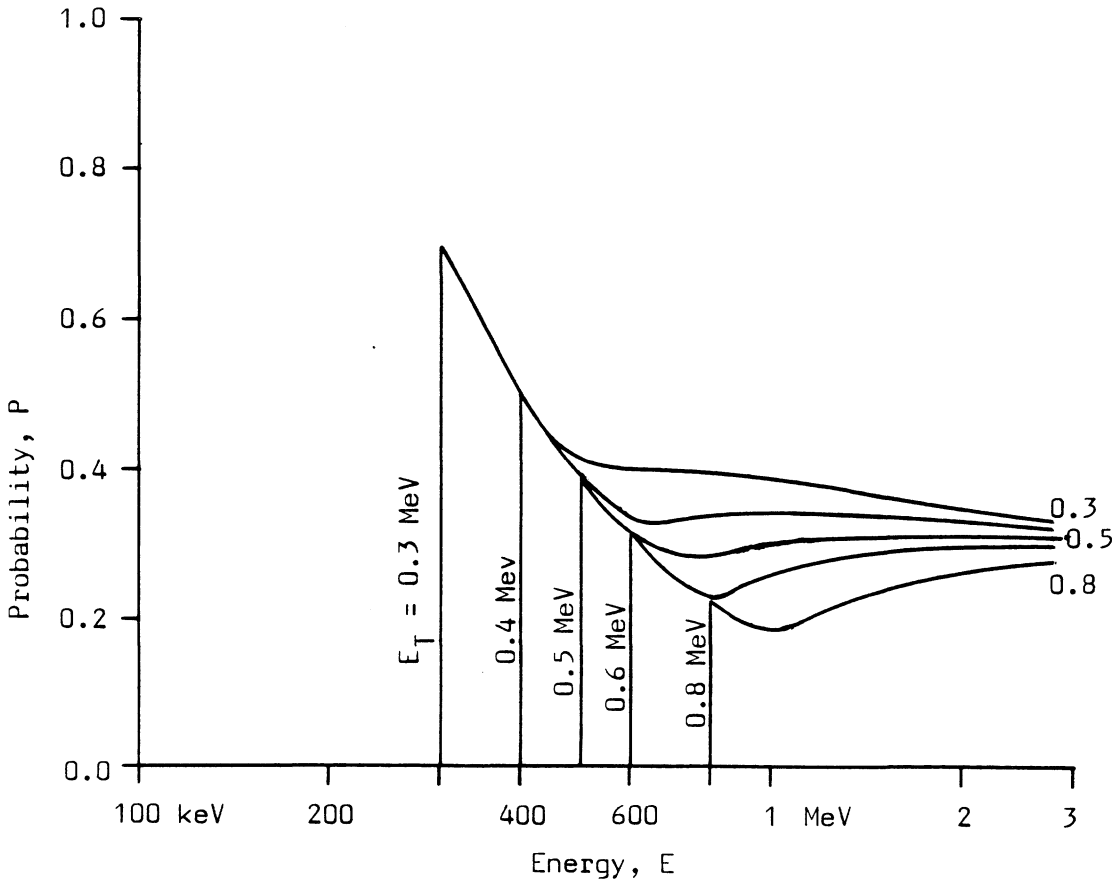

fraction of events, f, that deposit sufficient energy to be observed above the threshold energy

$$f = f_p + (1 - f_p)(1 - \frac{E_T}{E_c}), \quad \text{for } E > E_T \quad ---- \quad 5$$

Combining equations (5) and (3) we have an expression for the probability, P, of an incident photon being observed by the detector above the threshold energy

$$P = (1 - e^{-\mu g})[f_p + (1 - f_p)(1 - \frac{E_T}{E_c})] \quad ----- \quad 6$$

The variation of P with energy, for various threshold values, is given in figure 4.1.3. It can be seen that it is possible to set up an energy threshold, for instance near 0.5 MeV, such that the probability of detecting a high energy photon is approximately independent of the incident energy. It was concluded previously that the dose rate to calcium fluoride in a copper capsule was likely to be proportional to the number of high energy photons, independent of the gamma emitters present. Thus we can conclude that there is likely to be a threshold value above which the count rate in a sodium iodide crystal will be proportional to the dose rate in calcium fluoride in copper when exposed to an infinite gamma matrix, independent of the emitting isotopes present.

4.1.2 Experimental determination of threshold position

The confirmation of the existence of such a threshold position, and the determination of the threshold energy was undertaken experimentally. Initial measurements using a 1 inch diameter by 1.5 inch sodium iodide crystal suggested that indeed there was a threshold position above which the count rate was proportional to the calcium fluoride dose rate, but it also became obvious that the stability of the threshold was very important. As a result, a dedicated system was developed before carrying the measurements further.

4.1.3 Description of detector and associated electronics

The detector head consists of a 1.75 inch diameter by 2 inch high right cylindrical NaI(Tl) crystal with photomultiplier (Centronic type P4231BA) in a water tight tubular aluminium housing. This is

connected to a portable high voltage supply and amplifier/discriminator driving a scaler.

Gain stability is assisted by spectrum stabilisation, using an Am-241 source fixed against the end of the crystal by a lead/cadmium/copper laminate; the latter covers the end of the crystal and reduces the intensity of the low energy gamma rays which would otherwise interfere with the 60 keV stabilising peak. The stability of the detector will be discussed further in section 4.1.6.

The instrument is powered by nickel-cadmium rechargeable batteries and weighs about 4.5 kg.

4.1.4 The calibration facilities

The 20 inch cube concrete blocks mentioned in chapter 3 were used to calibrate the detector. Although it has been established (BOWMAN, 1976) that they only approximate to infinite matrices at high energies (greater than 1.5 MeV), below this they are considered effectively infinite. The consequences of this poor approximation for the eventual calibration must now be considered. The mass energy absorption coefficients of calcium fluoride do not vary sharply with energy above 0.2 MeV, and the ratio of these coefficients at 2.6 MeV to those at 0.5 MeV is about 0.80. This variation is to some extent cancelled out by the corresponding ratio of attenuation through the copper wall, of 1.06. If the threshold discussed in section 4.1.1 is placed at about 0.5 MeV, it is therefore to be expected that, to first order, the energy deposited by each photon on average is independent of photon energy. It was shown in section 4.1.1 that the relationship between the count rate and the number of photons above this threshold should also be independent of photon energy. Thus there should be a constant relationship with energy between dose deposited and the scintillator count rate. In that case the effect of the loss of some fraction of the highest energy photons from the uranium and thorium infinite matrix spectra as a result of the calibration blocks being too small will be to reduce the dose rate in the capsule, and to reduce the count rate in the scintillator, by the same fraction. Thus the non infinite block size should not significantly affect their use as a calibration facility.

The dose rates used, listed in table 4.1.1 are taken from BOWMAN (1976). The data shown is an average of all types of capsule employed, as the reproducibility of the results was not sufficient to distinguish between them. Reference to table 3.2.3 of chapter 3, indicates that this averaging should not introduce significant additional errors.

4.1.5 Spectra of calibration blocks

The output of the amplifier was fed to a pulse height analyser to obtain the spectra of the blocks. After subtracting the background spectrum (obtained from an inert 20 inch concrete cube) these were divided by the appropriate calcium fluoride dose rate, to give spectra normalised to a count time of one second and a dose rate of one mrad yr^{-1}. These are shown in figure 4.1.4 with the major photopeaks labelled.

These peaks were used to obtain the energy calibration curve shown in figure 4.1.5. Approximating this response with a straight line, linear regression gives

$$E = 0.0241\ C - 0.05 \qquad ------ 7$$

where $\underline{E}$ is the photon energy and
$\underline{C}$ is the channel number.
The error in the slope is $\pm$ 0.0005, in the intercept $\pm$ 0.03.

Figure 4.1.6 shows the integral spectra derived from figure 4.1.4 which clearly show a potential threshold position at about channel 20, above which the total count rate per unit dose rate is the same for all three blocks.

To evaluate this conversion figure, and to demonstrate the linearity of the response, the count rate above a threshold at channel 20 (0.43 keV $\pm$ 0.03) has been plotted against dose rate for all the blocks, including the background block, in figure 4.1.7. As is implicit in figure 4.1.6 the linearity is seen to be excellent and the equation of the line gives the conversion from scintillator count rate, $\underline{C_r}$ sec^{-1}, to dose rate, $\underline{D}$ mrad yr^{-1}, in calcium fluoride.

Table 4.1.1

Measured dose rates in calibration blocks, in mrad yr^{-1}

U-238	Th-232	K-40	Background
1224_{46}	652_{23}	170_{10}	60_{7}

Note:
1) dose rates are average results from dosimeter measurements using calcium fluoride in nylon, aluminium and copper capsules, derived from BOWMAN (1976).
2) errors are standard errors on the mean, and are shown in the least significant figures.
3) these dose rates have been corrected for the source recalibration of chapter 2.
4) the background dose rate given above has not been subtracted from the three active block dose rates shown.

Figure 4.1.4

Spectra from concrete blocks

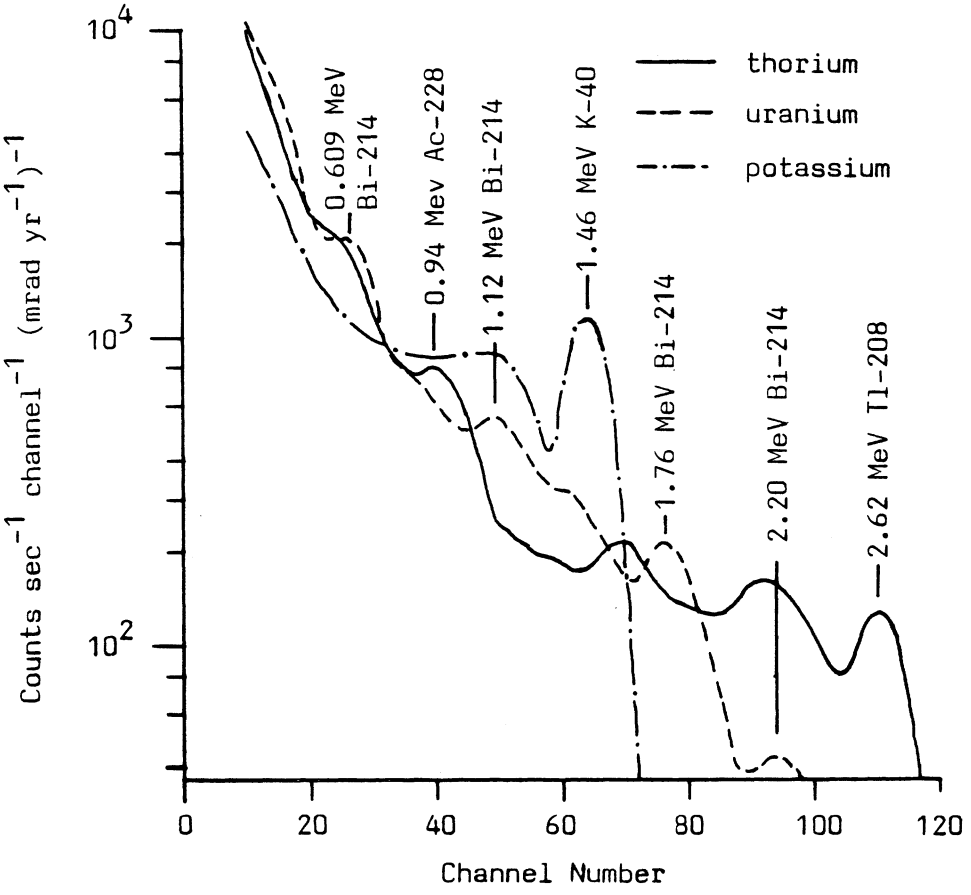

Figure 4.1.6

Integrated spectra from concrete blocks

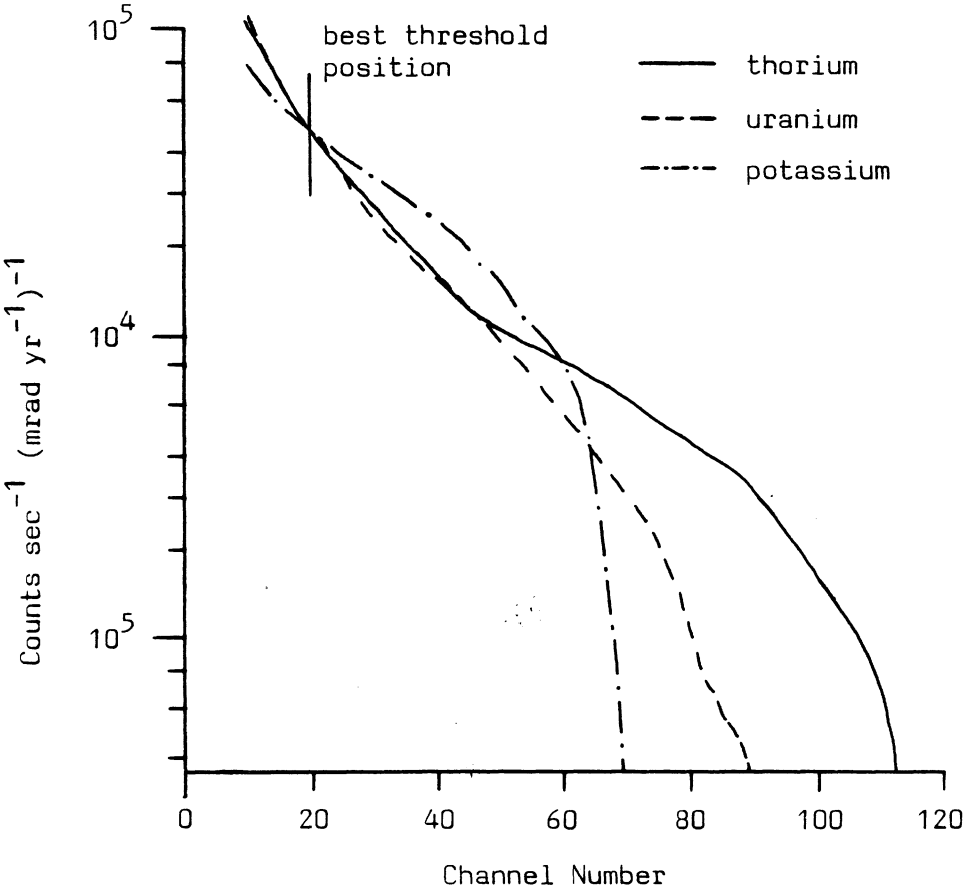

Figure 4.1.5

Energy calibration derived from figure 4.1.4

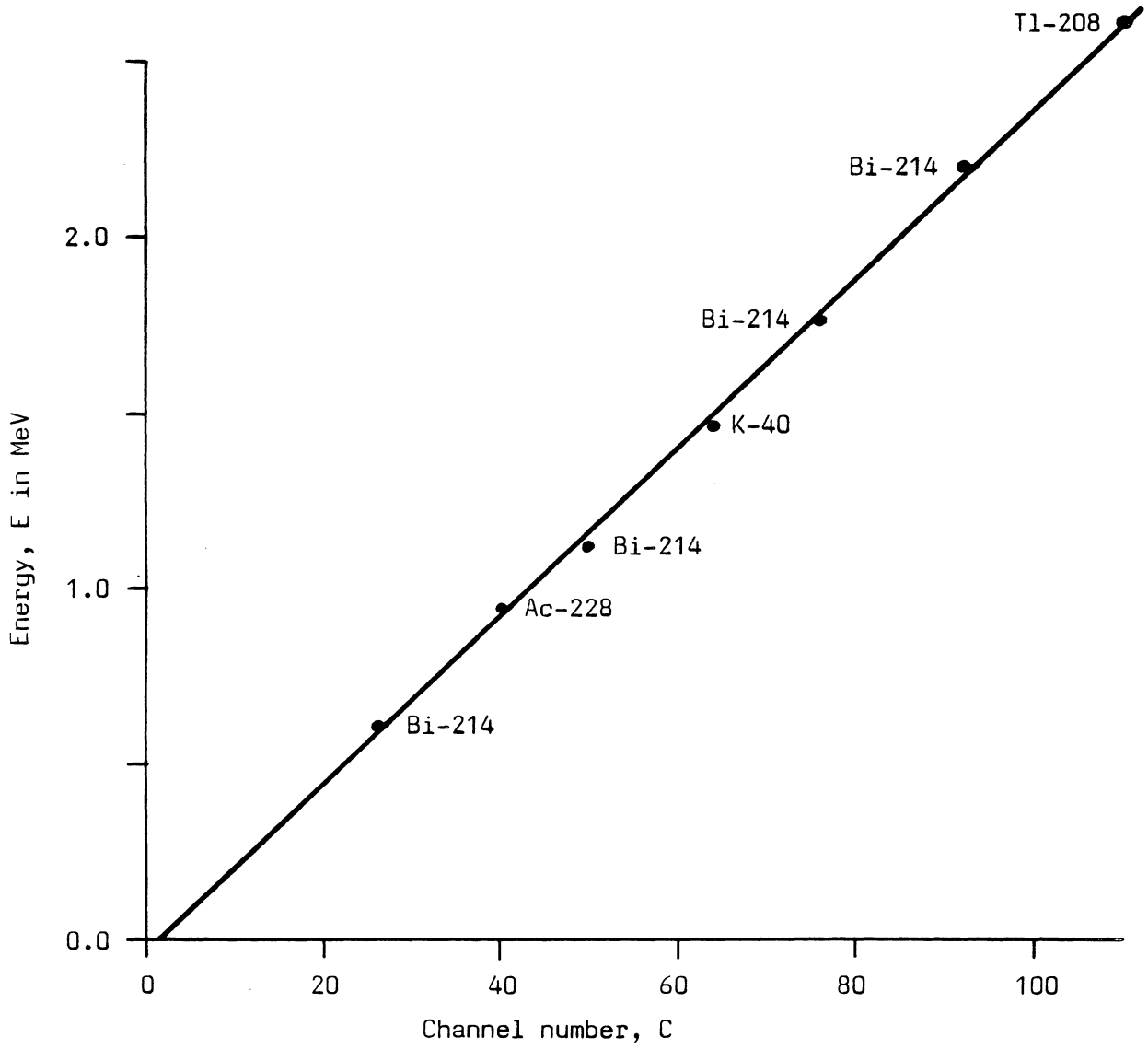

Figure 4.1.7 Count rate plotted against dose rate for threshold at channel 20 (0.43 MeV)

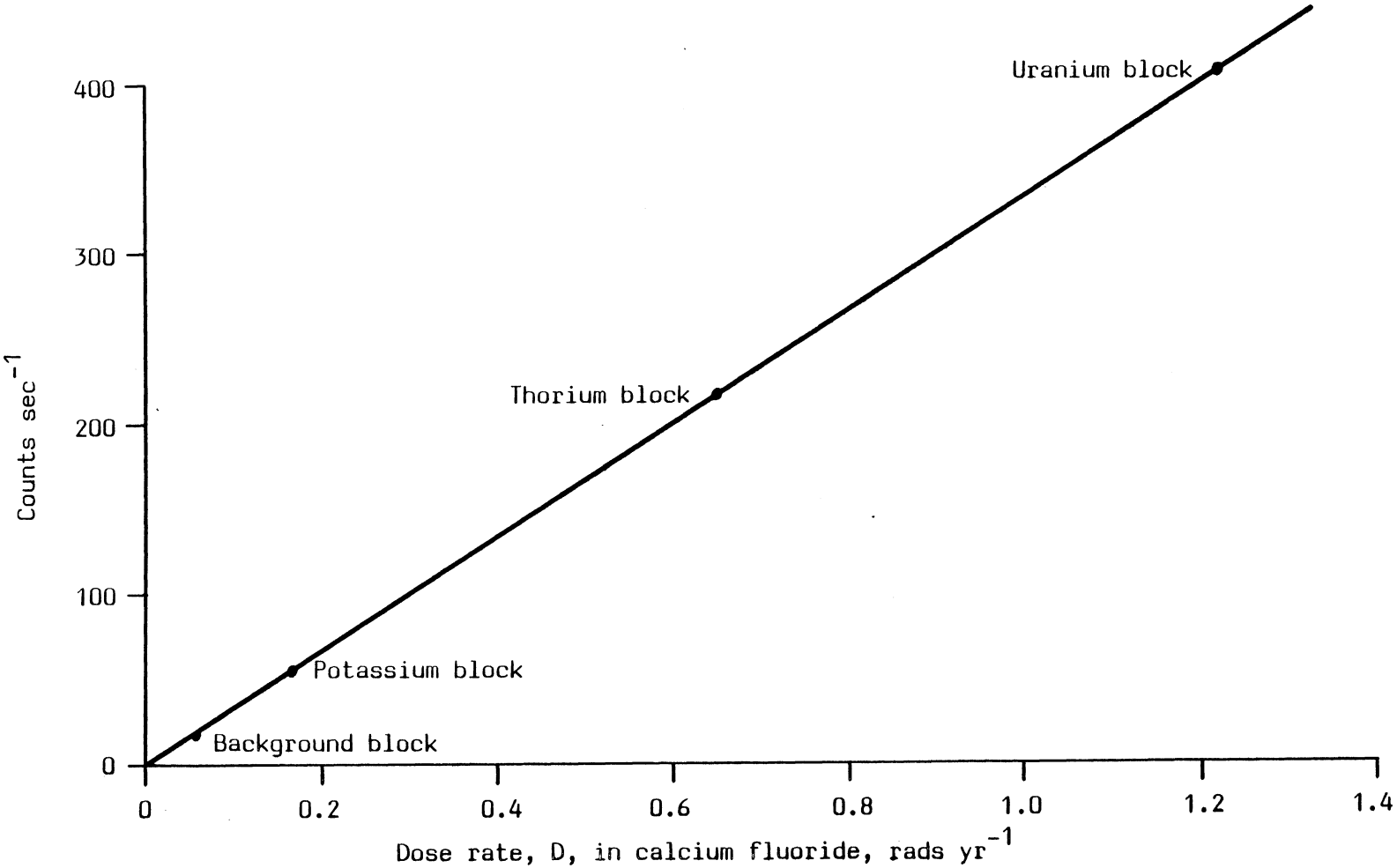

$$\text{i.e. } D = 3.00\, C_r + 0.9 \qquad \text{- - - - - - - - 8}$$

The error in the slope, obtained from a least squares fit, is $\pm$ 0.02, in the intercept $\pm$ 5.6.

As the detector will inevitably have some potassium contamination, in the crystal and/or the photomultiplier tube, the detector must always show some count rate even in the total absence of external radiation. In addition, the calibration has so far avoided the cosmic ray contribution to all four of the block dose rates. AITKEN (1968) has experimentally determined the cosmic ray dose rate to calcium fluoride at a depth of 50 cm in chalk to be 15.0 mrad yr^{-1} $\pm$ 0.15 at sea level in Britain (at latitude 51°N). This depth corresponds to the likely burial depth of the detector when in routine use. The count rate in the detector derived from the cosmic ray flux and also from the radioactive impurities in the detector head, has been established by submerging the head assembly in water, with at least 1.5 metres between the detector and the ground in all directions. This is sufficient to absorb the energy of about 97% of all 3 MeV photons emitted from the ground towards the crystal, and to scatter a further 1% to lower energies, i.e. the terrestrial spectrum should be attenuated by at least 97%, assuming that the activity of the water is negligible. The count rate observed with the threshold set at 0.43 MeV was 1.08 $\pm$ 0.05 sec^{-1}.

It is now possible to rewrite equation (8) taking these observations into account, to give

$$D = 3.00\,(C_r - 1.08) + 15.0$$

$$\text{or} \qquad D = 3.00\, C_r + 11.8 \qquad \text{- - - - - - - 9}$$

where the error in the intercept is now $\pm$ 0.2. This equation predicts a dose rate in the background block, for instance, of 66 mrad yr^{-1} with an error of $\pm$ 0.4 (The capsule-measured dose-rate is 60 mrad yr^{-1} $\pm$ 7.) However, this error term is only experimental, and it assumes that counting statistics are negligible. There is a further estimated 3% systematic error to add to this, which arises from the calibration of the beta sources used to measure the dose

rates in calcium fluoride (see chapter 2.) There will also be uncertainties arising from the stability of the threshold position, which will now be considered.

4.1.6 Threshold stability

A study of threshold stability with time and against temperature was undertaken. The linearity of the count rate against dose rate curve is sufficiently good for the slope of the best fit straight line to be a meaningful parameter at least over the energy range 0.35 MeV to 0.55 MeV. Figure 4.1.8 shows this variation of slope with threshold energy. If a maximum of $\pm$ 5% experimental error in a dose rate of 100 mrads yr^{-1} is acceptable, and statistical errors of $\pm$ 2% are expected (corresponding to a count time of about 1.5 minutes for a 100 mrad yr^{-1} dose rate) then errors arising from threshold fluctuations must be less than $\pm$ 4%. From figure 4.1.8 this corresponds to an energy fluctuation of $\pm$ 0.015 MeV about the threshold position of 0.43 MeV, i.e. $\pm$ 3.5%.

The detector and electronics were placed in a thermostatically controlled heat box, variable between room temperature and about 40°C. Using a point source of Ba-133, the integrated count rate was plotted against threshold energy (figure 4.1.9). It was found that for an energy threshold between 0.33 and 0.45 MeV the relationship between count rate C_r sec^{-1} and threshold energy E_T MeV could be described by

$$C_r = -2030\ E_T + 1000 \qquad \text{- - - - - - - 10}$$

The detector was first kept at room temperature and switched off and on repeatedly, and the variation of count rate about a nominal threshold of 0.39 MeV observed. The fluctuations in threshold were then calculated from equation (10) and found to be $\pm$ 1%. The temperature was then varied between about 25°C and 35°C, and the count rate observed after allowing the instrument time to reach thermal equilibrium. The variation of threshold energy over this 10°C interval was then calculated to be less than $\pm$ 1%.

Figure 4.1.8

Variation of slope of calibration line, i.e conversion from count rate to dose rate, plotted against threshold position

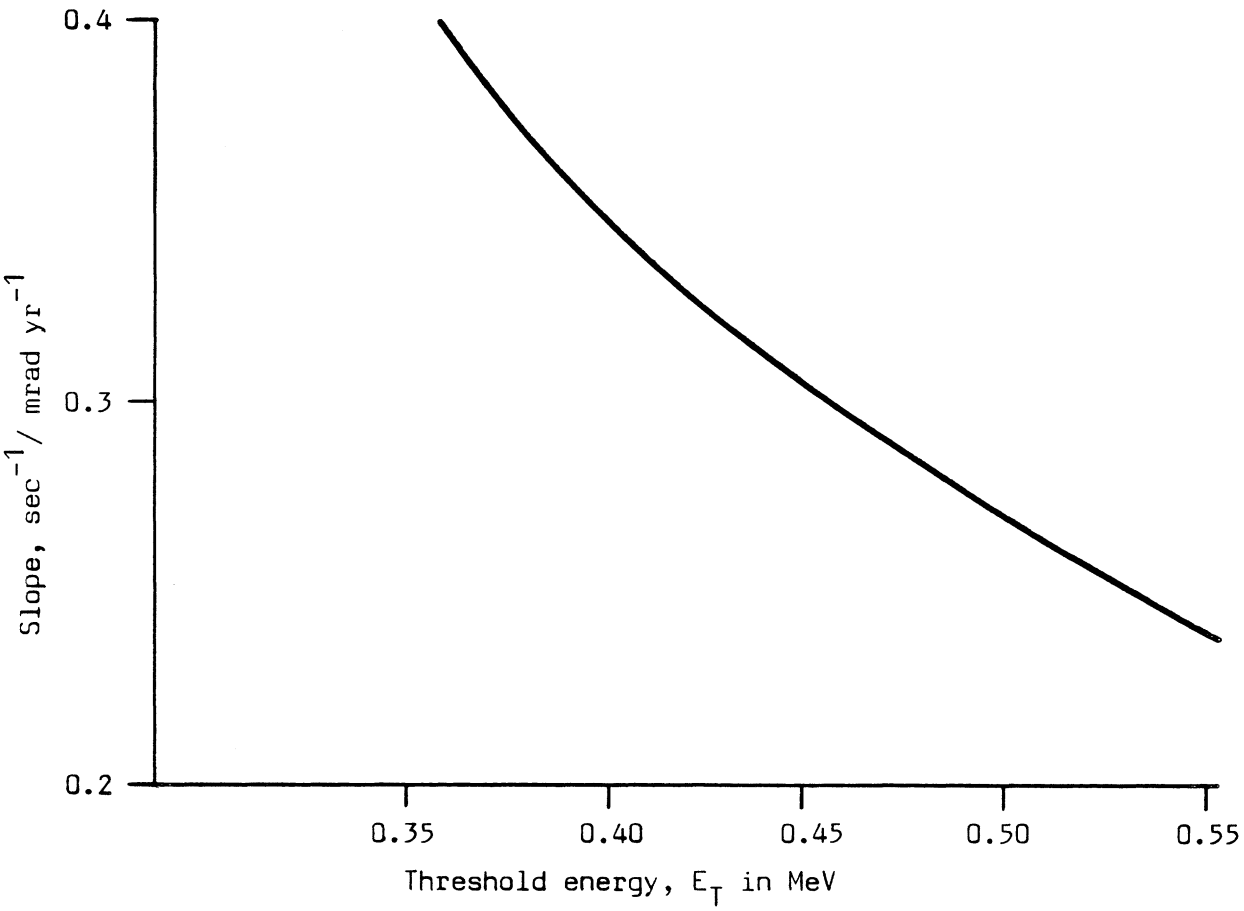

Figure 4.1.9

Integrated count rate above threshold from a Ba-133 point source

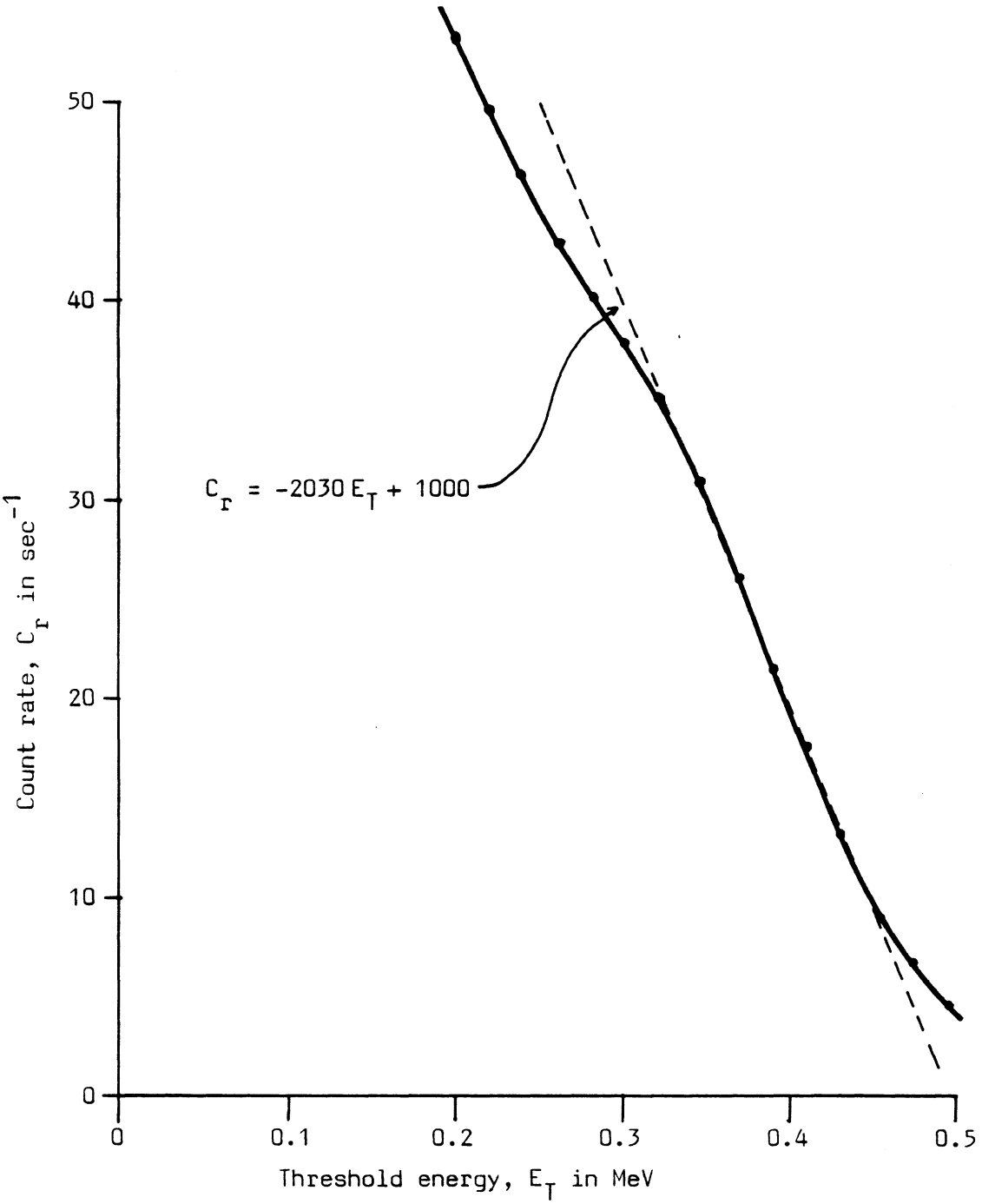

Thus the total stability of the threshold position for repeated use at different temperatures is estimated to be less than $\pm$ 1.5%. This is well within the required figure of $\pm$ 3.5%.

4.2 FIELD USE OF CALIBRATED DETECTOR

The detector described in the previous sections was used extensively on more than forty Peruvian archaeological sites in 1975. At sixteen sites it proved possible to bury calcium fluoride in copper capsules for eventual recovery. Ten of these sites were near sea level, all with soil water contents of less than 10%. The remaining six sites were all above 2500 metres in altitude, and all had soil water contents of between 80% and 10%.

The question of threshold position had not been considered as precisely as in the previous sections before this field work was undertaken. However, the threshold used, at 0.62 MeV, gives satisfactory linearity when the count rate is plotted against the dose rate in the calibration blocks. The background count rate when immersed in water was 1.1 sec^{-1} as before.

The calibration equation using the cosmic dose rate of 15 mrad yr^{-1} appropriate to a latitude of 51°N at sea level was

$$D = 4.44\ C_r + 10.0 \qquad \text{- - - - - - - - 11}$$

where D is the dose rate in mrad yr^{-1} and C_r is the count rate above threshold in sec^{-1}. The error in the slope is $\pm$ 0.13 and in the intercept $\pm$ 2.0. The effect of the variations in latitude and altitude on this equation when applied to the Peruvian measurements will be discussed in later sections.

4.2.1 The capsule results

Although it was usually possible to anneal the copper capsules only a few hours before burial, using a portable tube oven able to operate from a light socket, measurement in the Oxford laboratory was between ten and fifty days after recovery, including a flight of at least eighteen hours. During this time the capsules were stored in lead pots of 0.25 inch wall thickness. The maximum

capsule burial time was 72 days, and so it is clearly important to derive an accurate estimate of the 'carriage' dose rate, i.e. the dose rate from cosmic rays and terrestrial radiation penetrating the lead pot, and also the dose rate from the internal radioactivity of the calcium fluoride itself (termed 'self dose' rate). This 'carriage' dose rate was monitored by reserving one of every batch of capsules annealed, and storing this directly in a lead pot; the dose rates observed are shown in table 4.2.1. As all the sites visited were either below 500 metres or above 2500 metres, the storage time has been split up into the number of days at sea level, and in the highlands.

The average dose rate has a standard deviation of about 10%; this is unusually large if all the capsules were exposed to essentially the same radiation field. It is in fact unlikely that this is the case, primarily because of the increase in cosmic ray intensity with altitude. O'BRIEN (1974) suggests an increase of a factor of about 5 in total cosmic ray dose rate going from sea level to an altitude of 4 km at a latitude of 55°. Thus it is to be expected that the total dose will be a function of the time spent at various altitudes. Accordingly the 'carriage' dose rate has been recalculated making the simplified assumption of two discrete dose rates, one at sea level and one in the highlands (these include any contribution from the return journey by air, estimated at 3 mrad). These dose rates are also listed in table 4.2.1 with the associated errors, derived from a least squares fit to the data. The significant decrease in these errors gives confidence in the assumption of two 'carriage' dose rates. Using these figures the site dose rates listed in table 4.2.2, column 7, were calculated. A self dose rate in calcium fluoride of 11 mrad yr^{-1}, which had been previously assessed (AITKEN, 1968) for this type of calcium fluoride, was assumed during burial. During transport this is included in the 'carriage' dose rate.

4.2.2 Effects of variations in the cosmic ray intensity on the calibration of the sodium iodide detector.

Before comparing the capsule dose rates with those calculated from the sodium iodide detector, further thought must be given to

Table 4.2.1

Carriage dose rates as recorded by calcium fluoride in copper, in lead pots of 0.25 inch wall thickness

Capsule	Recorded dose mrad	Days at sea level	Days in highlands	Dose rate mrad yr^{-1}
III	24.2	57	40	91
VIII	22.5	47	40	94
XII	22.4	39	40	103
XVIII	20.3	31	38	107
LXVI	13.8	51	9	84
XXIII	31.8	43	66	106
LVIII	23.1	17	58	112
			average	100
			standard deviation	11%

Linear regression analysis, assuming two distinct dose rates:

	sea level	highland
dose rate, mrad yr^{-1}	73	125
standard deviation, %	6	3

the cosmic ray correction, which depends on both latitude and altitude.

i) Effect of change in latitude. The cosmic ray dose rate measured by AITKEN (1968) was at a latitude of 51°N; most of the sites visited in Peru were between 6°S and 12°S. Assuming the cosmic dose rate at a depth of 50 cm is only from the penetrating component, then the intensity at sea level in Peru is likely to be 0.91 times that in Britain (NCRP report 50, 1976) i.e. a dose rate of 13 mrad $yr^{-1} \pm 2$.

The scintillator count rate when surrounded by more than 1.5 metres of water was remeasured in Peru at an altitude of less than 250 m as 1.10 $sec^{-1} \pm 0.05$. Using this information the calibration equation (11) was recalculated as

$$D = 4.44 \ (C_r - 1.1) + 13$$

$$= 4.44 \ C_r + 8 \qquad \text{- - - - - - - 12}$$

where the errors will be similar to those of equation (11). This equation should be applicable to all measurements made at sea level in Peru.

ii) Effect of change in altitude. At an altitude of 4000 m the intensity of the penetrating component of the cosmic ray flux will be between two and three times that at sea level. LOWDER (private communication, derived from NCRP report 45, 1975, and O'BRIEN, 1974) calculates a dose rate of 30 mrad $yr^{-1} \pm \frac{8}{4}$.

The count rate submerged in water was remeasured at an altitude of 3500 m as 2.0 $sec^{-1} \pm 0.1$. Recalculating equation (11), using this highland data, gives

$$D = 4.44 \ (C_r - 2.0) + 30$$

$$= 4.44 \ C_r + 21 \qquad \text{- - - - - - - 13}$$

where the error in the slope is ± 0.13, and in the intercept $\pm \frac{8}{4}$. This equation should be applicable to all the measurements made in the highland region.

It is of interest to note that if the increase in count rate with altitude when submerged in water is solely attributed to the increase in cosmic ray intensity of a factor of 2.3, then the sea level count rate due to cosmic rays alone can be calculated as 0.4 sec^{-1}. This implies that the radioactive impurities in the detector head contribute about 0.6 sec^{-1} to the total count rate.

4.2.3 Comparison of the dose rates measured by the sodium iodide detector with those from calcium fluoride in copper capsules

The dose rates derived from the Peruvian observations with the sodium iodide detector, calculated from equations (12) and (13), as appropriate, are listed in table 4.2.2, column 8.

It is suggested that the results from sites P46 and P44 be discarded. Site P46 was very inhomogeneous, and both the detector and the capsules were placed at the boundary between a soil layer and loose slate and vegetation. $P44_1$, $P44_2$ and $P44_3$ were three capsules buried in the same borehole, after making the scintillator measurement. As $P44_2$ and $P44_3$ were nearest the position of the detector, and as they are in excellent agreement, it is considered that $P44_1$ may have detected a localised inhomogeneity.

A brief comparison of the scintillator and capsule results, columns 8 and 7, shows that although the lowland sites give moderate agreement, the sodium iodide detector consistently under responds (by 20% on average) when compared with the capsules in the highland sites.

Figure 4.2.1 shows these differences, $\underline{\Delta c}$, between the sea level and the highland capsule and scintillator results, expressed as a percentage of the capsule results, plotted against the soil water contents, $\underline{W}$. Some correlation can be seen, and if this data is approximated by the straight line shown, linear regression gives

$$\Delta c = \frac{1}{100} (0.66\ W - 4.9) \qquad \text{- - - - - - - - -} \quad 14$$

This equation may then be used to derive an average correction to the scintillator dose rates, depending on the site water content, such that

Table 4.2.2

Comparison of calcium fluoride and scintillator dose rates.

Site	Water cont. %	Total dose mrad	Burial time days	Carriage sea days	Carriage high land days	Dose rate mrad yr^{-1}	Scintillator dose rate, mrad yr^{-1} (a)	Scintillator dose rate, mrad yr^{-1} (b)
1	2	3	4	5	6	7	8	9
Sea level sites								
P02K	1.6	39.3	70	16	0	177	144	139
P04J	4.6	26.5	72	14	0	109	119	116
P06N	8.7	29.5	71	14	0	126	141	142
P10K	3.2	30.0	68	15	0	134	128	123
P12Q	8.1	24.2	67	14	0	105	112	112
P17L	1.8	22.8	62	17	0	103	120	114
P23	1.9	26.4	59	17	0	131	140	133
P34	3.1	19.7	51	17	0	105	112	108
P35I/J	0.6	26.8	54	14	0	151	142	133
P35K	0.6	21.4	54	12	0	117	127	119
P36A	1.2	15.0	53	14	0	73	91	86
Highland sites								
P37J	25	33.4	60	42	6	130	102	117
P37L	24	35.6	60	42	6	142	112	127
$P37Q_1$	30	27.1	60	42	6	90	81	96
$P37Q_2$	30	36.9	60	42	6	150	106	126
P39J	36	35.5	58	42	4	151	113	140
P40	76	25.3	58	42	4	87	66	104
$P44_1$	12	60.7	51	18	26	334	197	204
$P44_2$	12	44.5	51	18	26	218	197	204
$P44_3$	12	44.7	51	18	26	219	197	204
P45	11	32.1	56	18	21	128	97	100
$P46J_1$	-	45.9	51	17	7	276	174	-
$P46J_2$	-	34.7	51	17	7	196	175	-

Note: (a) uncorrected,
(b) corrected for water content according to equation (16).

Figure 4.2.1

Variation of Δc = (capsule - scintillator)/capsule dose rates with measured site water contents

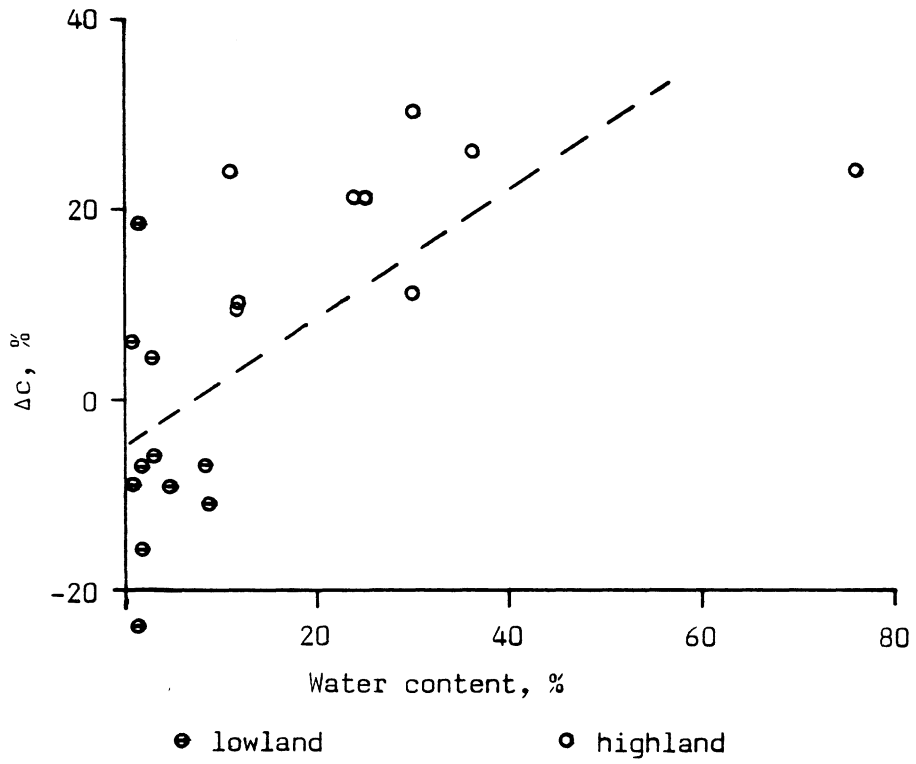

$$D'_c = D + D_{cap} . \Delta c \quad - - - - - - - - \quad 15$$

where D'_c is the corrected scintillator dose rate

D is the observed scintillator dose rate

and D_{cap} is the capsule dose rate.

Equation (15) cannot be generally applied to scintillator data, as it still involves the capsule dose rates. It can be shown, however, that the more useful equation

$$D'_c = D(1 + \frac{1}{100}(0.85\ W - 6.4)) \quad - - - - - - - - \quad 16$$

gives almost identical corrections to those derived from equation (15), and also gives a significant improvement in agreement between the scintillator and capsule measurements.

It is interesting to note that the intercept terms in equations (14) and (16) imply that no correction is necessary if the water content of the soil is approximately 8%, which is consistent with the water content of the calibration concrete blocks, measured as (8 $\pm$ 1)%, although the intercept errors are very large and this agreement must be largely coincidental.

The dose rates, corrected using equation 16, are listed in table 4.2.2, column 9, and on average, the scintillator over responds by 2% on the lowland sites, and under responds by 6% on the highland sites. In view of the large scatter, and the empirical nature of the correction, it would be unwise to associate errors of less than 15% with scintillator dose rates from wet sites, or less than 10% with dose rates from dry sites.

Finally, it is useful to consider a possible explanation for this correlation with water content. If it is accepted that the amount added for the cosmic contribution at high altitude is correct (it would need to be doubled to remove the discrepancy between the capsule and uncorrected scintillator results), then a possible explanation arises from the change in radon activity when the soil is disturbed to insert the detector head and capsules, especially on wet sites. It is well known that water plays an important part in the emanation and transport of radon (TANNER, 1964, 1978). Bearing

in mind that nearly all of the gamma dose rate and scintillator count rate from the uranium chain is derived from post radon daughters, the scintillator measures the count rate from these daughters with the soil in a recently disturbed state, partially dried out following excavation and with no overburden adjacent to the detector. The capsule, on the other hand, is buried and measures the dose rate with the surrounding soil close to its original condition, over a long period of time compared with the half life of Rn-222 (3.8 days). It will be seen in chapter 7 that soils from wet sites emanate considerably more radon than those from dry sites, and also that this escape is less before excavation (i.e. as during the capsule measurements), then when excavated and dry. This is consistent with the observed decrease in scintillator dose rates on wet sites, when compared with capsule results.

4.3 CONCLUSION

As was anticipated theoretically, it has been shown that an energy threshold position exists, at 0.43 MeV, such that the count rate from a sodium iodide crystal is proportional to the dose rate in calcium fluoride encapsulated in copper (the relationship of the latter to the dose rate in quartz and pottery was discussed in chapter 3). A scintillation detector using such a threshold has been calibrated using concrete blocks doped with uranium, thorium and potassium, and appropriate corrections for cosmic ray dose rate and count rate have been derived.

This detector has been field tested on more than 40 different Peruvian archaeological sites, and compared with TL dosimeter measurements from 16 of these. For those where the soil water content was less than about 10% of the dry weight, the agreement was good (within 6% on average) but for those with water contents much higher than this, the scintillator consistently under-responded by more than 20%. An empirically based correction formula was presented which reduced this under-response to less than 6%, and improved the agreement on the dry sites to within 2%. In view of the large corrections which of necessity were applied to both capsule and scintillator dose rates this agreement is considered

acceptable, and has permitted the interpretation of dose rates on sites where capsule measurements were not possible. However, conservative errors of 15% for wet sites and 10% for dry sites will be associated with scintillator based gamma dose rates, when they are used in chapter 5 in the calculation of Peruvian dates.

CHAPTER V

PERUVIAN SHERDS: A DATING PROGRAMME

The source calibration of chapter 2 and the enviromental gamma dose rate measurements using the capsules and scintillator described in chapters 3 and 4 have been put to practical use in dating a series of potsherds excavated from various Peruvian archaeological sites by the Oxford and Liverpool Archaeomagnetic Expedition of 1975. GUNN (1978) has made measurements of the magnitude of the earth's magnetic field at the time of firing using this series of sherds and other associated material. Thus a combination of the dates presented in this chapter with Gunn's archaeomagetic data provides a description of variation in the magnitude of the earth's magnetic field over the past two thousand years.

5.1 DESCRIPTION OF SAMPLES

Although the expedition visited more than 40 different sites covering an age range from about 3000 B.C. to the present day, and collected several thousand potsherds and other burnt material, only a limited range of about 2000 years has been attempted so far, derived from about 12 sites. Most of the sherds dated came from the valleys which cut across the coastal desert strip of Peru, in particular the Viru valley just south of Trujillo, although material from the highland areas around Ayacucho and Cusco have also given useful results. In general the coastal sites were dry, with soil water contents of less than 10% (see chapter 4); the highland sites were more variable.

After the excavation of the sherds, the enviromental gamma measurements described in chapter 4 were made, and associated soil samples taken. These were then sealed inside two polythene bags to allow measurement of the water content of the soils in the laboratory. The excavated sherds were washed and coded. The pottery varied in thickness, with an average of about 7 mm, although those selected for TL dating tended to be thicker than this. Most of the specimens used were hard and red, ranging in texture from very coarse to very fine grained, and were all well preserved, showing no obvious signs of secondary heating, such as carbon deposits. A copy of the site notes prepared from the expedition record book by N. Gunn, taken

from GUNN (1978), are reproduced in Appendix D. These describe in detail the origins of the samples used in this chapter and give references to material already published concerning the sites, and the names of archaeologists primarily concerned with their excavation.

5.2 DATING TECHNIQUE

Of the possible approaches outlined in chapter 1 only the fine grain technique (ZIMMERMAN, 1971) was employed. Attempts were made to use the quartz inclusion technique (FLEMING, 1970) but all five of the sherds tested gave anomalously high light levels after etching in hydrofluoric acid, each with an unacceptable beta plateau. (The predose technique was not considered sufficiently well understood to be employed routinely.) On the other hand the TL characteristics of the fine grains extracted from the Peruvian sherds were usually acceptable; of the 31 sherds attempted, only two were rejected because of their poor disc to disc reproducibility (> 3%). However, this is not regarded as a characteristic of the sherds, but rather a failure in deposition technique. All the TL measurements were made on discs from a single deposition, as recommended by HUXTABLE and MURRAY (1980). Errors have been calculated according to the recommendations of AITKEN and ALLDRED (1972) and AITKEN (1976).

5.3 MODIFICATIONS TO THE FINE GRAIN TECHNIQUE

Only one significant change in the dating procedure was adopted. ZIMMERMAN (1971) and later workers (e.g. HUXTABLE,1978) recommend the examination of the ratio between the natural glow curve and the natural and additive beta dose glow curve, as an indicator of thermal fading and spurious TL. It is anticipated that there is a region in the glow curve, usually between about 350°C and 450°C, where this ratio will be constant, indicating that over this temperature range the nature of the traps and luminescence centres giving rise to the TL from the additive beta dose (the 'artificial' TL) is very similar to that which gave rise to the natural TL. However, no such monitoring is normally undertaken of the response to alpha irradiation.

For the dates reported here, a more generalised plateau criterion was employed. The glow curve data was taken using a multiscaler (see

section 5.4) and the light intensity integrated over 25° intervals from 275°C to 500°C, after subtraction of the black body curve. The age calculations were then performed in their entirety at each of these temperature intervals. The resulting variation of age against temperature was then examined and temperature region found across which the age was considered constant. In practice this was usually found to be true in the range 350°C to 475°C; above this temperature the errors in subtracting the thermal radiation background become too large for the signal to be useful. If the age plateau, defined as the region wherein the calculated age varies by no more than $\pm$ 5%, was less than 75° wide the sherd was rejected, although the final decision as to what constitutes an acceptable plateau must always remain a matter for subjective judgement.

Only one sherd was rejected because there was no acceptable plateau; it should be noted that it did not show an acceptable beta plateau either.

It is also appropriate here to describe the procedure employed to detect anomalous fading (WINTLE,1973; WINTLE,1978). Two sample discs from which the natural TL had been erased in the course of measurement were used for each sherd. One was irradiated with a known beta dose and both were then stored in the dark. It has been shown that most of the fading, if any, occurs within the first few days or weeks; in this study storage was for at least two weeks, usually much longer (up to 18 months). After this period, the other disc was irradiated and both glowed out. The 'faded' and 'prompt' glow curves were then normalised before comparison using the respective natural light levels, as disc to disc reproducibility cannot be relied upon when comparing individual discs. It must be emphasized that this measurement was not an attempt to quantify the degree of anomalous fading, but was intended as a means of detecting its presence. If the measurement error associated with each glow curve was about 2%, then the error in the calculated ratio of the 'faded' to 'prompt' glow after normalization was about 4%. If the discrepancy between the two normalized glows was greater than 8% in the plateau region, i.e. twice the estimated standard deviation, then the sherd was discarded. Of the 23 sherds tested, none failed this test. (see section 5.5).

5.4 DESCRIPTION OF TL MEASURING EQUIPMENT

The glow curves were taken using a standard TL oven with a one inch wide nichrome heater strip capable of being heating up to 600°C at 10° per second, with the heating rate servo controlled by a ramp generator. (AITKEN et al, 1968). The oven chamber can be evacuated and oxygen free nitrogen gas flushed through. Pulses from the photo-multiplier tube (EMI 9635Q) are fed to a pulse height discriminator through a low noise preamplifier; the output of the former is fed to the Y axis of a 200 channel multiscaler. The X axis (equivalent to 0° to 500°C) is driven by a thermocouple spot welded to the centre of the underneath of the heater plate. The multiscaler has four separate stores; this permits the subtraction of the background thermal radiation from the glow curve before the output to an X-Y recorder and typewriter. Routinely the integral from 275°C to 500°C in 25° intervals is printed out in numerical form.

There is also an automatic irradiation facility which permits up to 15 discs to be beta irradiated for between 6 minutes and nine hours. Alpha irradiations were performed both using a Cm-242 source in air (AITKEN and BOWMAN, 1975), and Am-241 source under vacuum (SINGHVI and AITKEN, 1978).

5.5 TL DATA

In general the TL characteristics of the 26 sherds completed proved to be similar, and the glow curves of sherd P23A04, shown in figure 5.1 may be taken as typical. Figure 5.2(a) and figure 5.2(b) show the alpha and beta growth characteristics for the same sherd, for the temperature interval 400° to 425°C. A summary of the TL data collected for each sherd appears in table 5.1 for the temperature interval 400° to 425°C. The symbols have the same meaning as in chapter 1. This interval was selected because it falls within the age plateau of every sherd dated. A typical age plateau (sherd P04J01) is shown in figure 5.3.

Table 5.1 also gives the alpha count rate of the sherds. The sealed alpha count rate is used because in every case the build up in count rate on sealing the counting cell was less than 10%. According

Figure 5.1 Typical glow curve shapes from sherd P23A04

Note: the glow curves were measured about two hours after irradiation, and are shown with the thermal background subtracted. The alpha source strength, S, was 0.102 μm^{-2} min^{-1}.

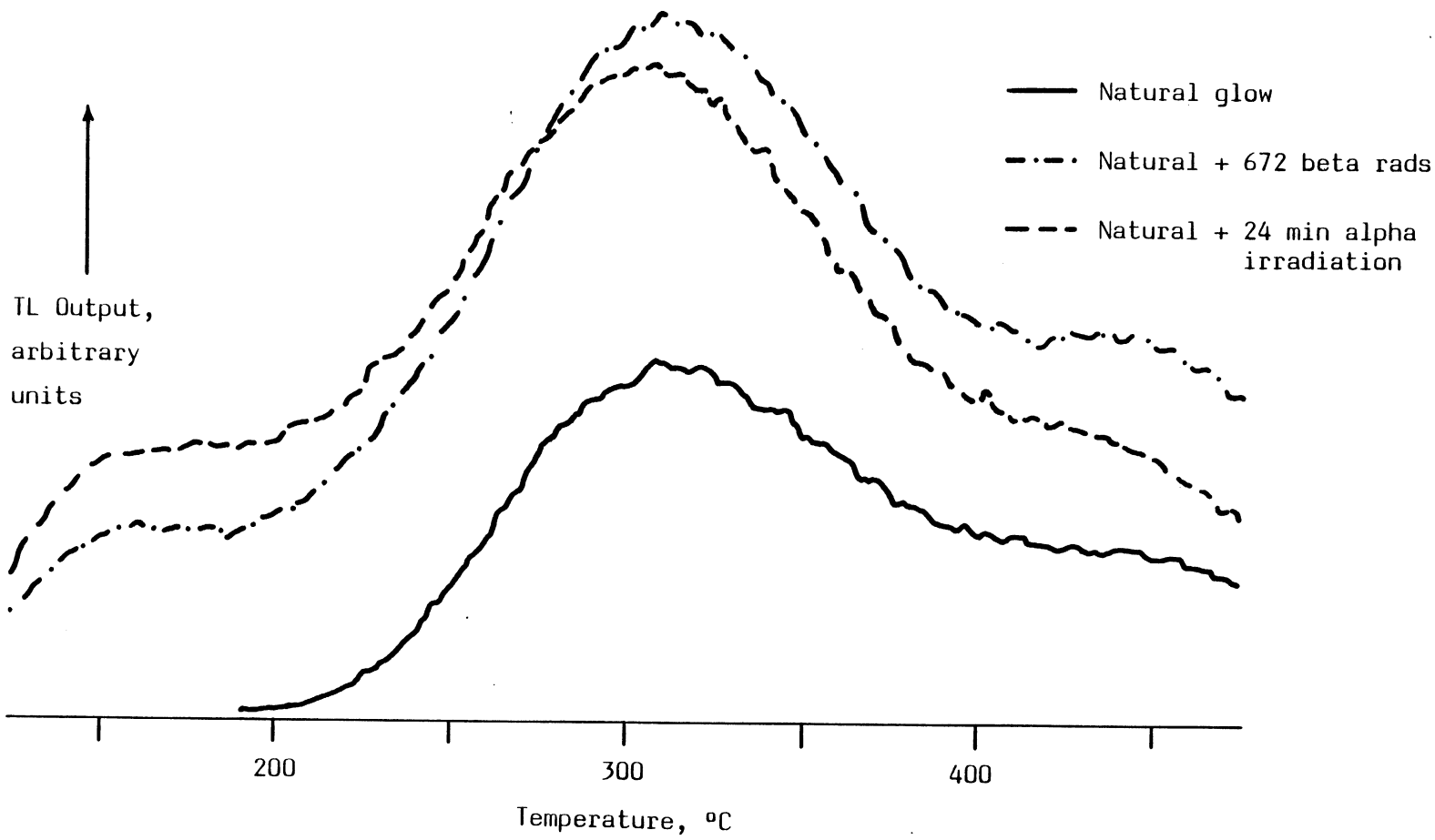

Figure 5.2

Alpha (a) and beta (b) growth characteristics for sherd P23A04 in the temperature interval 400°C to 425°C

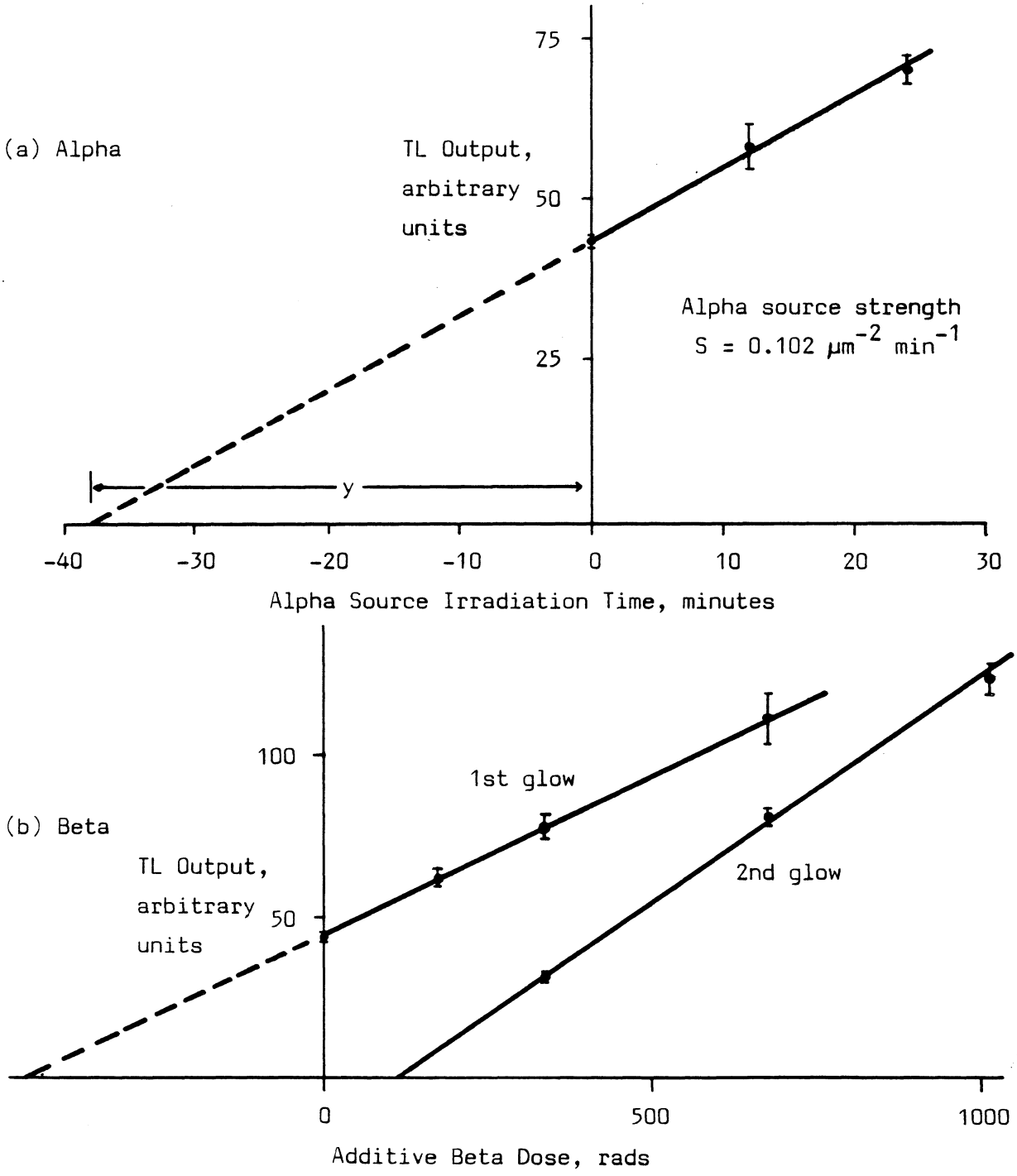

Figure 5.3 Calculated age plotted against glow curve temperature, showing an age plateau, for sherd P04J01

Note: error bars shown are total errors at each temperature.

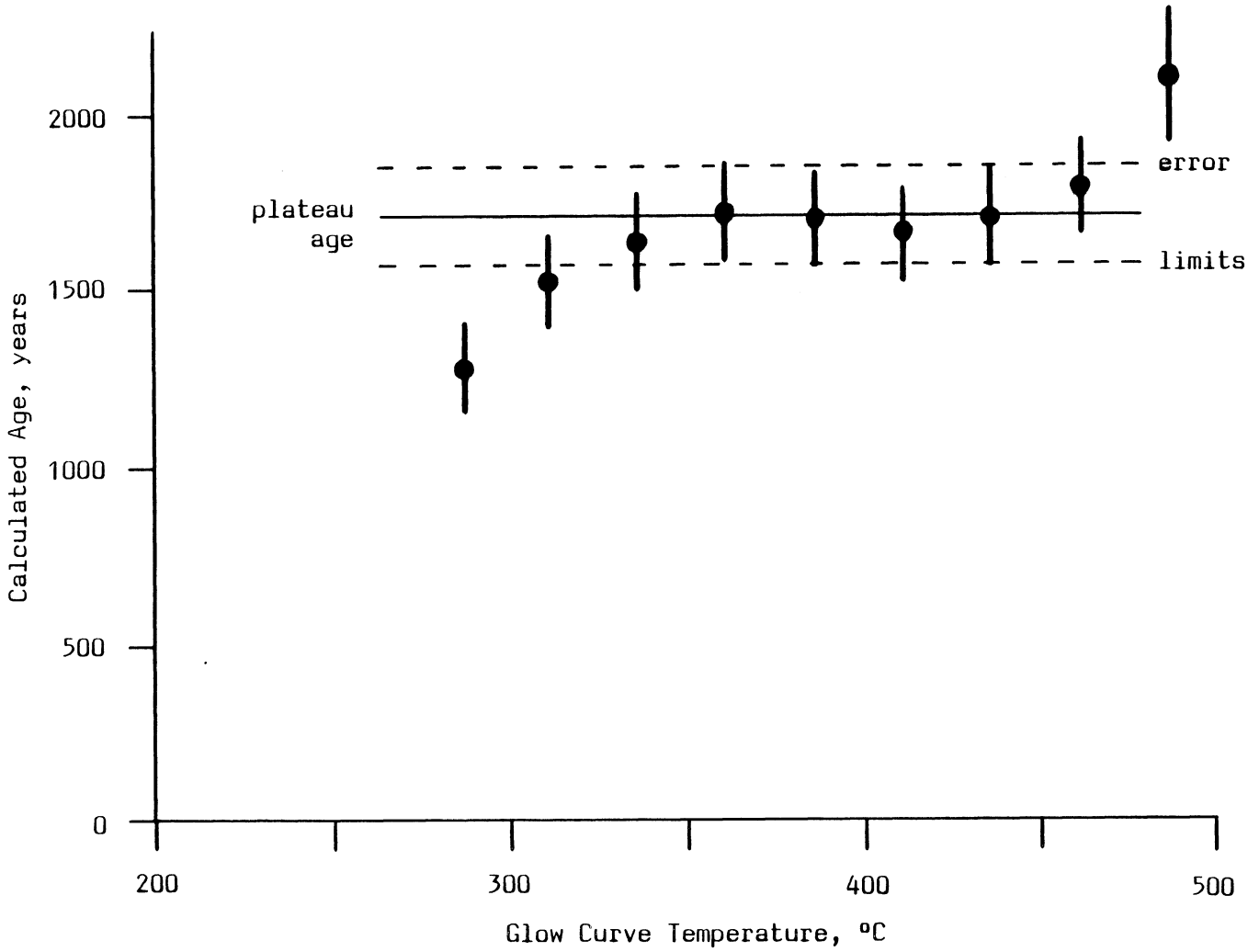

Table 5.1

TL data for 26 sherds from the glow curve temperature interval 400° to 425°C

Sherd	δ*	Saturated water content %	Q rad	I rad	a	α $ksec^{-1}$	D_β $rad\ yr^{-1}$	$D_{\gamma,c}$ $rad\ yr^{-1}$
P04J01	2 - 6	11	779	23	0.076	14.7	0.275	0.129
P04J03	2 - 6	12	810	161	0.111	13.4	0.291	0.129
P04K02	2 - 6	11	960	131	0.126	13.5	0.317	0.138
P07N73	3 - 9	13	583	191	0.125	10.8	0.225	0.130
P07N74	3 - 9	14	622	121	0.112	10.8	0.263	0.130
P12J04	3 - 10	11	583	125	0.160	10.0	0.249	0.135
P12K02	3 - 10	10	508	37	0.118	10.0	0.255	0.138
P12K10	4 - 11	12	536	112	0.133	9.4	0.266	0.138
P12M02	4 - 11	12	548	118	0.128	11.8	0.274	0.145
P12N02	4 - 12	14	495	261	0.126	10.3	0.250	0.125
P12P01	3 - 10	10	426	173	0.141	10.1	0.234	0.120
P12Q02	3 - 10	11	564	227	0.129	10.0	0.241	0.124
P13I01	1 - 4	13	471	146	0.097	11.7	0.287	0.108
P14A05	0 - 4	12	327	108	0.101	9.9	0.275	0.165
P17K04	1 - 4	14	593	89	0.114	15.9	0.280	0.131
P17L01	0 - 3	9	587	88	0.128	14.7	0.255	0.122
P18L02	0 - 4	12	564	94	0.102	11.9	0.293	0.126
P18M05	1 - 4	14	548	180	0.091	14.8	0.248	0.126
P23A04	1 - 3	14	416	97	0.081	15.4	0.245	0.155
P36A11	1 - 4	15	231	97	0.125	13.0	0.265	0.086
P41J07	3 - 10	16	502	99	0.110	15.4	0.460	0.198
P41J11	3 - 10	17	513	123	0.120	16.1	0.461	0.198
P42J02	2 - 7	15	824	89	0.078	34.2	0.592	0.198
P42J03	2 - 7	16	589	102	0.158	16.6	0.445	0.198
P44J09	2 - 6	12	1111	99	0.223	8.3	0.361	0.241
P44J13	2 - 7	13	863	154	0.114	9.3	0.415	0.241
	2 - 7	13	903	87	0.122			

Note: δ is the estimated range of mean sherd water contents during burial.

to AITKEN (1978b) this indicates little or no radon escape, and the sealed alpha count rate is recommended. However, work presented in chapters 7 and 8 questions the reliability of alpha counting, and the effect of this uncertainty is discussed in section 5.5 The beta dose rates given were measured using beta TLD (BAILIFF, 1976; BAILIFF and AITKEN, 1980). The gamma dose rates are derived from the dose rates reported in chapter 4, or from scintillator count rates alone, corrected as described in that chapter to give the gamma dose rate. The average historical water content of these sherds is uncertain, and is necessarily an informed guess based on the present day soil water content expressed as a fraction of its saturated uptake. After consultation with the archaeologist advising the project, this fractional uptake was adjusted to take account of the likely changes in the environment due to changes in settlement patterns and river courses. Large uncertainties were associated with the modified figures, and the final anticipated range of sherd water contents shown in table 5.1 was obtained by multiplying this expected fractional water uptake with the observed saturation water uptake, also listed in table 5.1. The resulting figures were then used to modify the alpha and beta dose rates as described in ZIMMERMAN (1978). The gamma dose rate should only be modified by the difference in water content between the present day and the assumed historical average, because both the capsule and corrected scintillator dose rates are for a soil matrix containing the present day water content. In practice the effect on the age is small, about 1%, and this correction was neglected.

Fading tests were carried out on all but three sherds, P13101, P44J09, and P44J13. None gave a ratio of 'faded' to 'prompt' of less than 0.94; this was not considered significant according to the criterion given in section 5.3. It is felt unlikely that the three untested sherds would give a different result.

From the data of table 5.1 the age of each sherd can be calculated for the temperature interval 400°C to 425°C. The sherd ages given in table 5.2 are the average of the calculated ages across all the temperature intervals accepted as part of the age plateau for each sherd as described earlier. It is interesting to note that the one sherd (P36A11) recovered from a site considered to be reliably historically dated to 1300 A.D. $\pm$ 50, is in good agreement with the TL date of 1375 A.D. $\pm$ 40.

Table 5.2

TL ages for 26 sherds averaged across the age plateau.

Sherd	date of last firing A.D.	random error years	total error years	archaeological date estimate
P04J01	390	85	130	300 B.C.
P04K03	295	115	155	to
P04K02	225	150	195	100 A.D.
P07N73	485	65	110	300 A.D. to
P07N74	550	100	130	700 A.D.
P12J04	720	95	130	700 A.D.
P12K02	870	115	145	|
P12K10	765	185	206	|
P12M02	860	70	110	to
P12N02	440	140	185	|
P12P01	745	55	110	|
P12Q02	335	130	180	300 A.D.
P13I01	800	70	85	300 B.C.
P14A05	1210	95	105	700 A.D. to 900 A.D.
P17K04	850	70	85	400 A.D. to
P17L01	895	55	70	600 A.D.
P18L02	695	115	135	?
P18M05	610	120	135	300 A.D.
P23A04	1065	110	115	1000 A.D.
P36A11	1375	30	40	1300 A.D. $\pm$ 50
P41J07	1220	35	105	800 A.D.
P41J11	1195	95	115	
P42J02	1100	40	80	1200 A.D.
P42J03	1270	75	95	
P44J09	430	80	115	
P44J13/1	575	95	125	600 B.C.
/2	640	90	115	

5.6 ERRORS

The error terms shown in table 5.2 can be considered in two stages. The first component, the random error, includes experimental uncertainties in $\underline{Q}$, $\underline{I}$, $\underline{a}$, $\underline{D'_\alpha}$, $\underline{D_\beta}$ and $\underline{D_{\gamma,c}}$. (These terms are defined in chapter 1.) The second error term shown is a total error which combines the random error with the terms associated with the source calibrations and the site and sherd water contents. In addition a random error term has been included to take account of the variations in calculated age across the plateau; this is usually small compared with the other contributions to the random error. The error terms are shown at approximately one standard deviation.

The possibility of undetected gross errors must be acknowledged. There are several potential sources, in particular the assumptions made about changes in the site water content or burial context of the sherd through archaeological time may be in error. Whereas there have been no great climatic changes over the last two thousand years, irrigation patterns have altered considerably, and it is likely that the changing settlement patterns, technology, and political structures, in particular in the coastal valleys of Peru, have caused fluctuations in the area of land under cultivation and in the water table levels. It is expected that in the worst possible case (i.e. sherds lying below the water table for a substantial period of their burial life) an age would be underestimated by about 10%. It is considered unlikely that the sites visited have ever been significantly drier for a prolonged period than they are today. Undetected errors arising from changes in burial context (e.g. sherds remaining on or close to the surface for centuries before complete burial) are unlikely to be greater than 10%.

Finally the risk of still undetected anomalous fading must be recognised (HUXTABLE, 1978) and the validity of the assumptions of equilibrium in the uranium and thorium decay chain (MEAKINS et al, 1979) and of the stability of the site and sherd radioactivity questioned. The second half of this thesis is devoted to examining the latter assumptions and some of the Peruvian dates are reconsidered in the light of this work. In particular the use of alpha counting is criticized in chapter 8. However, detailed analysis of sherds from P12 and P41 (section 7.4) shows that on average the dates presented here are

not likely to be systematically in error by more than about 8% as a result of the use of alpha counting to determine the alpha dose rate. This is well within the typical total error quoted in table 5.2.

5.7 DISCUSSION

The dates obtained must now be discussed in the context of drawing up a magnetic archaeomagnitude curve for Peru. At the beginning of the investigation, it was intended to make use of the archaeological stratigraphy to provide relative dates, (almost all material was recovered under the guidance of an archaeologist associated with the individual sites) and TL dating was to be restricted to a few key sherds collected and bagged with the soil samples, to relate these floating chronologies to an absolute time scale. It was decided to check the validity of this approach by examining the correlation between TL dates and stratigraphy for one site, P12, in some detail.

Material recovered from this site came from nine distinct levels (J-S) in a single section. The archaeological age estimates for the top and bottom of this section were A.D. 700 and A.D. 200, respectively. Figure 5.4 shows TL dates from table 5.2 plotted against stratigraphy, assuming the levels were laid down after equal intervals of time. It can be seen that although the overall range of TL dates is in good agreement with the archaeological estimates the correlation with stratigraphy is poor. Note that the error bars shown here are only the experimental errors on each sherd. The error component arising from uncertainties in the average sherd water content and from source calibration should not affect the relative ages of sherds within a site, but only the absolute ages. It seems most unlikely that the poor correlation is due to dating errors, and it must be concluded that the sherds recovered were not buried in a simple age sequence. This conclusion is borne out by Gunn's magnetic measurements. It was found that sherds from the same level in site P12 had very different archaeomagnitude values, but that the correlation between ages and magnetic results was improved if TL dates were used rather than stratigraphy. (GUNN and MURRAY, 1980, page 358).

Association and interpolation on a stratigraphic basis must now be presumed to be invalid, and so the uncertainties associated with any sherds dated by association must be comparable with the range of

Figure 5.4 Archaeological stratigraphy plotted against TL dates for site P12

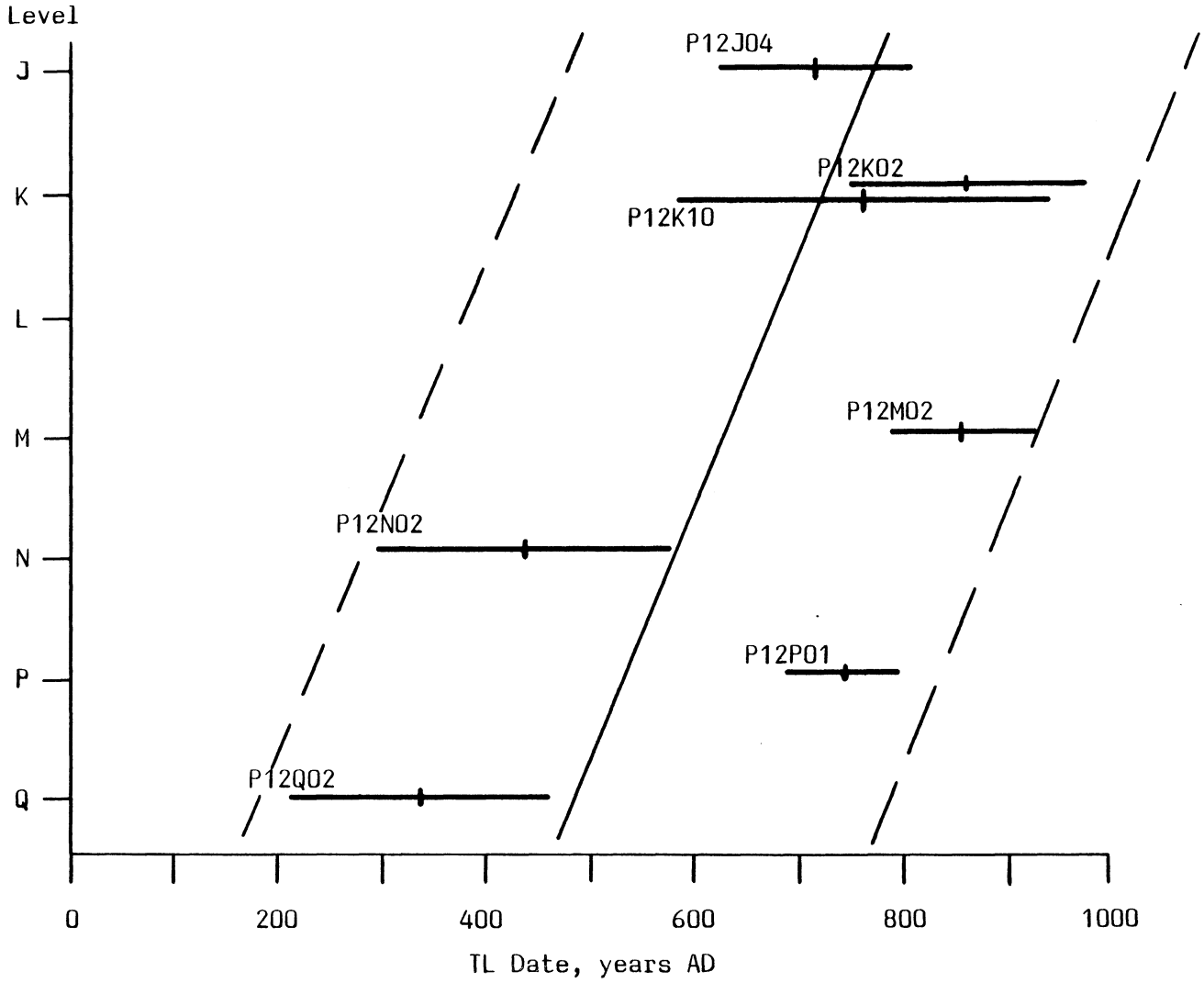

dates from the site as a whole. The procedure adopted in this case is illustrated in figure 5.4 by a solid oblique line connecting the assumed mean dates for the levels and two dotted lines marking the boundary of expected errors. Sherds for which no TL dates were attempted, but which provided archaeomagnitude information, were then dated by reference to these lines. It was felt that it was unsafe to assume any stratigraphic relationship for other sites and so all undated sherds were assigned arbitrary errors of $\pm$ 300 years. This obviously limits their usefulness in resolving any time variation of the earth's magnetic field, and emphasizes the value of TL dates in this project.

A copy of the curve of geomagnetic field magnitude versus time for Peru, taken from GUNN and MURRAY (1980) is given in figure 5.5. Discussion of the weighting assigned to the individual points when drawing the postulated smooth curve is given there. Note that the ages shown in figure 5.5 do not exactly correspond to those given in table 5.4. This is primarily because of the dose rate revisions of chapter 2, which were completed after the publication of figure 5.5.

5.8 CONCLUSION

The fine grain technique has been successfully employed to date 26 Peruvian sherds gathered from a range of sites. The only significant change to the established approach was the use of an age plateau rather than a beta plateau, which was made possible by the use of a multiscaler to intergrate the glow curve information and present it in numerical form. Nevertheless, in these samples the use of a beta plateau would not have led to different conclusions being reached.

These dates have been used to provide information about variations in the magnitude of the earth's magnetic field over the last two thousand years, for a region where existing data are sparse and of unreliable dates. Thus this new information may be regarded as a significant contribution to our knowledge of the earth's history.

From the point of view of this thesis, however, they serve primarily to illustrate the value of the work presented in chapters 2, 3 and 4. Without the source recalibration of chapter 2, the dates would be older by about 12% on average, which is of the order of total

Figure 5.5 Geomagnetic field magnitude versus time for Peru, with postulated smooth variation curve

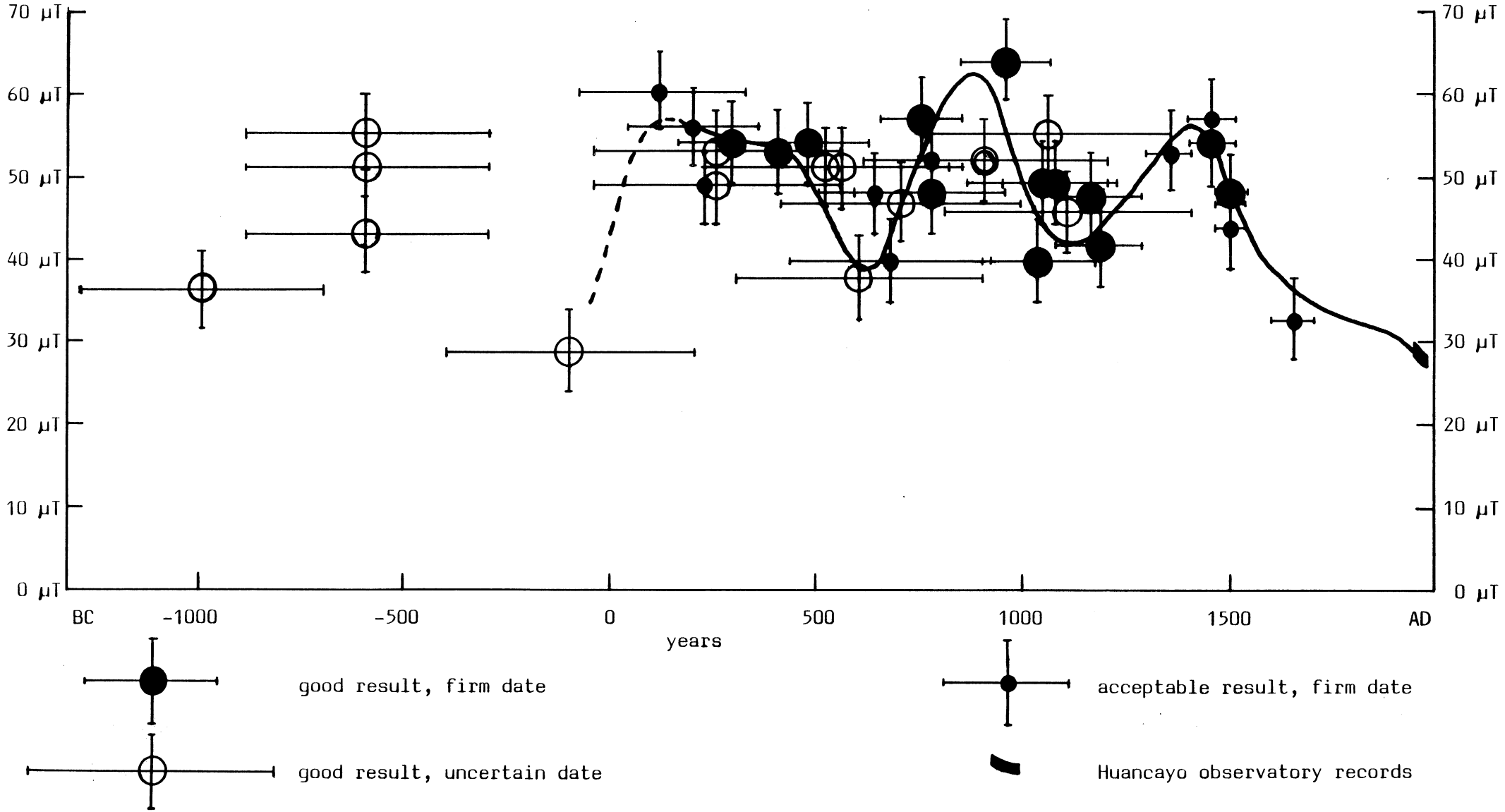

errors associated with the dates. Of the 26 sherds dated, 17 came from sites where it had proved possible to recover a buried capsule for gamma dose rate information. Without the scintillator information described in chapter 4, it would not have been possible to date the remaining 9 sherds with any accuracy at the time this dating programme was undertaken. This would have severely limited the age range that the project is able to cover, especially so in the earlier periods not yet dated, where most of the material comes from the relatively inaccessible mountain regions.

CHAPTER VI

DESIGN AND CALIBRATION OF A HIGH RESOLUTION, HIGH SENSITIVITY GAMMA SPECTROMETER FOR THE ANALYSIS OF NATURAL RADIOISOTOPES

6.1 INTRODUCTION

In this chapter the mechanisms giving rise to disequilibria in the uranium and thorium decay chains are described briefly and the long term stability of such disequilibria discussed. High resolution gamma spectrometry is proposed as a convenient means of obtaining more information on the state of equilibrium, and the design and calibration of a low level, high efficiency spectrometer is described.

Finally, various tests designed to confirm the calibration, and to investigate the stability and reproducibility of the spectrometer are also discussed.

6.1.1 Sources of Disequilibrium

The annual dose rate term in the general age equation given in Chapter 1 was broadly described in terms of approximately equal contributions from the uranium and thorium decay chains each of about 30% of the total, a further 40% from potassium (K-40) and a few percent from rubidium (Rb-87) and cosmic rays. Unfortunately this simple picture is complicated by the considerable risk of gross disequilibria in the uranium chains, with an additional less serious risk for the thorium series.

The concentrations in sediments of the various isotopes from the uranium and thorium series are affected by geographical location, grain size, whether they are contained in grains of the original mineral matrix, or freed from this matrix by weathering and subsequently retained in the soil by one or more of the following mechanisms (MITCHELL, 1964).

a) incorporated into the lattices of clay minerals forming in the soil,
b) adsorbed onto the surfaces of clay minerals,
c) associated with iron and aluminium oxides precipitated in the soil,
d) adsorbed or complexed by organic material in the upper layers of the soil.

Obviously only the first of these mechanisms can be considered

permanent on even an archaeological time scale; this point will be discussed further in section 6.1.4.

To study natural series disequilibria set up by the above mechanisms, it is usually sufficient to study the concentration of certain key isotopes. Table 6.1.1 shows the U-238 and U-235 series and the Th-232 series, in groups of isotopes based on the subdivision suggested by ROSHOLT (1959). The longest lived isotopes in each group and associated half lives are also shown. Although most disequilibria arise as a result of geochemical action, and hence only affect those isotopes with relatively long half lives, the short lived radon isotopes are sufficiently mobile that significant disequilibria are often set up.

6.1.2 Uranium series

i) Groups 1 and 2; U-238, U-235, U-234

It is generally assumed in geological studies of disequilibrium that the uranium isotope ratios are constant in nature. Except for the more unusual geological reactions, such as the marked deficiency of U-235 in the uranium ore of Oklo, Gabon (NAUDET, 1974) the U-235/U-238 atomic ratio of 0.00726 is in practice constant. However, the U-234 generated from decay of U-238 bound in a mineral matrix will be more readily mobilised by geochemical action than any U-238 or U-234 which was incorporated during lattice formation. This is illustrated by the activity ratios of U-234/U-238 in calcite deposits, typically around 1.2:1 (HENNIG, 1980), but on occasions as high as 10:1 (VOGEL, private communication), where both isotopes have been deposited in the matrix by evaporation of ground water, and also by U-234/U-238 activity ratios of less than unity in river sediments (e.g. SCOTT, 1968).

ii) Group 3; Th-230 and Pa-231

Both Th-230 and Pa-231 form insoluble hydroxides so that they are removed from ground water almost as soon as they are produced. This can result in an excess of Th-230 in river sediments which is often found to increase with decreasing grain size (SCOTT, 1968).

iii) Group 4; Ra-226

Any Ra-226 which escapes into ground water by recoil or break down of the host matrix is rarely in sufficient concentrations (because of

Table 6.1.1

Subdivisions in the natural decay series based on the likelihood of breaks in secular equilibrium

Series	Group	Long lived isotope	Half Life years
U-238	1	U-238	4.49×10^9
	2	U-234	2.48×10^5
	3	Th-230	7.52×10^4
	4	Ra-226	1600
	5	Rn-222	3.82 days
	6	Pb-210	22.3
U-235	1	U-235	7.04×10^8
	3	Pa-231	3.25×10^4
	5	Rn-219	3.96 sec
Th-232	7	Th-232	1.40×10^{10}
	8	Rn-220	55.3 sec

its relatively short half life of 1600 years) to be precipitated directly. It is usually immobilised by essentially physical processes such as electrostatic attraction or physical adsorbtion and containment. (NCRP 45, 1975). Thus Ra-226 can be considered potentially much more mobile than its precursor Th-230.

iv) Group 5; Rn-222 and Rn-219

Information on radon escape from materials of environmental interest has been comprehensively summarised by TANNER (1964, 1978). Briefly, the predominant escape mechanism seems to be as follows. A radon nucleus recoils out of the surface layer of a grain (about 50 nm thick) after it is produced by parent decay. If the pores between the grains are air filled, the nucleus will usually embed itself in other material around the cavity and be unable to escape. If, however, the pores are water filled, the nucleus will be stopped in the fluid and then can diffuse through the ground water and escape from the region where it was produced. DESAI (1975) confirmed that the presence of water did indeed increase the escape of Rn-222 from pottery samples in the laboratory.

Although the escape of Rn-220 will presumably be by this mechanism, it cannot be included in group 5, because its progenitors will not necessarily be included in the same mineral lattice as the U-238 and U-235 chains, and thus the level of escape may not be simply related to that of Rn-222, even after allowance is made for the different half lives. It is presumed that, with a half life of about 4 seconds no significant migration of Rn-219 occurs.

v) Group 6; Pb-210

As lead isotopes are readily ionised and adsorbed on the surface of clay grains, it is thought unlikely that any disequilibrium of Pb-210 compared with the short lived radon daughters that precede it will occur.

This is very useful as the Pb-210 activity should thus reflect the degree of Rn-222 escape for some time after a sherd or soil has been removed from the original context.

6.1.3 Thorium series

Groups 7 and 8; Th-232 and Rn-220

The most important potential source of disequilibrium in the thorium

chain in natural samples is the escape of Rn-220. Despite its short half life of only 55.3 seconds, DESAI (1975) observed levels of escape as high as 95% in five water saturated pottery samples, although she estimates her uncertainties to be about 30%. However, TANNER (1964) suggests typical diffusion lengths for Rn-220 in wet or dry soil of 2 cms. This is of the dimensions of a buried sherd; unless the burial context is of markedly different thorium activity to the sherd, it seems unlikely that significant overall disequilibrium would arise from this source, although it cannot be dismissed.

Some additional disequilibrium could be set up in very porous materials between Th-232 and Ra-228 (half life 5.8 years) but this is thought to be very unusual (NCRP 45, 1975).

6.1.4 Stability of disequilibria patterns

As it is only possible to make measurements on samples at the end of their burial period, it is important to have some confidence that the measurements made reflect the situation throughout this period. Unfortunately it is not always clear that this can be done. Although the dissolution of radioisotopes from the host matrix may take a considerable period of time by archaeological standards, deposition from ground water can be comparatively fast and localised. If the movement of ground water is disturbed, for instance by new irrigation patterns, an abrupt change in the radioisotope concentrations is possible.

Changing agricultural patterns may lead to changes in isotope deposition/removal in other ways. Plant growth continuously depletes the soil of many trace elements, and in doing so locally changes the relative concentration of metals in solution. Clearly such changes will have considerable effect on the rate at which ionic species are taken up or lost by clays. The decomposition of organic matter tends to immobilise uranium, but free radium and other very low concentration isotopes, and humic acids tend to increase the rate of decomposition of rock material (NCRP 45, 1975).

HEDGES and McLELLAN (1976) showed that two Roman sherds exhibited substantial ion exchange capacity, which in one case seemed to approach that of raw clay. They concluded that a sherd buried in ground waters of twice the uranium concentration (relative to other ions) of its

parent clay could easily experience a 10% increase in uranium concentration. A similar conclusion was drawn for thorium isotopes, and also for potassium. As archaeological pottery was often not manufactured from materials local to the burial context, this must be regarded as a serious risk.

KINGERY (1974) has shown that substantial rehydration of ceramics can take place during burial, especially in poorly fired sherds. This will tend to make any ion exchange behaviour vary with time.

As water is known to have considerable effects on the emanation of radon isotopes, it is to be expected that changes in ground water levels may result in large changes in the movement of these isotopes, into and out of buried sherds. In principle, the change on excavation can be allowed for by measuring the Pb-210 activity, but there is no means of determining whether or not changes took place earlier during burial.

Finally, if ground water effects are negligible, for instance on a desert site, there is the risk of changing disequilibria due to radioactive decay. For most TL dates this potential effect is limited to Ra-226, half life 1600 years. If there was considerable excess or deficit of this isotope in the clay used to make a sherd, this would decay or build up towards equilibrium with its parent Th-230 (half life 77,000 years). Thus the level of Ra-226 measured on excavation would not give the average level of radium activity during burial. For much older sites this could be complicated by radioactive decay of any Th-230 excess.

6.1.5 Existing measurements of chain disequilibria in archaeological contexts

Very little work has been done on the frequency or degree of disequilibria in archaeological contexts and sherds. MEAKINS et al (1979) reported values of Ra-226/U-238 activity ratios for four sherds and two clays of Middle Eastern origin, all of which showed significant disequilibrium (up to 40%). In addition they reported Th-232/U-238 activity ratios for these samples from 0.3 to 1.8. BOWMAN (1976) also gave Th-232/U-238 ratios of between 0.4 and 2.5

More has been done on the level of radon escape, using alpha counting

and gas cell analysis or Po-210 alpha spectrometry. For both wet and dry soils and sherds, levels of escape of 50% have been observed. (e.g. AITKEN, 1978b; DESAI, 1975).

6.1.6 Uncertainties in dose rate due to disequilibria

If disequilibria patterns are stable and the degree of disequilibrium of each group is known, there will be no dose rate uncertainty (from these sources at least). However, there is no technique in routine use in TL dating which provides all this information, and the uncertainties in dose rate will therefore depend on the technique used to estimate the activity of a sample. The parameters measured by these techniques are listed in Table 6.1.2, but without some quantitative knowledge of the likely degree of disequilibria, it is not worthwhile at this stage attempting to discuss the relative performance of these techniques. However, it is worth considering the effect of an unsupported Ra-226 excess at the time of firing a sherd in more detail.

Table 6.1.3 shows a breakdown of the alpha, beta and gamma dose rates for a 'typical' sherd containing 1 pCi g^{-1} of U-238 (with U-235), 1 pCi g^{-1} of Th-232, and 15 pCi g^{-1} of K-40. The decay chains are assumed to be in equilibrium. It can be seen that a substantial part of the total dose is from Ra-226 and its daughters. If the alpha contribution to the total dose is calculated assuming a relative efficiency for TL production of 0.1 compared with beta and gamma radiation, then these daughter products contribute about 22% of the total dose. Figure 6.1.1 plots the ratio, for various levels of Ra-226 excess at firing, of those doses calculated from a knowledge of only the U-238, Th-232 and K-40 concentrations to the true beta and gamma doses. This, for example, is what is determined by neutron activation and flame photometry. The discrepancy will be slightly smaller for alpha counting, because the residual Ra-226 excess at the time of measurement will contribute to the alpha count rate.

The maximum discrepancy for the 200% initial excess is after 6000 years, when the Ra-226 excess would have dropped to about 20%. For a sherd with such a discrepancy buried in a matrix of similar activity, but with no unsupported Ra-226 excess, and subsequently excavated and dated using either the fine grain technique or the quartz inclusion technique (i.e. including and not including the alpha contri-

Table 6.1.2

Summary of parameters measured by routinely used dosimetry techniques

alpha counting gas cell analysis	integrated alpha activity with and without radon escape
neutron activation	uranium and thorium contents
induced fission track analysis	uranium and thorium contents
beta TL dosimetry	integrated beta dose rate
gamma TL dosimetry	integrated gamma dose rate
flame photometry	total potassium content

Figure 6.1.1 Ratio of calculated beta and gamma dose to actual beta and gamma dose

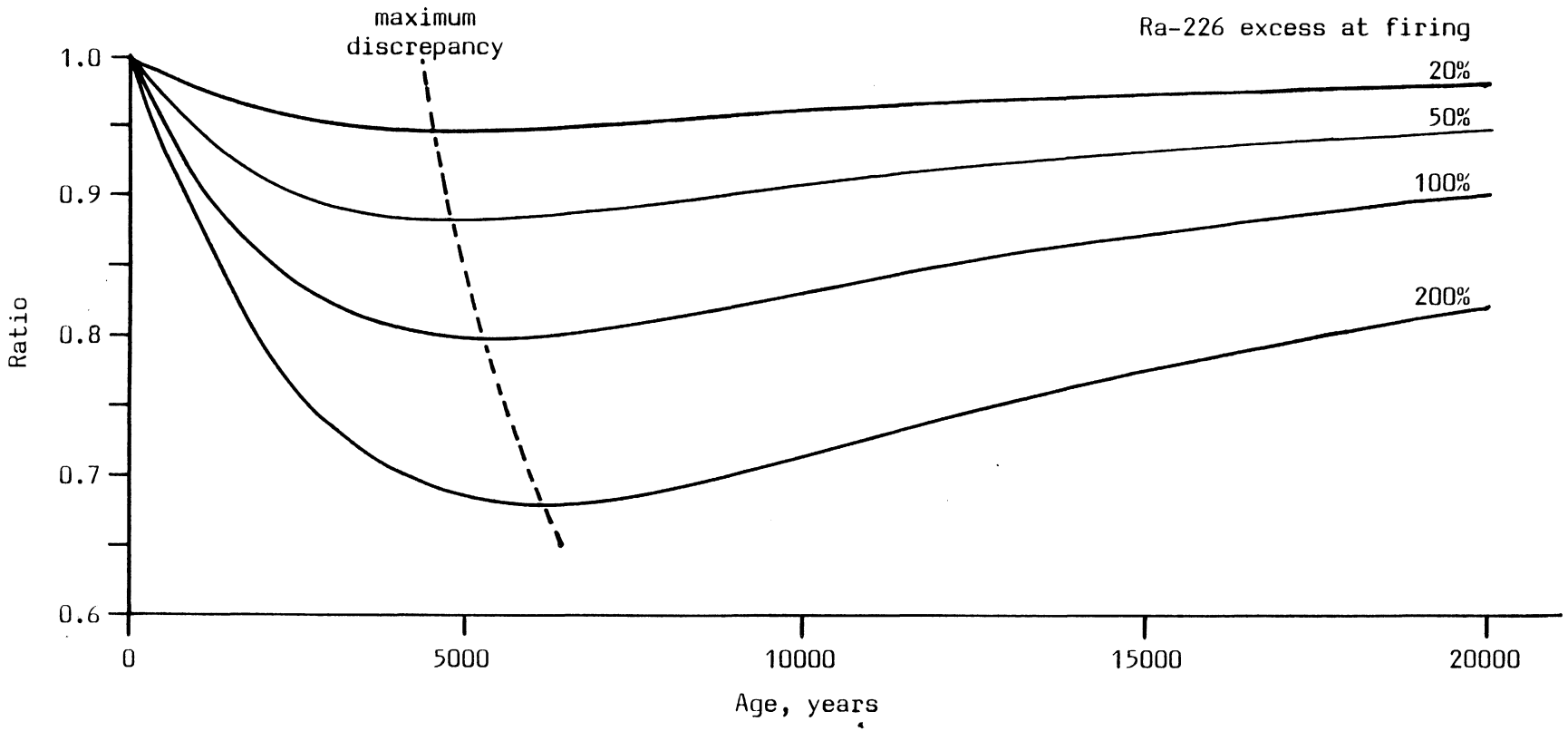

Table 6.1.3

Breakdown of the effective dose rate contribution of each group for a 'typical' sherd containing 1 pCi g^{-1} U-238 (+ U-235), 1 pCi g^{-1} Th-232 and 15 pCi g^{-1} K-40, with a cosmic ray dose rate of 15 mrad yr^{-1}

Group	Long lived isotope	Alpha % of total	Beta % of total	Gamma % of total
Uranium series:				
1	U-238	1.5	3.3	0.2
2	U-234	1.8	-	-
3	Th-230	1.5	-	-
4	Ra-226	1.8	-	-
5	Rn-222	6.9	3.5	6.4
6	Pb-210	2.0	1.6	-
1	U-235	0.1	-	-
3	Pa-231	0.3	-	-
5	Rn-219	0.4	0.2	-
Thorium series:				
7	Th-232	5.6	1.9	3.5
8	Rn-220	7.9	3.3	5.6
Potassium:				
	K-40	-	28.9	8.8
Cosmic ray dose rate contribution				3.0
Totals		29.8	42.7	27.5
Total dose rates, mrad yr^{-1}		151	216	139

Note: 1) decay chains are taken to be in equilibrium

2) the U-235 contribution was calculated using an atomic ratio to U-238 of 0.00726; this and other nuclear data are given in more detail in Appendix E

3) the effective alpha contribution is calculated assuming an alpha efficiency of 0.1 compared with beta and gamma rays at producing TL

bution) the calculated total dose would be about 24% low, giving an age 24% too old. Thus any sherds with even a small Ra-226 disequilibrium, such as those reported by MEAKINS et al (1979), must be treated with suspicion, unless it can be deduced that the disequilibrium exists further back in the chain, or that the Ra-226 is in fact supported in some other way, for instance by radium deposition from the ground water.

Clearly to improve the reliability of the estimation of the annual dose rate to buried pottery, a rapid, convenient technique for detailed radioisotope analysis of soils and sherds is needed. Alpha and gamma spectrometry can, in principle, give all this information. Alpha spectrometry can handle very low specific activities by concentrating samples chemically, but it involves considerable effort and is very slow. It would be very difficult to process a significant number of samples in a reasonable time. Gamma spectrometry, on the other hand, can provide very nearly as much information in a far shorter time.

6.2 GAMMA SPECTROMETRY AS A MEANS OF QUANTITATIVE RADIOISOTOPE DETERMINATION

The methods of gamma spectrometry and their application to quantitative isotope determination can only be discussed in terms of the type of gamma detector employed. Scintillation crystals, such as NaI(Tl) have typical line widths of about 40 keV at 661 keV, while solid state detectors, such as lithium drifted germanium, may have line widths of only 2 keV at the same energy. Thus the information that can be recovered by each system depends on the spacing and relative intensities of the gamma lines of interest. In the following sections the disequilibrium information available from high resolution spectra will be discussed.

6.2.1 High resolution spectrometry

The best approach to setting out the potential of gamma spectrometry is to consider spectra obtained with an actual detector system. The spectra used for illustration were taken with the germanium detector to be described later (section 6.3). The spectrum representing the uranium series is of a pitchblende ore diluted in dunite (NBL 74-A obtained from the U.S. National Bureau of Standards, New Brunswick Laboratory) sealed in polyester resin to minimize radon escape and

Figure 6.2.1

Illustrative gamma ray spectra of a uranium ore and a thorium ore, each in secular equilibrium

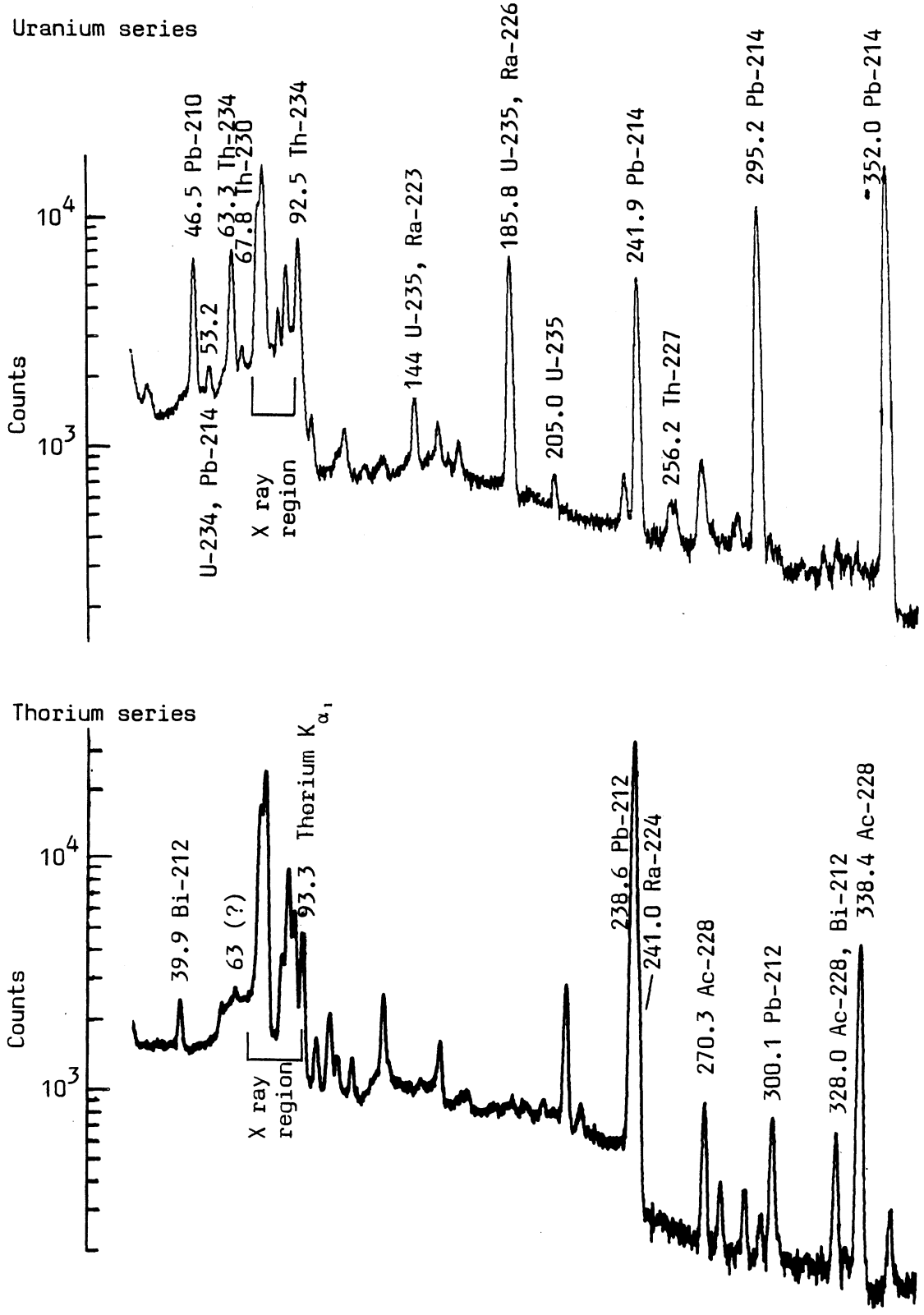

Figure 6.2.2

Illustrative gamma ray spectra of a uranium ore and a thorium ore, each in secular equilibrium (cont.)

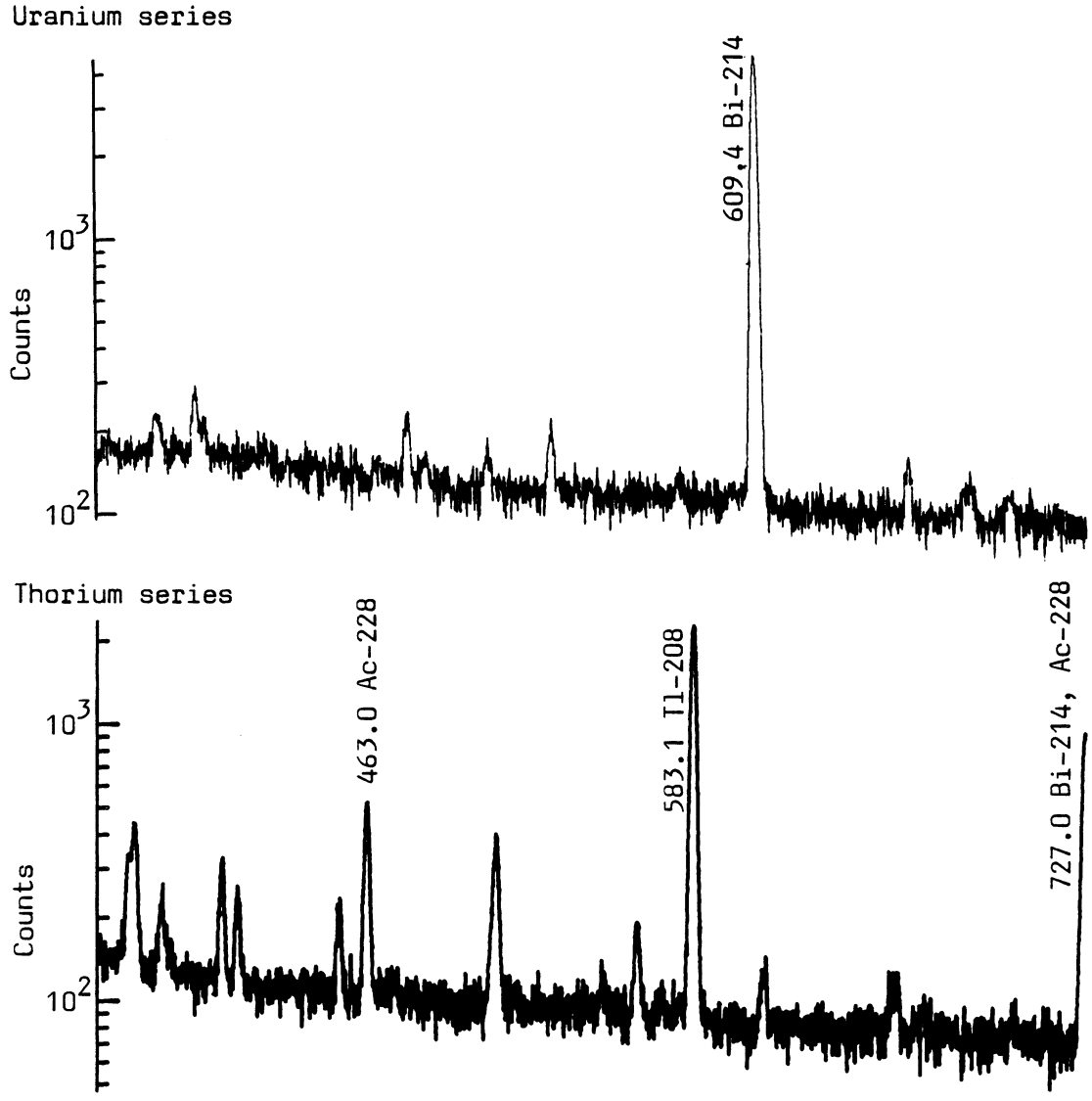

Figure 6.2.3

Illustrative gamma ray spectra of a uranium ore and a thorium ore, each in secular equilibrium (cont.)

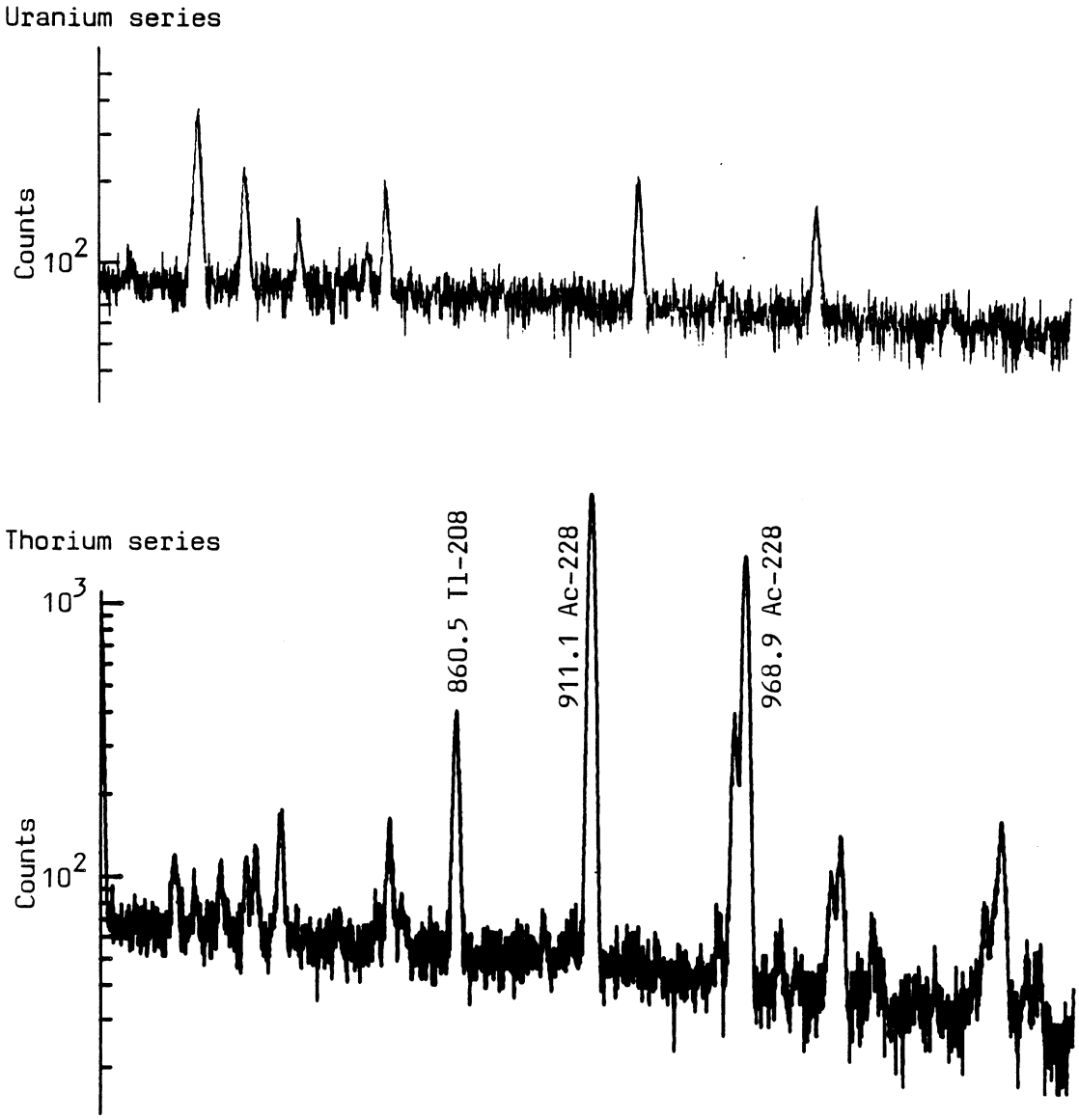

Figure 6.2.4

Illustrative gamma ray spectra of a uranium ore and a thorium ore, each in secular equilibrium (cont.)

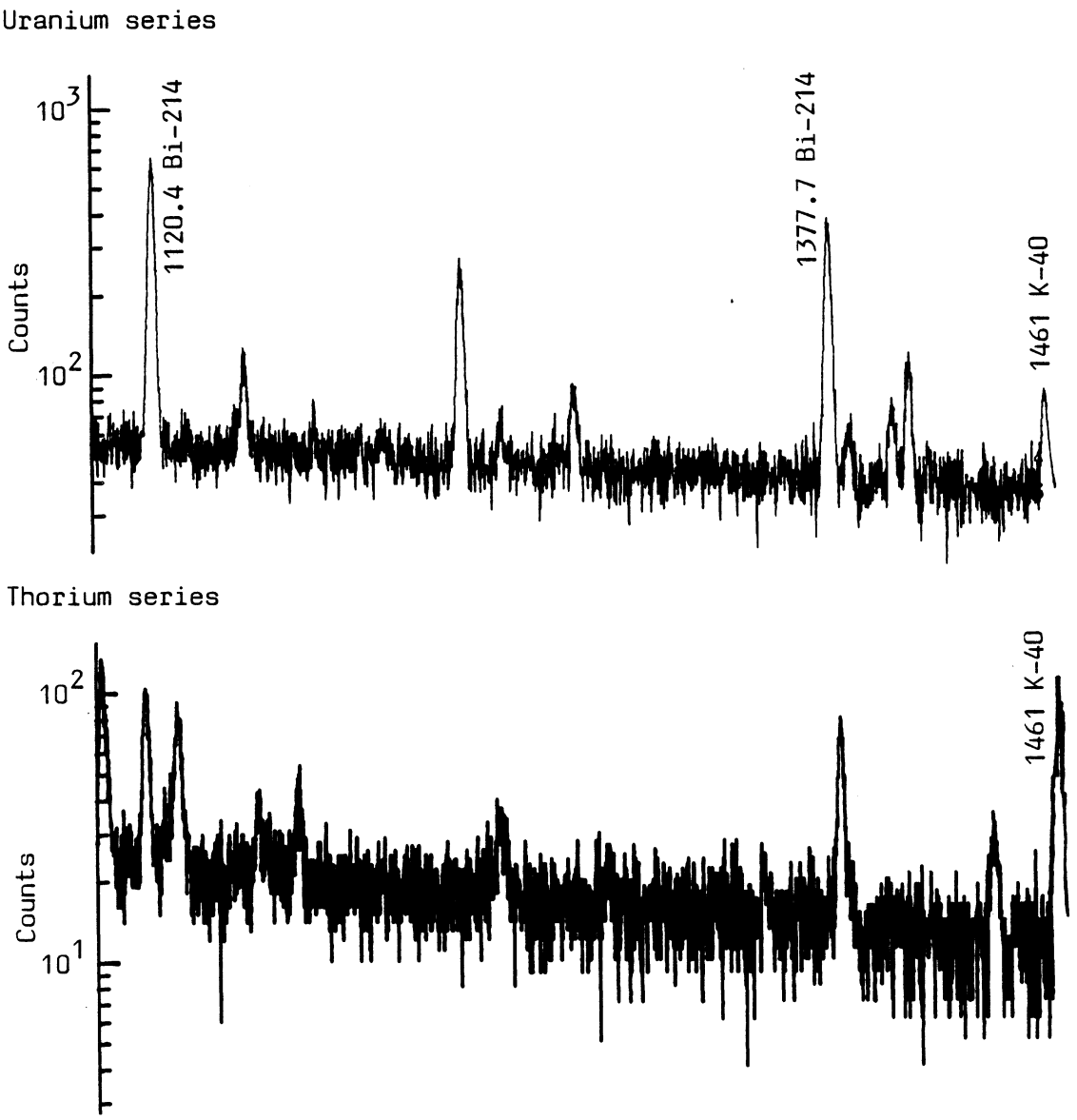

containing about 480 ppm uranium (168 pCi g^{-1}). The thorium series is represented by a thorite mineral (described in SMITH and WOLLENBERG, 1974) again diluted in dunite to a concentration of about 1600 ppm thorium (176 pCi g^{-1}).

Because of the extremely low activities of typical sherds and soils, of about 2 pCi g^{-1} of uranium and thorium in total, it is not necessary to go into great detail in considering these spectra, as only the strongest lines are potentially useful. A more comprehensive approach, describing application to high activity materials is detailed by SMITH and WOLLENBERG (1974).

These spectra are shown in figures 6.2.1 to 6.2.4; all the intense lines, and some of the weaker ones, are marked. The spectra will now be discussed under the group headings set out in section 6.1.

6.2.2 Uranium series

i) Groups 1 and 2; U-238, U-235, U-234

The U-238 activity can be determined from the gamma emissions from Th-234, in particular the line at 63.3 keV and the 92.4 + 92.8 keV doublet, represented here as a line at 92.5 keV. Unfortunately both of these energies have some interference from the thorium series; in particular, the peak at 92.5 keV from the 93.3 keV thorium X ray line. The degree of this interference cannot necessarily be corrected for, as the X ray yield will be dependent on the degree of localised inhomogeneity from grain to grain (SZOGHY and KISH, 1977) and this would tend to introduce a sample dependence. In addition, there is a small peak in the thorium spectrum at 63 keV, which is not assigned to any thorium series isotope. It is clearly important to be confident that it is not due to U-238 impurities; the origins of this peak and the problems of allowing for it correctly are taken up again in section 6.6.

The only intense peak that could be used for determining U-235 activity is that shown at 185.8 keV, but allowance must be made for the Ra-226 (Group 4) contribution of almost 50%, by sealing the sample to prevent radon escape, and storing for about one month to allow the Rn-222 and daughters (Group 5) to reach equilibrium with Ra-226. The activity of this group can then be determined using the peaks discussed in section 6.2.2 (iii). In this approach, the contribution of Ra-226

to the peak would then be calculated knowing the gamma intensity per unit activity from tables; the problems associated with this are discussed in section 6.6. The alternative would be to count a Ra-226 source in equilibrium with daughters, to obtain a direct ratio between Rn-222 daughter peaks and the Ra-226 peak. In practice, however, it is more likely that the U-235 contribution would be derived from the U-238 activity as measured by the Th-234 peaks (at 63.3 keV and 92.5 keV), assuming the U-235/U-238 activity ratio.

There is no intense peak from U-234, although the weak line at 53.2 keV is made up of about a 75% contribution from Pb-214 (Group 5) and 25% from U-234. It is very unlikely that this peak would be sufficiently intense to be of use in low activity samples.

ii) Group 3; Th-230, Pa-231

There is one weak line from Th-230 at 67.8 keV that could be useful, but only in the more active pottery samples.

There are two low intensity peaks that could give the Pa-231 activity. At 144 keV the peak is composed of gamma rays from both U-235 (Group 1) and Ra-223 (Group 3). The U-235 contribution could be assessed as described in section 6.2.2 (i). The other line is at 256.2 keV, but here there is in fact a doublet, with a weak line from Pa-234 (Group 1) at 258.2 keV. It is unlikely that for low activity samples, these lines could be satisfactorily resolved.

iii) Group 4; Ra-226

The only gamma emission from Ra-226 is in the peak marked at 185.8 keV. Approximately half of this peak derives from U-235; this contribution can be assessed from a knowledge of the U-238 activity, (assuming the U-235/U-238 activity ratio). The U-235 count rate can then be derived from tables, or, more satisfactorily, by counting a chemically separated uranium salt of natural isotopic abundance.

iv) Group 5; Rn-222, Rn-219

There are several strong lines suitable for determining the activity of Rn-222 from its short lived daughters. In the low energy region, the three Pb-214 gamma lines at 241.9, 295.2 and 352.0 keV are the most useful, although the 241.9 keV peak has serious interference from the

241.0 keV peak in the thorium series. At high energies, the 609.4 keV peak from Bi-214 is the only peak of sufficient intensity to be useful, although there are other weaker lines, at 1120 keV and 1378 keV for instance.

There is no suitable emission for determining the Rn-219 activity in samples likely to be of interest.

v) Group 6; Pb-210

There is only one gamma line of significance from this group, at 46.5 keV, from Pb-210 itself.

6.2.3 Thorium series

i) Group 7; Th-232

There are many lines suitable for the estimation of the activity of this group, all from Ac-228. The important ones are clearly marked, and all are free from significant uranium series interference except the 270.3 keV line. This is bracketed by two weak lines from Group 3 (Ra-223) and Group 5 (Rn-219). They are of sufficient intensity to make the estimation of the background continuum under the peak uncertain.

ii) Group 8; Rn-220

Again, there are many lines available, the most important of which is the Pb-212 peak at 238.6 keV, despite the interference from the Ra-224 peak at 241.0 keV (Group 7) and the 241.9 keV peak from Pb-214 (Group 5). At higher energies the 583.1 keV line from Tl-208 is also useful.

6.2.4 Potassium analysis

The 1461 keV line from K-40 is intense and well separated from strong uranium and thorium lines. The appearance of a peak at this energy in the uranium and thorium spectra is from the potassium contribution to the natural background.

6.2.5 Summary of the potential of high resolution spectrometry

From section 6.2.2 we can conclude that, in principle, the disequilibrium state of the entire U-238 chain could be determined using gamma spectrometry. However, for low activity samples, the gamma lines from Group 2 (U-234) will not be measurable. Th-230 (Group 3)

is only likely to be observed in exceptionally active archaeological samples. Although, again in principle, the entire state of equilibrium of the U-235 series could be determined, in practice only U-235 itself is likely to be measurable.

From section 6.2.3, the two groups of the Th-232 series (7 and 8) are both reaily determined, as is the concentration of K-40 (section 6.2.4).

6.3 SPECTROMETER DESIGN

It was concluded in the last section that the major features of the internal radioactivity of a sherd or soil sample can be resolved using high resolution gamma spectroscopy. Several authors have used this approach for active ore samples, e.g. SMITH and WOLLENBERG (1974) SZOGHY and KISH (1977), and MOXHAM and TANNER (1977), and although these examples are not directly applicable to this case, they do provide a guide as to what the instrument requirements will be to enable the desired analyses to be performed.

6.3.1 Spectrometer resolution

Obviously the spectrometer must be primarily capable of resolving the gamma lines of interest. Of the lines that are sufficiently intense to be potentially useful, the separation of the 63.3 keV Th-234 peak from the weak 67.8 keV peak of Th-230 is probably the most important low energy problem. At intermediate energies the U-235 and Ra-226 peaks at 185.7 keV and 186.0 keV are impossible to separate, while the triplet of Pb-212 at 238.6 keV, Ra-224 at 241.0 keV and Pb-214 at 241.9 keV presents a challenge to the best solid state detectors available. At higher energies there are no close doublets likely to be of importance, although there are many of relatively low intensity. Thus any practical detector must have a resolution of about one to two keV to be useful. This precludes the use of any type of scintillation spectrometer as the best resolution available for a 2½ inch diameter by 2 inch NaI(Tl) crystal is between 6 and 7% at 661 keV. Solid state detectors using silicon or germanium, on the other hand, have very good resolution characteristics, 2.0 keV at 1332 keV is not unusual for small detectors.

6.3.2 Efficiency

Gamma spectrometry depends on analysis of full energy release peaks, and as the photoelectric cross section increases with approximately Z^5, germanium is preferred to silicon for the energy range of interest here (40 to 1460 keV). To obtain useful efficiencies at higher energies a substantial detector volume is required (tens of cubic centimetres), owing to the small mass absorption coefficient of germanium. Moreover, as the volume of the detector is increased, the probability of total energy absorption through multiple Compton interactions increases.

The other main constraint on the detector design derives from the sample size and activity. Typical pottery samples such as that used for illustration in table 6.1.3 have about 1 pCi g^{-1} uranium, 1 pCi g^{-1} thorium and 15 pCi g^{-1} K-40 with a mass of rarely more than ten grams. Table 6.3.1 lists the gamma intensities of some of the stronger lines from such a sample.

We also require an estimate of the maximum acceptable error in the measurement of any one radioisotope group. If we consider the quartz inclusion technique, and aim for errors in dates of about 5%, then the total dose rate must be determined to significantly less than this, say about 3.5%. Assuming that the three main sources of this dose rate, the uranium chain, the thorium chain and K-40, contribute equally, we can tolerate errors in dose rates derived from the individual chains of less than about 6%. This figure is further increased for the individual groups depending on their relative importance as sources of dose rate. Nevertheless, it is useful to consider 5% as a target error for discussion. Assuming we can make calibration errors negligible, then the major source of this error will be statistical uncertainty due to finite count times.

Over the past few years, various high resolution detector systems have been built capable of detecting picoCuries of activity, e.g. LEWIS and SHAFRIR (1971), COOPER and PERKINS (1971, 1972), CAMP et al (1974), CARRUTHERS and MORGAN (1975), HUNT et al (1978). These systems have been primarily intended for use in environmental studies of fallout and other artificial nuclides in the environment. The most sensitive of these

Table 6.3.1

Gamma intensities of some stronger lines from a 10 g sample containing 1 pCi g^{-1} uranium, 1 pCi g^{-1} thorium and 15 pCi g^{-1} potassium, with all daughters in secular equilibrium

Group	Long lived isotope	Emitting isotope	Energy keV	Photons $ksec^{-1}$
1	U-238	Th-234	63.3	21.1
	U-235	U-235	185.7	9.3
2	U-234	U-234	53.3	<1
3	Th-230	Th-230	67.8	1.4
		Th-227	256.2	1.0
4	Ra-226	Ra-226	186.0	14.4
5	Rn-222	Pb-214	241.9	28.1
			295.2	69.9
			352.0	134.3
		Bi-214	609.4	158.4
6	Pb-210	Pb-210	46.5	15.2
7	Th-232	Ac-228	338.4	50.0
			911.1	120.9
			968.9	72.9
		Ra-224	241.0	14.9
8	Rn-220	Pb-212	238.6	187.7
		Bi-212	39.9	4.4
		Tl-208	583.1	124.9
	K-40	K-40	1461	561

Note: gamma energies and intensities derived from SMITH and WOLLENBERG (1974)

(CAMP et al (1974)) claims a 15% statistical error in measuring 5.5 pCi total activity of Cs-137 at 661 keV in a 235 gram sample counted for 60 ksec. However, the efficiency of their detector at detecting Co-60 gamma rays was only 10% of that of a 3 inch by 3 inch NaI(Tl) detector in the standard geometry (i.e. source to sample distance of 25 cms). This is equivalent to approximately 0.5% absolute efficiency, for a sample a few centimetres thick placed on the end cap of the detector. It is obvious from table 6.3.1 that to achieve the level of accuracy desired for this application in a practical count time of, say 85 ksec (about 24 hours), a very much higher detection efficiency will be required.

For small samples the most efficient geometry is that of a well counter, which can approach 100% detection efficiency at low energies. Figure 6.3.1 shows a typical absolute efficiency curve for a large (80 cm^3) Ge(Li) well detector. Both for ease of construction and to assist in producing a uniform potential gradient across the crystal, the well is in fact an axial hole the length of the detector. For our purposes this hole should be as long and thin as is practical, to minimise self absorption in the sample and to approximate more closely to 4π counting geometry. However, it is more difficult to decide on the optimum thickness of germanium around the sample. The external background in such a detector (assuming for this discussion, no peak structure) will be proportional to the volume, whereas at low energies there will be no further increase in sample count rate once there is sufficient thickness of detector material to totally absorb these low energy photons. (One centimetre of germanium will absorb 90% of all normally incident gamma rays with an energy of 130 keV). In addition the resolution tends to become poorer with increasing volume. Unfortunately, as well as detecting low energy gamma rays, we would also like to determine the K-40 line at 1461 keV. This requirement is incompatible with the above, as a very much thicker detector would be needed to detect a significant proportion of incident high energy gamma rays, and so a compromise is necessary. Various authors (CLINE (1968), MCKENZIE et al (1967), COOPER (1970)) have attempted to quantify these problems for Ge(Li) detectors to produce a figure of merit; this approach should enable design decisions to be taken on a more rational basis. The method proposed by COOPER (1970) is used here, although it must be emphasized that

Figure 6.3.1

Typical absolute efficiency and resolution curves for an 80 cm^3 Ge(Li) well detector

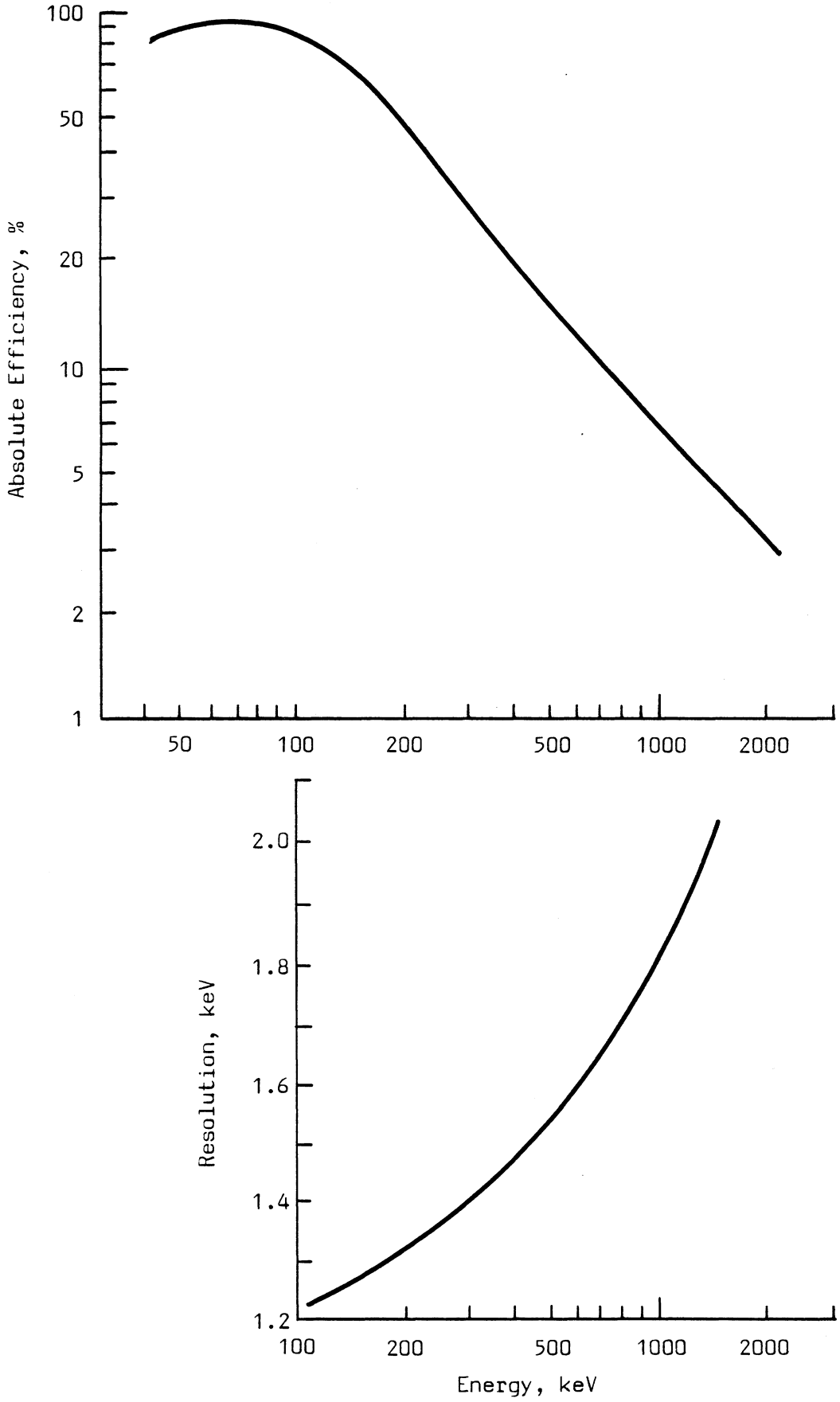

it is only approximate when low count rates are being considered (less than about 50 counts per channel). He suggests that the minimum disintigration rate $\dot{D}_m(E)$ at energy E that will give rise to a fractional error $1/A_m$ can be expressed as

$$\dot{D}_m(E) = \frac{A_m}{F(E)\ f\ t}\left([2\ b\ R(E)\ \overline{B} + A_m/4]^{\frac{1}{2}} + A_m/2\right) \text{ - - - } 1$$

where F(E) is the absolute detection efficiency at energy E,

f is the number of gamma rays produced on average by one disintegration,

t is the count time,

R(E) is the resolution at energy E expressed in channels,

b is that factor, which when multiplied by R(E), gives the number of channels included in the peak. It will take on a value close to 2 if the peak region is bounded by channels at 1/10 maximum peak height,

$\overline{B}$ is the average number of background counts in one channel. In this simplification for low count rates, this is the sum of the natural background and Compton scattered photons from high energy gamma rays emitted by the sample.

We define the acceptable fractional error $1/A_m$ as 0.05, i.e. A_m is 20, and a realistic count time as 85 ksec.

From figure 6.3.1 the efficiency of a Ge(Li) well detector may be estimated as 90% at 100 keV, 25% at 350 keV and 6% at 1400 keV.

ADAMS and DAMS (1970), page 170, give a background curve for a 42 cm^3 Ge(Li) detector, with only a moderate degree of shielding, 8 cm of lead, lined with cadmium and copper. Doubling their values for a detector of about 80 cm^3, which is approximately the volume of the detector used to derive figure 6.3.1, i.e. 15 cm of germanium surrounding a 2 cm diameter well, about 5 cm long, capable of holding about 10 g of sample, and assuming that the Compton background will be small compared with the total background, $\overline{B}$ takes values of 3000 counts/channel at 100 keV, 750 counts/channel at 350 keV and 75 counts/channel at 1400 keV. This assumes an energy conversion of 1 keV/channel. Using this conversion figure, and typical resolution figures from figure 6.3.1, R(100 keV) is 1.4

channels, R(350 keV) is 1.6 channels and R(1400 keV) is 2.5 channels. This gives values for the product $f\dot{D}_m(E)$ (i.e. the number of gamma rays that must be emmited by the sample per second to give the required fractional error), of

100 keV	350 keV	1400 keV
36	75	153

From table 6.3.1 typical gamma production rates are 15 and 21 at 46 and 63 keV, 50 and 134 at 338 and 352 keV, and 561 at 1461 keV. Thus detection of these lines is certainly possible, although it seems that attention must be paid to reducing the low energy background if the desired accuracy of 5% is to be reached.

The final design specifications for the detector are given in table 6.3.2 and figure 6.3.2.

Note that the well is 19 mm diameter, leaving 18 mm of germanium surrounding the sample. Not all of this well volume will be available, as the can dimensions must be allowed for. Thus the useful volume of well is about 6.2 cm^3. Densities for pottery and soils vary, but 1.5 g cm^{-3} is a representative figure, this implies about 9 g of sample in the well.

6.3.3 Background

The potential sources of background counts may be divided into two categories, that which is external to the detector shielding, and that which is part of the shielding or contained within it. These categories will be considered separately.

The external radiation field derives from the natural radioisotopes in the materials surrounding the shield, and from the cosmic ray flux. For our purposes the former may be considered to be entirely a gamma flux, the latter consists of high energy ionizing particles (mainly μ mesons and electrons) and neutrons and gamma rays. The effective reduction of the gamma background requires massive shielding, usually lead. Unfortunately this increases the mass of material close to the detector which is then available to interact with the primary cosmic ray flux, to produce a greater number of low energy particles to be included in

Table 6.3.2

Detector Specifications

Material:	Intrinsic germanium	
Resolution:	<2.4 keV at 1332 keV	
Efficiency:	>15% at 1332 keV	
Dimensions:		
	length	40 mm
	outer diameter	55 mm
	well diameter	19 mm
Supplier:	PGT (Europa)	

Note: efficiency is specified as that relative to the efficiency of a 3 inch by 3 inch NaI(Tl) crystal, with the source at 25 cm from the detector in each case.

Figure 6.3.2

Cross-section of detector and vacuum can

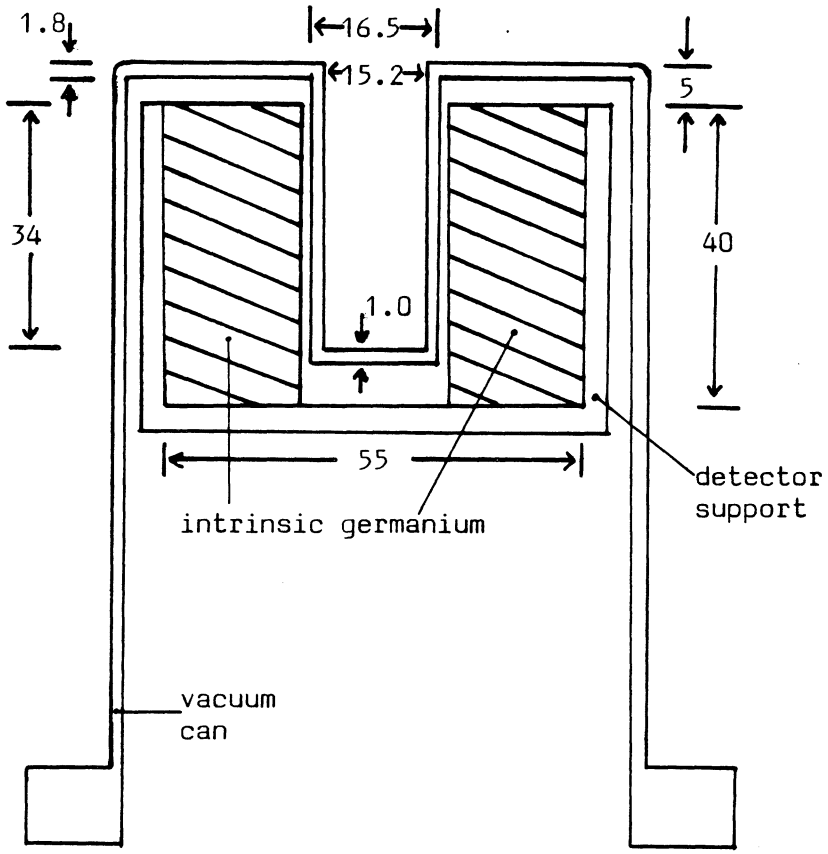

Note: 1) all dimensions in mm.

2) can and detector support fabricated from magnesium alloy, type A180 supplied by Magnesium Elektron, Manchester

the background count rate. In particular, lead shielding increases the neutron flux seen by the detector. However, as the gamma ray detection efficiency of solid state detectors is much greater than that for neutron detection, the main emphasis may safely be placed on the reduction of the gamma flux.

Potentially more serious than the external gamma flux, which at least in principle can be effectively attenuated, are those gamma rays arising from radioactive contamination of the lead shield and those parts of the detector assembly contained within the shield. A summary of measured activities of those materials likely to be useful in the spectrometer is given in CAMP et al (1974). As these are the components most readily under the experimenter's control, a detailed examination of the proposed materials was undertaken.

(i) Lead Shielding

Lead was chosen for the external bulk shielding for reasons of cost and availability. The other two possible materials, concrete and steel are more difficult to obtain in a sufficiently inactive form. Even the lead used must be selected with care, as the ore inevitably contained some uranium and thus the purified metal will contain appreciable activity from the radioactive isotope Pb-210, which has a half life of 22 years. This is the major reason why aged lead (more than 100 years old) is to be preferred. However, there are additional potential sources of activity, including other isotopes from the uranium and thorium series, which may be present as trace impurities. Some of this can be avoided by special refining techniques (GRINBERG and LE GALLIC,1961). Aged lead is invariably scrap metal, and if it has been exposed to the atmosphere, as roofing material for instance, it may also be contaminated by fallout.

To provide a check on some of these possibilities, samples of aged lead were obtained from the supplier of the lead castle (ERD, Slough) and the alpha activity counted in the same geometry as used for pottery samples. A correction was applied for the differences in alpha ranges in lead and pottery (taken to be close to that of neon according to AITKEN and BOWMAN (1975)). Portions of the same samples were brought into solution, and the Po-210 extracted for alpha spectrometry. The results of the two techniques are summarized in table 6.3.3. As the activity of the Pb-210, as measured by Po-210 alpha spectrometry, is easily sufficient

Table 6.3.3

Alpha counting and Po-210 analysis of lead sample

		$ksec^{-1}$
alpha count rate, for a thick source, 42 mm diameter		4.7 2
applying range correction for lead compared with pottery		1.6 1
		$pCi\ g^{-1}$
Deduced from above assuming only uranium chain present,		
	if full chain	0.34 2
	if Ra-226 + daughters	0.47 3
	if Pb-210 + daughters	2.9 2
from alpha spectrometry,		
	activity of Po-210	3.2 3

Note: 1) for conversion from alpha count rate in pottery to isotope activity, see Appendix E.

2) errors are in the least significant figures.

to explain all the observed alpha count rate, these levels are considered acceptable. If there had been more total alpha activity than could be explained by the Pb-210 activity, there would have been a risk of significant high energy gamma activity, which could not have been disregarded. The gamma line from group 6, Pb-210, is only 46 keV, however, and is readily shielded with, say, a few millimetres of electrolytic copper, should this prove necessary.

The final layout of the shield and cryostat is shown in figure 6.3.3. Note the long side arm cooling the detector head. This has the important advantage of keeping the molecular sieve, which is housed near the cryostat, outside the shielding, without a 'line of sight' view of the detector head through the entry port. As this sieve is made from zeolite which contains significant quantities of uranium, this is very desirable.

ii) Materials close to the detector

In addition to checking the lead activity, samples of the various materials used in the detector head were obtained for alpha counting.

These results are summarised in table 6.3.4 corrected for the differences in alpha range compared with pottery. Of the three plastic materials supplied, only one proved to have significant activity, and this was not used in the final construction. However, all the various samples of aluminium alloy tested, intended for the internal support for the crystal and for the vacuum can, can be seen to have detectable alpha activity. It seems that in the electrolytic refinement of aluminium from bauxite, small amounts of uranium and daughters, especially radium, are concentrated into the metal. This has long been recognised in low background work using NaI(Tl) scintillators, where electrolytic copper is often used as a substitute (WATT and RAMSDEN, 1964). COOPER and PERKINS (1972) made do with selected aluminium (type 1100) for the vacuum cap, which they state contained acceptable amounts of uranium, thorium and potassium. They fabricated the crystal support from magnesium; CAMP et al (1974) used magnesium for both the support and vacuum cap. It was therefore decided to estimate the total activity contained in an aluminium support and can in the immediate vicinity of our detector and compare this with the likely sample activity. The volume of material surrounding the detector was divided into three

Figure 6.3.3 Layout of detector and lead castle

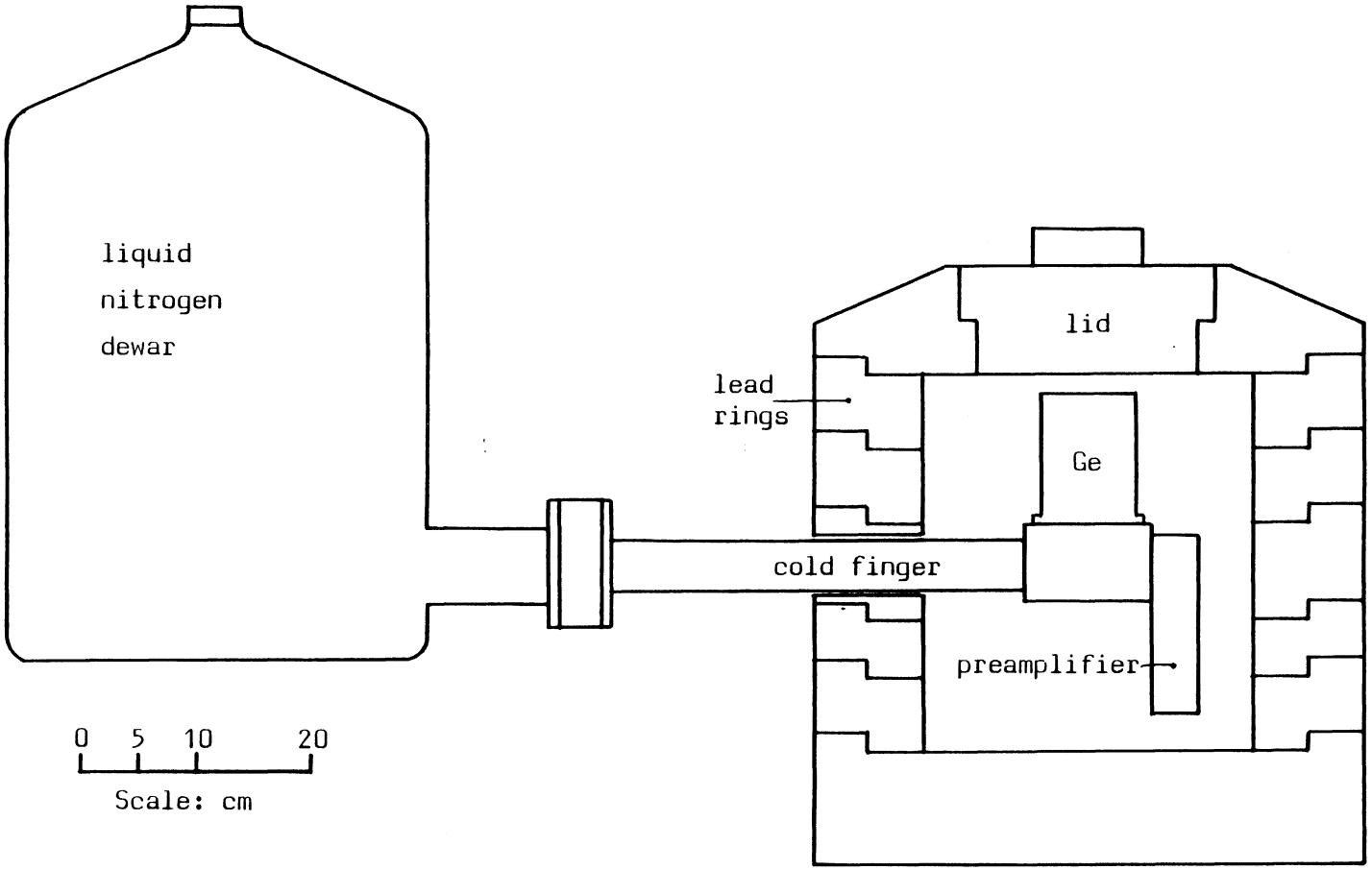

Table 6.3.4

Activity measurements on proposed materials for use in the detector head

	alpha count rate $ksec^{-1}$	
On P.G.T. samples:		
'Nylon'	<0.1	
colourless plastic	<0.1	
green fibreglass	0.5_{1}	
aluminium alloy	0.66_{1}	
On other aluminium samples:		
1. 99.999% pure metal	0.60_{9}	
2. aluminium alloy	0.65_{10}	
3. " "	0.84_{16}	two ends of same rod
" "	0.24_{19}	
4. " "	0.45_{12}	two ends of same rod
" "	0.52_{20}	
5. NaI(Tl) crystal aluminium can	0.86_{11}	

Alpha spectrometry on sample 2 gave a Po-210 activity of 0.26 ± 0.03 pCi g^{-1}
Assuming only uranium chain present, the alpha count rate on sample 2 corresponds to:

	pCi g^{-1}
if full chain	0.14
if Ra-226 + daughters	0.19
if Pb-210 + daughters	1.2

Note: 1) for conversion from alpha count rate in pottery to isotope activity, see Appendix E.
2) errors are in the least significant figures.
3) alpha count rate is for a 42 mm diameter sample, with a threshold set as described in Appendix E.

parts; that contained within the well, that in contact or close to the detector at each end, and that surrounding the circumference of the detector. The volumes of these three components may be estimated from figure 6.3.2. That contained within the well was assumed to be in a counting geometry of 0.8 x 4 π steradians, that at the ends in 0.8 x 2 π steradians, and that around the circumference in 0.8 x π steradians. The total effective volume is thus calculated to be 18 cm^3, normalized to the counting geometry of material contained in the well. This is also assumed to be the sample counting geometry. For aluminium, this corresponds to a mass of about 48 g, with an activity of about 0.23 pCi g^{-1} (from table 6.3.4). This implies that the can and support would have an activity equivalent to 11 pCi contained in the well and emitting the same gamma lines as those to be investigated. Table 6.3.1 indicates that the total uranium activity of a typical sample is about 10 pCi. This is clearly unacceptable.

The conventional alternatives to aluminium, i.e. beryllium and copper, are also unacceptable. It would be impossible to produce the complex design of the end cap in beryllium, and copper would have to be impractically thin to avoid large attenuation at low energies.

Magnesium, as mentioned above, has infrequently been used as part of the detector support material, although most workers avoid it for the can as it tends to be porous. The magnesium vacuum can for CAMP et al (1974) was specially poured and machined by the Ames Research Laboratory, Iowa, because of this problem. It has the advantage of a lower mass attenuation coefficient than aluminium at low energies (0.298 cm^2 g^{-1} at 50 keV instead of 0.334 cm^2 g^{-1}) and a much lower density (1.7 g cm^{-3} instead of 2.7 g cm^{-3}). It is also easy to machine. Accordingly, two samples of pure metal were alpha counted to see if it was a possible candidate. Both samples gave alpha count rates about six times smaller than the various aluminium samples listed in table 6.3.4.

Further samples of pure magnesium metal and two different alloys were obtained from Magnesium Elektron of Manchester. These were alpha counted and analysed by alpha spectrometry. The results are listed in table 6.3.5. The pure metal sample 'Norsk', and the alloy 'ZW3' prepared from it, were refined by an electrolytic method. The 'Domal' sample and the alloy 'A180' derived from it, were refined by a thermal

Table 6.3.5

Alpha activities of magnesium samples

	alpha count rate $ksec^{-1}$	Po-210 activity from alpha spectrometry $pCi\ g^{-1}$
Preliminary samples:		
Norsk pure metal	0.18_{1}	
ZW3 alloy	0.05_{5}	
Domal pure metal	0.025_{25}	0.013_{7}
A180 alloy	0.05_{4}	0.024_{7}
Longer counts on A180, bar used for first detector can:		
disc 1	0.04_{6}	0.026_{8}
	0.01_{4}	0.029_{3}
disc 2	0.05_{4}	
disc 3	0.05_{4}	0.034_{1}
fine turnings	0.01_{4}	0.049_{13}
bar used for second can:		
disc 4	0.04_{7}	0.023_{8}
average for discs 1,3,4 and fine turnings	0.03_{1}	0.033_{6}

This count rate corresponds to an activity of 0.05 ± 0.02 pCi g^{-1}, if only Pb-210 + daughters are assumed to be present.
(if the complete U-238 chain is present 0.006 ± 0.002 pCi g^{-1},
if Ra-226 + daughters present 0.009 ± 0.003 pCi g^{-1})

Note: errors are in the least significant figures

method. Although there is no apparent difference between the activities it was decided to use thermally extracted material, to avoid the risk of preferential separation of the uranium series as seems to occur in aluminium, although SMITH (private communication) states that he has found the primary impurity in his magnesium samples to be the thorium chain. The alloy 'A180' was the final choice because of its fine grain structure and good machining qualities. The Pb-210 activity of this alloy is estimated at 0.03 pCi g^{-1}, nearly ten times less than that in aluminium, and the alpha count rate is consistent with this. Taking the effective volume of the can and support to be 18 cm^3 as before, the total effective mass normalised to material contained in the well, is now only 30.6 g, with a corresponding activity of less than 1 pCi. Magnesium is clearly a much better choice than aluminium.

The first can turned was porous, but this was traced to an error in supplying untested material containing flux cavities. The second attempt proved entirely satisfactory. The can was turned in one piece from a solid bar, in two stages. First the inside was machined out, to final dimensions, and filled with a low melting point alloy (about 70°C) with a very small expansion coefficient. The outside was then turned down permitting a well wall thickness of only 0.5 mm to be accurately produced. The finished can was gently warmed to release the filling. No surface treatment was given.

6.3.4 Anti-Compton shield

Shortly after the orders for the detector and shielding had been placed, financial support for a modest anti-Compton guard ring became available. Such devices reduce the background continuum seen by the germanium detector in the following manner.

A high efficiency gamma detector, such as NaI(Tl) or a large plastic scintillator, is placed around the germanium crystal; ideally this central detector would be completely surrounded. Now consider first a gamma ray from the sample interacting in the germanium detector. If the gamma energy is totally absorbed in the germanium then it will contribute to the full energy release peak, as desired. If, however, only part of the energy is absorbed in the germanium, the rest escaping as a Compton scattered photon, then this normally contributes to the

background continuum. But if this escaping photon deposits part or all of its energy in the surrounding scintillator a pulse will be produced which can be used, in conjunction with timing circuits, to reject the germanium pulse, thus reducing the Compton continuum. Similarly if a photon in the external background gives rise to interactions in both detectors, these background pulses can be ignored. It then becomes important to minimise the 'dead' material between the scintillator and the germanium, as scattered photons may be totally absorbed in this material and remain undetected. The choice of magnesium instead of aluminium for the central detector can and support again proves to be of value, magnesium being some 40% less dense. The scintillator should also be as large as is necessary to efficiently detect all the scattered gamma rays. There will also be a simple shielding effect. (The scintillator obviously must be of very high radioactive purity).

The choice between NaI(Tl) and plastic is largely dictated by space requirements, as a given detection efficiency of NaI(Tl) costs about the same as the same efficiency of plastic, despite large differences in size. As the diameter of the lead shield had already been decided, a plastic system was not considered, as insufficient material could be placed around the well to make the improvement worthwhile. However, it was practical to consider the benefits of placing 4 cm of NaI(Tl) around the detector, with a plug of scintillator on top.

Using a slightly more favourable geometry than proved to be possible here, (i.e. a better enclosure of the central detector) and a 3 inch wall thickness of NaI(Tl), COOPER and PERKINS (1972) achieved the continuum suppression figures given in table 6.3.6. For Compton suppression, it is possible to predict the behaviour of a 1.5 inch guard ring, if we assume the same threshold detection levels for both detectors. To reduce the continuum at 100 keV in the central detector, we are interested in efficiently detecting gamma rays of about 560 keV in the guard ring for an incident energy of 661 keV. Similarly, to reduce the continuum at 400 keV we need to detect gamma rays of about 250 keV. Note that the assumption of similar threshold levels is critical here; the interaction giving the detection pulse in the guard ring may be of very low energy, and high threshold levels will lose such interactions. The value of the linear attenuation coefficient of

Table 6.3.6

Continuum count rate reduction factors using an Anti-Compton guard ring

for 3 inches of NaI(Tl), from Cooper and Perkins (1972)

Energy keV	Compton reduction for Cs-137	Background reduction
100	3	5
400	16	10
expected for 1.5 inches of NaI(Tl)		
100	2	4
400	15	10

NaI(Tl) at 560 keV and 250 keV is 0.31 cm^{-1} and 0.85 cm^{-1} respectively, (GRODSTEIN, 1954). Thus we expect 1.5 inches of NaI(Tl) to be 0.76 as efficient at detecting 560 keV photons as 3 inches of NaI(Tl), and 0.96 as efficient at 250 keV. These are the scaling factors used in table 6.3.6 to predict the behaviour of a 1.5 inch guard ring. It is impossible to adopt a similar approach to the background without knowing the shape of the incident background flux. For these purposes, however, the scaling factors have been assumed to be the same as for the Compton suppression, in order to estimate the effect of such an anti-Compton ring on the minimum detectable disintegration rate of equation (1) of section 6.3.1.

Assuming again that the continuum is likely to be dominated by the natural background, and using the background reduction factors given in table 6.3.6, then the values of $f\dot{D}_m(E)$ are

	100 keV	350 keV
no anti-Compton suppression	36	75
with anti-Compton suppression	22	10
typical real values, from table 6.3.1	15,21	50,133

Obviously this improvement at low energies is very helpful in achieving the counting errors required.

6.3.5 Encapsulation of the anti-Compton guard crystals

As discussed, the aluminium cans usually fitted to scintillation crystals are significantly radioactive. In this case, replacing with magnesium, the obvious solution, was not practical because it would have delayed the project unacceptably, and so the only alternative available was electrolytic copper. Unfortunately this seriously affects the ability of the system to detect low energy scattered photons, and thus degrades the suppression factors to be expected at high energies. However, the high energy performance of the detector, even without suppression, was acceptable; it is the performance at low energies that is critical. Thus it seems more important to avoid placing any additional

sources of activity close to the central detector than to optimise high energy suppression, and so a thin electrolytic copper can has been used. All the other parts of the encapsulation, such as support flanges, are also copper, except for the photomultiplier spinnings, which are thin aluminium. It was not felt to be worthwhile replacing the photocathode windows with potassium free quartz.

A cross section of the completed detector assembly is shown in figure 6.3.4.

6.3.6 Electronics

A block diagram of the electronics is shown in figure 6.3.5. The germanium detector signal is fed to a preamplifier with FET input (type RG11, Princeton Gamma Tech). This in turn drives a Tennelec 205A spectroscopy amplifier. The amplifier output feeds a Tracor TN-1211 50 MHz analogue to digital convertor. The semiconductor memory has 8,192 channels, and the analyser is set up to cover the energy range 0 to 1500 keV, at a conversion of about 0.18 keV/channel.

The high voltage for the germanium detector is provided by a Brandenberg Alpha Series II high tension supply, model no. 2507. The memory is accessed by a microprocessor and data fed to one of three output facilities.

(a) To a monitor display, which in addition to the spectrum, shows the counts in a channel of interest, the elapsed 'live' counting time, and the total counts in a variable integration area.

(b) To a fast paper tape punch, which will output up to five regions of interest, or the entire memory store.

(c) To a chart recorder or X-Y plotter, which plots the area currently displayed on the monitor display.

The anti-Compton guard crystal is viewed by six EMI 9843B photomultiplier tubes, each of which has a variable resistor in the dynode chain to allow gain matching. The centre plug has an EMI 9656 KB tube, which is similarly gain matched. The seven photomultipliers are fed to an interface panel which allows the output of each tube to be examined separately without disconnecting the common high voltage supply, (Harshaw NV-25A). This parallel output feeds the guard input of a

Figure 6.3.4 Detector and anti-Compton guard ring

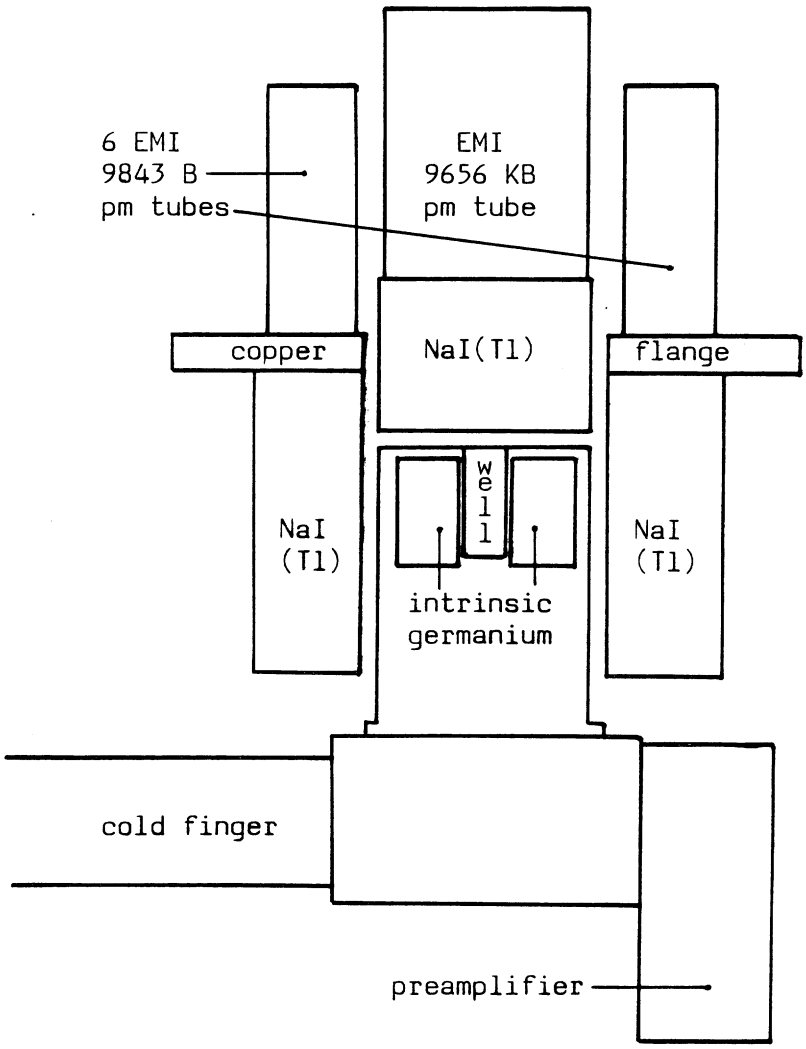

Figure 6.3.5 Block diagram of electronics

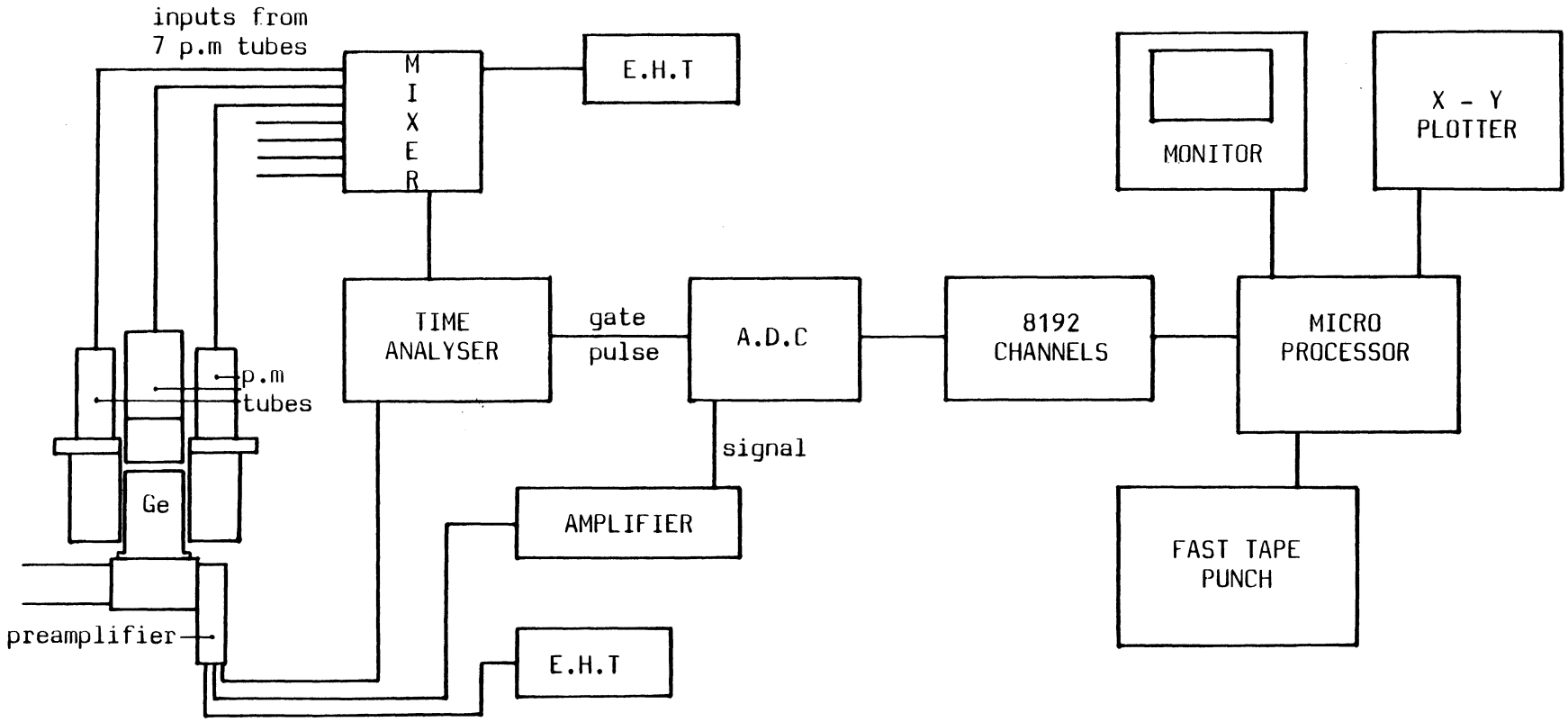

Harshaw NC-26R anti-Compton analyser; the central detector input is taken direct from the germanium preamplifier. The output of the NC-26R is used to gate the A.D.C. directly.

All of the electronics were set up and operated as described in the operator manuals. Only those points of particular interest will be discussed in later sections.

6.3.7 Reduction of data

Usually the entire 8,192 channels are punched out on paper tape. This is loaded into filestore at the University Computing Centre, where analysis is performed using 'SAMPO', an existing FORTRAN program for computer analysis of gamma spectra, (ROUTTI, 1969; ROUTTI and PRUSSIN, 1969). The use of this program is discussed briefly in Appendix A, and some examples are given. It is sufficient here to point out that it determines the energy of a gamma peak, and the area under the peak, both with associated error estimates.

6.3.8 Sample geometry

All samples to be counted were packed into a polypropylene tube and capped with a thin aluminium disc (see figure 6.3.6). To reduce the risk of contamination of the well, especially with Rn-222 daughters from active samples, this was followed by a silicone rubber sealant (Dow Corning) and finally a push fit polypropylene cap. The sample volume was 4.18 cm^3. Each end of the tube was then labelled, with sample number and weight. The intention behind this encapsulation was to keep the sample volume fixed, so that the sample weight would be a direct measure of the bulk density. In practice the wall thickness (1.1 mm) was not sufficient to ensure constant diameter, but the effect of the small variation in volume because of the expansion of the tube as it was packed is not considered to be important, in view of the excellent reproducibility (1%) obtained from active samples, where other errors become small. The maximum variation in sample weight observed has been from about 5.0 g, for fine ground pottery ($<250\ \mu m$) to 10.5 g for a solid calcite plug. In general, however, the range was between 6.0 g and 8.5 g. These correspond to bulk densities of 1.4 g cm^{-3} and 2.0 g cm^{-3} respectively.

Figure 6.3.6

Dimensions of standard sample container

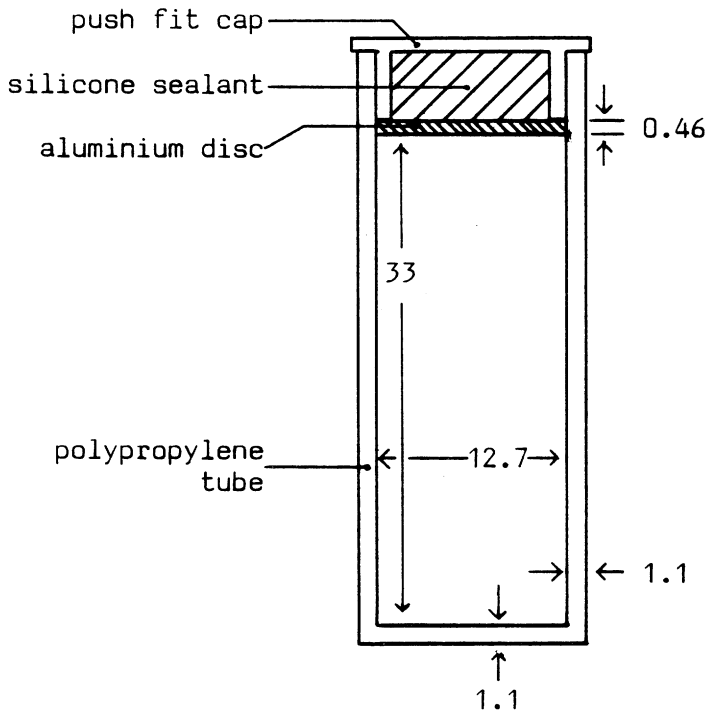

Note: 1) all dimensions in mm.

2) sample volume is 4.18 cm^3.

6.4 SPECTROMETER PERFORMANCE

The performance characteristics of the spectrometer may be considered in two stages; the resolution and efficiency of the detector itself, and the response of the complete system. The latter includes discussion of backgrounds and Compton suppression.

6.4.1 Resolution

With the detector bias at the manufacturer's recommended value of 2500V, and with optimum amplifier settings, the resolution (full width at half maximum, FWHM) at 1332 keV (Co-60), for a point source 47 cms from the front face of the can of the detector was 2.73 keV, full width at tenth maximum (FWTM) was 5.02 keV and the peak to Compton ratio was 23.6/1. The detector bias was then varied, and the resolution measured, (see figure 6.4.1). A slight improvement at 2300V was observed, and this was adopted as the bias setting for further work. Figure 6.4.2 shows the FWHM as a function of energy for a distributed source filling the well. The sources used are described in Appendix B.

The final resolution of 2.65 keV FWHM is poor compared with the specified figure of better than 2.4 keV. This is due to the manufacturer's difficulty in obtaining good quality 'hyper-pure' material.

6.4.2 Efficiency

The manufacturer specified the efficiency of the detector as 15% at 1332 keV relative to a 3 inch x 3 inch NaI crystal, with a source/detector distance of 25 cm. Although useful for comparison with other systems, this figure is meaningless for the intended geometry. The efficiency of the detector has been measured with uniformly distributed sources contained in the standard polypropylene sample holders, (see figure 6.4.3). The sources used are those described in Appendix B.

However, it is important to realise that this type of curve cannot be used for accurate determination of any but those isotopes with very simple decay schemes, such as Cs-137. This is an unfortunate side effect of the very large solid angle subtended by the detector at the source, and will be discussed in more detail in section 6.5 on calibration.

Figure 6.4.1 Variation of detector resolution with bias voltage

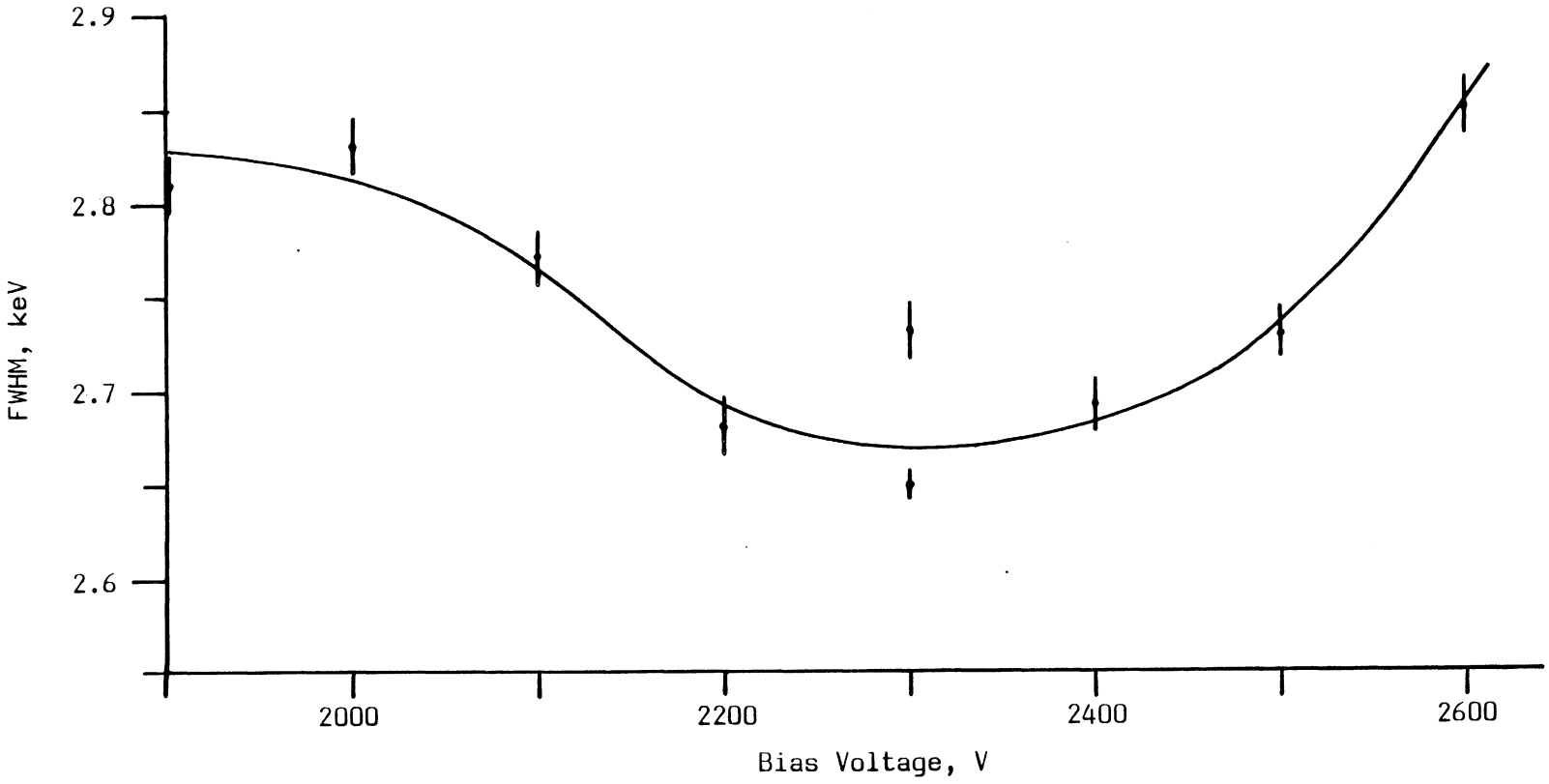

Figure 6.4.2 Variation of spectrometer resolution with energy

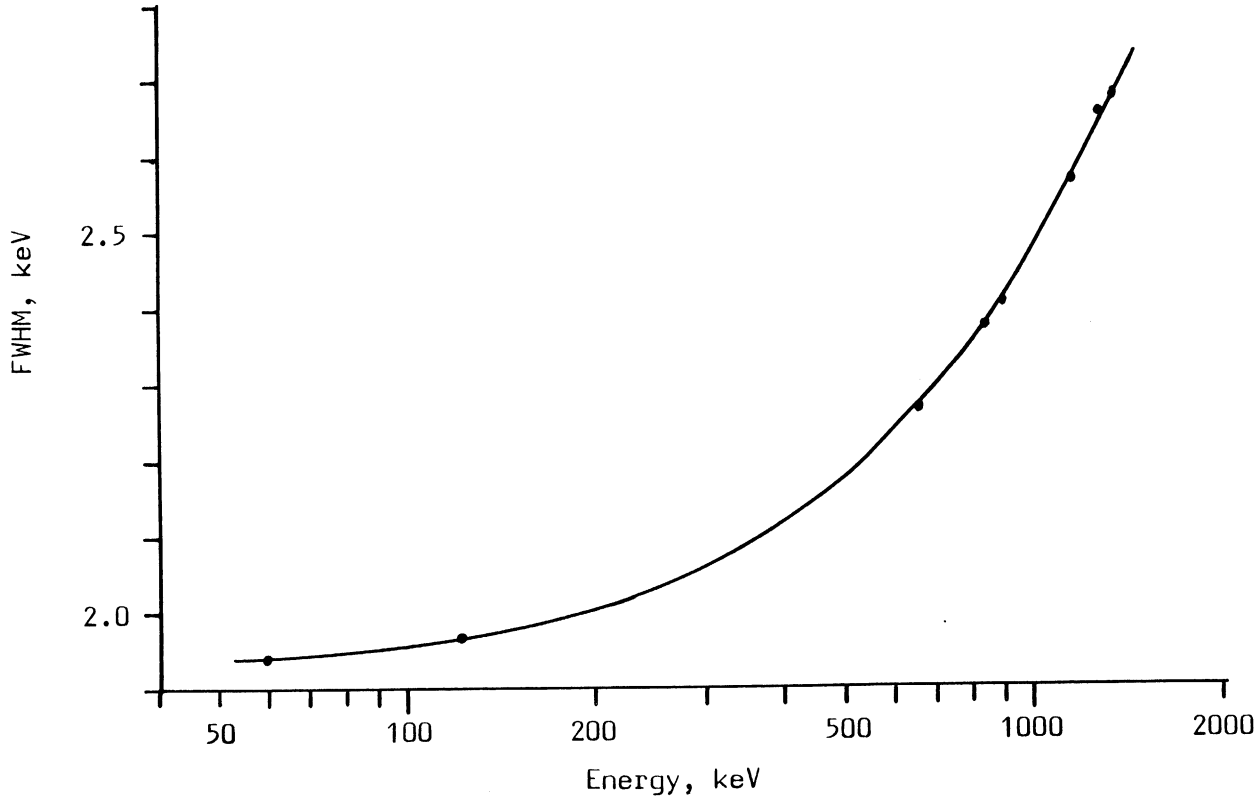

Figure 6.4.3 Variation of absolute efficiency with energy

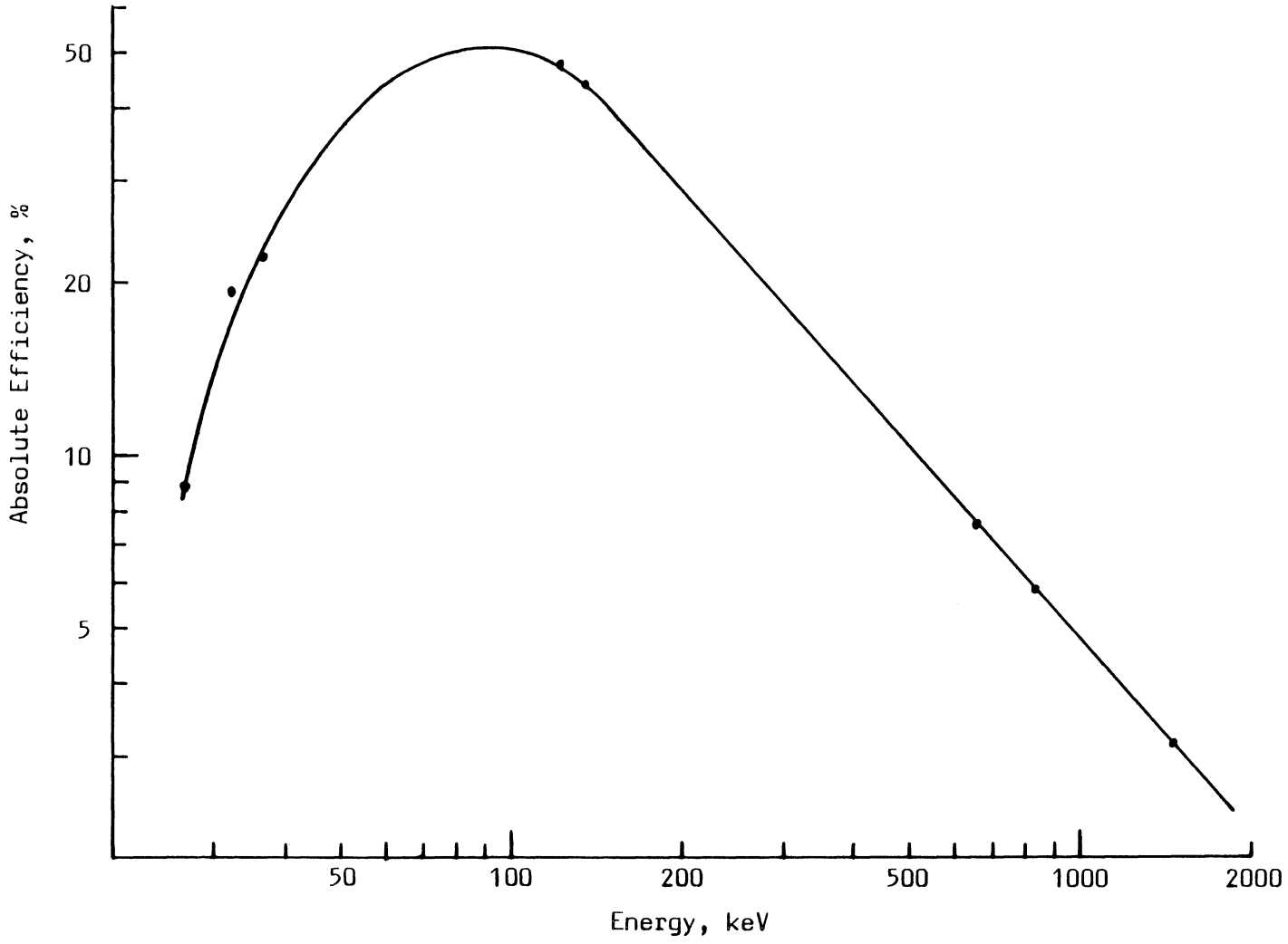

6.4.3 Compton Suppression

The effect of the anti-Compton shield on a point source Mn-54 spectrum can be seen in figure 6.4.4. The source was placed at the geometric centre of the well. At low energies the reduction in the Compton continuum is a factor of 2, as was predicted, at higher energies, however, it is very much less than was predicted (a factor of 3.6 instead of 15). This implies that a larger proportion than expected of the lower energy gammas escaping from the germanium are not being detected by the guard ring, probably because they interact with the relatively large amounts of 'dead' material surrounding the well, especially the copper can of the NaI(Tl) crystal, a possibility that was mentioned in section 6.3.4. Nevertheless, it is at low energies that the reduction in continuum is needed, and this has been satisfactorily achieved. Figure 6.4.5 shows two spectra, with and without suppression, for a Mn-54 source distributed uniformly in a finely ground mineral matrix (dunite, <200 μm).

6.4.4 Background

Figure 6.4.6(a) and figure 6.4.6(b) present a background scan with the detector surrounded by the lead castle and the NaI(Tl) shield. The coincidence detection circuitry was in use, and the well was empty. The various low energy peaks are presumably due to impurities in the shield detector, canning material, and the air inside the lead shield. (The count time was 85 ksec.)

It is not necessary to determine the background continuum accurately, using a completely inert material of the appropriate density, because the detector resolution permits this determination from the spectrum directly. However, we do need to accurately determine the intensity of interfering peaks in the background. These intensities will be slightly affected by material in the well. If some of the background impurities are contained within the walls of the well, then a sample in the counting position will scatter the gammas from these impurities predominately out of the photopeaks, although there will be some elastic scattering. Higher energy gammas from outside the well, which have passed through the detector without interacting may also be scattered elastically, to enter the germanium and be detected. Thus

Figure 6.4.4

Effect of anti-Compton guard ring on a Mn-54 spectrum: point source

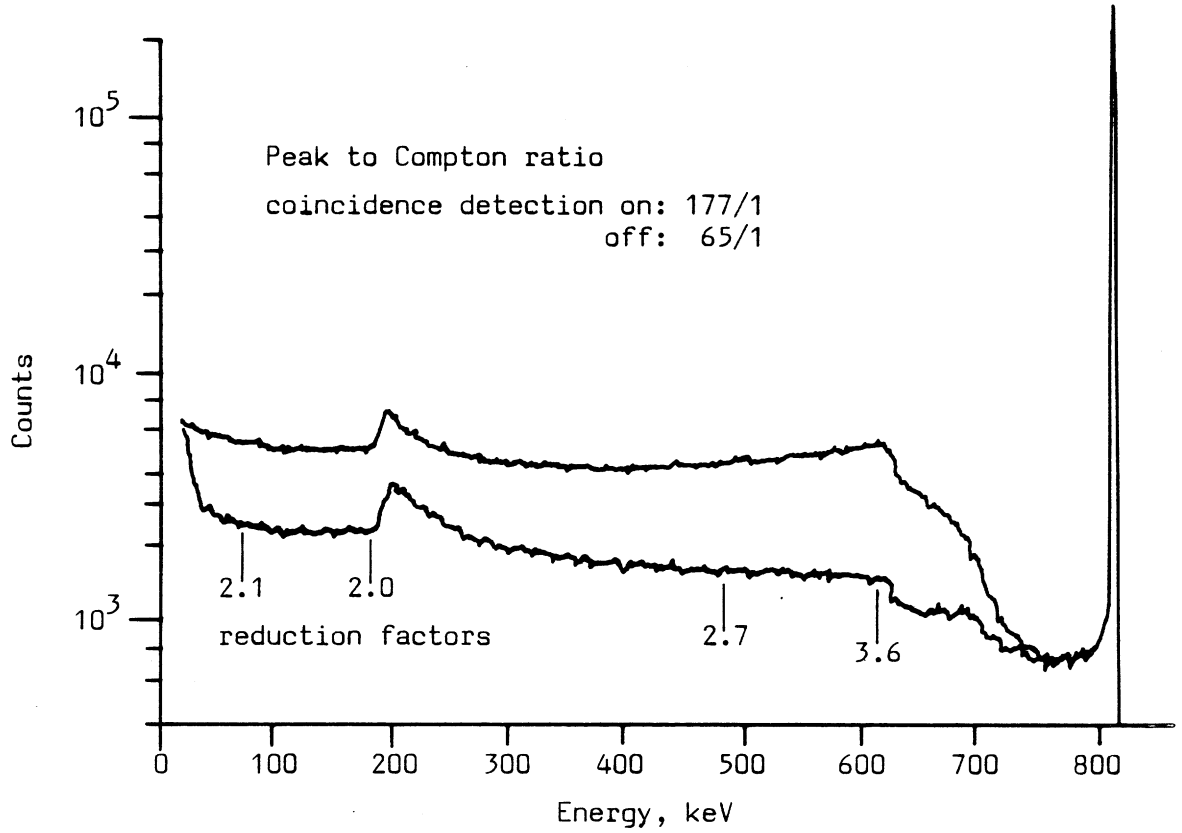

Figure 6.4.5

Effect of anti-Compton guard ring on a Mn-54 spectrum: distributed source

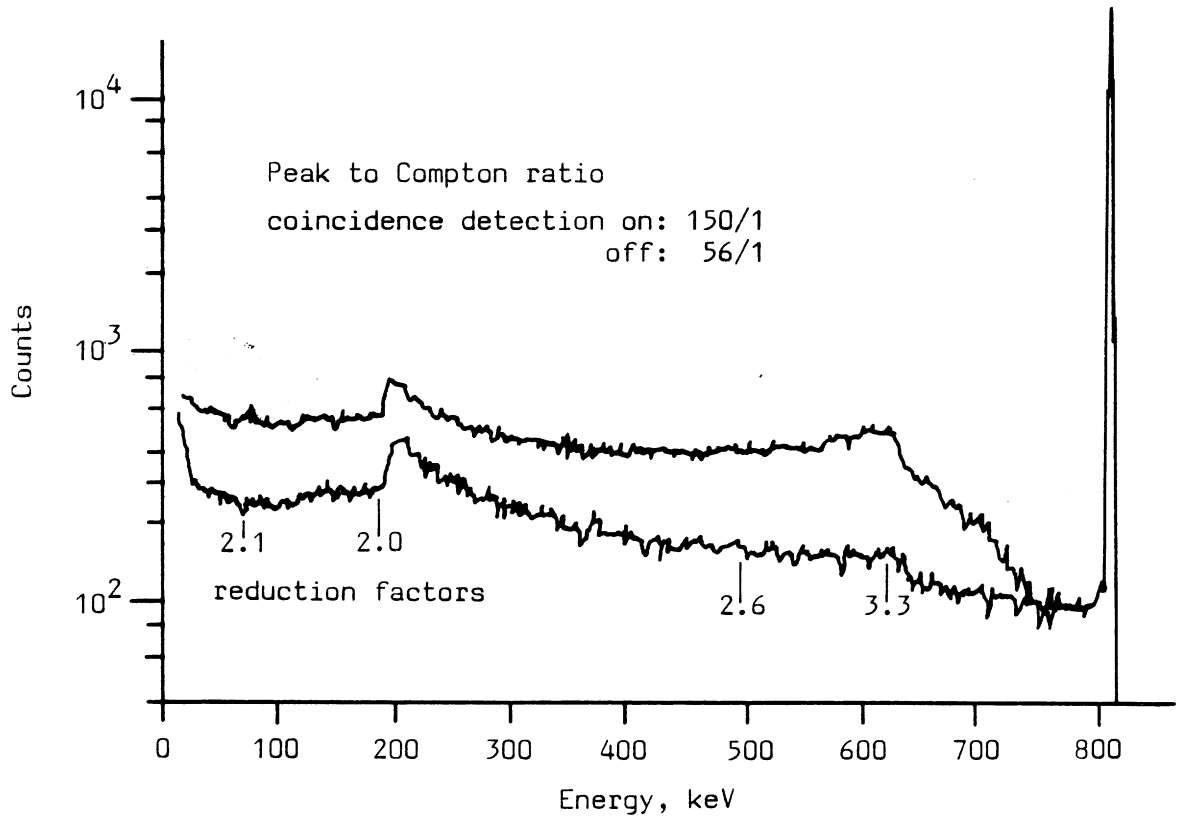

Figure 6.4.6(a)

Shielded background spectrum with detector well empty

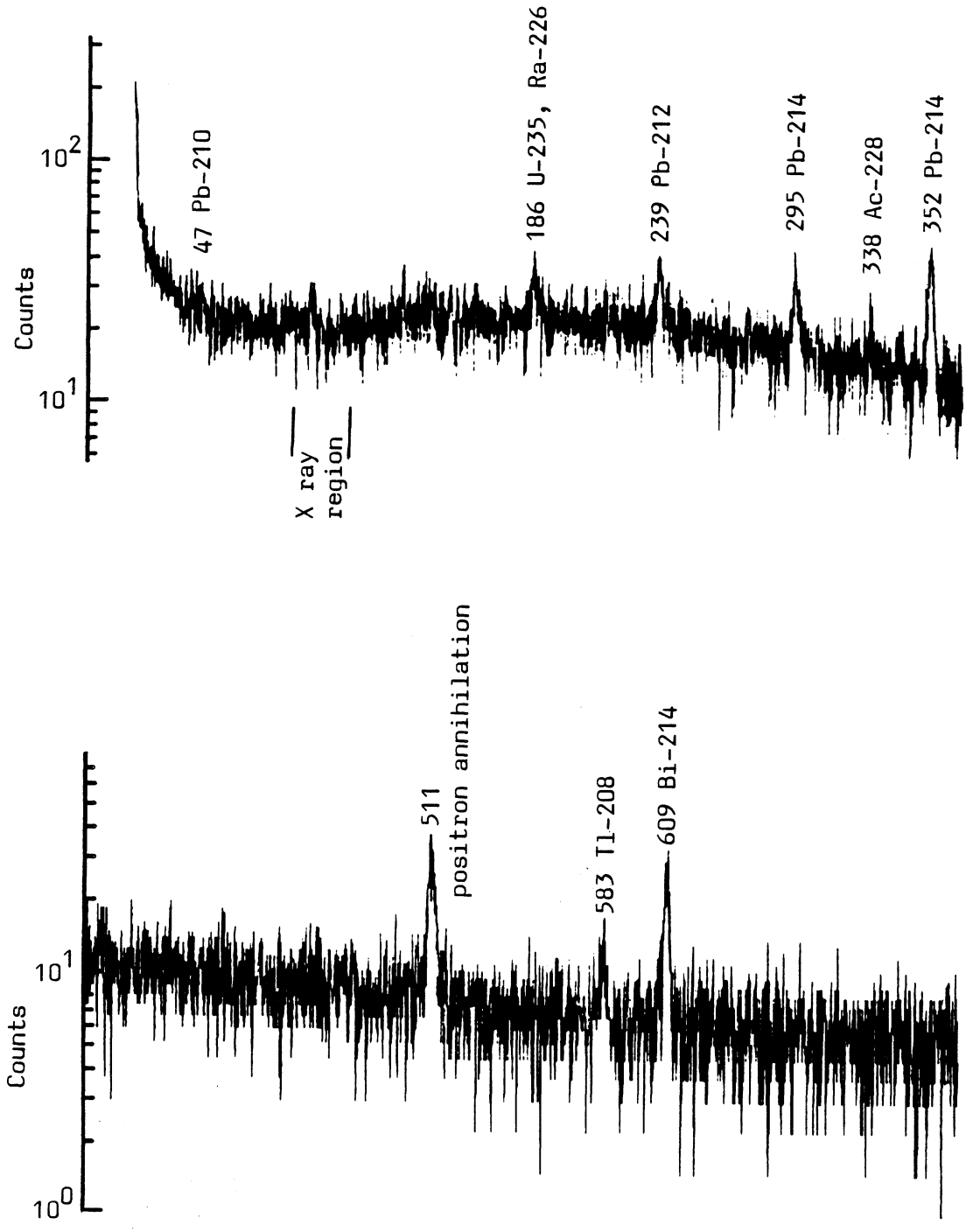

Figure 6.4.6(b)

Shielded background spectrum with detector well empty (cont.)

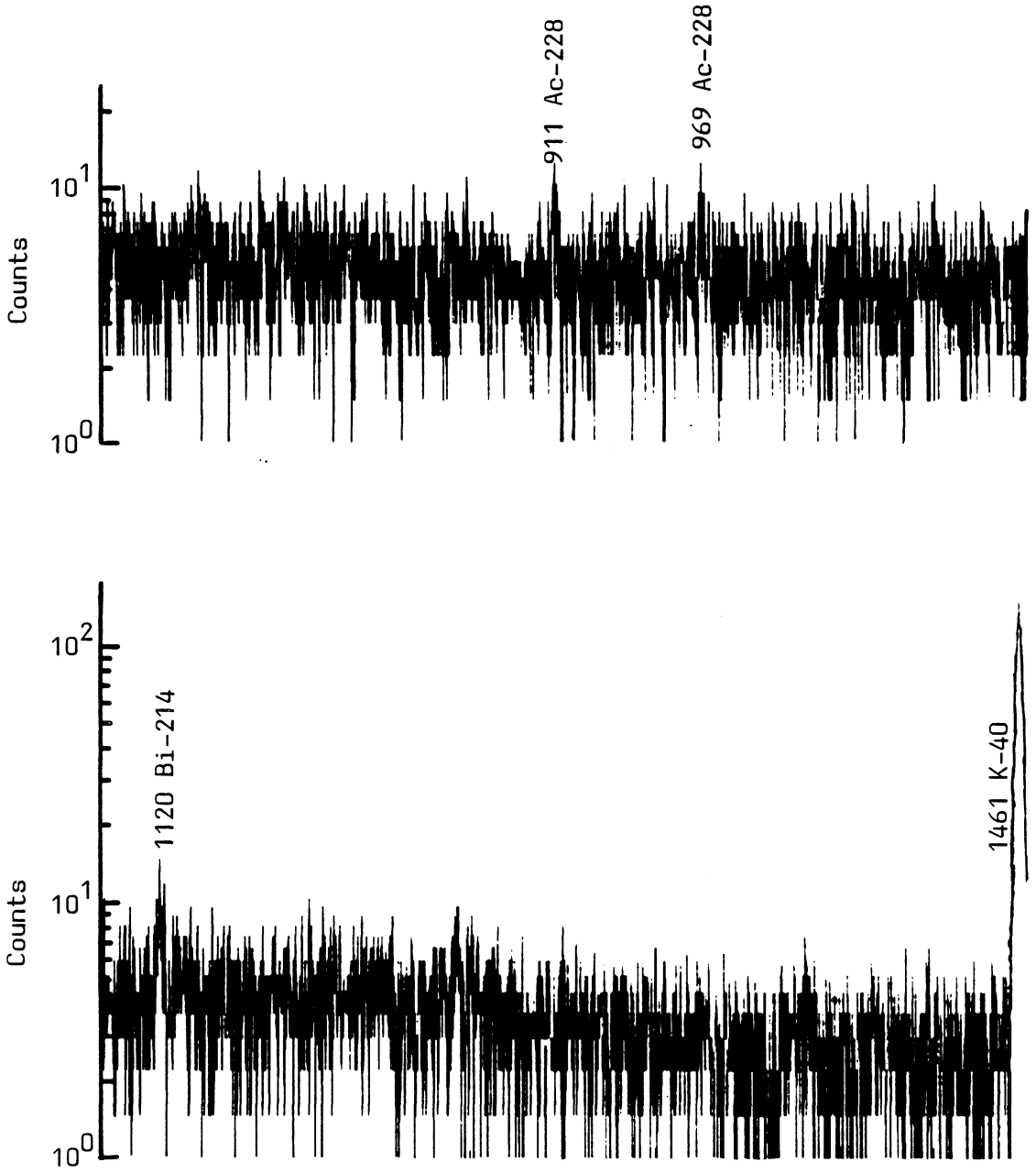

it is desirable to determine the background peaks with an appropriate inert material. Figure 6.4.7 shows background scans with and without anti-coincidence detection using 6.5 g of 'Analar' sodium hydrogen carbonate ($NaHCO_3$) in the well, packed in the standard geometry. This compound has a guaranteed potassium content of less than 0.01%, and an alpha count rate of less than 0.1 $ksec^{-1}$. The continuum reduction of about a factor of 2 at 63 keV compares well with that predicted earlier. Again, the high energy reduction (a factor of 1.7 at 1000 keV) is not as large as was hoped for.

With the exception of some of the lines derived from airborne Rn-222 daughters, it is unlikely that the intensity of the peaks in the background would vary with time. The background has in fact been measured five times at intervals of about one month, and no significant variations detected in any peak. Averaged peak intensities determined using 'SAMPO' (see Appendix A) for those peaks which were later found to interfere with peaks of interest in sample spectra are tabulated in table 6.4.1. Although on average these values are lower than those obtained with the well empty, the differences are not significant.

6.4.5 Summary

The resolution and detection efficiency of the detector have been described. Unfortunately the resolution, 2.7 keV at 1330 keV, was not as good as anticipated. The reductions in the Compton continuum and background when the anti-Compton shield is employed are described and are found to be consistent with the expected performance. The reduction in the background at low energies of a factor of 2 is particularly useful. No significant variation was found in the intensities of the peaks in the background spectra, over a period of about five months.

6.5 SAMPLE NORMALISATION PROCEDURES

Before the calibration procedures can be considered, the problems of normalisation of sample weight and composition must be discussed. It is to be expected that the bulk densities of both soils and potteries will vary considerably, and so the amount of sample packed into the constant volume sample container described in section 6.3.8 will also vary. Thus some normalisation technique is mandatory.

Figure 6.4.7(a)

Shielded background spectra with 6.5 g of inert sodium hydrogen carbonate in well

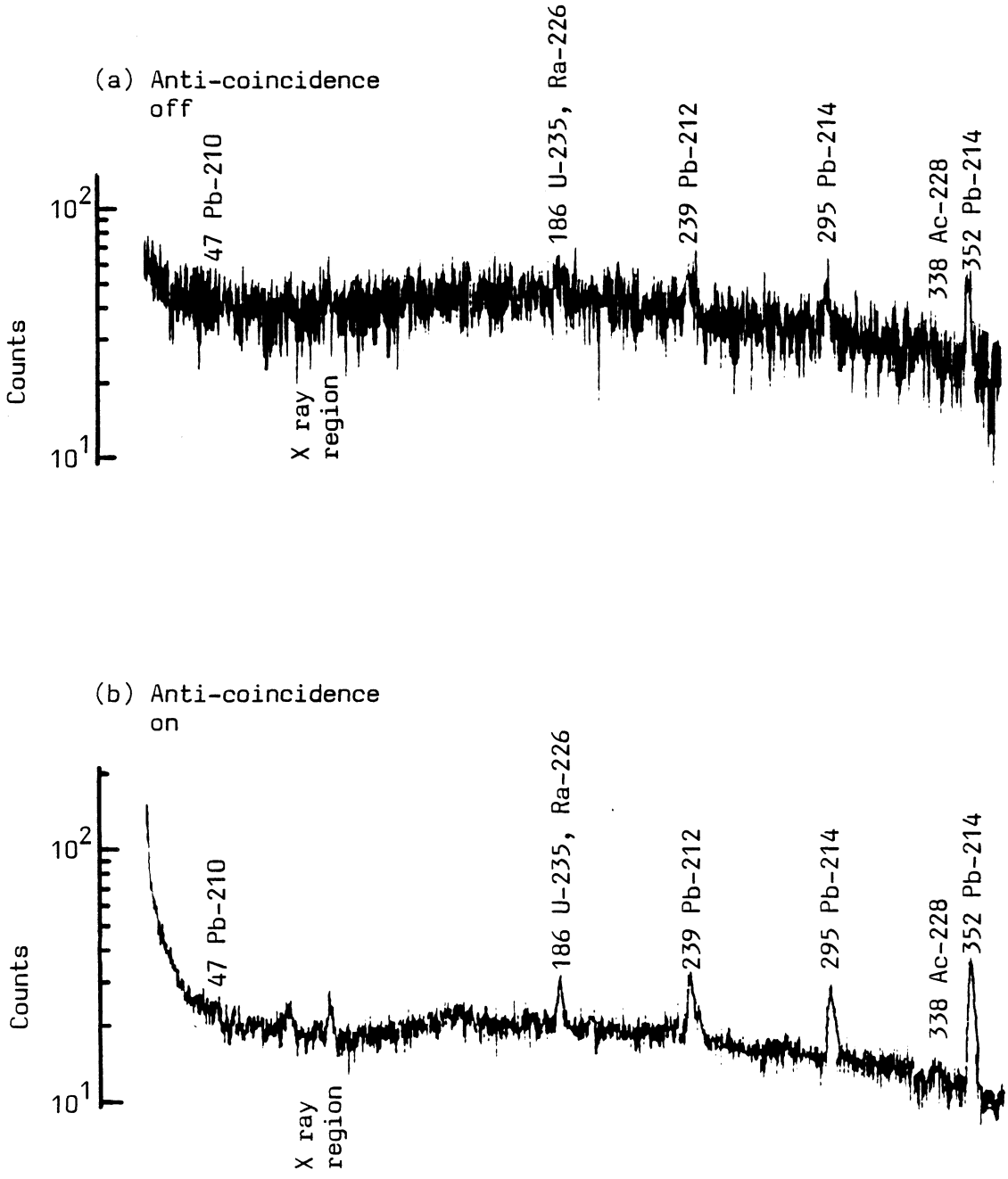

Note: (a) was counted for 85 ksec, (b) for 650 ksec. Both are normalised to 85 ksec in the above.

Figure 6.4.7(b)

Shielded background spectra with 6.5 g of inert sodium hydrogen carbonate in well (cont.)

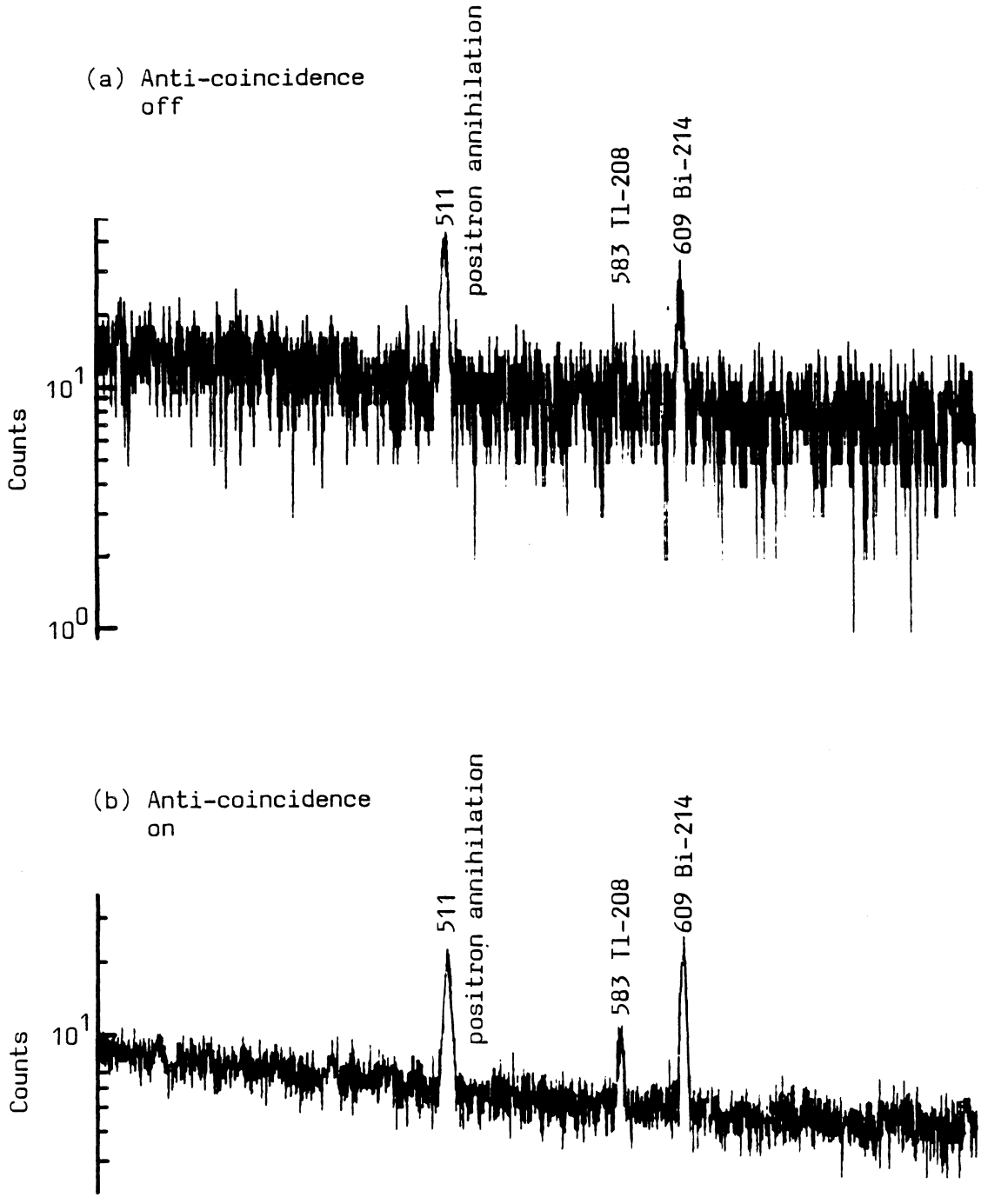

Note: (a) was counted for 85 ksec, (b) for 650 ksec. Both are normalised to 85 ksec in the above

Figure 6.4.7(c)

Shielded background spectra with 6.5 g of inert sodium hydrogen carbonate in well (cont.)

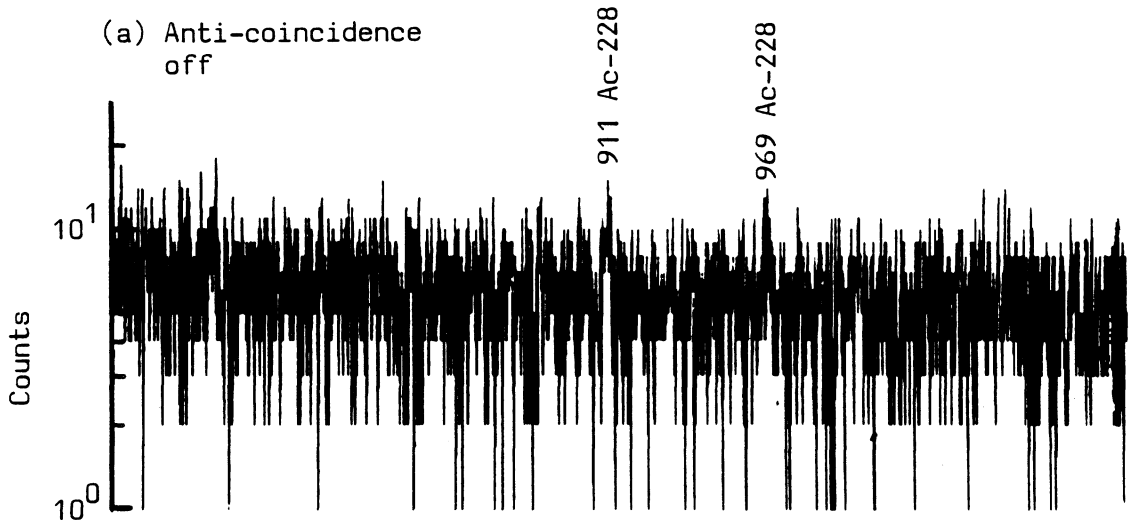

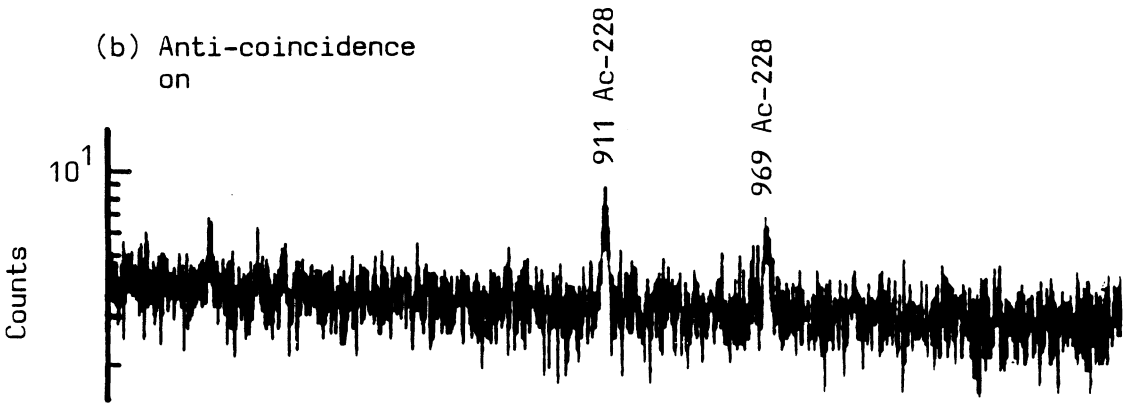

Note: (a) was counted for 85 ksec, (b) for 650 ksec. Both are normalised to 85 ksec in the above.

Figure 6.4.7(d)

Shielded background spectra with 6.5 g of inert sodium hydrogen carbonate in well (cont.)

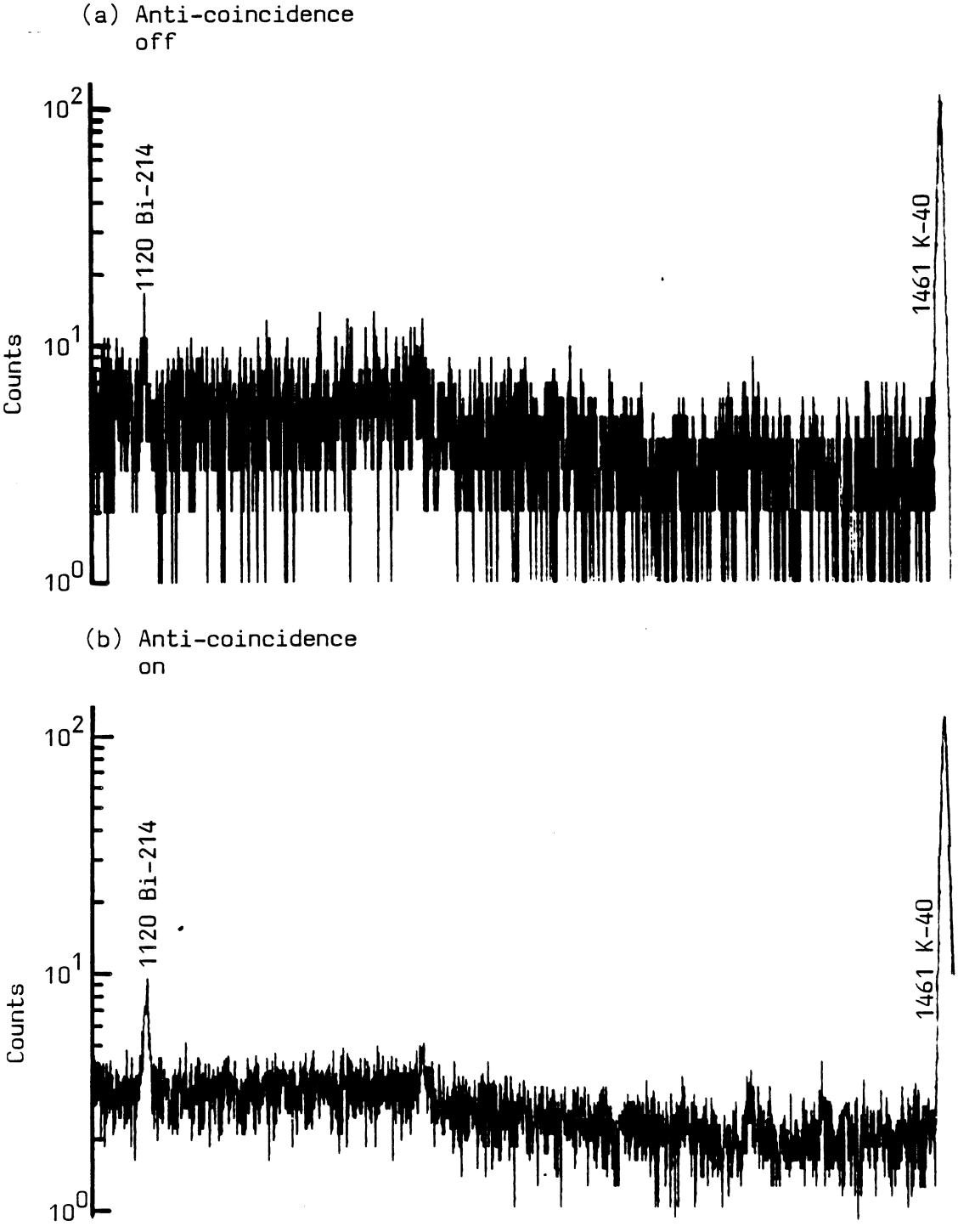

Note: (a) was counted for 85 ksec, (b) for 650 ksec. Both are normalised to 85 ksec in the above.

Table 6.4.1

Background peak intensities

Group	Long lived isotope	Emitting isotope	Energy keV	Count rate $ksec^{-1}$
1	U-238	Th-234	63	0.20 5
			92.5	1.06 11
	U-235	U-235	186 (+ Ra-226)	1.40 15
3	Th-230	Th-230	68	0.05 5
4	Ra-226	Ra-226	186 (+ U-235)	1.40 15
5	Rn-222	Pb-214	242 (+ Ra-224)	1.2 4
			295	2.17 16
			352	4.20 23
		Bi-214	609	3.40 20
6	Pb-210	Pb-210	46	0.6 2
7	Th-232	Ac-228	338	0.4 1
			911	0.8 1
			969	0.5 1
		Ra-224	242 (+ Pb-214)	1.20 15
8	Rn-220	Pb-212	238	2.2 3
		Tl-208	583	0.89 14
	K-40	K-40	1461	24.8 5

Note: errors shown are in the least significant figures

6.5.1 Sample Self Attenuation

FITZGERALD et al (1967) deal explicitly with the self attenuation of a uniformly distributed cylindrical source, but the solution is approximate. Nevertheless it can be shown using this solution that the gamma flux, I, at measurement points close to the side wall of the cylinder can be approximately described by

$$I = C\, I_o e^{-g\mu} \qquad \text{- - - - - - - - - 1}$$

where

I_o is the emitted intensity per unit volume,
μ is the linear attenuation coefficient of the source material,
C and g are constants.

This relationship is only valid if the product of the attenuation coefficient and the cylinder radius is less than 0.7. As the value of μ for pottery increases to about 0.7 cm^{-1} at 46 keV (see section 6.5.4) and the cylinder radius is 0.64 cm, the condition is easily satisfied down to at least this energy.

However, μ is the product of the mass attenuation coefficient (μ/ρ) which is strongly element dependent at low energies, and the bulk density of the attenuating medium. As the sample holder is of constant volume, equation (1) may be written

$$I = C\, I_o \exp\left(-\frac{g}{v}(\mu/\rho)m\right) \qquad \text{- - - - - - - 2}$$

where

m is the sample weight
v is the volume of the sample holder (4.18 cm^3 from section 6.3.8).

In order to normalise between samples of different weights or elemental compositions, the mass attenuation coefficient and the geometrical constant g must be known or determined. As the elemental composition of pottery and soil is not usually known, this is not necessarily straightforward.

6.5.2 Typical elemental composition of pottery and soils

(i) Pottery

Because of the synthetic nature of ceramics the constituents have,

to some extent, been artificially selected, and it has been found that the major atomic components of archaeological ceramics show a degree of uniformity worldwide. HATCHER (private communication) suggests the concentrations shown in table 6.5.1 as typical, based on analyses of about one hundred predominantly European sites.

For various technological reasons it is frequently necessary to add materials to the clay before firing. Sand, limestone, iron bearing minerals or even crushed sherds, have all been used as additives (RADO, 1969). Thus it is possible to find sherds with variations of up to 100% in the calcium and iron content, although these concentrations usually vary inversely because both of these elements act as fluxes, and an excess makes the pottery difficult to fire. In addition, aluminium and silicon will replace each other to varying degrees depending on the type of clay mineral present, although the sum of these two elements does not usually vary strongly.

(ii) Soil

It is recognised that all materials making up the lithosphere can be traced back to igneous rock minerals (PATON, 1978) and so in considering the likely elemental composition of a burial context the major elements contained in igneous rocks, shown in table 6.5.1, are relevant. Considerable information is available concerning the major element concentrations in soils. However, this is of limited use here because the material analysed tends to be from the top few centimetres of topsoil, and is usually only from areas of agricultural interest. The average concentrations for a range of soils, derived by LEEPER (1964) from the literature, are also shown in table 6.5.1. It is expected that most archaeological sites will have element concentrations broadly similar to the rock and soil figures given. For the purposes of discussion in later sections, the typical context is taken as the average of these two sets of figures.

In addition, carbonaceous material will always be present to some degree, typically less than 5% in the topsoil, and less at greater depths, (BUCKMAN and BRADY, 1960). Of this 5%, about 2% is carbon and 2% oxygen. Thus the effect on the major element concentrations is negligible, unless the burial context is such that there has obviously been an unusual concentration of decay resistant organic matter, such as wood.

Table 6.5.1

Typical concentrations of major elements in pottery, crustal rocks and soil

Element	Pottery[2] %	Rock[3] %	Topsoil[4] %
O	47	45	50
Si	28	27	36
Al	10	8.0	6.9
Ca	7 ± 7	5.1	0.5
Fe	3 ± 3	5.8	3.5
Mg	3 ± 3	2.8	0.4
K	2 ± 2	1.7	1.5
Na	1 ± 1	2.3	0.6
Ti	1 ± 1	0.9	0.6

Note: 1) percentages are by weight

2) the errors given encompass the range of concentrations found by HATCHER (private communication)

3) from KAYE and LABY (1973)

4) from LEEPER (1964)

6.5.3 Mass attenuation coefficients of pottery and soils

Using the mass attenuation coefficients for individual elements tabulated in EVANS (1968b), and assuming the Bragg additivity rule, i.e.

$$\overline{(\mu/\rho)} = \sum_i (\mu/\rho)_i \, w_i$$

where

$(\mu/\rho)_i$ are the attenuation coefficients of the 'i'th element at a particular energy.

w_i is the fraction by weight of the 'i'th element and

$\overline{(\mu/\rho)}$ is the average mass attenuation coefficient for the mixture at a given energy, it is possible to calculate the average coefficients of such mixtures of elements as were presented earlier. Figure 6.5.1 shows such characteristics for the 'typical' pottery and soil from table 6.5.1 and for silica (SiO_2). The curve for an 'atypical' potsherd containing 13% calcium and 6% iron by weight (i.e. twice the typical figures) is also shown.

No element concentrations of less than 1% have been included. At these levels only very heavy elements would have a significant effect on the attenuation characteristics, and such concentrations do not occur except near ore deposits - and of course in pottery glazes, which are readily identified.

It is to be expected that the characteristics of silica and 'atypical' pottery easily encompass the range of variation in normal potsherds and soils; for the majority of samples the reduced limits used in the next section are more likely. These limits are displayed in figure 6.5.1 as a band around the 'typical' attenuation characteristics, and from this it is expected that most matrices analysed should have a range of about $\pm$ 15% in the value of the mass attenuation characteristics at low energy (40 keV). This range falls to only 8% at 60 keV, and less than 1% by 150 keV.

The sample weights have been found to vary from about 5.5 grams up to about 8.0 grams for pottery and soil, although weights of up to 9 grams

Figure 6.5.1 Mass attenuation characteristics of various materials

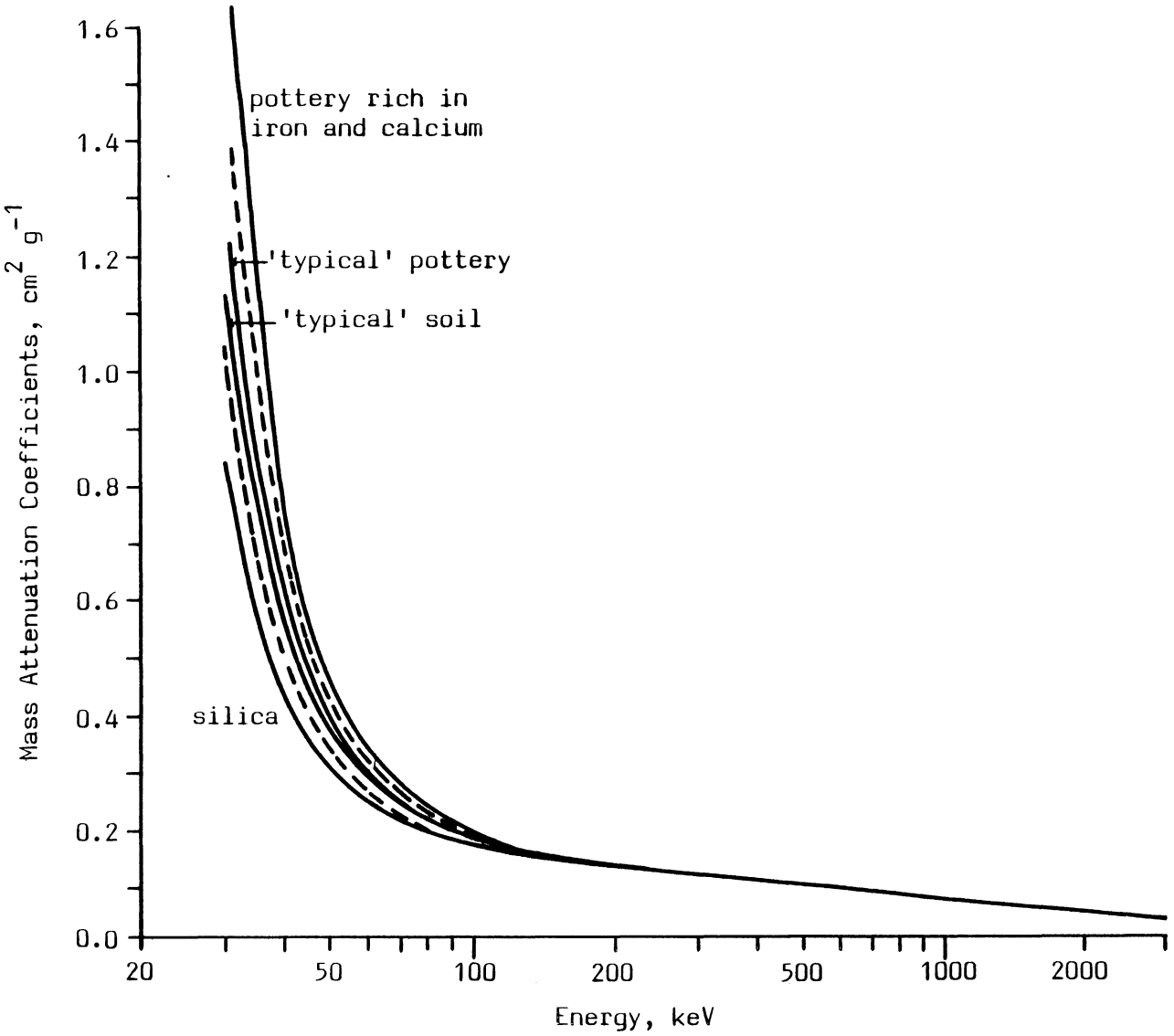

have been found for crushed dunite. The nett effect of these two sources of variation in the linear attenuation coefficient is determined experimentally in the next section.

6.5.4 Evaluation of variations in sample self attenuation with sample weight, using a range of elemental compositions.

Two materials of very different bulk densities were used in the initial stages of this study. The first, a black Romano-British sherd (site reference, 69 pot 18), the second, a coarse ground dunite, supplied by the New Brunswick Laboratories, U.S. Department of Energy; this is the same material as used to dilute the standard NBL uranium and thorium ores discussed in the next section. BOWMAN (1976) after discussion with NBL, assumed the dunite to be mainly iron silicate (Fe_2SiO_4), and this assumption was used at first in this work. However, it subsequently became clear that this was unlikely and both the pottery and dunite were analysed using atomic absorption spectroscopy for the major elements. The results of these analyses are shown in table 6.5.2. The calculated mass attenuation coefficients for dunite are indistinguishable from those calculated for typical pottery, shown in figure 6.5.1. The mass attenuation coefficients for the pottery, 69 pot 18, are calculated to be about 5% higher at 40 keV and within 1% above 80 keV.

About 30 grams of each of these materials was then doped with a solution of seven radioisotopes, emitting X and gamma rays over the whole energy range of interest (see Appendix B). Table 6.5.3 lists the activities of the various isotopes used after dispersion in the two matrices, with the energies of the peaks studied taken from Appendix B. Note that these activities are not identical with those of table B.1, because of half life corrections. These two materials were packed into three sample holders, two containing the doped pottery matrix, one the dunite, and then counted. The weights of these samples are also given in table 6.5.3.

Partly to extend the range of sample weights, and partly to ensure that the range of element concentrations analysed was representative of the variations likely to be encountered, three further samples were prepared, two by mixing the pottery and dunite matrices with silica flour, and one by mixing calcium carbonate with the pottery matrix. The calculated element compositions of these three samples are listed in

Table 6.5.2

Analysis of Romano-British sherd 69 pot 18, and NBL dunite

	69 pot 18	Dunite
	% by weight	
O	47.4	49.5
Si	31.3	38.5
Al	8.0	0.3
Ca	0.4	0.4
Fe	6.9	6.3
Mg*	3	3
K	1.3	0.3
Na*	1	1

Note: 1) *not analysed, and so typical values taken

2) the concentration of Si is calculated by differences, and that of O by taking all elements in oxide form

3) analyses of Al, Ca, and Fe have been provided by HATCHER (private communication) using atomic absorption spectroscopy, analysis of K by HUXTABLE (private communication) using flame photometry

Table 6.5.3

Calculated isotope activities and energies analysed for doped pottery and dunite matrices

Isotope	Energy keV	Pottery nCi g^{-1}	Dunite nCi g^{-1}
Am-241	26.35 $_5$	0.479	1.185
	59.57 $_5$		
Co-57	122.083 $_1$	0.329	1.232
	134.4709 $_3$		
Cs-137	32.10 $_5$	0.726	2.211
	36.60 $_5$		
	661.65 $_1$		
Mn-54	834.84 $_2$	0.457	1.149
Y-88	898.02 $_2$	0.301	0.914
Co-60	1173.21 $_1$	0.698	2.111
	1332.47 $_1$		
Na-22	1247.51 $_3$	1.384	2.110

	Pottery/1	Pottery/2	Dunite/1
Weight, g	5.507	6.529	8.497

Note: 1) the weights tabulated are the weights of sample packed into the sample holders

2) the errors in the energies are in the least significant figures

3) further description of these matrices is given in Appendix B

table 6.5.4, as are the weights obtained when packed into sample holders. The major element concentrations of dunite with silica, and pottery with calcium carbonate, give the mass attenuation curves used in figure 6.5.1 to delineate the likely range of sample variation. Note that the bulk densities obtained are strongly dependent on factors such as the range of grain sizes, the grain structure, and the method of packing employed; indeed it was primarily to give a low packing density that silica flour was used.

From section 6.5.1 we can expect the observed gamma intensity, normalised to the radioisotope concentration per gram of matrix, to be exponentially dependent on the sample weight, but only if the variation from sample to sample of the mass attenuation coefficients at appropriate energies is small compared with the variation in sample weight. From figure 6.5.1 it can be seen that this should certainly be true above 150 keV. Figure 6.5.2 shows the observed gamma intensity normalised to isotope activity per gram, on a semi-logarithmic scale, plotted against sample weight for a representative range of energies. It can be seen that over the range of sample weights shown, the data can be approximated by a straight line down to and including 32 keV. Table 6.5.5 gives the slopes of these straight lines, with the associated errors, determined by at least squares fit, at all the energies studied.

6.5.5 Treatment of experimental data

There are two ways to make use of the data presented in the previous section. The simplest is to plot the values of the slopes given in table 6.5.5 against energy. This gives a graph of what can be called the total attenuation coefficient from which values at the energies of interest can be read. These attenuation characteristics can then be used in an equation of the form of equation (1), i.e.

$$I = C' I_o e^{-k'm}$$

where

I is the observed specific count rate, $ksec^{-1}\ g^{-1}$,

I_o is the normalised specific count rate,

k' are the total attenuation coefficients, g^{-1}

m is the sample weight, g

C' is a constant

Table 6.5.4

Calculated concentrations of major elements in three mixtures, given in % by weight

	Dunite and silica	Pottery and silica	Pottery and calcium carbonate
O	51.5	50.1	47.5
Si	42.9	38.5	24.7
Al	0.1	4.3	6.3
Ca	0.2	0.2	8.8
Fe	3.0	3.7	5.4
Mg	1.4	1.6	2.4
K	0.1	0.7	1.0
Na	0.5	0.6	0.9
C	-	-	2.5
Weight, g	4.307	4.104	6.015

Note: 1) element concentrations for pottery and dunite alone are given in table 6.5.2

2) the weights tabulated are those packed into the sample holders

Figure 6.5.2

Variation of observed count rate with sample weight for various materials

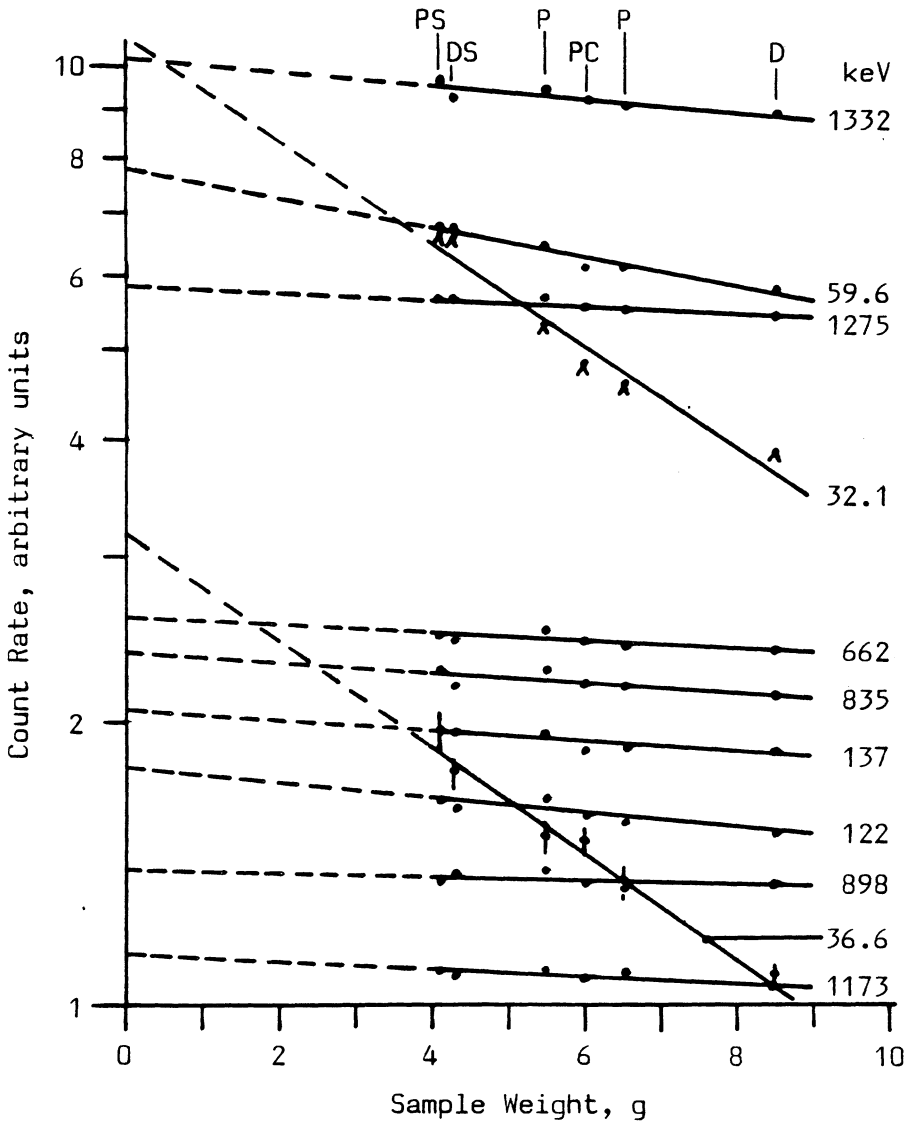

Symbol code:

P	pottery
D	dunite
PS	pottery and silica
DS	dunite and silica
PC	pottery and calcium carbonate

Note: major element composition of these compounds is given in tables 6.5.2 and 6.5.4. The radioisotopes added are listed in table 6.5.3.

Table 6.5.5

Values of the slopes of the straight lines shown in figure 6.5.2

Energy keV	Slope g^{-1}
32.1	0.127_{13}
36.6	0.127_{11}
59.6	0.036_{3}
122.1	0.018_{4}
136.5	0.020_{4}
661.6	0.009_{5}
834.8	0.010_{7}
898.0	0.005_{6}
1173.2	0.010_{4}
1274.5	0.011_{3}
1332.5	0.013_{5}

Note: errors are in the least significant figures, and are obtained from a least squares fit to the data of figure 6.5.2

Such an equation would contain the implicit assumption that the effect of variations in (μ/ρ) from sample to sample is small, which is justified by the good approximation of the data of figure 6.5.2 to straight lines, at least down to 60 keV. However, such a curve would not make full use of the information available. From section 6.5.1, equation (2) was

$$I = C\ I_o \exp(-\frac{g}{v}(\mu/\rho)\ m) \qquad ------- 2$$

In this case an observed specific gamma intensity, I, from a sample of weight m grams and mass attenuation coefficient (μ/ρ) is to be normalised to a standard of mass attenuation $(\mu/\rho)_c$ and mass m_c. Then we may rewrite equation (2) as

$$I = C\ I_o \exp(-k\ m\ (\mu/\rho)/(\mu/\rho)_c)$$

$$= C\ I_o \exp(-k\ m') \qquad -------- 3$$

$$\text{where } k = \frac{g}{v}(\mu/\rho)_c \qquad -------- 4$$

Figure 6.5.3 shows the intensity data of figure 6.5.2 replotted against m', and the slopes of the best straight lines (in the least squares sense) are shown in table 6.5.6. These correspond to values of k in equation (3). A least squares fit of these values of k against known values of $(\mu/\rho)_c$ and v in equation (4) gives

$$g = 0.42 \pm 0.02 \text{ cm}$$

Thus values of k can be calculated at any desired energy using equation (4). We can now derive from equation (3),

$$\frac{I_c}{I} = \exp(-k\ m_c + k\ m')$$

$$= \exp[\ k(m' - m_c)] \qquad -------- 5$$

where I_c is the normalised specific activity.

This equation can now be explicitly evaluated at any energy, provided the attenuation characteristics of the sample are known.

However, in routine radioisotope analysis of pottery and soil samples, it is obviously undesirable (and impractical) to submit each sample for major element analysis as well. Thus, in general,

Figure 6.5.3

Data of figure 6.5.2, after normalising to weights corresponding to samples of the same mass attenuation coefficients

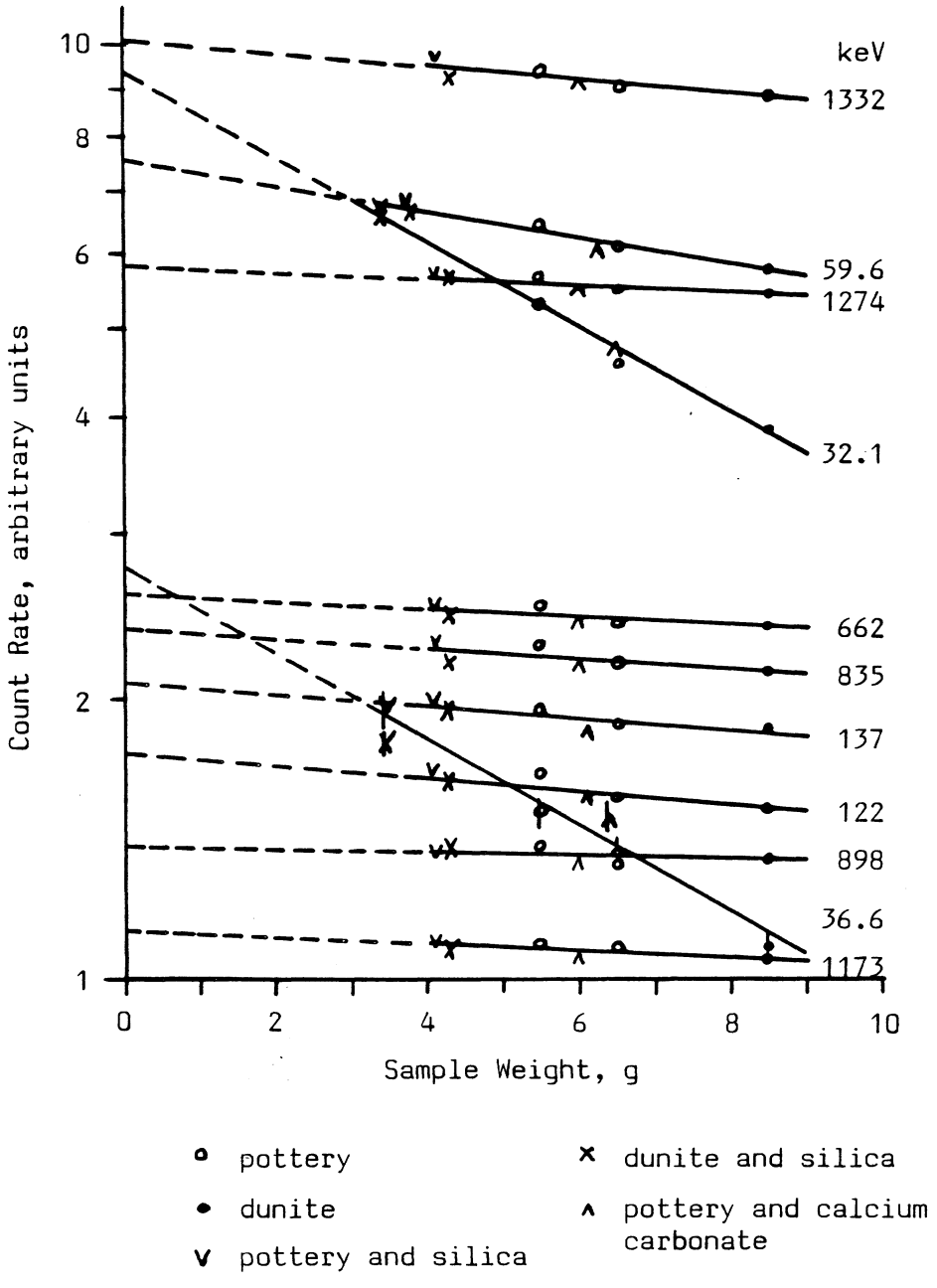

Note: major element composition of these compounds is given in tables 6.5.2 and 6.5.4. The radioisotopes added are listed in table 6.5.3.

Table 6.5.6

Values of the slopes of the straight lines shown in figure 6.5.3

Energy keV	Slopes g^{-1}
32.1	0.110_{4}
36.6	0.100_{20}
59.6	0.034_{3}
122.1	0.019_{4}
136.5	0.020_{4}
661.6	0.009_{4}
834.8	0.011_{5}
898.0	0.008_{6}
1173.2	0.011_{4}
1274.5	0.013_{3}
1332.5	0.013_{4}

Note: errors are in the least significant figures, and are obtained from a least squares fit to the data of figure 6.5.3

equation (5) cannot be used directly, as it requires a knowledge of (μ/ρ) of each sample. It is instructive to consider the likely size of errors introduced by approximating m' with m, the true sample mass. Equation (5) is assumed to give a 'correct' normalisation factor; with m' replaced by m it gives a 'routine' factor. The values obtained for these two normalisation procedures are given at three energies in table 6.5.7 with 7.00 g of 'typical' pottery (table 6.5.1) taken as standard. Samples 2,3 and 4, dunite and silica, dunite, and pottery and calcium carbonate, have the compositions given in tables 6.5.3 and 6.5.4, and are taken to represent the typical spread in sample compositions expected. The weights used are approximately those found in practice. Samples 1 and 5, silica, and pottery rich in Fe and Ca, were suggested in section 6.5.4 as representing the most extreme cases likely to be encountered. Weights for these samples were chosen on the grounds that for low values of (μ/ρ) such as for silica, the biggest discrepancy between the 'routine' and 'correct' approaches will occur for the largest sample weight, and vice versa for the 'atypical' pottery with large concentrations of calcium and iron. Silica flour and quartz grains less than 250 μm were each separately packed into sample tubes and the heaviest weight found was 6.4 g; accordingly, an upper limit of 7.0 g was assumed for silica. As the pottery weights that have been observed have almost all been greater than 5.5 g, this lower limit is taken for the 'atypical' pot.

The effects of the differences of the (μ/ρ) values in the different materials are negligible (less than 1%) above 150 keV, as would be expected from figure 6.5.1. At 46 keV, the lowest energy of interest, the usual range of variation gives errors of about $\pm$ 4%, with extreme values of $\pm$ 10%. These have fallen to $\pm$ 2% and $\pm$ 4%, respectively, by 60 keV. In practice, these errors are acceptable; as will be seen, peak intensities at 46 keV are rarely measured to better than 8% in pottery and soil samples. The high level samples to be discussed in section 6.6.7 were all dispersed in dunite or pottery (69 pot 18), and so the question of uncertainties in (μ/ρ) does not arise. The values of k used for

Table 6.5.7

Comparison of normalisation factors obtained using the 'correct' and 'routine' approach

	1 Silica	2 Dunite and silica	3 Dunite	4 Pottery and $CaCO_3$	5 Pottery rich in Fe and Ca
Weight, g	7.0	4.5	8.5	6.0	5.5
at 45 keV					
'routine'	1.00	0.89	1.07	0.95	0.93
'correct'	0.90	0.85	1.06	0.97	0.98
at 60 keV					
'routine'	1.00	0.93	1.05	0.97	0.96
'correct'	0.96	0.91	1.04	0.98	0.98
at 150 keV					
'routine'	1.00	0.97	1.02	0.99	0.98
'correct'	1.00	0.97	1.02	0.99	0.98

Note: 1) the choice of the weights in columns 1 and 5 is discussed in the text, the weights in columns 2,3 and 4 are those actually found for these materials.

2) above 150 keV the two approaches to calculating the normalisation factors give the same result for all samples, to within 1%.

normalisation in later sections, derived from equation (4) are shown in table 6.5.8 at the energies of interest. The errors shown are based on the experimental errors in $\underline{g}$ at high energies, but below 150 keV they also include the likely errors derived from table 6.5.7 (i.e. $\pm$ 4% at 46 keV and $\pm$ 2% at 60 keV).

6.5.6 Summary

The expected range of sample major element composition has been discussed, and the corresponding values of the mass attenuation characteristics calculated. It has been shown that for given values of the mass attenuation coefficients the observed gamma intensity has an approximately exponential dependence on the sample density. A technique for normalising the observed intensity from arbitrary samples to that observed from a sample of standard composition and weight has been derived, and the effect of assuming the mass attenuation characteristics to be constant from sample to sample discussed. At energies above 150 keV the errors arising from this assumption are negligible; at 60 keV the typical range of samples will produce uncertainties of $\pm$ 2%, and at 46 keV, the lowest energy of interest, these increase to $\pm$ 4%. As other sources of experimental error are usually larger than this, these levels are considered acceptable.

6.6 CALIBRATION

It is impossible to use an efficiency curve, such as that shown in figure 6.4.3, for the accurate determination of the gamma activities of isotopes with complex decay schemes, if there is a large solid angle seen by the sample at the detector. When two photons are emitted in cascade (such as in the decay of Co-60) there is a large probability of detecting some interaction from each of the two photons with such a dectector. As they are often only nanoseconds apart, the detector will be unable to resolve them in time and they will be counted as the sum of two signals. This will result in a count in the sum peak, if both photons are absorbed completely, or a count at any energy up to about 200 keV below this, if one or both the photons are detected by a Compton interaction. Obviously this problem does not only apply to calibrating the detector, but also to using it. The decays of several isotopes in the natural decay chains (e.g. Pb-214, Bi-214, Ac-228) are in cascade and thus the apparent intensities of some gamma rays from these isotopes would not reflect the

Table 6.5.8

Calculated values of k derived from equation 4, with predicted uncertainties

Energy keV	k g^{-1}	Predicted uncertainty
Uranium series:		
46	0.048	0.003
63	0.028	0.001
68	0.026	0.001
92.5	0.019	0.001
186	0.0129	0.0005
242	0.0117	0.0004
295	0.0108	0.0004
352	0.0101	0.0004
609	0.0077	0.0003
1120	0.0060	0.0002
1377	0.0054	0.0002
Thorium series:		
238	0.0180	0.0004
241	0.0117	0.0004
270	0.0112	0.0004
300	0.0107	0.0004
338	0.0102	0.0004
463	0.0090	0.0003
583	0.0081	0.0003
727	0.0074	0.0003
860	0.0068	0.0002
911	0.0066	0.0002
969	0.0064	0.0002
Potassium:		
1461	0.0052	0.0002

real gamma production rate. In principle, these summation effects could be corrected for; DEBERTIN and SCHOTZIG (1978) discuss this problem for a coaxial lithium drifted germanium crystal, and describe an algorithm to evaluate correction factors for arbitrary known decay schemes. The difficulty in evaluating these correction factors would be increased by the use of an anti-Compton guard ring. However, the other approach of calibrating the detector with those nuclides that are to be measured is both easier, and in this case at least, more accurate, as no knowledge of absolute gamma intensities is required.

In general, the attempt has been made here to use absolute standards of known parent isotope concentrations, and, where possible, known equilibrium state. For some parts of the decay chains (Rn-222 daughters, down to Tl-210, and the daughter isotopes of Rn-220) this was not possible, and relative standards were used.

6.6.1 Dispersion procedure for standards

As all of the absolute standards to be described in the following sections were handled in solution, it is appropriate here to describe the procedure adopted to disperse an accurately known quantity of standard uniformly throughout a mineral matrix.

Each standard solution was diluted down to an appropriate level of activity (usually about 10 nCi g^{-1}) in glass volumetric flasks, using the same solvent as was used to prepare the original concentrated solution. Details of those standardised solutions which were provided by the Radiochemical Centre are given in Appendix B. The degree of dilution was calculated from the weights of the components, not the volumes. About 15 g of finely ground (<250 μm) dispersing matrix, either dunite or pottery, was then selected, and 0.5 cm^3 of the dilute solution was dropped onto this matrix in such a manner as to avoid wetting the container. The solution was added to an accurately known weight of dry powder, and the solution weight calculated from the total weight of the wet powder. Thus a known quantity of activity had been entirely transferred to the matrix. This was then evaporated to dryness, (usually about 4 hours at 50°C) and tumbled to distribute the activity evenly. A known weight of this powder was packed into a sample tube as described earlier (section 6.3.8). Usually, four such standards were independently prepared from each dilute solution, two containing about

6 g of pottery, and two about 8.5 g of dunite. The activities of these standards were of the order of a few nanocuries.

6.6.2 Group 1: U-238 and U-235 standards

Although mineral sands of well known uranium content are available (for instance from the U.S. National Bureau of Standards) the state of equilibrium is not always well known. In addition, it is necessary to establish the 'correct' ratio of the U-235 peak at 185.7 keV, compared with the Th-234 peaks at 63.3 keV and 92.6 keV, so that the appropriate correction can be made to the Ra-226 peak at 186.1 keV. This correction was discussed in more detail in section 6.2.2. This can only be done if the two parts of the U-238 decay chain can be measured separately, i.e. if the U-238 (with U-235) and short lived daughters Th-234 and Pa-234 can be separated from Ra-226.

Because of the long half life of Th-230 (80,000 years), any chemically prepared uranium salt will have negligible amounts of Th-230 daughters, including Ra-226. Such salts will be in natural isotopic composition if derived directly from natural minerals (rather than from 'depleted' uranium).

Accordingly uranium nitrate refined directly from uranium ore and supplied by British Drug Houses, was diluted in 2M nitric acid. The purity of the salt was certified as better than 98% ('Analar' salt of natural isotopic composition was not available). For the purpose of calculating the concentration of the solution a composition of $(99 \pm 1)\%$ was assumed. As uranium nitrate, $UO_2(NO_3)_2.6H_2O$, is deliquescent, the salt was placed in a dessicator for a few hours before dilution to minimise the uncertainty in water content. An error of plus or minus half a water of crystallisation was then assumed, to cover the risk of slight degradation of the crystal structure (in fact unobserved). This gave a total uncertainty of 2% in the concentration of natural uranium in the solution.

Using the decay constants given in Appendix E, the final concentration of U-238 in the dilute solution was calculated to be 11.37 nCi g^{-1} $\pm$ 2%. This solution was then dispersed in two pottery and two dunite matrices as described in section 6.6.1.

6.6.3 Groups 2 and 3: U-234, Th-230, Pa-231 standards

Only Th-230 and Th-227, a daughter of Pa-231, have gamma emissions sufficiently intense to be potentially useful, although in practice none of the emissions can be resolved with a useful accuracy in low level natural samples. Even in active standards the 67.8 keV line from Th-230, or for instance, the 256.2 keV line from Th-227, can only be resolved to an accuracy of about 5%. Accordingly, it was considered sufficient to obtain the ratio of the intensities of these two gamma lines to that of Th-234 at 63.3 keV from two US National Bureau of Standards uranium counting standards, NBL 74-A in dunite, and NBL 42-1 dispersed in pottery.

The U-238/Ra-226 activity ratio is known from chemical analysis by the NBS to be in equilibrium to better than 2%. This is confirmed by the independent analyses using the spectrometer reported in section 6.7.1 It is therefore assumed that Th-230 and Pa-231 are also in secular equilibrium in these samples.

6.6.4 Group 4: Ra-226 standard

A standardised solution of Ra-226, supplied by the Radiochemical Centre, Amersham, (see Appendix B) was diluted in 0.5M HCl to a final activity of 12.84 nCi g^{-1}. The estimated total error was 1.5%. This solution was then dispersed into four matrices as described earlier.

6.6.5 Group 5: Rn-222 standard

Radon isotopes, particularly Rn-222 with its 3.8 day half life, are very mobile, and thus difficult to contain reliably. Indeed, the sample tubes are estimated to retain less than 5% of that Rn-222 which is free to escape (see section 6.6.12). In the case of the Ra-226 standard, where all the activity has been deposited on the surface of the grains, the amount of Rn-222 that escapes is likely to be a large percentage of the total produced.

In mineral samples it is possible, in principle, to determine the degree of radon escape using the activity ratio Pb-210/Ra-226. However, this is not reliable if the material has been processed in any way likely to affect the degree of gas escape within the last 100 years, say, (i.e. about four half lives of Pb-210). Nevertheless, by comparing a uranium mineral against the U-238, Ra-226 and Pb-210 absolute standards, it is possible to estimate the maximum degree of Rn-222 escape, if the date of

preparation is known (i.e. when crushed, mixed, etc.) The NBS sand NBL 74-A contains 1000 ppm uranium in a dunite matrix and the maximum likely degree of emanation in this material is about 20%, (see Appendix C), which is clearly not sufficiently close to equilibrium to be used as a standard for radon daughters.

To attempt to reduce this escape to an acceptable level, a mixture of the dunite sand with polyester resin was prepared (0.483 g sand/g total) and poured into a sample tube to set. A small disc of the same mix was also cast (3.256 g total). This sample was placed in a sealed cylindrical cell (a gas cell, see chapter 8), one face of which consisted of a glass disc on which zinc sulphide had been deposited, (DESAI, 1975; AITKEN, 1978b). The sample was placed in a tray such that the only alpha particles able to reach the zinc sulphide were those from escaped radon and daughters; the scintillations from the zinc sulphide were observed by a photo-multiplier tube, and the build up of radon and daughters was followed. A further 1.374 g of loose dunite sand was also placed in a similar gas cell, and the build up of radon and daughters followed again.

After 10.4 days (2.7 half lives of Rn-222) the ratio of the count rate per gram of sand, from the sand in the resin, to the count rate from the loose sand was less than 0.016 ± 0.001. As the loose sand is estimated to emanate less than 20% of the radon produced, (see Appendix C) for the sand in resin this should be reduced to less than $(0.3 \pm 0.15)\%$. This is negligible. Accordingly, the dunite sand cast in resin (7.016 g total) was adopted as a relative standard to give the equilibrium intensity of the Rn-222 daughters compared with that of the Ra-226 parent.

Unfortunately the ratios of the Th-234 peak at 63 keV or 92.5 keV to the U-235 peak at 185.7 keV, which can be derived from the Group 1 standards, are not valid for this sample because the approximations made in the normalisation procedure developed in section 6.5 are no longer valid, as the attenuation characteristics of the dunite/resin mix are very different from any of the materials considered there. Thus a slightly different approach to determining the radium component of the 186 keV peak was employed. This was achieved by counting the dunite sand only, (for which the normalisation procedures do, of course, apply) and determining the fraction of the counts at the 186 keV peak

derived from Ra-226, by comparison with the group 1 standards. This contribution then applies when the material is mixed with resin, and so the ratio of the count rate from the higher energy radon daughter peaks to the Ra-226 count rate was reliably determined, as the resin has a negligible effect on sample self absorption above about 150 keV and thus the normalisation procedures can be used in this region.

6.6.6 Group 6: Pb-210 standard

A standardised solution of Pb-210, supplied by the Radiochemical Centre, Amersham, (see Appendix B) was diluted in 2 M nitric acid to a final activity of 11.90 pCi g^{-1}. The estimated total error was 1.0%. This dilution was in fact prepared with the solution containing the natural uranium described earlier, to reduce the number of calibration samples. (There is no interference between the gamma lines from the short lived daughters of U-238 or U-235 and that from Pb-210 at 46.5 keV).

6.6.7 Group 7: Th-232 standard

Aged thorium nitrate was used for the Th-232 standard. Supplied by the Radiochemical Centre, Amersham, this nitrate was refined in 1906. As the longest lived daughter (Ra-228) has a half life of 5.8 years, this material is easily old enough to guarantee equilibrium at least as far as Rn-220. A chemical analysis of the compound carried out by R.C.C. gives 41.7% thorium. This is very close to the theoretical 42.03% expected from the formula $Th(NO_3)_4.4H_2O$.

A quantity of the salt was placed in a dessicator for a few hours to reduce uncertainties in the water content, and an uncertainty of half a water of crystalisation was assumed. From the impurities listed in Appendix B, it can be seen that an uncertainty of 1% in the chemical purity is generous. Combining these two uncertainties gives a total error of 2%.

The salt was dispersed in 2M nitric acid, to give a solution of 3.28 nCi g^{-1} of Th-232. This was dispersed in the usual manner, to give one pottery and one dunite standard. A second solution of 3.32 nCi g^{-1} was also prepared, and dispersed to give two further standards.

6.6.8 Group 8: Rn-220 standard

Although the half life of Rn-220 is sufficiently short (55.3 seconds) for significant escape from the sample holder to be unlikely,

nevertheless a USNBS thorium ore sample NBL-80 was mixed in resin to guarantee retention of Rn-220. This sample was then stored for several days to allow the daughters of Pb-212 (half life 10.64 hours) to reach equilibrium before counting. The ratio of gamma lines from Rn-220 daughters to the strong lines from Ac-228 were then determined, and comparison with the Th-232 standards gave a calibration for this group.

Note that there is no significant uncertainty here arising from the different self absorption characteristics of the resin and the dunite matrix, as the attenuation coefficients derived in that section are valid for dunite/resin samples above about 150 keV.

6.6.9 Potassium standard

Unfortunately no enriched source of K-40 is available and so the natural isotopic abundance of 0.01167% (STEIGER and JAGER, 1977) must be assumed. Two potassium salts were used as standards, potassium hydrogen carbonate and potassium bromide, both of 'Analar' grade, supplied by British Drug Houses. Both were placed in a dessicator overnight, and a water content uncertainty of $\pm$ 1% assumed. Uncertainties in purity are negligible compared with this figure. One standard was packed from each salt.

6.6.10 Thorium series interference with the Th-234 peak at 63 keV

It was mentioned in section 6.2.3 that there is a small peak at 63 keV in the thorium spectrum obtained from a thorite ore thought to have a negligible uranium content. This peak is not assigned in the literature and some authors (e.g. SZOGHY and KISH, 1977) assume it to be from trace U-238 contamination of their thorium ores. If so, it can be safely ignored, but if it is indeed from the thorium chain, the appropriate allowance must be made.

By examining the region of the thorite spectrum where the Bi-214 609 keV peak should occur, SMITH and WOLLENBERG (1974) set an upper limit of 17 ppm uranium in the thorite mineral shown in section 6.2, assuming full chain equilibrium. However, it is possible (although very unlikely in such a sample) that considerable disequilibrium could be present, which would increase this limit significantly. Accordingly, a piece of the thorite was examined using X-ray fluorescence, and an upper limit on the uranium/thorium atomic ratio of 0.1% determined

(KACZMARCZYK, private communication). From a comparison of this thorite mineral, diluted in pottery, after appropriate allowance for the pottery background, with the Th-232 absolute standards (see section 6.6.7) a concentration of about 181 pCi g^{-1} Ac-228 was derived. The expected count rate at 63 keV due to the maximum likely uranium contamination can then be calculated to be 2.5 $ksec^{-1}$. The observed count rate at this energy, after background subtraction, was 65 $ksec^{-1}$. Clearly this peak cannot be attributed to uranium contamination.

A similar strong peak at 63 keV is observed in the spectra of the absolute thorium standards. Note that here there is even less likelihood of significant uranium contamination, as this material has been chemically refined.

The intensity ratios of this peak at 63 keV to three other well known thorium chain gamma lines (normalised to 7.000 grams) have been calculated for three diluted thorite samples, and two of the absolute Th-232 standards. These are given in table 6.6.1.

A Th-228 source was then prepared, from a solution of Th-228 in equilibrium with its daughters dispersed in a dunite matrix, and analysed. There was no peak at 63 keV. It is estimated that an intensity ratio, of the 63 keV peak to the 238 keV peak from Pb-212, of greater than 0.001 would have been detected. As the observed ratio in samples where the earlier part of the Th-232 chain is present is 0.017 $\pm$ 0.001 (table 6.6.1) it is concluded that the 63 keV gamma ray is emitted by an isotope in the earlier part of the Th-232 chain, probably Ac-228, but certainly in group 7.

In practice a correction to the Th-234 63 keV peak is estimated from the weighted average of the predicted intensities from the observed intensities of the 338 keV and 911 keV Ac-228 peaks, with an associated error of about 10%, but anyway large enough to cover the spread in prediction.

6.6.11 Summary of calibration standards

The activities and associated errors of all the absolute calibration standards discussed are shown in table 6.6.2. These sources were each counted for a sufficient period of time that the statistical errors associated with the peak areas of interest were negligible. However, sample to sample reproducibility after weight normalisation was usually

Table 6.6.1

Ratio of the count rate in the unknown peak at 63 keV to that of three well known thorium chain gamma lines

Derived from:-		ThP/1	ThP/2	ThP/3	$ThNO_3P/1$	$ThNO_3P/2$
ratio to	keV					
Ac-228	338	0.15	0.13	0.11	0.11	0.10
Ac-228	911	0.22	0.19	0.15	0.15	0.15
Pb-212	238	0.021	0.018	0.014	0.015	0.015

Averages from above:

		keV	
Ratio of peak at 63 keV to	Ac-228	338	0.12_1
	Ac-228	911	0.172_{14}
	Pb-212	238	0.017_1

Note: standard errors are given in the least significant figures.

Table 6.6.2

Absolute calibration standards

		Activity nCi	Estimated uncertainty %	Weight g	Matrix
Uranium series:					
U-238	D/1	3.54	2.0	8.569	Dunite
Pb-210		3.65	1.0		
U-238	D/2	3.62	2.0	8.559	Dunite
Pb-210		3.74	1.0		
U-238	P/1	2.60	2.0	6.016	Pottery
Pb-210		2.68	1.0		
U-238	P/2	2.52	2.0	6.018	Pottery
Pb-210		2.60	1.0		
Ra-226	D/1	3.56	1.5	8.937	Dunite
Ra-226	D/2	3.40	1.5	8.722	Dunite
Ra-226	P/1	2.43	1.5	6.011	Pottery
Ra-226	P/2	2.45	1.5	5.995	Pottery
Thorium series:					
Th-232	D/1	0.996	2.0	9.185	Dunite
Th-232	D/2	1.040	2.0	8.628	Dunite
Th-232	P/1	0.697	2.0	5.769	Pottery
Th-232	P/2	0.729	2.0	5.997	Pottery
Potassium:					
K/1		1.98	1.0	5.932	$KHCO_3$
K/2		1.92	1.0	6.842	KBr

Note: 1) Pb-210 activities corrected to May 1979.

2) the sources of error are discussed in Appendix B, and in sections 6.6.2 to 6.6.11.

about 1%, and this source of error must be added to the absolute errors to give the total errors given in table 6.6.3. Here the count rate for an activity of 1 pCi g^{-1} of each of the groups shown is given, normalised to a weight of 7.000 g of 'typical' pottery.

The two relative standards, NBL 74-A in resin (for Rn-222 daughters) and NBL 80 in resin (for Rn-220 daughters) were also counted for sufficient time that the statistical errors in the daughter/parent peak ratios were small compared with the absolute errors in the parent activities of the standards. The derived count rates for these peaks are also shown in table 6.6.3, with the total errors.

The important peak intensity ratios for determining the U-235 correction to the 186 keV peak, and the thorium chain contribution to the 63 keV peak are also given, with the estimated errors.

Typically the total errors in the count rates given are about 2%. Inevitably these errors are to some degree subjective, and so it is important to offer experimental confirmation of at least some of these calibration figures. The parent concentrations of the USNBS uranium and thorium ores are well known, and have not been used at any stage in the derivation of the calibration data. Thus analysis of these ores provides a check on the quality of this data. Such comparisons are presented in the following sections.

6.6.12 Effect of sealing on determining levels of radon escape in unsealed samples

Although not strictly a calibration problem, it is appropriate here to discuss the uncertainties introduced as a result of sealing a sample into the standard plastic holder. If a radon emanating material is packed into a sample holder and counted immediately for 85 ksec, then some allowance for the build up of daughter activity should be made if the unsealed level of escape is required. Initially, let us assume that the sample holder successfully retains all the radon; then

$$I = I_o + I_R (1 - e^{-\lambda t'}) \quad - - - - - - - - - 6$$

where

I is the total radon activity at time t'

I_o is the radon activity of the unsealed sample

Table 6.6.3

Count rates from calibration standards, normalised to an activity of 1 pCi g^{-1} and a sample weight of 7.000 g

Group	Isotope	Energy keV	Count rate $ksec^{-1}$	Total error %
1	Th-234	63.3	4.49	2.1
		92.5	5.99	2.1
3	Th-230	67.8	0.40	9.0
	Th-227	256.2	0.18	3.3
4	Ra-226	186.1	3.18	1.6
5	Pb-214	242.0	4.36	1.8
		295.2	9.34	1.8
		352.0	14.6	1.8
	Bi-214	609.4	4.29	1.9
		1120.4	0.629	2.3
		1377.4	0.374	2.1
6	Pb-210	46.5	4.19	1.7
7	Ac-228	270.3	0.717	2.7
		338.4	3.89	2.2
		463.0	0.473	2.1
		911.1	2.68	2.0
		968.9	1.57	2.1
	Ra-224	241.0	2.96	2.6
8	Pb-212	238.6	27.56	2.2
		300.1	0.547	2.8
	Bi-212	727.0	0.920	2.4
	Tl-208	583.1	2.68	2.2
		860.5	0.429	2.8
	K-40	1461	0.852	1.2

Also, ratios derived using above:

U-235 at 185.7 / Th-234 at 63.3	0.5107	0.9
U-235 at 185.7 / Th-234 at 92.5	0.3827	0.7
? at 63 / Ac-228 at 338.4	0.12	8
? at 63 / Ac-228 at 911.1	0.17	8

See notes on following page.

Notes to table 6.6.3

1) total errors shown are experimental errors combined with calibration errors from table 6.6.1.

2) errors in ratios are standard errors derived from at least 4 separate counting samples, and do not include calibration errors.

3) the peaks at 328.0 keV (Ac-228) and 727.0 keV (Bi-212) do in fact have a small contribution from Bi-212 and Ac-228 respectively.

4) the origins of the unknown peak at 63 keV in the thorium series are discussed in section 6.6.10.

I_R is the radon activity that escapes from an unsealed sample and

λ is the radon decay constant.

Integrating this with respect to t', from $t' = 0$ to $t' = t$,

$$\int_0^t I dt = I_o t + I_R t - \frac{I_R}{\lambda}(1 - e^{-\lambda t})$$

or $$\overline{I} = I_o + I_R - \frac{I_R}{\lambda t}(1 - e^{-\lambda t}) \quad \text{- - - - - - - - -} \quad 7$$

where

$\overline{I}$ is the average radon activity in the sample over the counting time t.

(i) Rn-222

Evaluating (7) for t = 85 ksec, and λ = 2.1×10^{-3} $ksec^{-1}$ for Rn-222.

$$I = I_o + 0.084\ I_R \quad \text{- - - - - - - - - - - - - -} \quad 8$$

As $I_o + I_R$ is known (in this case the parent activity of Rn-222, i.e. Ra-226), it is possible to derive I_o, the level of activity in the unsealed sample.

However, there is strong evidence that these sample holders retain very little, if any, of the Rn-222 able to escape from the matrix.

A crushed sample of concrete doped with 3000 ppm uranium ore (see chapter 3) was sealed into a sample holder, counted immediately, and stored for three months before recounting. One pottery sample and one soil sample were also recounted after storing for longer than one month (more than 5 half lives of Rn-222). The ratio of the average activity of the two Pb-214 lines at 295.2 keV and 352.0 keV to the Ra-226 activity derived from the 186 keV peak are shown in table 6.6.4 for each of these samples. (A discussion of the reproducibility of low activity measurements will be found in section 6.8). Clearly the sample holder does not significantly hold back any of the emanated Rn-222. Thus no correction should be necessary when estimating the activity of Rn-222 in the unsealed state.

(ii) Rn-220

It is not obvious that the above conclusion applies to the escape

Table 6.6.4

Fraction of Rn-222 retained by sample holder

	Immediate measurement	Delayed measurement
Uranium doped concrete ($A10_2$)	0.82 $_{2}$	0.81 $_{2}$
Pottery (69 pot 18)	0.70 $_{11}$	0.83 $_{13}$
Soil (S164p)	0.72 $_{7}$	0.75 $_{8}$

Note: 1) the soil was dry, but otherwise unchanged from the buried state. The pottery was dry and crushed to less than 200 μm, the concrete dry and less than 500 μm.

2) the fraction of Rn-222 retained is calculated from the appropriate Rn-222 levels divided by the average Ra-226 level of the two counts.

3) errors are in the least significant figures.

of Rn-220. Indeed, as the half life is very much shorter (56.4 seconds) it seems unlikely that any Rn-220 should escape from the mineral matrix. This is borne out by the fact that there was no sample found which showed sufficient Rn-220 escape to make an experiment such as just described for Rn-222 worthwhile. Note that here the important half life is not that of Rn-220, when the rate of build up towards equilibrium is discussed. Rn-220 will reach equilibrium with its parent Rn-224 within about five minutes of sealing; however, it is the daughter Pb-212 which is detected and this has a half life of 10.64 hours. Using equation (7) substituting $\underline{\lambda} = 1.81 \times 10^{-2}$ ksec^{-1} for Pb-212, and $\underline{t}$ = 85 ksec,

$$I = I_o + 0.49\ I_R \qquad - - - - - - - - - - - 9$$

Again $\underline{I_o} + \underline{I_R}$ is known (the activity of the Rn-220 parent), and so $\underline{I_R}$ can be calculated. Although in practice very little such disequilibrium is observed (as is reported in the following chapters) equation (9) enables upper limits to be placed on the escape of Rn-220 in the unsealed sample.

6.7 COMPARISON OF CALIBRATION DATA WITH OTHER WELL KNOWN STANDARDS

Five absolute mineral standards, two uranium and three thorium, whose concentrations are well certified, have been analysed using the calibrations derived in the previous section. In addition a uranium series sample, uraninite dissolved in aqua regia, was dispersed in dunite in the usual manner, and counted. This sample is known to be in secular equilibrium at least as far as Rn-222 (IVANOVICH, private communication), although its absolute activity is not well known. Details of the five absolute standards are given in table 6.7.1.

6.7.1 Uranium series

Two samples supplied by the New Brunswick Laboratory, U.S. National Bureau of Standards, NBL 74-A and NBL 42-1 (which was subsequently diluted in pottery) were analysed, and the results from some of the important gamma peaks are listed in table 6.7.2.

The parent activities derived from the gamma spectrometer measurements can be converted to parent concentrations using the nuclear constants listed in Appendix E. It is of course assumed that Th-234 is in secular

Table 6.7.1

Standards analysed to confirm calibrations

	Parent concentration	Standard deviation %	Certified by
Uranium series:			
NBL 74-A	1040 ppm in dunite	0.96	U.S.N.B.S. New Brunswick Lab.
NBL 42-1	4.04% in dunite	0.5	U.S.N.B.S. New Brunswick Lab.
Thorium series:			
NBL-80	1010 ppm in dunite	1.5	U.S.N.B.S. New Brunswick Lab.
NBL-109	104 ppm in silica	1.4	U.S.N.B.S. New Brunswick Lab.
GSP-1	109.7 ppm	2.5	Flanagan, 1969.

Note: The error given for GSP-1, from the U.S. Geological Survey, is the standard deviation of the 14 thorium analyses reported by Flanagan (1969).

Table 6.7.2

Comparison of spectrometer analyses with known concentrations: uranium

Group	Isotope	Energy keV	NBL 74-A pCi g^{-1}	NBL 42-1 pCi g^{-1}
1	Th-234	63.3	342_{7}	13590_{260}
3	Th-230	67.8	311_{42}	14830_{1700}
4	Ra-226	186.1	329_{8}	14220_{310}
5	Pb-214	241.9	320_{10}	13850_{280}
		295.2	315_{10}	13630_{280}
		352.0	290_{10}	13500_{280}
6	Pb-210	46.5	332_{8}	12990_{230}

Ratio of the predicted concentration from group 1 to that given in table 6.7.1:

NBL 74-A	0.985_{25}
NBL 42-1	1.007_{20}

Note: 1) errors are given in the least significant figures.

2) NBL 42-1 was diluted in ground pottery to a concentration of 0.02355 grams of standard in 1 gram of total. The errors associated with this dilution are included in the spectrometer predictions.

3) conversion from activity to concentration uses data presented in Appendix E.

equilibrium with U-238. The ratio of concentrations to those given in table 6.7.1 are also shown. The spectrometer measurements are considered to be in good agreement with the published values.

6.7.2 Thorium series

The three thorium standards analysed are of different origins. Two, NBL 80 and NBL 109, are again from the New Brunswick Laboratories: one, GSP-1 is a U.S. Geological Survey standard (FLANAGAN, 1969).

Using the data from Appendix E, the concentration of the parent, Th-232, can be calculated from the group 7 activities, and the ratio to the values given in table 6.7.1 are also shown in table 6.7.3. The agreement is considered good.

6.7.3 Uranium series equilibrium

The uraninite sample diluted in dunite, and shown in table 6.7.4 clearly illustrates the equilibrium condition expected, except in the case of the short lived Rn-222 daughters. It is assumed that all the Rn-222 escaped while the sample was in solution, although the observed activity of Pb-210 shows that there was no significant radon escape from the sample when it was in the original mineral form.

6.7.4 Conclusions

It is considered that these analyses prove that, with the exception of the short lived radon daughters, the uranium and thorium series calibrations have been confirmed within the limits of experimental error. It was not considered necessary to confirm the calibration for the short lived daughters of Rn-222 and Rn-220, or for K-40.

6.8 ANALYSIS OF LOW ACTIVITY SAMPLES

In the preceding sections it was stated that the overall reproducibility of the calibration samples, after correction for weight differences, was better than 1%. However, these analyses were all performed at activities of nanocuries per gram, where the background contribution and the errors in peak fitting were negligible.

Neither of these conditions are fulfilled in the analysis of low activity samples. A typical spectrum from a pottery sample is shown in figure 6.8.1 a, b, and the intensities of the labelled peaks, as

Table 6.7.3

Comparison of spectrometer analyses with known concentrations: thorium

Group	Isotope	Energy keV	NBL 109 pCi g^{-1}	NBL 80 pCi g^{-1}	GSP-1 pCi g^{-1}
7	Ac-228	270.3	11.9_{7}	114_{4}	12.3_{7}
		338.4	11.6_{3}	111_{3}	11.8_{3}
		463.0	10.7_{7}	112_{3}	10.7_{7}
		911.1	11.2_{3}	116_{2}	12.1_{3}
		968.9	11.8_{4}	-	12.3_{4}
	Ra-224	241.0	11.9_{4}	110_{3}	12.6_{5}
8	Pb-212	238.6	11.6_{3}	113_{3}	12.0_{3}
		300.1	10.9_{9}	124_{4}	11.5_{8}
	Bi-212	727.0	11.2_{5}	111_{3}	-
	Tl-208	583.1	12.2_{4}	110_{3}	12.1_{3}
		860.5	10.9_{8}	104_{3}	11.4_{6}

Ratio of the average concentration predicted from group 7 to that given in table 6.7.1

NBL 109	1.015_{25}
NBL 80	1.008_{23}
GSP-1	0.980_{33}

Note: 1) errors are in the least significant figures.
2) conversion from activity to concentration uses data presented in Appendix E.

Table 6.7.4

Spectrometer analysis of material known to be in secular equilibrium

Group	Isotope	Energy keV	Activity pCi g^{-1}
1	Th-234	63.3	30.9_{7}
		92.5	30.5_{7}
3	Th-230	67.8	31.5_{40}
	Th-227	256.2	28.4_{10}*
4	Ra-226	186.1	29.5_{8}
5	Pb-214	241.9	3.2_{2}
		295.2	3.3_{2}
		352.0	3.9_{2}
	Bi-214	609.4	2.8_{2}
6	Pb-210	46.5	31.6_{8}

Note: 1) * although a member of the U-235 chain, the activity of this isotope has been expressed in pCi g^{-1} of the U-238 chain, assuming the natural isotopic ratio (Appendix E), in order to illustrate the equilibrium condition.

2) errors are in the least significant figures.

Figure 6.8.1(a)

Typical spectrum of pottery sample, lab. ref. P12N02

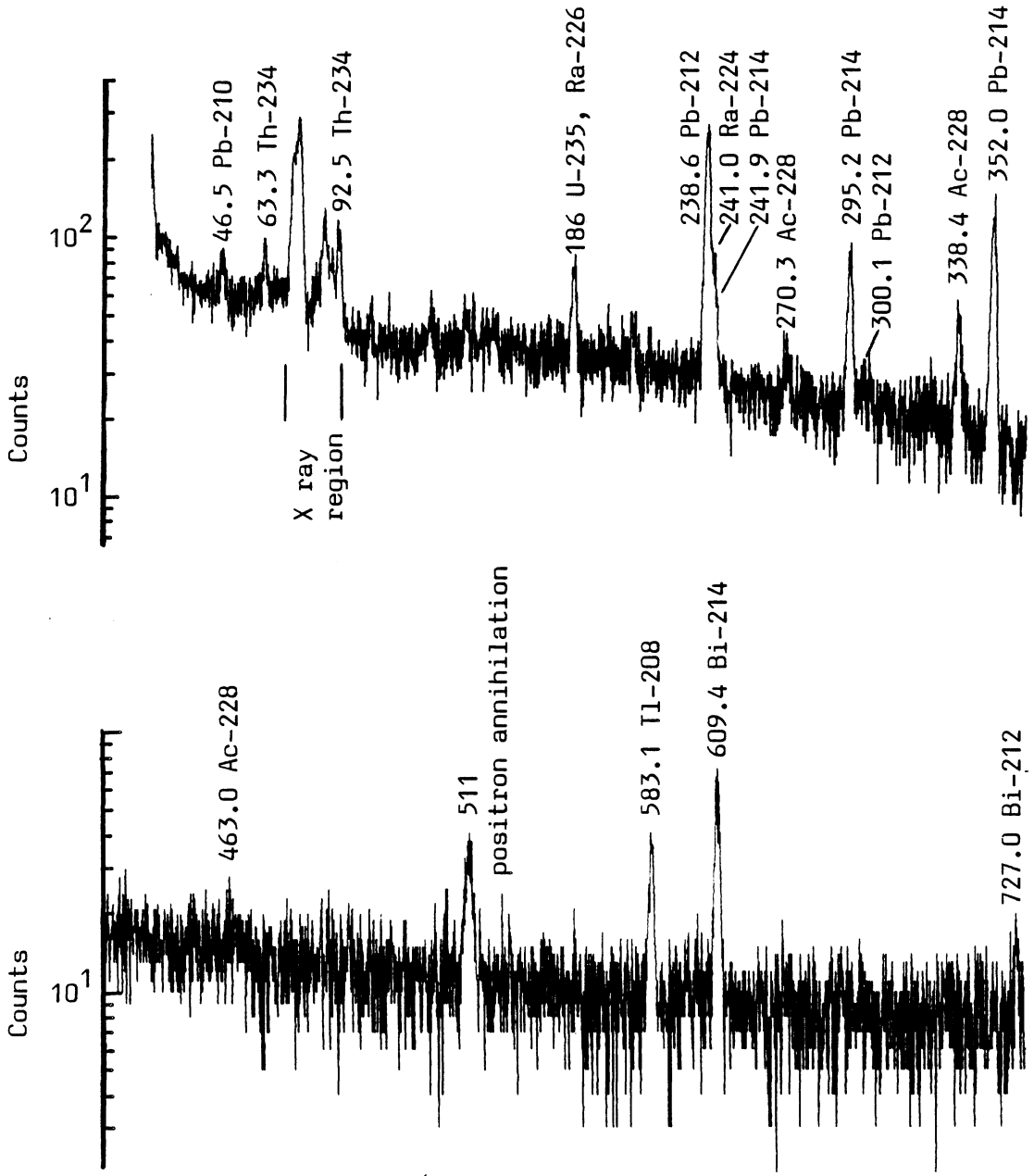

Note: 7.32 g counted for 85 ksec

Figure 6.8.1(b)

Typical spectrum of pottery sample, lab. ref. P12NO2 (cont.)

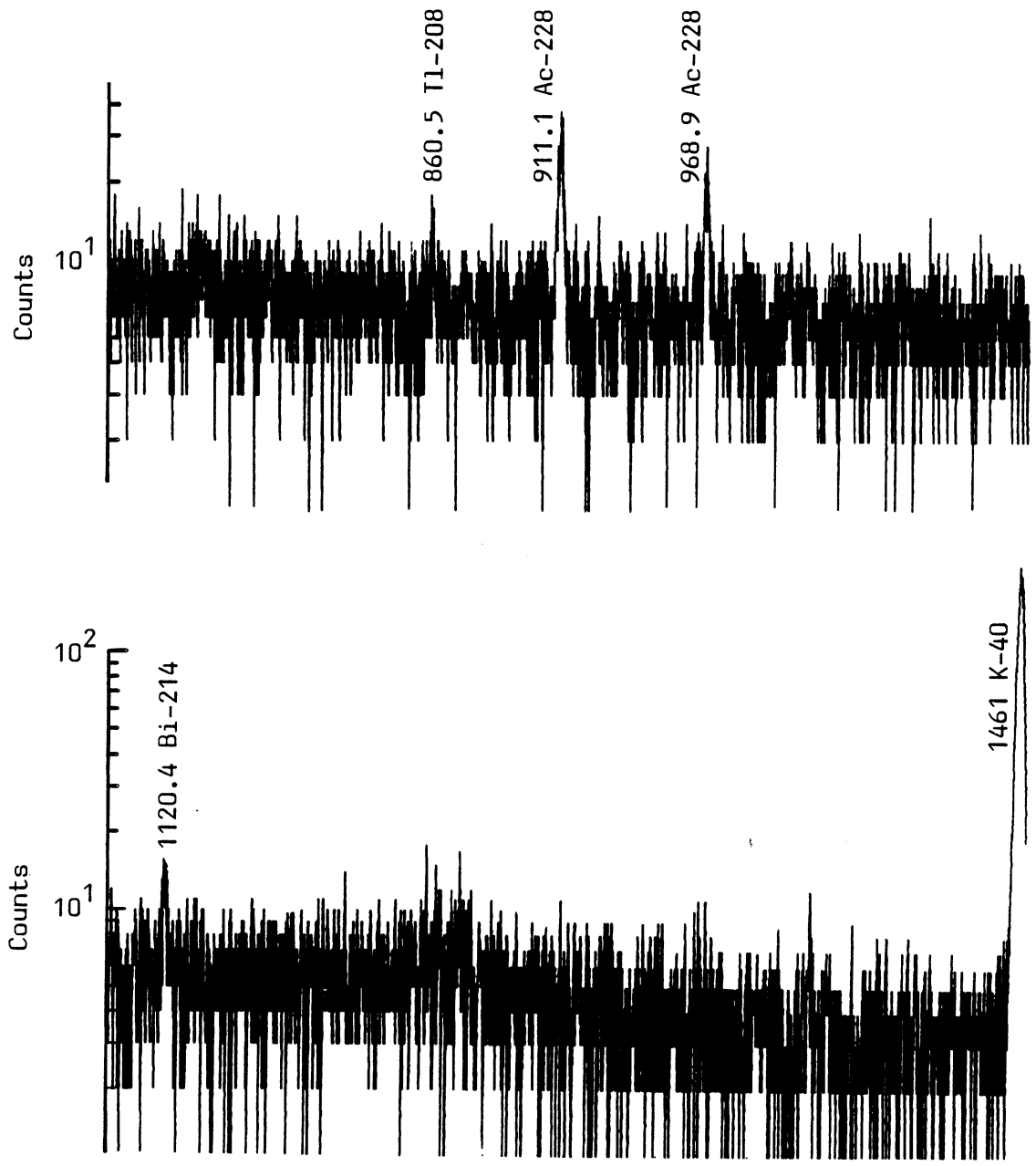

Note: 7.32 g counted for 85 ksec

found by the peak fitting routine (see Appendix A) are listed in table 6.8.1. Here the fitting errors are much larger than calibration errors, and it is clearly necessary to establish the validity of these results from the analysis procedure. Firstly, it is desirable to show that the error estimates given by the peak fitting routine are comparable with the observed reproducibility, and secondly it must be shown that no significant systematic errors arise from the analysis of low intensity peaks - because of incorrect background continuum corrections, for instance.

6.8.1 Comparison of observed reproducibility with the errors from the peak fitting routine

To obtain a measure of the true overall reproducibility from low intensity peaks a solid sample of potsherd, machined to fill a sample container, was counted five times over a period of three months. This is the same sample as shown in figure 6.8.1.

The results of the five analyses are tabulated in table 6.8.2, with the mean of the results obtained at each energy, weighted according to the error assigned by the fitting routine. Peaks which, for various reasons, were not analysed in all five spectra, are omitted.

Of the 65 peaks analysed, 49 (75%) lie within 1 sigma of the appropriate weighted mean, 11 (17%) lie between 1 and 2 sigma, and 5 (8%) between 2 and 3 sigma, with no results outside 3 sigma. There is thus no evidence for suggesting that the intensity error given by the analysis program cannot be used as a useful estimate of the error in the peak area, even at low intensities.

As a further indicator that the observed errors are not severe underestimates of the true error, the minimum possible error on statistical grounds has also been calculated. These are presented in the final column of table 6.8.2. Errors for the two peaks at 63 keV and 186 keV have been omitted because of the corrections applied to these intensities.

6.8.2 Systematic errors in the peak fitting of low intensity peaks

To look for the presence of systematic errors from the peak fitting routine, when analysing low intensity peaks in the presence of both the uranium and thorium series and significant background contribution, three simulated pottery spectra of known composition were accumulated each for a total of 85 ksec.

Table 6.8.1

Peak intensities for a typical sherd (lab. ref. P12N02) derived by the peak fitting routine for those peaks shown in figure 6.8.1 a,b

Group	Isotope	Energy keV	Count rate $ksec^{-1}$	Estimated error
Uranium series:				
1	Th-234	63.3	4.7	0.4
		92.5	7.5	0.6
3	Th-230	67.8	1.0	0.4
4	Ra-226 (+ U-235)	186	6.4	0.3
5	Pb-214	295.2	9.7	0.4
		352.0	17.4	0.5
	Bi-214	609.4	7.2	0.3
		1120.4	1.5	0.2
6	Pb-210	46.5	4.2	0.4
Thorium series:				
7	Ac-228	270.3	1.7	0.2
		338.4	4.9	0.3
		463.0	1.0	0.2
		911.1	3.7	0.2
		968.9	2.5	0.2
8	Pb-212	238.6	34.4	0.7
		300.1	0.7	0.3
	Bi-212	727.0	1.4	0.2
	Tl-208	583.1	4.3	0.3
		860.5	0.7	0.2
Potassium:				
	K-40	1461	39.4	0.7

Note: the estimated error is derived by the peak fitting routine described in Appendix A.

Table 6.8.2 Observed reproducibility of some low intensity peaks

Group	Isotope	Energy keV	No 1	No 2	No 3	No 4	No 5	Weighted mean	$\sqrt{N + 2B}$
1	Th-234	63.3	0.89_{11}	0.91_{9}	0.86_{11}	0.81_{9}	0.84_{10}	0.86	-
4	Ra-226	186	0.55_{15}	0.97_{17}	0.98_{14}	0.99_{9}	0.90_{9}	0.91	-
5	Pb-214	295.2	0.93_{4}	0.85_{4}	0.93_{4}	0.80_{4}	0.76_{4}	0.85	3
		352.0	0.89_{3}	0.91_{3}	0.88_{3}	0.87_{3}	0.86_{3}	0.88	3
6	Pb-210	46.5	0.79_{16}	0.97_{16}	0.96_{16}	0.77_{16}	0.84_{9}	0.81	5
7	Ac-228	338.4	1.19_{8}	0.80_{6}	1.02_{5}	0.98_{5}	0.90_{6}	0.96	5
		463.0	1.97_{30}	1.34_{36}	1.56_{36}	1.19_{31}	1.41_{39}	1.53	23
		911.1	0.88_{6}	1.01_{6}	0.95_{7}	0.90_{7}	0.86_{5}	0.91	5
		968.9	0.84_{9}	0.85_{5}	0.92_{11}	0.95_{11}	0.99_{13}	0.88	7
8	Pb-212	238.6	0.91_{2}	0.88_{2}	0.90_{2}	0.90_{2}	0.89_{2}	0.90	2
		300.1	0.62_{33}	0.24_{32}	1.02_{36}	1.06_{35}	0.53_{39}	0.68	8
	Bi-212	727.0	1.18_{17}	0.97_{13}	0.73_{17}	0.54_{13}	0.95_{16}	0.85	9
	K-40	1461	16.9_{9}	17.0_{9}	17.6_{9}	18.7_{9}	16.4_{9}	17.3	4

Note: 1) activities are in pCi g^{-1}, but the errors shown in the least significant figures are derived from the experimentally observed counting errors only.

2) the final column gives the ratio of the square root of the sum of the total background count and the total background plus sample count, to the total sample count, expressed as an absolute error on the weighted mean.

The uranium series component was derived from NBL 42-1 pitchblende in dunite diluted in ground pottery (<200 μm grain size), to a concentration of about 320 pCi g^{-1} (955 ppm uranium). The thorium contribution was derived from a subsequent count of ThP/1, thorite in ground pottery. The activity of this source is about 170 pCi g^{-1} (1560 ppm thorium). The potassium contribution was obtained from the potassium hydrogen carbonate standard, of 334 pCi g^{-1} K-40. These three components were each counted for a sufficient time to produce, when added together, the peak intensities that would be observed from a pottery sample containing about 1 pCi g^{-1} uranium and thorium, and about 15 pCi g^{-1} potassium. The spectrometer was then left to accumulate a background component using the sodium hydrogen carbonate inert sample discussed in section 6.4.4, for a total count time of 85 ksec. This process was repeated three times, and the resulting composite spectra were then analysed in the usual manner.

Table 6.8.3 tabulates the intensity ratios obtained by dividing the observed peak intensities (less background) by expected intensities derived from longer counts of the individual components, counted and analysed separately. The weighted average of these ratios is also shown at each energy.

Note that the 609 keV (Bi-214) and 583 keV (Tl-208) intense peaks have been omitted from both tables 6.8.2 and 6.8.3. During one of the intervals in taking these spectra the temperature of the detector was accidentally allowed to rise with the bias voltage on. Active uranium, thorium and potassium samples were immediately recounted, and although the energy resolution appeared unaffected, the intensities of the 609 keV and 583 keV peaks were found to have changed significantly relative to all the other major peaks, for which the efficiency calibration was unchanged. It is assumed that the time resolution of the detector was affected by the warm up, changing the coincidence detection efficiency in the detector itself. Thus the errors associated with these two peaks have not been systematically checked in this section, although they are known to be in good agreement with other intense peaks when the appropriate calibration is used, and so are frequently included when reporting sample activities in later chapters.

Table 6.8.3

Ratio of observed to expected peak intensities for simulated pottery spectra

Group	Isotope	Energy keV	No 1	No 2	No 3	Weighted mean
Uranium series:						
1	Th-234	63.3	1.04_{10}	0.97_{6}	0.96_{10}	1.01_{4}
		92.5	0.86_{8}	1.27_{8}	1.27_{8}	1.12_{5}
3	Th-230	67.8	-	2.41_{94}	-	-
4	Ra-226	186(1)	0.81_{9}	1.07_{7}	0.90_{10}	0.93_{5}
5	Pb-214	295.2	1.07_{5}	0.97_{6}	1.00_{5}	1.02_{3}
		352.0	1.02_{5}	1.02_{6}	1.06_{5}	1.03_{3}
6	Pb-210	46.5	0.93_{5}	1.14_{11}	1.13_{10}	1.01_{4}
Thorium series:						
7	Ac-228	270.3	- (2)	1.28_{50}	1.15_{44}	1.21_{33}
		338.4	-	1.16_{6}	0.97_{6}	1.07_{4}
		463.0	-	1.70_{50}	1.67_{46}	1.68_{34}
		911.1	-	1.14_{10}	0.95_{8}	1.02_{6}
		968.9	-	1.03_{11}	-	-
8	Pb-212	238.6	-	1.00_{2}	0.98_{2}	0.99_{1}
		300.1	-	0.53_{39}	0.95_{35}	0.76_{26}
	Bi-212	727.0	-	1.11_{19}	1.36_{18}	1.24_{13}
	Tl-208	860.5	-	2.02_{220}	1.07_{35}	1.09_{35}
Potassium:						
	K-40	1461	0.92_{17}	1.03_{18}	0.98_{18}	0.98_{10}

Note: 1) the U-235 correction to the 186 keV Ra-226 peak was derived from the Th-234 63.3 keV measurement of the uranium activity

2) an error was made in recording the count time for the first thorium spectrum. The count times for the other spectra were:

U series, no 1 - 264 sec, no 2 and 3 - 265 sec

Th series, no 2 and 3 - 643 sec

Potassium, no 1 - 3613 sec, no 2 and 3 4242 sec

6.8.3 Discussion

(i) Uranium series: groups 1-6

In these groups the only two results outside the 3 sigma level compared with the source counted on its own (i.e. compared with 1.00) are from the 92.5 keV composite peak from Th-234. Although this does not necessarily reflect any systematic error, especially in view of the first Th-234 result of 0.86 (standard deviation 0.08) it is considered that these large deviations probably reflect the contribution from the 93.3 keV thorium X-ray peak. As was mentioned in section 6.2.3, allowance for this cannot be made reliably; this peak is not used in further analyses unless the thorium activity is less than 10% of the uranium activity.

Of the remaining peaks, the error on the only measurement of Th-230 at 67.8 keV is, as expected, too large for this peak to be useful. Note that the Th-234 peak at 63 keV has been successfully analysed, with no sign of systematic error, despite the Th-232 chain correction that has to be made (see section 6.6.10). This is particularly reassuring as it is from this measurement that the U-235 contribution to the Ra-226 peak at 186 keV is calculated.

(ii) Thorium series: groups 7 and 8

There are no results which deviate significantly from the predicted value in these groups. Here the accurate analysis of the 238.6 keV peak (Pb-212) is noteworthy, because of the substantial interference at 241 keV and 242 keV from Ra-224 and Pb-214, respectively. This illustrates the value of computer assisted analysis, as this is the most intense, and hence potentially the most accurately measureable peak in the thorium series, but only if these interfering peaks can be successfully unfolded.

6.8.4 Conclusion

It has been shown that repeat analyses of the same low level sample over a three month period using the program 'SAMPO' give substantially the same peak intensities, with realistic assessment of the associated errors.

Further tests on simulated low level spectra have shown that there are no apparent systematic errors in the analysis of the important peaks,

or in converting these peak intensities into activities. The work presented in these last three sections has established the spectrometer as a reliable analytical tool which produces useful estimates of the associated errors. The remaining chapters will present the results obtained from the routine use of the spectrometer.

C H A P T E R VII

LOW LEVEL RADIOISOTOPE ANALYSIS OF SAMPLES OF ARCHAEOLOGICAL INTEREST

The reliability and accuracy of the gamma spectrometer as an analytical tool was demonstrated in the preceding chapter, and it is now appropriate to consider the data obtained using gamma spectrometry as a routine method.

The results presented in section 7.1 will demonstrate the range of activities found in a variety of sherds from around the world. The homogeneity of activity in a pottery sample fired recently in a replica Roman kiln is then examined, and preliminary experiments to investigate the potential mobility of the various radioisotopes present are described in section 7.3.

A detailed investigation of four archaeological sites is then presented in sections 7.4 and 7.5, in which TL dates calculated using a detailed knowledge of the radioisotope concentrations in both soils and pottery samples are compared with those calculated using established radioactivity analysis procedures. The sources of possible error due to inherent uncertainties are also considered.

Measurements made on material from a fifth site, as yet undated by TL, are used to indicate those regions of the site likely to have received the most stable annual dose rate.

Finally, in section 7.8 the evidence for isotope mobility is collected together to permit more generalised observations to be made.

7.1 MEASURED ACTIVITIES IN A RANGE OF POTTERY SAMPLES

Potsherds from eleven separate sites around the world were analysed to provide an indication of the likely range of activities and states of equilibrium to be found. The activities of these sherds are listed in table 7.1.1. To assist discussion, ratios of the activities of Th-232/U-238, and those of daughter/parent groups, are also listed in table 7.1.1. All the samples were dry (although

Table 7.1.1 Group activities of sherds from various geographical locations, in pCi g^{-1}

Group	Long lived isotope	169j2 Portugal	547b Zaire	215a2 Egypt	141c5 England	132k17 France	200g17 India	505a5 Iran	200g18 Italy	7b Australia	P07J04 Peru	563 England
1	U-238	0.96_{14}	1.03_{11}	0.68_{13}	0.74_{11}	1.16_{6}	0.79_{12}	0.60_{8}	1.21_{14}	0.29_{8}	0.92_{11}	1.07_{13}
4	Ra-226	2.16_{16}	1.80_{14}	0.31_{12}	0.78_{15}	1.19_{11}	1.37_{15}	0.51_{12}	1.71_{14}	0.42_{13}	1.22_{16}	1.38_{12}
5	Rn-222	1.34_{4}	1.46_{3}	0.58_{3}	0.85_{3}	0.93_{3}	1.42_{4}	0.53_{2}	1.46_{4}	0.42_{3}	0.94_{3}	0.98_{3}
6	Pb-210	0.93_{12}	1.41_{9}	0.56_{10}	0.61_{12}	0.99_{9}	1.48_{6}	0.27_{7}	1.70_{12}	0.48_{10}	0.88_{9}	0.89_{11}
7	Th-232	1.31_{6}	1.50_{5}	0.66_{5}	0.99_{6}	0.74_{5}	2.20_{8}	0.69_{5}	2.08_{8}	0.63_{6}	0.93_{6}	1.63_{7}
8	Rn-220	1.22_{4}	1.57_{4}	0.60_{3}	1.05_{3}	0.74_{2}	2.26_{6}	0.56_{2}	1.97_{5}	0.67_{3}	1.02_{3}	1.61_{5}
	K-40	17.4_{9}	2.8_{7}	8.4_{9}	18.8_{10}	16.7_{8}	25.6_{10}	13.6_{9}	23.9_{10}	7.4_{9}	20.5_{11}	17.2_{10}
Derived from above:												
Th-232/U-238		1.36_{21}	1.12_{13}	0.97_{20}	1.34_{21}	0.64_{5}	2.78_{43}	1.15_{16}	1.72_{21}	2.17_{63}	1.01_{14}	1.52_{20}
Ra-226/U-238		2.25_{37}	1.75_{23}	0.46_{20}	1.05_{11}	1.03_{11}	1.73_{32}	0.85_{23}	1.41_{20}	1.45_{60}	1.33_{24}	1.29_{19}
Rn-222/Ra-226		0.62_{7}	0.81_{7}	1.87_{73}	1.09_{21}	0.78_{8}	1.04_{12}	1.04_{25}	0.85_{7}	1.00_{32}	0.77_{11}	0.71_{7}
Pb-210/Ra-226		0.43_{7}	0.78_{8}	1.81_{77}	0.78_{21}	0.83_{11}	1.08_{13}	0.51_{18}	0.99_{11}	1.14_{42}	0.72_{13}	0.64_{10}
Rn-220/Th-232		0.93_{5}	1.05_{4}	0.91_{8}	1.06_{7}	1.00_{7}	1.03_{5}	0.81_{7}	0.95_{4}	1.06_{11}	1.10_{8}	0.99_{5}

Note: errors are in the least significant figures.

not dessicated) and in viced form.

The Th-232/U-238 ratio varies from about 0.6 to 2.2 (for most routine analysis using alpha counting this is normally assumed to be unity). There is evidence for U-238/Ra-226 disequilibrium in several samples, especially 169j2 . As was to be expected, Rn-222 escape is common, and in at least two cases, 169j2 and 505a5, it may be very different from that when the sample was buried, as indicated by the Pb-210 activity.

There is firm evidence for escape of Rn-220 in sherd 505a5 and possibly in 169j2, but, again as expected, the overall evidence is that the escape of Rn-220 is less than that of Rn-222, at least in the dry viced state.

It is informative to predict alpha count rates and results from flame photometry potassium analyses from the isotope activities of table 7.1.1 using the data presented in Appendix E. Such comparisons are considered in detail in chapter 8.

7.2 VARIATIONS OF ACTIVITY WITH GRAIN SIZE IN A POTTERY SAMPLE BEFORE AND AFTER FIRING

As was discussed in chapter 6, there is considerable evidence from geochemical studies that the radioisotope concentration in river sediments varies with grain size, and it was decided to investigate such variations in a pottery sample before and after firing.

The pottery sample was a 'waster' (i.e. a pot broken during firing) from a reproduction of a Romano-British pit kiln (lab. ref. 565) fired in 1979 in the New Forest, Hampshire. The pot had been manufactured from local sand and clay, samples of which were also obtained. All three samples (i.e. including the pot) were analyzed without grain size fractionation, and these activities are shown in table 7.2.1. The clay was also separated into two fractions, greater than and less than 10 μm. A quantity of the clay was agitated in 10 cm of distilled water in an ultrasonic bath, and allowed to settle for 20 minutes. ALLMAN and LAWRENCE (1972) state that according to Stoke's Law, particles of less than 10 μm diameter should still be in

Table 7.2.1 Activities of the various components of a reproduction Romano-British pot, in pCi g^{-1}

Group	Long lived isotope	Clay whole	Sand whole	Pottery whole	Clay >10 μm	Clay <10 μm	Pottery 2 to 8 μm
1	U-238	0.90_{6}	0.32_{8}	0.94_{8}	0.93_{8}	0.99_{12}	1.37_{11}
4	Ra-226	1.06_{7}	0.06_{10}	1.11_{9}	1.03_{9}	1.19_{15}	0.90_{17}
5	Rn-222	0.84_{5}	0.14_{2}	0.98_{3}	0.59_{3}	0.64_{3}	1.23_{4}
6	Pb-210	1.10_{6}	0.28_{7}	0.82_{6}	0.88_{10}	1.13_{10}	1.49_{13}
7	Th-232	1.42_{6}	0.16_{3}	1.52_{5}	1.31_{6}	1.74_{7}	2.09_{10}
8	Rn-220	1.27_{4}	0.16_{1}	1.41_{4}	1.11_{4}	1.38_{4}	2.16_{6}
	K-40	17.3_{6}	0.3	18.8_{6}	12.7_{9}	17.2_{9}	20.8_{13}
Derived from above:							
Th-232/U-238		1.58_{12}	0.50_{16}	1.62_{15}	1.41_{14}	1.76_{22}	1.53_{14}
Ra-226/U-238		1.18_{11}	0.19_{32}	1.18_{14}	1.11_{14}	1.20_{21}	0.66_{14}
Rn-222/Ra-226		0.79_{7}	2.3_{38}	0.88_{4}	0.57_{6}	0.54_{7}	1.37_{26}
Pb-210/Ra-226		1.04_{9}	4.7_{79}	0.74_{6}	0.85_{12}	0.95_{15}	1.66_{35}
Rn-220/Th-232		0.89_{5}	1.0_{2}	0.93_{4}	0.85_{5}	0.79_{4}	1.03_{6}

Note: errors are in the least significant figures.

suspension after this time. The suspension was poured off, and the separation repeated on the suspension for a second time. As no special precautions were taken to limit coagulation of the grains, it is likely that the larger grain size fraction contains a proportion of grains less than 10 μm. However, it is less likely that the reverse is true. The dry weight of the smaller grain size fraction was 10% of the total.

A similar separation was undertaken using the fired pottery, but this was done using 'viced' material, suspended in acetone. In this case the 2 to 8 μm fraction was extracted, i.e. the grain size fraction used in fine grain dating and the recovered material amounted to less than 1% of the total, indicating that considerable grain growth had taken place during firing. Three of these fractions, the two clay samples and the 2 to 8 μm pottery sample, were then analysed and these results are also shown in table 7.2.1.

7.2.1 Discussion

Consider first the bulk clay, sand and pottery samples. The most obvious difference is in the activities of the sand and clay, which reflects their very different mineralogy. As the clay and sand were mixed in the proportions of 3:1 to prepare the pottery, it was to be expected that these measurements would reflect this. For instance the expected Th-232 concentration in the pottery, derived from the activities of the sand and clay, is 1.11 ± 0.05 pCi g^{-1}. However, the observed activity was 1.52 ± 0.05 pCi g^{-1} and in general the pottery activities are not distinguishable from those of the clay alone. It could be assumed that either the mixing was not carried out very thoroughly or that the stated ratio was not adhered to very carefully. However, it would be necessary to believe that little or no sand was incorporated into the sherd, and this is thought unlikely. A more likely possibility is that flotation of the clay was used to separate a particular range of grain sizes prior to mixing with the sand. (The reasons why this might be significant will become apparent in the following discussion.) Nevertheless, it must be accepted that a firm explanation of this discrepancy is not available.

It is interesting to note that the degree of Rn-222 escape has probably been decreased slightly by the firing process, which may be

due to the aggregation and annealing of grains, reducing the total surface to volume ratio of the bulk material.

We can now turn to the various grain size fractions. Consider the two clay samples. There is no significant difference in the concentrations of any of the isotopes of the uranium series between these two fractions, but there is an increase of about 30% in the Th-232 concentration (group 7). There also appears to be less potassium in the larger fraction, although this may be a result of the suspension in water during separation. Similarly the increase in apparent Rn-222 escape compared with the bulk clay sample is likely to result from the grain separation procedure, as the presence of water would enhance the escape of Rn-222 from the grains. (The samples were counted immediately after drying, before the Rn-222 had returned to the degree of equilibrium in the dry state.)

However, it is in the fine grain pottery sample that the largest discrepancies appear. The uranium concentration is 46% higher than that in the total sample, and the Th-232 38% higher. This is in marked contrast with the less than 10 μm clay sample. Taking this in conjunction with the observation that the recovery of the 2 to 8 μm grain size was less than 1% of the total fired material, compared with 10% recovery for the less than 10 μm clay fraction, there is strong indication that the fine grains extracted from this sample resulted from growth and/or amalgamation of smaller grain sizes during firing, and thus these fine grains have radioisotope concentrations appropriate to unfired grains of much smaller size. Referring to SCOTT (1968), it is clear that clay samples of less than 2 μm may have 20% more U-238, or up to 60% more Th-232 than the larger 2 to 20 μm fraction, which is consistent with the above.

The implications of these measurements for fine grain dating could be considerable. For dry sites, where little or no rehydration of sherds takes place, it is likely that the fine grains recovered from a viced sample will have a similar excess of activity compared with the bulk sample that is normally used for radioactivity analysis; indeed, often the residue after the removal of the fine grains is used. While the effect of such separations on the beta dose rate calculations is likely to be negligible, as most of the beta dose comes from the bulk of the sample, the effect on the alpha dose rate

could be considerable. Consider the sample just described. The predicted alpha count rate for the bulk sample is 11.0 $ksec^{-1}$, that for the fine grain fraction is 15.6 $ksec^{-1}$, (see Appendix E). Thus the difference in the effective alpha dose rate that would be calculated from these two fractions is 40% of the lower value. In fact the true alpha dose rate will lie somewhere between the two calculated figures, because not all of the alpha dose rate to a 10 μm grain comes from internal radioactivity. Nevertheless, it is clear that there is considerable uncertainty in the true alpha contribution in such samples. Fortunately this contribution is usually about 40% of the total dose rate, and uncertainties of, say, ± 15% in the alpha dose rate reduce to ± 6% in the total dose rate. This is not negligible, however, and there is no guarantee that this is the largest uncertainty likely to be encountered.

Unfortunately, the significance of these grain size effects in archaeological samples is difficult to ascertain, as a 1% recovery of fine grains and a six gram sample requires 0.6 kg of sherd. Although many sherds produce more than 1% fine grains, these are less likely to show strong grain size dependence as rehydration or more limited grain growth is likely to be important. While it might seem that such samples which have a suite of grain sizes closer to the original suite before firing will be less affected by this problem, and thus more amenable to dating, there are other complications associated with rehydrated or poorly fired samples which result from an increased ion exchange capacity. These will be discussed further in the following sections.

7.2.2 Conclusion

It has been shown that the clay and sand used to manufacture a reproduction Romano-British pot contained very different radioisotope concentrations, and that there was a weak dependence of Th-232 concentration on clay grain size.

More importantly, it was found that the fine grains extracted from the pottery were about 40% more active than the bulk sample. As these grains only account for 1% of the total weight of the fired sample, as against 10% in the unfired clay, it was concluded that growth or amalgamation of much smaller grain sizes, which are known

to be more active, was responsible for the increase in activity of this fraction, going from the unfired to the fired state. If a fine grain date had been attempted on such material, errors of about ± 6% would arise from the resulting uncertainties in the alpha dose rate.

7.3 STABILITY OF RADIOISOTOPE CONCENTRATIONS

It is well known that clays possess considerable ion exchange properties, and the problems that such characteristics might cause if they were also present in pottery were discussed in chapter 6. HEDGES and McLELLAN (1976) studied the ion exchange properties of two pottery samples and concluded that the recovery of exchange properties after firing was related to the degree of rehydration of the ceramic matrix. Although it is not within the scope of this thesis to consider the chemical parameters that might change the degree of mobilization of radioisotopes interacting with such ion exchange media, it was considered useful from the point of view of stability of the annual dose rate to consider whether or not a significant proportion of the activity of either the sherds or soils from archaeological sites is potentially mobile. In particular it would be useful to distinguish those samples where all or most of the radioisotopes present appeared to be firmly bound to the mineral matrix, as the dose rate calculations made after excavation could then be applied with some confidence throughout the history of the site.

7.3.1 Experimental Technique

The experimental approach employed to distinguish that fraction of the activity closely bound to the matrix from that more loosely bound by ion exchange mechanisms was to measure the radioisotope concentrations of one portion of a sample, and in a second portion, to attempt to replace all the activity retained on ion exchange sites with an inert ion. This was then analysed, assuming that only the firmly bound activity was still present. The inert ion used was Ba^{2+} as described in HEDGES and McLELLAN (1976). A 10 g sample of the crushed sherd or soil was stirred in 500 cm^3 of 0.5M $BaCl_2$ solution, held at pH 8 in a triethanolamine/HCl buffer, for 30 minutes. The sample was then centrifuged and replaced in a fresh

solution for a further 24 hours. At the beginning of both immersions the sample was placed in an ultrasonic bath for a few minutes to disperse the grains, and then kept agitated with a magnetic stirrer throughout the exchange period. It was then centrifuged, washed with distilled water, centrifuged, and dried. After packing into a sample container, it was analysed within 48 hours of being withdrawn from the $BaCl_2$ solution. The sample was subsequently stored for as long as possible (at least 10 weeks) to allow some return to secular equilibrium of short lived isotopes, especially Th-234 with a half life of 24 days, and recounted. It should be emphasized at this point that although concentrated Ba^{2+} solutions are not normally found in nature, the results obtained here and in following sections are not unique to Ba^{2+}. Other more common metal ions, such as Na^{+} or Ca^{2+} could be expected to have produced similar results, although not necessarily on the same time scale. In particular, for sites where inundation by sea water is a possibility, such as the two Hong Kong sites discussed in section 7.5, these experiments are very relevant.

Two samples, one clay and one sherd, were analysed using this technique as an initial investigation to examine the significance of potential radioisotope mobility. The clay sample was that used in the previous section, sieved to reject those grains greater than 150 μm; the sherd was a genuine Romano-British sample, lab. ref. 563. The results of these analyses are listed in table 7.3.1.

7.3.2 Discussion

It is sufficient at this stage to draw attention to the significant changes and inconsistencies in radioisotope concentrations. It is not worthwhile to consider the interpretation of these changes in any great depth, as this will be done in subsequent sections where a number of interrelated results will be presented, permitting more detailed analysis.

Consider first the uranium series. The Th-234 activity in the clay sample dropped slightly immediately after the exchange, and continued to drop during the storage period. This can be attributed to a loss of U-238 in the exchange process, but not of Th-234.

Table 7.3.1 Isotope activities before and after ion exchange, in pCi g^{-1}

Group	Long lived isotope	Isotope measured	Half life	Site 565, clay, <150 μm Before exchange	Within 48 hrs	After 80 days	Site 563, pottery, crushed Before exchange	Within 48 hrs	After 94 days
1	U-238	Th-234	24 days	1.04_{10}	0.85_{9}	0.44_{10}	1.07_{13}	0.74_{12}	0.93_{10}
4	Ra-226	Ra-226	1600 yr	1.03_{14}	0.83_{12}	1.11_{16}	1.38_{12}	1.19_{16}	1.11_{15}
5	Rn-222	Pb-214	27 min	0.88_{3}	0.76_{3}	0.77_{3}	0.98_{3}	0.97_{3}	1.06_{3}
6	Pb-210	Pb-210	21 yr	1.24_{10}	0.65_{9}	1.11_{13}	0.89_{11}	0.93_{11}	1.04_{11}
7	Th-232	Ac-228	6 hr	1.52_{7}	0.69_{5}	0.91_{5}	1.63_{7}	1.50_{7}	1.33_{7}
8	Rn-220	Pb-212 Bi-212 Tl-208	10.7 hr 1 hr 3 min	1.36_{4}	0.80_{3}	1.51_{5}	1.61_{5}	1.89_{5}	1.99_{5}
	K-40	K-40	1.2×10^{9} yr	17.3_{11}	18.8_{12}	16.6_{10}	17.2_{10}	15.8_{10}	16.9_{8}

Note: errors are in the least significant figures.

This isotope then decayed (according to its 24 day half life) towards equilibrium, during the storage period. This is important because of the effect on the interpretation of the intensity of the 186 keV peak from Ra-226 and U-235. It will be recalled that the U-235 contribution to this peak is deduced from the Th-234 activity, assuming secular equilibrium between Th-234 and U-238, and assuming the U-235/U-238 ratio is invariant. In this case the first of these assumptions is invalid, until the sample has been stored for a sufficiently long period of time after exchange. Thus the Ra-226 concentration determined immediately after the exchange will be erroneously low. It is assumed that there is no significant fractionation between the various uranium isotopes during the ion exchange which is primarily an electrochemical process, and relatively insensitive to small variations in atomic weight.

There is no firm evidence for uranium series mobilization in the pottery sample, although some temporary loss of Th-234 may have occurred.

In the thorium series significant changes occur in both samples in the first part of the thorium chain, group 7. It is possible to postulate mechanisms which account for the changes seen, based on the 6 hour half life of Ac-228, the isotope actually measured, and the half life of 5.8 years of the parent Ra-228. In both cases, from the results after storage, it seems that significant Ra-228 has been removed from the samples. No conclusion can be drawn about the mobility of the radium parent Th-232, as this is blocked by the Ra-228 half life.

In the second half of the Th-232 chain, the changes in the case of the clay sample can be attributed to loss of Rn-220 during exchange, followed by build up, with the apparent isotope activity being dominated by the 10.6 hour half life of Pb-212, the first of the three isotopes actually determined (see chapter 6). However, in the pottery sample the activity of this group after storage is greater than before the exchange experiment. This may be due to sample inhomogeneity, or to contamination of the exchange solution. Analysis of solid $BaCl_2$ in the spectrometer did indeed show the presence of Th-228 daughter products, but no activity from isotopes further back in the Th-232

chain. Thus the discussion of ion exchange properties in subsequent sections does not include group 8.

7.3.3 Conclusion

In view of the limited data it would be unwise to attempt to draw too much information from these samples. Nevertheless, it can be safely concluded that significant loss of activity was found in both cases, with a larger amount of replaceable activity in the unfired material, as expected. It was felt that these results were sufficiently important to make it worthwhile examining a large proportion of the samples to be presented in the following sections for such potentially mobile activity, in order to permit estimates to be made of the uncertainties in calculated ages for those samples where the stability of the annual dose rate could not be guaranteed.

7.4 SITES SHOWING LITTLE U-238/Ra-226 DISEQUILIBRIUM

7.4.0 Huaca Gallinazo, Viru Valley, Peru

It was decided to examine material from this site first, as it was anticipated from the nature of the site, and from previous measurements, that disequilibrium was unlikely to present a serious problem.

Sherds from this site have been dated using the fine grain technique and routine dosimetry methods; these dates were reported in chapter 5. The site is part of a large habitation mound, which has fallen out of use since the Spanish conquest of the sixteenth century. Although the water content of the sandy matrix surrounding the excavated sherds was measured at only 8%, (the saturation water content was 34%), there is considerable uncertainty as to the average historical water content. Indeed, for the purpose of dating the site in chapter 5, this was conservatively estimated at (50 $\pm$ 30)% of saturation. The site is located at the edge of one of the river valleys that cut across the coastal desert plain of Peru, and the age is estimated on archaeological grounds at between 1100 and 1800 years.

7.4.1 Samples analysed

Four sherds and one soil sample were analysed. One of the sherds, P12NO2, was in solid form, the other three were viced, as

used for alpha counting, i.e. coarsely crushed with the fine grains removed for dating. The solid sample was that used in section 6.8 to examine spectrometer reproducibility. One of the viced samples, P12KO2, was also used for ion exchange measurements, as described in previous sections. These sherds were excavated from a very fine, dry sand, containing a few consolidated lumps, probably the remains of mud bricks. The top level, P12J, was about 20 cm below the present surface, the bottom, P12Q, about 3 metres. However, this excavation pit had been open for some time when these sherds were excavated, and it is known that the original surface was at least 20 cm higher. The sherds recovered were all hard and red, suggesting well fired material which had undergone little or no degradation during burial.

Table 7.4.1 lists the averaged group activities of these sherds and soil with the activity ratios of interest, derived from those individual gamma lines described in section 6.8.

7.4.2 Discussion

Because of the size of the errors, it is impossible to distinguish disequilibria of less than about 20% in the uranium chain, except in sherd P12NO2, where five counts have been averaged. In this case, the only likely disequilibrium greater than about 5% is in the Ra-226 to Pb-210 stage, which indicates a loss of (11 $\pm$ 6)% when the sample was buried. With this in mind, let us consider the remaining less accurate measurements.

Although the soil, P12N, and the sherd, P12KO2, may seem to have some degree of disequilibrium between U-238 and Ra-226, it is important to note the levels of Rn-222, which are known much more accurately. These are the levels of radon activity contained in the samples in the laboratory, and so the Ra-226 levels must be equal to or greater than these. Using these minimum values for Ra-226, it becomes unlikely that such disequilibrium actually exists. There is no evidence for significant Rn-222 escape in the laboratory; the only indication that there was escape before excavation is from P12NO2, as already discussed.

If we now consider the Th-232 chain, the only possible evidence for Rn-220 escape is again from P12NO2, where an escape of (4 $\pm$ 3)%

Table 7.4.1 Group activities of samples from Huaca Gallinazo, P12, in pCi g^{-1}

Group	Long lived isotope	P12N soil	P12J04 sherd	P12K02 sherd	P12N02 sherd	P12Q02 sherd
1	U-238	1.05_{12}	0.68_{4}	1.04_{10}	0.86_{4}	0.84_{9}
4	Ra-226	0.82_{14}	0.85_{11}	0.68_{15}	0.91_{5}	0.73_{13}
5	Rn-222	0.91_{3}	0.88_{3}	0.88_{4}	0.87_{2}	0.77_{8}
6	Pb-210	0.82_{11}	0.80_{9}	0.85_{11}	0.81_{3}	0.77_{9}
7	Th-232	1.17_{9}	1.14_{5}	1.13_{7}	1.14_{3}	1.05_{5}
8	Rn-220	1.20_{3}	1.13_{3}	1.05_{4}	1.10_{2}	1.10_{4}
	K-40	14.6_{10}	17.5_{11}	17.9_{13}	17.3_{4}	18.2_{13}
Derived from above:						
Th-232/U-238		1.11_{15}	1.68_{23}	1.09_{12}	1.33_{7}	1.25_{15}
Ra-226/U-238		0.78_{16}	1.25_{23}	0.65_{16}	1.06_{8}	0.97_{18}
Rn-222/Ra-226		1.11_{19}	1.04_{14}	1.29_{23}	0.96_{6}	1.05_{21}
Pb-210/Ra-226		1.00_{22}	0.94_{16}	1.25_{34}	0.89_{6}	1.05_{23}
Rn-220/Th-232		1.03_{8}	0.99_{7}	0.93_{7}	0.96_{3}	1.05_{6}

Note: 1) errors are in the least significant figures.
2) results for P12N02 are taken from section 6.8, and are the averages of five analyses.

is indicated. From equation 4 of section 6.6.12 it is possible that this measurement underestimates the true laboratory escape by a factor of two, due to build up of Rn-220 daughters during counting. Unfortunately there is no way of knowing whether this was also the case when the sample was buried, although AITKEN (1978a) suggests that the level of Rn-220 escape increases when the sherd is dry, because the increased stopping of the recoiling Rn-220 nuclei in the pores of the sample when wet is more than compensated for by the reduced diffusion of Rn-220 in water compared with air.

Note the similarity in the absolute levels of both thorium and potassium in the four sherds. This is evidence that the raw materials used were of common origin, and reinforces the idea that the possible differences in U-238 and Ra-226 activities are statistical artefacts.

7.4.3 Potential isotope mobility

Sherd P12K02 was large enough to permit measurements of the proportion of activity retained on ion exchange sites. The experimental technique was described in section 7.3. Table 7.4.2 lists the apparent group activities measured immediately after exchange, and then again after 87 days storage. Bearing in mind the comment made in the last section concerning the true Ra-226 activity of this sherd there is little evidence for any loss of activity from the uranium chain during exchange, except for a slight decrease in the Rn-222 levels, which is probably associated with the immersion in water. Thus it can be concluded that only a small fraction, if any, of the uranium series isotopes are retained on accessible ion exchange sites.

Unfortunately the contamination of the $BaCl_2$ solution has again confused the situation in the thorium series, but there is no overall change in the activity of the first group. It is again assumed that the apparent increase in the activity of Rn-220 is due to absorption of Th-228 from the $BaCl_2$ solution.

The stability of the radioisotope concentrations in this sherd is consistent with the state of preservation. As the other sherds are similarly well preserved, and as they show very similar levels of activity, it is assumed that the conclusions drawn above apply equally to all four sherds. It should also be noted that if this lack of

Table 7.4.2 Group activites for P12K02 before and after exchange, in pCi g^{-1}

Group	Long lived isotope	Before exchange	Within 48 hr after exchange	87 days after exchange
1	U-238	1.04 $_{10}$	0.82 $_{11}$	0.77 $_{9}$
4	Ra-226	0.68 $_{15}$	0.93 $_{14}$	1.07 $_{14}$
5	Rn-222	0.88 $_{4}$	0.74 $_{3}$	0.93 $_{3}$
6	Pb-210	0.85 $_{11}$	0.68 $_{10}$	0.97 $_{11}$
7	Th-232	1.13 $_{7}$	0.98 $_{6}$	1.12 $_{6}$
8	Rn-220	1.05 $_{4}$	1.73 $_{5}$	2.34 $_{6}$
	K-40	17.9 $_{13}$	16.9 $_{9}$	16.8 $_{9}$

Note: errors are in the least significant figures.

exchangeable activity does indeed reflect little or no rehydration, rather than an absence of radioisotopes in the ground water, then the implication is that the assumption of an historical site water content of (50 $\pm$ 30)% is probably an overestimate, and that the true average water content was in fact much closer to the 8% measured immediately after excavation.

7.4.4 Effect of the spectrometer data on age evaluation

The three components of the annual dose rate derived from spectrometer data are compared with the existing measurements from chapter 5 in table 7.4.3. In calculating the dose rates from group activities, it has been assumed that:

i) no disequilibrium in fact exists between U-238 and Ra-226 in any of the samples,
ii) the Rn-222 activity before excavation is given by the Pb-210 activity,
iii) there was no escape of Rn-220 before excavation,
iv) there was no significant radioisotope mobility during burial.

Data for conversion from the activities of table 7.4.1 to dose rates are given in Appendix E, and an explanation of the calculation of the effective alpha dose rate is given in Appendix F.

The agreement between the two sets of measurements of the beta dose rates is considered good, as is the agreement between the two gamma dose rate measurements. In view of the similarity between the Pb-210 and the Rn-222 activities this is not surprising. (The existing beta dose rates were determined using beta TLD, with the samples in the laboratory state.) However, the agreement between the alpha dose rate measurements is poor; the spectrometer predicts effective alpha dose rates about 13% lower than those derived from thick source alpha counting. This discrepancy cannot be accounted for by the slight differences between the Pb-210 and Rn-222 activities, and is discussed in detail in chapter 8.

The nett effect of these dose rate revisions using spectrometer data on the sherd ages is shown in table 7.4.4. As only one soil sample was analysed by spectrometry, and as the resulting gamma dose rate was in good agreement with the existing measurement, the field

Table 7.4.3 Comparisons of annual dose rates derived from spectrometer analysis with existing measurements, in mrad yr^{-1}

	P12J04 sherd	P12K02 sherd	P12N02 sherd	P12Q02 sherd
effective alpha dose rate from:				
spectrometer	178_{6}	133_{4}	143_{6}	141_{6}
alpha counting	203_{10}	150_{8}	165_{8}	164_{8}
beta dose rate from:				
spectrometer	231_{12}	241_{14}	232_{8}	239_{10}
beta TLD	249_{12}	255_{13}	250_{13}	241_{12}
gamma dose rate from:		P12N soil		
spectrometer		118_{11}		
gamma scintillator		125_{13}		

Note: 1) errors in the effective alpha dose rates do not include errors in the a value, which are common to both methods of calculation (see Appendix F).

2) the gamma dose rate includes an allowance for site water content of 17%. and a cosmic contribution of 13 mrad yr^{-1}, as some allowance for these effects is included in the gamma measurement (chapters 4 and 5).

3) errors of 5% (shown above as absolute errors) are usually assumed to apply to the existing alpha and beta dose rates.

4) errors shown are in the least significant figures.

Table 7.4.4 Effect of spectrometer data on sherd ages

Age, years, from:	P12J04	P12K02	P12N02	P12Q02
spectrometer data	1375_{130}	1235_{150}	1600_{180}	1705_{180}
existing dose rates (chapter 5)	1260_{130}	1110_{145}	1540_{185}	1645_{180}

Note: 1) dose rates have been corrected for water content (see chapter 5).

2) TL data at a representative temperature are presented in chapter 5.

3) errors are in the least significant figures, and are total errors.

measurements reported in chapters 4 and 5 (from gamma TLD and portable scintillator) are used to provide the appropriate gamma dose rates. Total errors have been given for comparison.

The overall effect of the spectrometer dose rates is to increase the TL ages by between 4% and 11% primarily because of the change in alpha dose rates. However, these increases are easily within the total errors associated with the dates, confirming the suggestion that for such unweathered material, with the decay chains substantially in equilibrium, few problems are likely to be encountered, with the possible exception of difficulties arising from variations of activity with grain size (section 7.2), which could not be investigated with these sherds because of sample size.

7.4.5 Huari, Ayacucho, Peru

Samples from this site were chosen for gamma spectrometry as the context is representative of highland Peruvian sites of moderate water content. Of the three sherds and one associated soil sample analysed, two sherds showed satisfactory TL behaviour; the TL data for these samples are reported in chapter 5.

The samples were extracted from the side of a road-cut through a largely unexcavated city, on archaeological evidence about 1200 years old. The soil from which the sherds were removed had a measured water content of 16%, and a saturation water content of 45%. As this sample was taken within about 15 cm of the exposed face of the road-cut, it is likely that the 16% is an underestimate of the average annual soil water content. For the purpose of calculating dose rates, an average water content of (20 $\pm$ 10)% was assumed.

7.4.6 Samples analysed

The three sherds were all of a very hard red, fine grained pottery, suggesting well fired material, and showed no visible signs of degradation during burial. All four samples (three sherds and one soil sample) were analysed in the same state as for alpha counting, i.e. coarsely crushed ('viced') and dry, after the removal of the fine grains used for dating. One of the sherds, P41J11, was large enough to permit measurement of the fraction of activity retained on ion exchange sites. This measurement was also made on the soil sample.

Table 7.4.5 Group activities of samples from Huari, P41, in pCi g^{-1}

Group	Long lived isotope	P41J soil	P41J07 sherd	P41J10 sherd	P41J11 sherd
1	U-238	1.42_{11}	1.68_{14}	1.58_{9}	2.05_{14}
4	Ra-226	1.19_{14}	1.77_{19}	1.57_{18}	1.63_{21}
5	Rn-222	1.04_{3}	1.63_{4}	1.68_{3}	1.78_{6}
6	Pb-210	1.05_{6}	1.31_{12}	1.58_{14}	1.63_{13}
7	Th-232	1.38_{6}	1.76_{18}	1.91_{8}	1.84_{8}
8	Rn-220	1.34_{4}	1.54_{5}	1.80_{5}	1.80_{5}
	K-40	20.8_{14}	32.2_{12}	31.4_{11}	35.7_{10}
Derived from above:					
Th-232/U-238		0.97_{9}	1.05_{14}	1.21_{9}	0.90_{7}
Ra-226/U-238		0.84_{12}	1.05_{14}	0.99_{13}	0.80_{12}
Rn-222/Ra-226		0.87_{11}	0.92_{10}	1.07_{12}	1.09_{15}
Pb-210/Ra-226		0.88_{12}	0.74_{10}	1.01_{14}	1.00_{15}
Rn-220/Th-232		0.97_{5}	0.88_{9}	0.94_{5}	0.98_{5}

Note: errors are in the least significant figures.

The average group activities of the soil and sherds are shown in table 7.4.5.

7.4.7 Discussion

The most striking feature of these samples is the similarity in the absolute activities between the three sherds and the marked difference between the sherds and the soil sample. There is some evidence for disequilibrium between U-238 and Ra-226; the soil, P41J, and the sherd, P41J11, may show a 20% difference, although this is barely significant. Similarly there is little evidence for loss of Rn-222 from the unsealed crushed samples, but consideration of the Pb-210/Ra-226 ratios suggests that there was some escape of Rn-222 before excavation, at least in sherd P41J07.

Bearing in mind the result of section 6.6.12, that any observed Rn-220 escape in a sample counted immediately after sealing is likely to underestimate the true escape by up to 50%, it seems that there may also have been about 10% loss of Rn-220 in the unsealed samples. However, the suggestion by AITKEN (1978a), that this escape would be substantially less before excavation, is again relevant here.

Finally, it is worth noting that the Th-232/U-238 activity ratios are close to unity, as is assumed for dose rate calculations based on alpha counting, and that the potassium activity is about twice that of a 'typical' sherd.

7.4.8 Potential isotope mobility

The apparent group activities of the sherd P41J11 and the soil P41J, before exchange, immediately after exchange, and after about 90 days storage, are shown in table 7.4.6. Unfortunately the sherd measurement immediately after exchange is not available.

Consider first the uranium chain. In both cases a considerable fraction of the U-238 activity is shown to be held on ion exchange sites. As was to be expected, the soil retains considerably more activity on exchangeable sites (60% of the total U-238) than the sherd (25%). The soil analysis immediately after exchange indicates that the Th-234 activity has only decreased by about 35% in the exchange process. It then decays towards equilibrium with the parent U-238, with a half life of 24 days. Thus the true equilibrium

Table 7.4.6 Group activities for P41J (soil) and P41J11 (sherd) before and after exchange, in pCi g^{-1}

Group	Long lived isotope	P41J			P41J11	
		before exchange	after exchange within 48 hr	after exchange 89 days	before exchange	after 92 days
1	U-238	1.42_{11}	0.80_{12}	0.41_{13}	2.05_{14}	1.52_{16}
4	Ra-226	1.19_{14}	1.28_{14}	1.50_{12}	1.63_{21}	1.75_{19}
5	Rn-222	1.04_{3}	0.96_{3}	1.29_{4}	1.78_{6}	1.84_{5}
6	Pb-210	1.05_{6}	0.67_{6}	1.02_{12}	1.63_{13}	1.95_{16}
7	Th-232	1.38_{7}	1.30_{7}	1.35_{8}	1.84_{8}	1.68_{8}
8	Rn-220	1.34_{5}	1.33_{5}	1.69_{4}	1.80_{5}	2.08_{6}
	K-40	20.8_{11}	16.4_{11}	14.3_{11}	35.7_{10}	29.8_{12}

Note: errors are in the least significant figures.

concentration will be a few percent lower than that found after 90 storage. In neither case is there evidence for loss of Ra-226.

There is no indication of loss of Ac-228, as shown by the activity of group 7 immediately after exchange, or of its parent Ra-228, as shown by analysis after storage. No comment can be made as to the stability of Th-232, because of the 5.8 year half life of Ra-228. The activity of group 8 has again increased in both samples, and again this increase does not appear immediately after exchange (at least in the soil sample) indicating that it results from the absorption of Th-228 from the solution, with subsequent ingrowth of Ra-224 (half life 3.6 days) and short lived daughters. In these samples a significant proportion of K-40 has also been removed, 25% in the case of the soil, and about 15% in the case of the sherd. As will be seen, this is unusual.

7.4.9 Effect of spectrometer data on age evaluation

In order to calculate the average annual dose rates to these sherds from the spectrometer data, various assumptions must be made. In particular it is assumed that:

i) disequilibrium between U-238 and Ra-226, if any, is in fact between U-234 and Th-230. This assumption would only give rise to significant errors if the disequilibrium was in fact between Th-230 and Ra-226, and in addition, the Ra-226 was unsupported by leaching in from ground water. As U-238 (and presumably U-234) has been shown to be potentially mobile by the exchange experiments, whereas Ra-226 was not, it seems likely that any possible disequilibria arose because of the movement of U-238 (and U-234) by leaching processes.

ii) escape of Rn-222 before excavation is given by the Pb-210 activity, and that there was a negligible escape of Rn-220.

iii) the average activity of U-238 (and U-234) is that measured today. However, large errors must be associated with this assumption because of the potential mobility of these isotopes. In these cases, an uncertainty of $\pm$ 15% is associated with the uranium concentration of the sherds, and $\pm$ 40% with that of the soil. Similarly, the K-40 activity of the sherds was assigned an

error of ± 10%, and that of the soil ± 15%. No such firm conclusion as to the stability of Th-232 can be made, as the measurements made do not relate directly to Th-232, but to Ra-228. However, the potential mobility of this isotope is small, and it is reasonable to assume that the more readily trapped Th-232 will be even less mobile. It is assumed that there was negligible movement of the short lived daughter isotopes before excavation.

These dose rates are compared with the existing dose rate measurements in table 7.4.7. In all cases the agreement with the spectrometer predictions of the earlier measurements of the annual dose rates is considered acceptable. The revised dates are given in table 7.4.8, and as would be expected from the dose rate agreement, there has been only a small change in the TL ages. Of greater interest in this case is the negligible effect of the large assumed uncertainties in the true average uranium and potassium activities. It will be shown in later examples that this does not apply when the uncertainties are in more critical parts of the decay chains, such as Ra-226.

7.5 SITES SHOWING CONSIDERABLE U-238/Ra-226 DISEQUILIBRIUM

7.5.0 Sham Wan, Lamma Island, Hong Kong

Measurements by DESAI (1975) gave early indication that sherds from this site show strong radon escape, and the gas cell technique and Po-210 alpha spectrometry have been extensively applied in an attempt to deduce the true levels of gas escape in the buried state. HUXTABLE and AITKEN (1978) report this work in some detail, and because of various assumptions made in that publication, it was decided to study the material again, using gamma spectrometry.

7.5.1 Samples studied

The sherds analysed came from the bottom layer of the site at a depth of 1.5 to 2.0 metres, from a sandy soil assumed to have been almost saturated with water throughout the archaeological period. Two sherds and two soil samples were measured, one of the soil samples was counted twice. One sherd and both soil samples were also used to determine the proportion of activity carried on ion exchange sites.

Table 7.4.7 Comparisons of annual dose rates derived from spectrometer analysis with existing measurements, in mrad yr^{-1}

	P41J soil	P41J07 sherd	P41J10 sherd	P41J11 sherd
effective alpha dose rate from:				
spectrometer	-	193_{7}	270_{9}	247_{9}
alpha counting	-	215_{11}	309_{15}	245_{12}
beta dose rate from:				
spectrometer	-	414_{31}	419_{31}	469_{35}
beta TLD	-	460_{23}	469_{23}	461_{23}
gamma dose rate from:				
spectrometer	158_{16}	-	-	-
gamma scintillator	171_{27}			

Note: 1) errors in the effective alpha dose rates do not include errors in the a value, which are common to both methods of calculation. (see Appendix F).

2) the gamma dose rate includes an allowance for site water content of 20%, and cosmic contribution of 30 mrad yr^{-1}, as some allowance for these effects is included in the gamma measurement (chapters 4 and 5)

3) errors of 5% (shown above as absolute errors) are usually assumed to apply to the existing alpha and beta dose rates.

4) errors shown are in the least significant figures.

Table 7.4.8 Effect of spectrometer data on sherd ages

	P41J07	P41J10	P41J11
Age, years, from:			
spectrometer data	875_{75}	895_{105}	785_{125}
existing dose rates	760_{70}	775_{90}	785_{130}

Note: 1) the TL data for P41J07 and P41J11 is given in chapter 5 at a representative temperature. The corresponding data for P41J10 are archaeological dose, AD : 703 rads, a value : 0.136.

2) errors shown are in the least significant figures, and are total errors.

Table 7.5.1 presents the averaged group activities of these samples before ion exchange, with the activity ratios of interest, derived from those individual gamma lines described in section 6.8.

7.5.2 Discussion

Consider first the similarity between the two soil samples. This should not be surprising, as the separation into two samples was on an archaeological rather than a mineralogical basis. There are differences, however, between the two sherds.

In all four samples there is significant disequilibrium between U-238 and Ra-226, and in all cases Ra-226 is in excess. Despite large variations in absolute activities, the level of this disequilibrium is similar in both the sherds and the soil S164p. (The error associated with this step in the other soil sample, S164m7, is too large to decide whether or not it is significantly different.)

There are also wide differences in the absolute activities of the Rn-222 daughters (group 5), but again broad similarities in the ratio of Rn-222/Ra-226 can be seen. All four samples emanate about 30% of the total radon activity in the laboratory state. Although the emanation during burial, as given by Pb-210 activities, shows greater scatter, if each sample is considered individually, it is seen that the degree of gas loss did not change a great deal on excavation.

In the thorium chain, there are again differences in the absolute activities of Th-232 (group 7) between the soils and each of the two sherds, although there is no evidence for any Rn-220 escape. The K-40 activities also very considerably.

7.5.3 Potential radioisotope mobility

The proportion of activity carried on ion exchange sites has been investigated in both soil samples, and also in the sherd 164m9. These results are shown in table 7.5.1. It can be seen that a small but significant fraction of the total activity is held on ion exchange sites, especially in the sherd.

There is no evidence for any potential mobility of U-238 activity, as can be seen from a comparison of the initial activity with that

Table 7.5.1 Group activities before and after exchange for samples from Sham Wan, lab. ref. 164, in pCi g^{-1}

Group	Long lived isotope	S164p (soil) before exchange	S164p (soil) after 4 days	S164m7 (soil) before exchange	S164m7 (soil) within 48 hrs	S164m7 (soil) after 88 days	164m4 (sherd)	164m9 (sherd) before exchange	164m9 (sherd) within 48 hrs	164m9 (sherd) after 88 days
1	U-238	0.83_{8}	1.04_{11}	1.04_{24}	1.09_{10}	1.13_{12}	2.65_{18}	2.01_{17}	1.49_{13}	1.91_{14}
4	Ra-226	1.47_{15}	1.42_{15}	1.27_{20}	1.21_{13}	1.20_{14}	4.67_{26}	4.03_{22}	3.49_{20}	3.11_{26}
5	Rn-222	1.07_{3}	0.89_{3}	0.96_{3}	0.86_{2}	0.94_{3}	2.84_{6}	2.83_{5}	2.41_{6}	2.80_{6}
6	Pb-210	1.20_{8}	1.14_{10}	1.15_{12}	0.98_{10}	1.16_{12}	2.36_{14}	2.81_{15}	1.61_{11}	1.77_{13}
7	Th-232	1.95_{4}	1.57_{6}	2.07_{10}	1.61_{7}	1.53_{7}	4.05_{11}	2.96_{10}	2.17_{9}	2.30_{9}
8	Rn-220	1.95_{3}	2.17_{6}	2.12_{6}	1.53_{4}	2.15_{5}	4.12_{10}	3.08_{7}	2.45_{6}	3.16_{8}
	K-40	10.4_{6}	10.9_{8}	8.40_{9}	11.5_{8}	10.2_{8}	21.3_{11}	14.5_{8}	15.2_{9}	15.2_{9}
Derived from above:										
Th-232/U-238		2.35_{23}		2.0_{5}			1.53_{10}	1.47_{13}		
Ra-226/U-238		1.77_{25}		1.2_{3}			1.76_{15}	2.00_{20}		
Rn-222/Ra-226		0.73_{8}		0.76_{12}			0.61_{4}	0.70_{4}		
Pb-210/Ra-226		0.82_{12}		0.91_{17}			0.51_{8}	0.70_{8}		
Rn-220/Th-232		1.00_{3}		1.02_{6}			1.02_{4}	1.04_{4}		

Note: 1) S164p before exchange is the average of two counts.
2) errors are in the least significant figures.

measured 88 days after exchange. (Unfortunately this delayed measurement is only available for one of the soil samples S164m7. However, for the reasons given earlier, these results are also considered to apply to the soil S164p).

The same conclusion can be applied to the Ra-226 concentration in the soils, but not in the sherd 164m9. Here the Ra-226 activity has dropped by about (23 $\pm$ 8)%, and the degree of Rn-222 escape from (30 $\pm$ 4)% to (10 $\pm$ 8)%. This clearly suggests that in this sample at least, most of the escaping Rn-222 activity originates from Ra-226 held on accessible ion exchange sites, rather than from activity firmly bound to the mineral lattice.

The Pb-210 activity in the soils does not show any change, although a loss of (37 $\pm$ 6)% has occurred in the sherd. This is very unfortunate because it is possible that some part of this fraction of the Pb-210 activity could be supported by an influx of Pb-210 ions in the ground water. Thus the observed activity can no longer be safely assumed to reliably reflect the degree of Rn-222 escape before excavation.

Turning now to the thorium series, in all three cases there is a decrease of about 20% in the apparent activity of group 7, probably of Ra-228. Again of course no comment can be made as to the stability or otherwise of Th-232 itself.

There is little sign of the Th-228 contamination problems of the earlier samples. This probably reflects the use of a different (older) batch of barium chloride, which had been in the laboratory for at least four years, thus allowing any Th-228 to decay.

7.5.4 Effects of spectrometer data on age evaluation

In attempting to calculate the annual dose rate from the spectrometer data already presented, one important question needs to be considered. Was the Ra-226 excess supported during burial, either by Th-230 or by leaching in of activity, or on the other hand, has it been decaying from some larger excess at the time of firing?

In the last section it was found that 23% of the Ra-226 activity of the sherd is retained on ion exchange sites, compared with a Ra-226

excess of (100 ± 17)%. Although the soil shows similar Ra-226 excess, none of this is held on ion exchange sites, and thus it is likely that this radium is supported by excess Th-230; this conclusion would only be invalidated if there had been recent geological activity, such as volcanic action, to provide new minerals of an age comparable with the half life of Ra-226 (1600 years). Although there is some pumice found at this site, it is all thought to have been transported by sea action, and CHIU (1978) states that there has been no geologically recent volcanic action on Sham Wan.

If the sherds were manufactured locally, it is likely that the supported Ra-226 in the soils would also be present to some degree in the sherds. However, this cannot be guaranteed as the absolute values of Ra-226 excess are greater in the sherds than in the soils, and thus in calculating an annual dose rate two possibilities must be considered, i.e. that all the Ra-226 excess is supported, and thus does not vary with time due to radioactive decay, or that it is unsupported, and has been decreasing exponentially since firing. Nevertheless, in view of the wetness of the site, and the fact that 25% of the Ra-226 activity in sample 164m9 is held on ion exchange sites, it is thought that the supported hypothesis is the most likely. Leaching of U-238 would easily account for the increased Ra-226/U-238 ratio.

For the purpose of calculating dose rates, it is assumed that the exchange measurements made on 164m9 also apply to 164m4. It is further assumed that:

i) Ion exchange processes do contribute to the uncertainty in the average historical radioisotope concentration. In order to put an estimate on the importance of this contribution, arbitrary errors of two thirds of the observed fraction of activity held on such sites are assumed. This is not an accurate estimate of the true range of possible activities, which is not normally distributed about the observed activity. At one extreme, the possible range is bounded by the non-replaceable activity, in the case of Ra-226 about 23% below the present value. At the other extreme, the limit is set by the total exchange capacity of the sherd. Thus the true error margins are heavily skewed and those used are gross simplifications.

Applying this approach in the case of Ra-226, a concentration of (100 ± 15)% of the present day value is assumed to be the average historical concentration if the radium excess is supported. In the alternative assumption of an unsupported excess then this is also the value used in calculating the dose rate dependence with time. The additional error introduced by this simplification does not add significantly to the total age uncertainties.

ii) The percentage escape of Rn-222 before excavation is given by the ratio of Pb-210/Ra-226. This ratio is assumed to apply whether or not the Ra-226 is supported by Th-230. Unfortunately, about 35% of the Pb-210 activity was replaceable, and so uncertainties of ± 23% are assumed for the average historical activity.

iii) There has been no significant escape of Rn-220. However, errors of ± 13% are associated with the activity of Ra-228 (and daughters) due to ion exchange properties. This assumption implies that the half lives of Ra-228 daughters are too short to allow significant transport, even if they are mobilised. Only Th-228 has a half life (1.8 years) long enough to be likely to invalidate this assumption, but unfortunately there is no information available from the ion exchange experiments as to its potential mobility.

iv) The number of available ion exchange sites in both soils and sherds has been constant since the sherds were buried. This is likely to be true for the soil, but will only be true for the sherds if the rehydration process which made available sites lost in firing, and opened up new sites, occurred over a short time compared with the burial period. Unfortunately, little is known of the time scale required for such processes, and this assumption is certainly a simplification which will tend to give an upper limit to the dose rate uncertainties arising from activity held on ion exchange sites.

Using these assumptions the annual dose rates and derived ages have been calculated as outlined in Appendix F, using the dose rate data of Appendix E. The annual dose rate terms derived for the supported Ra-226 hypothesis are given in table 7.5.2. The errors given are derived from measurement errors in isotope activities only.

Table 7.5.2 Comparison of annual dose rates derived from spectrometer analysis with published dosimetry information, in mrad yr^{-1}

	164m4	164m9	S164m7
effective alpha dose rate derived from:			
spectrometer data	480_{21}	344_{16}	-
published data	463	329	-
beta dose rates from:			
spectrometer data	411_{16}	327_{12}	-
published data	324 (421)	340 (326)	-
gamma dose rate from:			
spectrometer data	-	-	139_{8}
published data	-	-	162
total dose rates from:			
spectrometer data	890_{32}	726_{25}	-
published data	826	745	-

Note: 1) the errors, in the least significant figures, arise solely from measurement error in isotope activities. Specifically they do not include uncertainties in isotope stabilities.

2) the gamma dose rate calculated from spectrometer data includes an allowance for site water content of 16%, and cosmic ray correction of 10 mrad yr^{-1}, as some allowance for these effects is included in the published data (based on gamma TLD).

3) errors in the effective alpha dose rates do not include errors in the a value, which are common to both methods of calculation (see Appendix F).

4) water content corrections have not been included in the alpha and beta dose rates. They are included in the total dose rates.

5) the figures shown in parentheses below the beta dose rates are from beta TLD measurements (HUXTABLE, private communication). They were not available from HUXTABLE and AITKEN (1978) and are not used in calculating the total dose rates, or in calculating the routine dates of table 7.5.3.

The total dose rates for the unsupported hypothesis are about 15% larger than the total dose rates shown. Dose rates derived from the earlier measurements of HUXTABLE and AITKEN (1978) are also given for comparison. The ages derived from the spectrometer data are then compared with the published ages in table 7.5.3.

7.5.5 Discussion

The individual dose rates derived from routine analysis are in general in good agreement with those from gamma spectrometry, with the exception of the beta dose rate from sherd 164m4. This was derived from alpha counting and flame photometry, and as can be seen from section 8.5 (table 8.5.1), flame photometry underestimated the K-40 content by 60%. This is confirmed by the much improved agreement of the beta TLD measurements (HUXTABLE, private communication, shown in parentheses in table 7.5.2). The agreement between the alpha dose rates is surprising, as the unsealed alpha count rate observed was 18% higher than that predicted by gamma spectrometry. However, this error was almost exactly compensated for by an overestimation of the 'lost' count rate by gas cell analysis. These comparisons are detailed in sections 8.1 and 8.2, respectively.

The average age of the two sherds derived from routine data is within 130 years (2.5%) of that derived from the spectrometer data (5110 years) using the preferred hypothesis of supported Ra-226 activity. (The average age using the unsupported hypothesis is 4470 years.)

The errors given in tables 7.5.2 and 7.5.3 do not include uncertainties arising from potential isotope mobility. However, when estimates of these uncertainties based on the assumptions of the last section are included the total errors in the two TL ages increase by about 20%. This is a relatively small contribution, and is primarily because the TL errors are large; contrast this with the results of the next section, where the TL errors are small, and the effect of ion exchange uncertainties becomes more obvious.

7.5.6 Cheung Chan, Hong Kong

Sherds from this site have been dated using routine techniques by HUXTABLE (private communication) but produced an unacceptable

Table 7.5.3 Effect of spectrometer data on sherd ages

	164m4	164m9
Age, years, from:		
spectrometer data	4985_{510}	5235_{755}
published data	5370_{740}	5100_{850}

Note: 1) errors are in the least significant figures.
2) errors in dates derived from spectrometer data do not make allowances for isotope mobility.

scatter in the ages. It was therefore thought worthwhile to examine this material for possible disequilibria that might not be detected by routine techniques.

As with Sham Wan, this site is in loose sandy soil, the particular level studied (214b) was situated on a ridge about 1.5 m above sea level.

7.5.7 Samples measured

Eight sherds and one soil sample were analysed, all recovered from a depth of 0.5 m below the present surface. The sherds were in 'viced' form, as used for alpha counting. The averaged group activities of these samples are listed in table 7.5.4, with those ratios likely to be of interest.

7.5.8 Discussion

i) Groups 1 and 4; U-238 and Ra-226

All the sherds and the soil sample show Ra-226 excess to some degree, with the U-238 concentrations being more similar than those of Ra-226. The average U-238 concentration in the sherds is 2.0 pCi g^{-1}, and the largest deviations from this are numbers 13 and 18 at -20% and +20%, respectively. On the other hand the average Ra-226 concentration is 5.0 pCi g^{-1}, with the largest deviation, number 17, being 54%.

ii) Groups 5 and 6; Rn-222 and Pb-210

All of the sherds and the soil emanate Rn-222 considerably. The average escape from the sherds in the laboratory state is (50 $\pm$ 9)%; (40 $\pm$ 4)% escapes from the soil sample. However, the Pb-210 activities reveal that the soil sample was probably closer to equilibrium during burial, whereas there was greater Rn-222 escape from most of the sherds, except perhaps numbers 15, 16 and 18. The average loss of Rn-222 during burial for the remaining five sherds is (66 $\pm$ 5)%.

iii) Groups 7 and 8; Th-232 and Rn-220

The soil is significantly higher in Th-232 activity than all the sherds, except numbers 15 and 16. There is little or no

Table 7.5.4 Group activities of samples from Cheung Chan, lab. ref. 214, in pCi g^{-1}

Group	Long lived isotope	S214b soil	214b7 sherd	214b8 sherd	214b13 sherd	214b14 sherd	214b15 sherd	214b16 sherd	214b17 sherd	214b18 sherd
1	U-238	1.34_{12}	1.93_{13}	1.79_{14}	1.60_{16}	1.75_{16}	2.17_{14}	2.13_{15}	2.20_{18}	2.40_{16}
4	Ra-226	2.25_{14}	2.91_{17}	3.63_{18}	6.37_{23}	4.88_{24}	7.01_{26}	3.89_{22}	7.69_{28}	3.65_{19}
5	Rn-222	1.55_{3}	1.96_{4}	1.79_{4}	2.69_{5}	2.15_{6}	2.98_{7}	2.25_{5}	3.56_{8}	1.88_{4}
6	Pb-210	1.74_{5}	0.92_{11}	1.42_{9}	2.01_{14}	1.34_{16}	2.75_{16}	2.03_{19}	3.02_{19}	1.94_{8}
7	Th-232	6.15_{15}	3.28_{10}	4.06_{12}	3.54_{12}	3.80_{13}	5.80_{16}	3.57_{12}	7.15_{21}	4.03_{13}
8	Rn-220	6.27_{14}	3.47_{8}	4.31_{11}	3.55_{9}	3.74_{9}	5.66_{13}	3.43_{9}	6.98_{16}	3.84_{9}
	K-40	1.41_{46}	8.5_{10}	12.1_{9}	5.2_{11}	6.7_{12}	7.2_{10}	10.8_{7}	<1	7.0_{10}
Derived from above:										
Th-232/U-238		4.59_{43}	1.70_{17}	2.27_{19}	2.21_{23}	2.17_{21}	2.67_{19}	1.68_{13}	3.25_{29}	1.68_{12}
Ra-226/U-238		1.68_{18}	1.51_{13}	2.03_{19}	3.98_{42}	2.79_{29}	3.23_{21}	1.83_{17}	3.50_{31}	1.52_{10}
Rn-222/Ra-226		0.69_{4}	0.67_{4}	0.49_{3}	0.42_{2}	0.44_{2}	0.43_{2}	0.58_{2}	0.46_{2}	0.52_{3}
Pb-210/Ra-226		0.77_{5}	0.32_{4}	0.39_{3}	0.32_{2}	0.27_{3}	0.39_{3}	0.52_{6}	0.39_{3}	0.53_{4}
Rn-220/Th-232		1.02_{3}	1.06_{4}	1.06_{4}	1.00_{4}	0.98_{4}	0.98_{4}	0.96_{4}	0.98_{4}	0.95_{4}

Note: errors are in the least significant figures.

evidence for Rn-220 escape, and the comment by AITKEN (1978a) that any such escape is even less likely to occur when buried is again relevant.

Finally the K-40 concentrations are variable, with some surprisingly low. In one case, b17, it is below measurement level.

7.5.9 Potential radioisotope mobility

The proportion of activity carried on ion exchange sites has been investigated for two of these sherds and the soil sample. The activities of these samples, before exchange, immediately after exchange, and after between 50 and 90 days storage, are shown in table 7.5.5.

Although in the case of the soil sample there has probably been no overall U-238 loss, the sherds show a decrease in activity of 45% and 35%. The Ra-226 losses in the soil (25%) and the sherds (24% and 21%) are very similar, while those of Pb-210 are 25% from the soil and 20% and 60% from the sherds. Contrast these observations with those from Sham Wan, where there was no detectable U-238 loss from soil or sherd. The Ra-226 loss was 23%, and that of Pb-210 was 35%, but in this case only in the sherd.

Although there have been large losses in group 7, probably of Ra-228, no conclusion can be made as to the possible losses of Th-232. Nevertheless, as in the case of Sham Wan, this large proportion, up to 50%, of the Ra-228 activity held on ion exchange sites must be regarded as potentially mobile; it may be considerably out of equilibrium with Th-232 for many years after excavation, due to influx or removal of radium isotopes by the ground water. Group 8 shows a slight overall increase which is again attributed to Th-228 contamination of the $BaCl_2$.

7.5.10 Effect of spectrometer data on age evaluation

This site shows an alarming Ra-226 excess of up to 400% in all the sherds. The soil sample also shows a 60% excess (30% after exchange) and it is presumed that this excess must be supported by a combination of excess Th-230, and Ra-226 carried in the ground water. The presence of the much greater excesses in the sherds suggests that additional mechanisms may also be present in some cases and in particular the possibility of unsupported Ra-226 must

Table 7.5.5 Group activities before and after exchange for samples from Cheung Chan, lab. ref. 214, in pCi g^{-1}

Group	Long lived isotope	S214b (soil) before exchange	S214b (soil) within 48 hrs	S214b (soil) after 92 days	214b8 (sherd) before exchange	214b8 (sherd) within 48 hrs	214b8 (sherd) after 88 days	214b13 (sherd) before exchange	214b13 (sherd) within 6 days	214b13 (sherd) after 51 days
1	U-238	1.34_{12}	1.50_{6}	1.26_{12}	1.79_{14}	1.11_{12}	1.01_{11}	1.60_{16}	0.80_{15}	1.07_{15}
4	Ra-226	2.25_{14}	1.69_{16}	1.67_{15}	3.63_{18}	2.93_{12}	2.77_{15}	6.37_{23}	5.85_{19}	5.02_{20}
5	Rn-222	1.55_{3}	1.36_{4}	1.33_{4}	1.79_{4}	1.46_{4}	2.15_{4}	2.69_{5}	2.71_{6}	3.46_{7}
6	Pb-210	1.74_{5}	1.31_{12}	1.47_{13}	1.42_{9}	0.75_{7}	0.33_{7}	2.01_{14}	1.50_{14}	1.62_{15}
7	Th-232	6.15_{15}	4.14_{13}	4.18_{12}	4.06_{12}	1.98_{6}	1.95_{8}	3.54_{12}	2.55_{8}	2.40_{9}
8	Rn-220	6.27_{14}	5.42_{13}	6.72_{16}	4.31_{11}	2.60_{7}	4.21_{10}	3.55_{9}	3.46_{9}	4.71_{11}
	K-40	1.41_{46}	1.7_{8}	0.5_{7}	12.1_{9}	10.7_{8}	9.7_{8}	5.2_{11}	2.9_{9}	4.2_{9}

Note: errors are in the least significant figures.

be considered. However, the preferred hypothesis is again that all this Ra-226 is in fact supported, and it is suggested that the increased disequilibrium between Ra-226 and U-238 arises from the removal of uranium isotopes by leaching processes.

All the samples examined contained a considerable proportion of activity held on ion exchange sites, and so the daughter isotopes concerned, Ra-226, Ra-228 and Pb-210 may be very much out of equilibrium with their immediate precursors. Furthermore, the observed level of activity may or may not have been stable throughout the archaeological period. Thus large errors must be associated with any such activities.

The arbitrary errors of two thirds of the observed replaceable activity, as described in section 7.5.4, are again employed here. Thus sherd b8 has 45% of the Ra-226 held on ion exchange sites and so uncertainties of $\pm$ 30% are assumed in using the present day activity as a measure of the average historical activity. For those sherds where ion exchange measurements were not made, the average losses from sherds b8 and b13 were used as a guide in estimating uncertainties.

In addition it is assumed that:

i) the U-234 activity is the same as that of U-238. The Th-230 activity is taken to be given by U-238 for the assumption of unsupported Ra-226 excess, but as given by the fixed Ra-226 activity in the case of supported Ra-226 excess.

ii) in the unsupported hypothesis, Ra-226 excess is given by the difference between the total Ra-226 and the total U-238 activity.

iii) the ratio Pb-210/Ra-226 gives the amount of Rn-222 retention independent of the origins of the Ra-226 activity, i.e. whether it is supported or unsupported, exchangeable or fixed. The errors in the Pb-210 activities are primarily derived from uncertainties arising from the proportion of activity held on ion exchange sites.

iv) the uncertainties in Ra-228 concentration (group 7) due to the proportion of potentially mobile activity dominate the uncertainties in the activities of the rest of the Th-232 chain. This assumption was discussed in section 7.5.4.

v) the number of available ion exchange sites in both soil and sherds has been constant since the sherds were buried. This was also discussed in section 7.5.4.

Using these assumptions, the annual dose rates given in table 7.5.6 have been calculated as outlined in Appendix F using the dose rate data presented in Appendix E, and the TL data from table 7.5.7. The dose rates from the unsupported hypothesis are on average 14% larger than these shown. The resulting sherd ages are given in table 7.5.8. The dose rates and ages derived by HUXTABLE (private communication) using the same TL data,but orthodox dosimetry techniques, are also shown for comparison.

7.5.11 Discussion

The dose rates derived from routine techniques are in poor agreement with those from spectrometer analysis. In particular the routine alpha dose rates (derived from alpha counting and gas cell analysis) vary from +89% (b7) to -12% (b14). This discrepancy is again attributable to the unreliability of thick source alpha counting, and is discussed in detail in sections 8.1 and 8.2. As a result of this disagreement, the average site age from routine data is 11% less than that from gamma spectrometry.

The scatter in the ages of the eight sherds, which are believed on archaeological grounds to be contemporaneous, is 22% from routine techniques, and 18% from gamma spectrometry data. Thus although the use of the latter has reduced the spread in sherd ages, it is still large compared with that expected from the errors shown on the individual dates. However, these errors are derived from the measurement errors on the isotope concentrations of the sherds; when the estimated uncertainties from isotope mobilities, discussed in the previous section, are included, the error on the TL age for each sherd increases to $\pm$ 20% on average. This is consistent with the observed scatter, and seems to give strong support for the suggestion that isotope mobility has contributed significantly to the spread in the dates. Unfortunately, we cannot rely on this spread as a measure of the importance of this effect, as there will probably be a systematic component which affects all sherds, and which will

Table 7.5.6 Comparison of annual dose rates derived from spectrometer analysis with those from existing measurements, in mrad yr^{-1}

	214b7	214b8	214b13	214b14	214b15	214b16	214b17	214b18
effective alpha dose rate from:								
spectrometer	820_{23}	598_{16}	393_{11}	464_{22}	1250_{59}	639_{17}	1160_{46}	537_{19}
existing data	1548	660	488	407	1181	687	1192	695
beta dose rate from:								
spectrometer	228_{19}	294_{12}	222_{14}	227_{16}	326_{12}	283_{23}	298_{9}	258_{13}
existing data	248	256	207	266	301	266	285	259
gamma dose rate from soil sample S214b:								
spectrometer	294_{17}							
existing data	349							
total dose rate from:								
spectrometer	1210_{92}	1064_{72}	769_{43}	902_{48}	1415_{106}	1113_{56}	1329_{100}	958_{49}
existing data	1920_{192}	1141_{120}	887_{84}	944_{118}	1407_{181}	1196_{101}	1401_{163}	1146_{103}

Please see notes on following page.

Notes to table 7.5.6

1) the estimated errors in the routine individual alpha, beta and gamma dose rates are not known in detail, but may be assumed to be between 5 and 10%. The errors in the routine total dose rates were calculated by HUXTABLE (private communication), from whom all the routine data were obtained. All the errors are shown in the least significant figures.
2) water content corrections are not included in the individual alpha and beta dose rates. They are included in the gamma and total dose rates.
3) routine dose rates are based on alpha counting, with gas cell analysis, flame photometry, and beta TLD (see chapter 8).
4) errors given in the spectrometer dose rates are measurement errors only. Those uncertainties arising from isotope mobilities are discussed in the text.
5) errors in $\underline{a}$ values are not included in the individual alpha dose rates, as they are common to both sets of measurements. They are included in the total dose rates.

Table 7.5.7 TL and saturation water content data for sherds from Cheung Chan

	214b7	214b8	214b13	214b14	214b15	214b16	214b17	214b18
archaeological dose, AD, rads	4364 4%	5162 4%	3575 3%	3949 3%	6300 4%	5445 4%	4940 4%	6050 4%
a value	0.29 10%	0.17 10%	0.11 5%	0.14 2%	0.24 4%	0.19 6%	0.19 6%	0.15 5%
saturation water content, %	12.5	14	26	12.5	35	11	35	17.5

saturation water content of soil: 25%

Note: 1) sherds and soil are assumed to have been 0.8 ± 0.2 of saturation throughout the burial period.

2) data kindly provided by J. Huxtable.

Table 7.5.8 Effect of spectrometer data on sherd ages

Age, years, derived from:	214b7	214b8	214b13	214b14	214b15	214b16	214b17	214b18
spectrometer	3610_{360}	4850_{450}	4650_{380}	4380_{350}	4450_{440}	4890_{400}	3720_{380}	6320_{530}
routine data	2270_{270}	4520_{560}	4030_{480}	4180_{580}	4480_{640}	4550_{490}	3530_{470}	5280_{590}

Average site age from:		standard deviation
spectrometer	4610	840 (18%)
routine data	4110	890 (22%)

Note: 1) all errors are in the least significant figures, and are total errors.

2) dates derived from routine data are from HUXTABLE (private communication).

3) errors in spectrometer ages do not contain contributions from uncertainties arising from ion exchange properties.

not reveal itself as random scatter.

7.5.12 Alpha spectrometry analyses

In sections 7.5.4 and 7.5.10, where the assumptions necessary for the calculations of the annual dose rate to material from site 164, Sham Wan, and 214, Cheung Chan, were set out, it was acknowledged that there was uncertainty in the level to which Ra-226 was supported by Th-230. In an attempt to resolve some of these uncertainties, four sherds were submitted for analysis by alpha spectrometry at the 'Physical Tracers Studies Group', Harwell. The actual samples used were those which had previously been analysed by gamma spectrometry; they were each divided into two aliquots, and the observed isotope activities are given in table 7.5.9 (IVANOVICH, private communication). The relevant gamma spectrometry analyses, taken from tables 7.5.1, 7.5.4 and 7.5.5, are also shown, as are the ratios of the average alpha spectrometry activities to those derived from gamma spectrometry.

The agreement between the U-238 measurements on the three sherds before exchange is good. However, the remaining U-238 analyses of sherd 214b8 88 days after exchange are very discrepant. This is unlikely to be a result of disequilibrium between U-238 and Th-234, the isotope actually measured by gamma spectrometry, because the activity of Th-234 should be within at least 8% of equilibrium with that of U-238 at the end of the 88 day storage period. However, it is possible that gamma spectrometry underestimates the activities of low energy peaks, such as that at 63 keV from Th-234 because of the presence of barium in exchanged samples, although this is not thought to be a significant effect. The ratio of the mass attenuation coefficient of barium to that of pottery at 60 keV is about 30/1, which implies that barium would have had to replace more than 10% of the dry weight of the sherd in order to explain the 80% difference observed in the apparent U-238 activities. Even in raw clays, this would be extremely unlikely. In addition, there is evidence from two soil samples from site 222, one from site 214, and one sherd from site 164, that the concentration of barium is not sufficient to interfere with these analyses at any rate. In the two soils from site 222 (section 7.6), numbers 2 and 28, the intensity of the 46 keV peak has remained

Table 7.5.9 Activities of sherds from alpha and gamma spectrometry, in pCi g^{-1}

Group	Long lived isotope	Analytical technique	164m9 before exchange	164m9 after 88 days	214b8 before exchange	214b8 after 88 days	214b13 before exchange	214b13 after 51 days
1	U-238	alpha	1.94_{5}	-	1.97_{5}	1.73_{5}	1.70_{5}	-
		alpha	1.88_{5}	-	1.97_{5}	1.81_{5}	1.67_{6}	-
		gamma	2.01_{17}	1.91_{19}	1.79_{14}	1.01_{11}	1.60_{16}	1.07_{15}
		alpha/gamma	0.95	-	1.10	1.75	1.05	-
2	U-234	alpha	2.16_{6}	-	1.99_{5}	1.81_{5}	1.62_{5}	-
		alpha	1.94_{5}	-	2.00_{5}	1.83_{5}	1.59_{6}	-
3	Th-230	alpha	1.62_{11}	-	1.63_{23}	2.82_{25}	1.06_{17}	-
		alpha	1.74_{10}	-	2.42_{15}	2.40_{23}	1.07_{9}	-
4	Ra-226	gamma	4.03_{22}	3.11_{26}	3.63_{18}	2.77_{15}	6.37_{23}	5.02_{20}
7	Th-232	alpha	1.62_{11}	-	2.00_{24}	3.52_{31}	1.27_{20}	-
		alpha	2.30_{13}	-	3.19_{19}	2.91_{27}	1.57_{13}	-
		gamma	2.96_{10}	2.30_{9}	4.06_{12}	1.95_{8}	3.54_{12}	2.40_{9}
		alpha/gamma	0.66	-	0.64	1.65	0.40	-

Note: 1) the average alpha spectrometry results (IVANOVICH, private communication) are used in calculating the ratios.
2) errors are in the least significant figures.

constant despite changes of 60% and 45%, respectively, in the U-238 activity as measured by the 63 keV Th-234 peak. Sherd 164m9 and soil S214b show a reverse trend; the 63 keV peak stayed constant, but the Pb-210 peak at 46 keV dropped in intensity. Thus it is thought to be very unlikely that in the particular sample in question here, enough barium had been adsorbed in the exchange process to seriously undermine the reliability of the measurement of U-238 after exchange by gamma spectrometry.

On the other hand, the presence of barium was thought to interfere in the dissolution of the sample, a step leading to the extraction and analysis of the uranium isotopes. Preferential loss of the spike uranium isotope is thought to be a possible reason for the observed discrepancy (IVANOVICH, private communication). The same would of course apply to the U-234 measurements in this sample.

Now consider the Th-232 results. Bearing in mind that the gamma spectrometer actually determines the activity of Ra-228 (half life 5.8 years) by analysing the Ac-228 activity (half life 6 hours), it could be concluded that for the three samples before exchange Ra-228 is consistently in excess by between 40% and 60%. This would imply that the excess radium was supported by adsorption from ground water during burial. However, this is not in fact believed to be the explanation for these discrepancies. Consider sherd 214b13. The activity of Ra-228 after exchange indicates that the fixed (and therefore presumably supported by Th-232) Ra-228 is 50% above the larger of the two alpha spectrometry measurements of the Th-232 activity. When this evidence is taken into consideration with the large scatter in the Th-232 results, of between 18% and 45%, it is apparent that some large variable systematic error is affecting the Th-232 analyses by alpha spectrometry. This is consistent with Ivanovich's observations that all these samples, especially sherd 214b8 after exchange, were difficult to bring into solution satisfactorily.

Clearly if the Th-232 results cannot be relied upon, the same conclusion must also apply to the Th-230 analyses. It is interesting to note that if correction factors derived from the alpha/gamma ratios for Th-232 are applied to the Th-230 results, they then become consistent with the fixed Ra-226 activities observed by gamma spectrometry,

at least in the case of sample 164m9 and 214b8. However, it must be reluctantly concluded that alpha spectrometry has not resolved any of the uncertainties that arose from the gamma analyses of these three samples, and so the assumptions made in calculating the average annual dose rates to these sherds must remain assumptions.

7.6 SAMPLE SELECTION USING RADIOISOTOPE ANALYSIS

7.6.0 La Cotte, Guernsey

This site was examined in detail using gamma spectrometry before the investment of significant TL research effort. It consists of a series of floor levels in a partially collapsed granite cave on a headland on the island of Guernsey, and is unusual in that the material to be dated is burnt flint. At the time of writing no reliable TL data has been obtained. Nevertheless, it serves to illustrate the use of detailed radioisotope analysis in selecting the material most likely to give accurate dates.

The dosimetry of burnt flint is relatively simple, as the internal activity is usually very low. Thus almost all the archaeological dose is derived from environmental gamma and cosmic rays. The problem is then to ensure that the soil matrix is such that the gamma dose can be measured accurately and that it is likely to have been stable over the period of interest.

7.6.1 Material studied

Five soil samples were analysed, four of these were subsequently used in ion exchange experiments. The samples were lightly crushed to break up agglomeration of grains, and had been dried after excavation. The averaged group activities of these five samples are shown in table 7.6.1.

7.6.2 Discussion

This is clearly a very complex site! The five samples fall into two well defined groups on the basis of their U-238 series activities, namely numbers 2, 28 and 29, and numbers 10 and 23. The three low activity samples have Ra-226/U-238 ratios within 30% of equilibrium. Of the remaining two, the Ra-226 activity of sample 23 is within 4% of equilibrium, whereas that of sample 10 is only 50% of

Table 7.6.1 Group activities before and after exchange for samples from La Cotte, lab. ref. 222, in pCi g^{-1}

Group	Long lived isotope	222/2 before exchange	222/2 after 75 days	222/10 before exchange	222/10 after 80 days	222/23 before exchange	222/23 after 81 days	222/28 before exchange	222/28 after 84 days	222/29 before exchange
1	U-238	1.41_{7}	0.60_{6}	11.2_{4}	5.9_{2}	13.1_{4}	9.4_{3}	0.69_{11}	0.39_{11}	0.74_{7}
4	Ra-226	1.00_{14}	1.23_{12}	6.0_{3}	6.4_{2}	12.7_{4}	10.4_{3}	0.82_{15}	0.79_{12}	0.81_{13}
5	Rn-222	0.77_{2}	0.68_{5}	3.30_{7}	3.61_{6}	3.71_{8}	5.6_{1}	0.42_{3}	0.52_{2}	0.44_{3}
6	Pb-210	1.16_{10}	1.11_{10}	3.8_{2}	2.07_{11}	6.4_{2}	3.3_{2}	0.94_{11}	1.0_{1}	0.91_{9}
7	Th-232	1.24_{7}	0.65_{5}	2.43_{10}	1.43_{6}	1.24_{7}	0.97_{7}	0.47_{4}	0.46_{8}	0.65_{5}
8	Rn-220	1.11_{3}	1.63_{5}	2.16_{6}	2.55_{6}	1.04_{4}	1.92_{5}	0.44_{2}	1.79_{5}	0.53_{2}
	K-40	19.1_{7}	7.28_{10}	22.4_{8}	19.9_{9}	34_{1}	34.5_{11}	4.4_{10}	6.2_{9}	7.6_{9}
Derived from above:										
Th-232/U-238		0.88_{7}		0.22_{1}		0.095_{6}		0.68_{12}		0.88_{11}
Ra-226/U-238		0.71_{11}		0.54_{3}		0.97_{4}		1.19_{29}		1.09_{20}
Rn-222/Ra-226		0.77_{11}		0.55_{3}		0.29_{1}		0.51_{11}		0.54_{9}
Pb-210/Ra-226		1.16_{16}		0.63_{5}		0.50_{2}		1.15_{25}		1.12_{21}
Rn-220/Th-232		0.90_{6}		0.89_{5}		0.84_{6}		0.94_{9}		0.82_{7}

Note: errors are in the least significant figures.

Figure 7.7.3 Fractional Rn-222 retention plotted against the fraction of non-exchangeable Ra-226

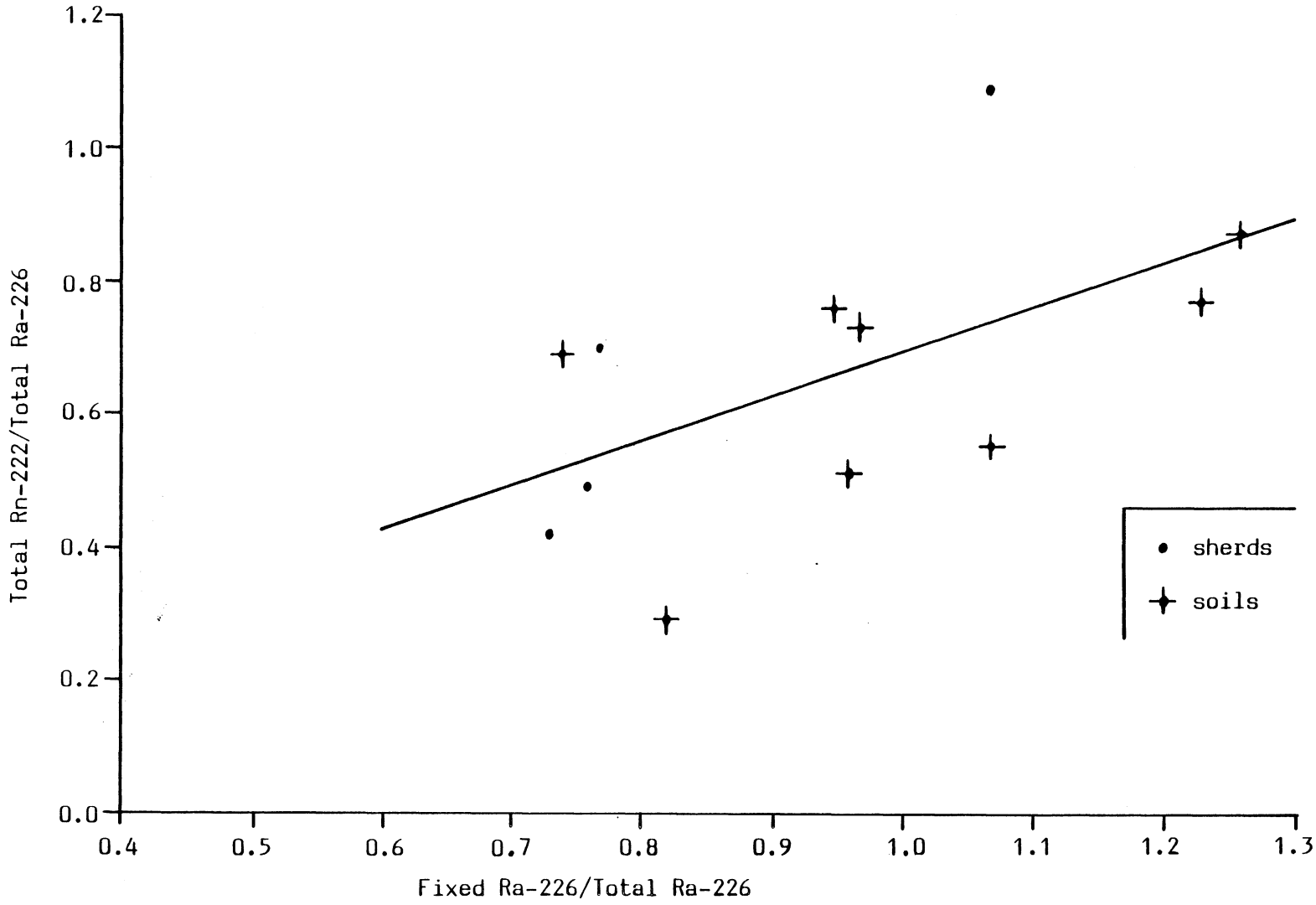

daughter products would imbed themselves in the grains of the low activity soils in a similar manner to that discussed earlier (section 6.1.2) in connection with Rn-222 escape mechanisms. Such high Rn-222 levels are likely in view of the radium activities and emanation levels of the other two soils from this site.

In the thorium series, losses from group 7 of between 22% and 48% occur in three samples, but no. 28 shows no detectable loss. There is the usual increase of the activity of group 8, again attributed to contamination.

One sample, soil 2, shows a 60% loss of K-40, the other potassium activities remain stable.

7.6.4 Conclusion

As the TL information is not yet available the detailed calculation of the dose rates will not be presented. However, it can be concluded that the uncertainties in the gamma dose rates derived from samples 10 and 23 are about $\pm$ 23%, and thus these dose rates will be much less reliable than those from the other three soils, nos. 2, 28 and 29, with associated uncertainties of about $\pm$ 10%. Thus the dating effort should be directed in the first instance to flints associated with the latter soil samples.

7.7 PATTERNS AND TRENDS IN THE DATA ALREADY PRESENTED

The preceding sections have presented detailed analysis of some 30 sherds and 11 soils and clays. Five of these sherds and 9 soils and clays have been further analysed for ion exchange properties. It is thus possible to re-examine this data for general patterns and trends which can be expected to apply to samples independent of origin.

Various possible combinations of isotope ratios, activities held on exchange sites and water contents have been examined for correlations but only a few patterns stand out sufficiently clearly to be worth discussing in any detail, and these primarily concern the behaviour of Rn-222 before and after excavation, and the conclusions to be drawn from this behaviour.

the U-238 activity. There is a considerable degree of Rn-222 escape from all samples, ranging between 30% (no. 2) and 70% (no. 23). However, the Pb-210/Ra-226 ratios again confirm the division into two groups. The three low activity samples all have ratios greater than unity (although not significantly) whereas the two high activity samples indicate a loss of Rn-222 daughters in the buried state of about 45%. This is discussed further in the next section.

All samples show evidence of Rn-220 escape; calculations given in section 6.6.12 indicate that this escape (12% on average) should be doubled to give the Rn-220 escape before sealing into the sample holder.

Finally the Th-232/U-238 ratio of 0.095 $\pm$ 0.006 from sample 23 is worthy of notice as the lowest value observed in all the samples described in this thesis.

7.6.3 Potential radioisotope mobility

Four soils were examined for ion exchange properties in the usual way. The apparent group activities after storage are included in table 7.6.1. The activities immediately after exchange were analysed, but have been omitted to permit the presentation of all the data on one table. In general, the Th-234 activity appeared to have dropped markedly during the exchange, and then decayed by only 8% on average during the storage period. There were no significant changes in the Pb-210 or Ra-228 activities with storage, as expected.

All four samples lost between 30% and 50% of the initial U-238 concentration in the exchange process; on the other hand only no. 23 shows a measurable loss (about 20%) of Ra-226. Only samples 10 and 23 lost significant Pb-210 activity, about 47%. This may indicate a mechanism to explain why the Pb-210/Ra-226 activity ratios of the three low activity samples are close to unity, or perhaps even slightly above. As none of the Pb-210 is exchangeable, it is unlikely to be due to Pb-210 ions in the ground water. Similarly, it is unlikely to be due to retention of the radium daughters of the samples themselves, as they all emanate considerably both before and after ion exchange. However, if the Rn-222 activity in the ground water and soil gas is high, then it is possible that the recoil nuclei of

7.7.1 Laboratory escape of Rn-222, and Ra-226 excess

Figure 7.7.1 shows the activity ratio Rn-222/Ra-226 plotted against that of Ra-226/U-238 for sherds. Figure 7.7.2 shows the same data for soils. Note that the points plotted include data for 15 Peruvian soils listed in section 7.7.3. It can be seen that, for sherds at least, there is a trend of decreasing Rn-222 retention with increasing Ra-226 excess, and it is tempting to suggest that this trend is related to Ra-226 trapped on ion exchange sites. This possibility is considered further in the next section.

7.7.2 Deductions from ion exchange behaviour

The activity ratio of Rn-222/Ra-226 before exchange is plotted against the ratio of the Ra-226 activity after exchange to that before for both soils and sherds in figure 7.7.3 and there is a clear tendency for the fractional radon retention to increase as the fraction of exchangeable radium decreases. The equation of the straight line shown, derived from linear regression, is:

$$\left(\frac{\text{Ra-222}}{\text{Ra-226}}\right)_{\text{before exchange}} = 0.02 + 0.68 \left(\frac{\text{Ra-226}}{\text{Ra-226}}\right)^{\text{after exchange}}_{\text{before exchange}}$$

The correlation coefficient is 0.58, which implies that we may be 95% confident that there is a relationship between the two parameters, (NATRELLA, 1963). The estimated standard deviations in both the slope and intercept is 0.3. While it would be desirable to establish this relationship more firmly, by collecting more data, it is in any case useful to consider the reason for this observed correlation.

The conventional mechanism to describe the escape of radon from a grain by direct recoil into the surrounding air and water was described earlier (section 6.1.2). However, it is recognised that although this model successfully predicts the increase in emanation with increasing water content, it is not sufficient to account for the degree of escape observed. The 'indirect recoil' model (TANNER, 1978) increases this theoretical escape by suggesting that the fraction of those recoil radon nuclei that are not stopped in the spaces between grains, perhaps because these spaces are air filled, may still escape from the mineral phase. As these recoil nuclei collide with

Figure 7.7.1 Fractional Rn-222 retention plotted against Ra-226 excess: sherds

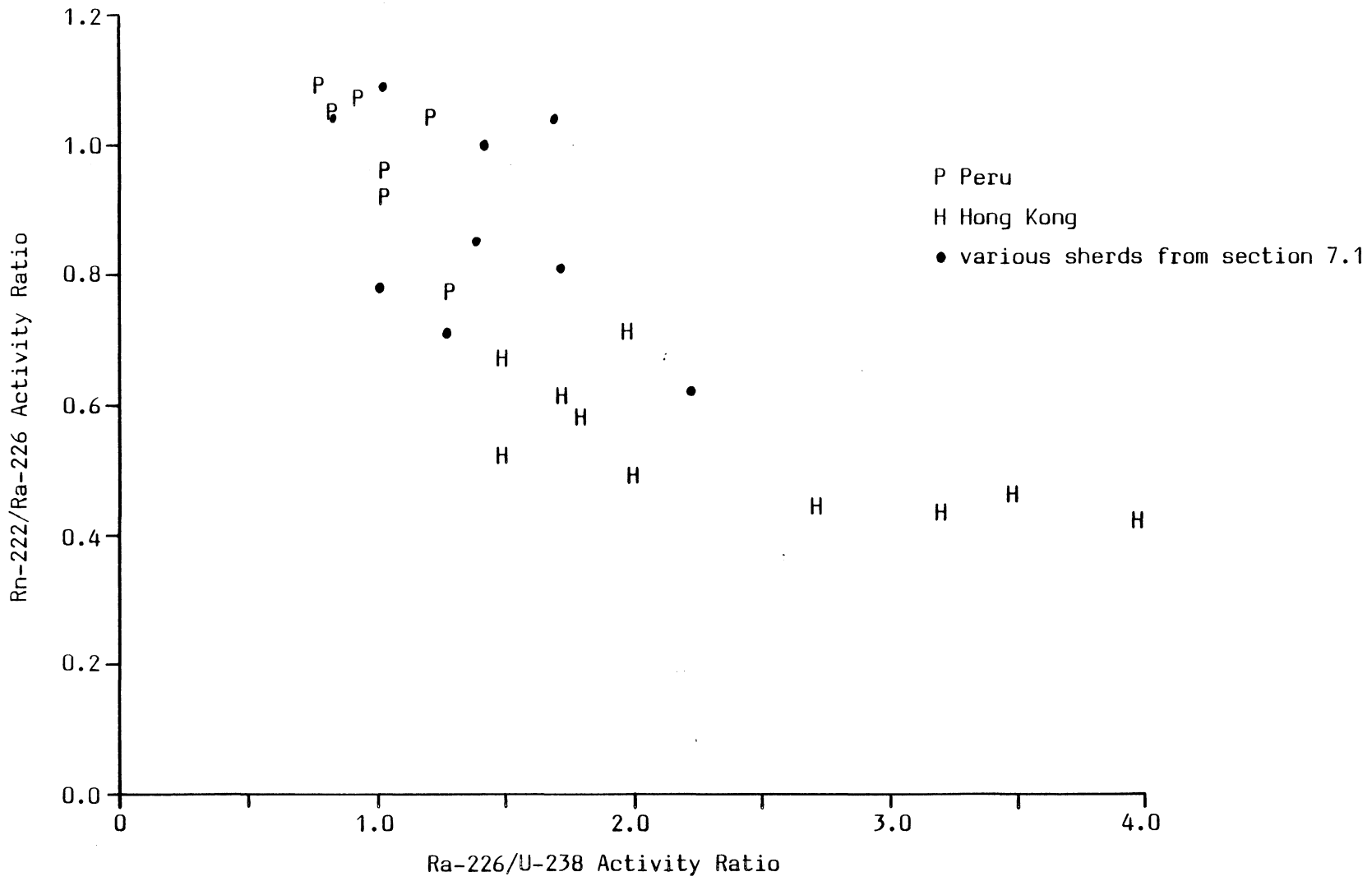

Figure 7.7.2 Fractional Rn-222 retention plotted against Ra-226 excess: soils

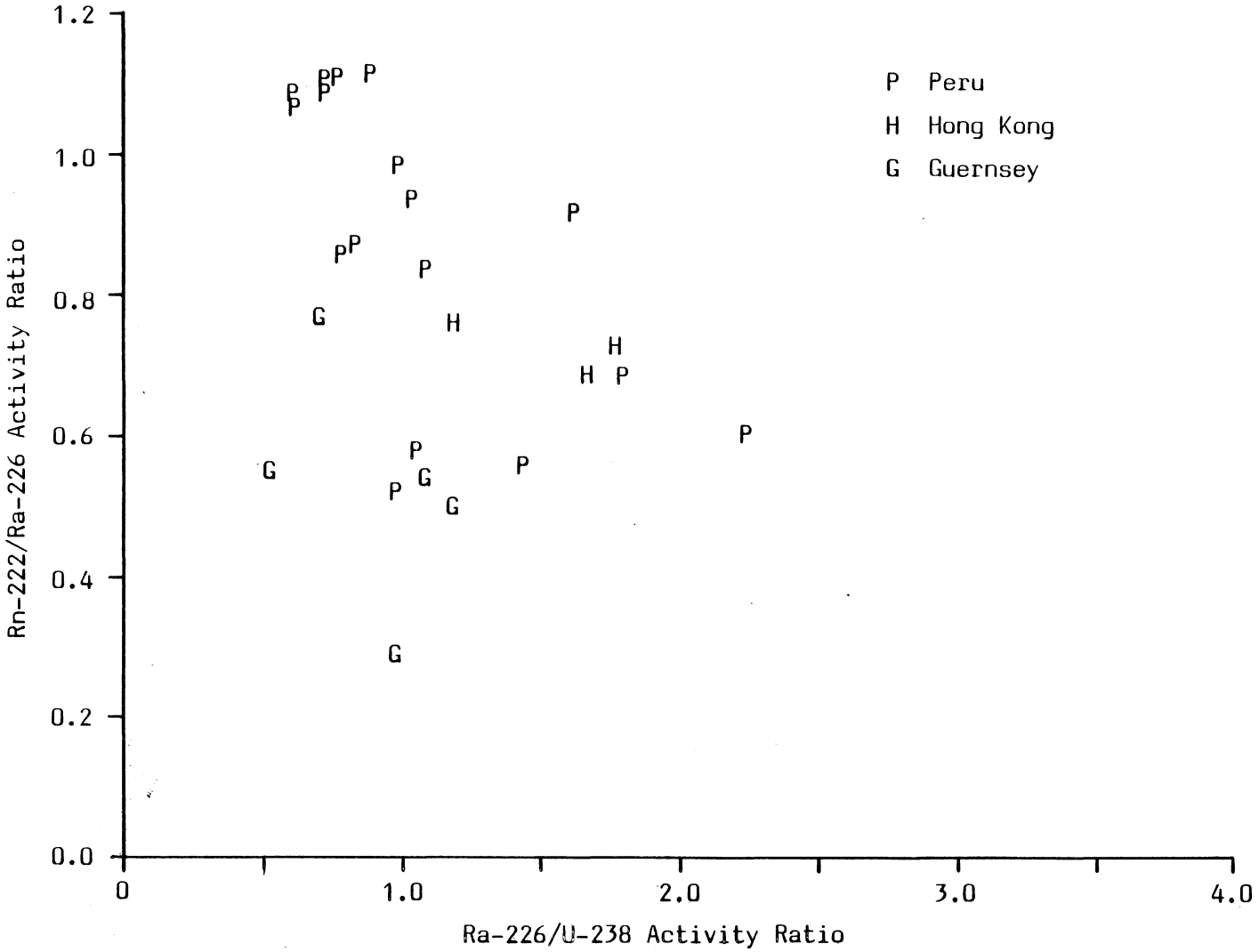

adjacent grains, they embed themselves in a pocket of highly disturbed material (estimated as up to 10 nm deep and 1 nm wide by ZIMEN and MERTENS, 1971). The energy of the interaction is such that this material is in fact vapourised, which gives a significant probability that the nucleus will diffuse back into the cavity between the grains, thus increasing the total amount of radon emanation. However, even if all the radon produced in the outer 70 nm shell of a grain (the maximum range of a recoil nucleus in a mineral lattice, QUET, 1975) is able to escape, this still only allows a maximum of about 20% emanation if the parent radium is homogeneously distributed throughout a 2 μm diameter grain. Much larger degrees of escape have been observed for samples with larger average grain sizes than this - for example, most of the soils described in this chapter - and so TANNER (1978) concludes in his extensive review of the literature that the development of large internal surfaces, such as may result from chemical corrosion, weathering, or intensive fracturing on a microscopic scale, is necessary before the emanation levels observed can be accounted for. He also postulates the existence of secondary crusts or films of radium on the surface of intact crystals of host minerals.

From the data presented earlier in this chapter, it is apparent that in at least two sites (164 and 214, both from Hong Kong) a significant fraction of Ra-226 was held on ion exchange sites accessible to aqueous solutions. Both of these sets of samples were recovered from deep layers on beach sites and the proportion of decayed organic material in both sherds and soils was apparently small; it is concluded that clay minerals are probably responsible for this exchange behaviour. On this basis the following model of a clay lattice structure with Ra-226 atoms held on ion exchange sites between the lattice plates in layers of water molecules is used for discussion. These layers are typically less than 30 nm wide, the lattice plates themselves are less than 10 nm, (MARSHALL, 1977), and so a recoiling radon nucleus could punch through one or two such layers before coming to rest. If it stopped in a water layer, then it would be free to diffuse (direct recoil); if it stopped within a lattice plate, then the indirect recoil mechanism would obviously be

very important. Thus it seems likely that any radium held in hydrated clays will produce radon with a high probability of escape. The majority of such radium will be ion exchangeable, and so we expect to see a correlation between an increased fractional retention of radon and decreased fraction of radium held on ion exchangeable sites as was found in figure 7.7.3.

With the model of radon escape developed in the preceding paragraph, let us re-examine the ion exchange data. As discussed above, the exchangeable radium is likely to be held by hydrated clays. The non-exchangeable (fixed) Pb-210 should be a measure of the radium activity held deep within intact crystals and unhydrated clay grains. The difference between the activities of fixed Ra-226 and fixed Pb-210 gives a measure of the Ra-226 activity held in such intact crystals and unhydrated clay grains within 70 nm of the grain surface. If it is assumed that 50% of the radon derived from this radium recoils into the grain rather than out, and that the grain is large compared with the recoil range, then approximately 60% of the daughter activity of radium from this shell region will have recoiled out of the grain before the Pb-210 step in the chain. (There are 4 alpha decays between Ra-226 and Pb-210). Thus the difference between the fixed Pb-210 and fixed Ra-226 activity represents about 60% of the Ra-226 held within this 70 nm layer around the emanating grain. Knowing the ratio of this radium activity to that of the total radium within the whole grain permits a calculation of the effective grain size of the average radium containing grain. The details of this calculation, and the assumptions made therein, are given in Appendix G. Table 7.7.1 gives the measured values of the fixed Pb-210 to the fixed Ra-226 ratios, and the derived effective grain sizes, read from figure G1 in Appendix G. Unfortunately no detailed grain size analysis of these samples was made, but nevertheless, some general comments are possible.

The soils were made up of coarse, sand sized grains, (i.e. greater than about 100 μm) especially those from sites 164 and 214. However, the effective grain size for most of the soils is about 1 μm or less. This supports TANNER (1978) in his conclusion that intensive fracturing on a microscopic scale is important in the escape of radon. In both the Hong Kong sites the effective grain size of the sherds appears to be significantly smaller than that of the soils, which

Table 7.7.1

Effective grain size derived from Pb-210/Ra-226 activity ratios after ion exchange

Sample	Pb-210/Ra-226 activity ratio	Effective grain diameter, μm
P12K02	0.81_{7}	$0.90^{+0.56}_{-0.26}$
P41J*	0.68_{10}	$0.51^{+0.25}_{-0.13}$
P41J11	1.11_{15}	>4
S164p*	0.80_{11}	$0.9^{+1.1}_{-0.3}$
S164m7*	0.88_{12}	$1.5^{+}_{-0.7}$
164m9	0.54_{5}	$0.34^{+}_{-}0.04$
S214b*	0.83_{9}	$1.0^{+1.2}_{-0.4}$
214b8	0.20_{2}	$0.16^{+}_{-}0.02$
214b13	0.32_{2}	$0.20^{+}_{-}0.02$
S222/2*	0.71_{9}	$0.57^{+0.28}_{-0.12}$
S222/10*	0.32_{2}	$0.20^{+}_{-}0.01$
S222/23*	0.34_{2}	$0.21^{+}_{-}0.01$
S222/28*	1.22_{20}	∞

Note: 1) errors in the activity ratios are in the least significant figures.

2) samples marked with an asterisk are soils.

3) for a discussion of the errors in grain diameters, see Appendix G.

is not surprising when the components of pottery and the effects of rehydration are considered. However, for the samples from site P41 the reverse is true, and this is thought to reflect the well preserved nature of the fired material recovered from this site (see section 7.4.6). In this case it is presumed that the grain growth arising during the firing process is still an important factor. Generally the effective grain size of the two Peruvian sherds, P12K02 and P41J11, is greater than that of the three Hong Kong sherds, and this is consistent with the expected levels of rehydration inferred from the site water contents and the ion exchange behaviour.

Finally, consider the results from site 222. Both the low activity soils have large effective grain sizes compared with the high activity samples (nos. 10 and 23), indeed the grains of soil 28 are apparently infinite! In both cases the Pb-210/Ra-226 activity ratios after exchange are much closer to equilibrium than those of the high activity soils, despite an average Rn-222 escape in the laboratory of 40% after exchange. It was suggested in section 7.6.3 that although the Pb-210 activity in these two samples is not exchangeable, nevertheless, some fraction of it may be the decay product of Rn-222 produced some metres away, and then transported, by the ground water or soil gas, into the low activity soils. If the levels of Rn-222 escape immediately after exchange are used instead of Pb-210 in the Pb-210/Ra-226 ratios, and the grain sizes recalculated, then effective diameters of 0.35 μm and 0.48 μm are obtained from soils 2 and 28, respectively, which are much closer to the effective diameter of 0.2 μm of the other two soils from the site.

7.7.3 Radon migration before and after burial

It has been suggested by AITKEN (1978a) and others that Rn-222 escape should be greater during burial than after excavation because of increased wetness during burial. Although this has been demonstrated in the laboratory (e.g. DESAI, 1975) little evidence for such increased escape 'in the field' exists.

The activity ratios of Pb-210/Rn-222 before exchange for 28 sherds (two were rejected because the errors were atypical) and 20 soils (including those of table 7.7.2) have been calculated. For

Table 7.7.2

Some activity ratios for 15 Peruvian soils

Sample	Pb-210/Rn-222	Rn-222/Ra-226	Ra-226/U-238
P02	1.10_{8}	0.69	1.82
P04J	0.98_{19}	1.09	0.62
P06	1.33_{18}	0.83	0.80
P10K	1.07_{15}	1.11	0.74
P17L	1.07_{13}	1.14	0.74
P23A	1.03_{14}	0.84	1.11
P34	0.85_{13}	0.92	1.62
P35J	1.08_{10}	1.12	0.91
P35K	1.14_{14}	0.99	1.01
P37J	1.08_{10}	0.58	1.06
P37L	1.45_{16}	0.56	1.45
P37Q	1.46_{16}	0.52	0.99
P39J	1.24_{12}	0.94	1.06
P40J	1.41_{16}	0.61	2.25
P45J	1.51_{29}	1.07	0.63

Note: the errors given are in the least significant figures.

the sherds the average was 0.88; only one sherd had a value for this ratio greater than unity. The corresponding average for soils was 1.15; two soils had values below unity. If we can assume that on average the Pb-210 activities reflect the buried Rn-222 activities, then it appears that most soils retain more Rn-222 before excavation than after despite a higher water content. This is probably because of the soil overburden inhibiting gas migration. (Note that site 222 has been omitted from this averaging, not because it does not show these trends, but because it shows them atypically strongly). For sherds, on the other hand, the laboratory findings of DESAI (1975) are confirmed. In general sherds emanate more before excavation than they do in the dry laboratory state.

Finally, the ratios of Rn-222 activity before and immediately after immersion in the ion exchange solution have also been calculated where possible. This ratio is presumed to give an estimate of the maximum increase in Rn-222 escape going from a dry crushed sample of sherd, or loose dry soil, to a sample dispersed in water. (The presence of $BaCl_2$ in the solution should not significantly affect this escape, as Rn-222 exists as a neutral atom, and so should not participate in exchange reactions). This information is only available for four sherds, and the average ratio is 0.88, standard deviation 0.04. For four soils the average ratio is also 0.88, standard deviation 0.04. These figures suggest that for both soils and sherds under similar physical conditions, the increase in escape going from a dry to a saturated state is similar, at about 10 to 15%. Thus it appears likely that the differences observed between soils and sherds, in the escape of Rn-222 before excavation and in the laboratory, arises from the differing porosity and structure of sherds compared with soils rather than because of basic differences in the behaviour of their component mineral grains under dry and wet conditions.

7.8 CONCLUSION

Gamma spectrometry has been used in the radioisotope analysis of both soils and sherds, and the data that has been presented shows that it is a valuable tool in unravelling the complex origins of the annual dose rate term.

The first part of this chapter (sections 7.1 to 7.3) described work undertaken in an attempt to identify problems worth further investigation. The most interesting feature that appeared from a study of the radioisotope concentrations of 11 sherds from various geographical locations was the presence of excess Ra-226 activity, compared with the activity of U-238, in almost every sherd. The problem of inhomogeneity of activity with grain size was discussed in section 7.2, and measurements made on a recently fired pottery fragment described. It seems probable that the 40% increase in activity of the 2 to 8 μm fraction compared with that of the bulk sample may be an important effect in unweathered pottery, but unfortunately, it is rare that archaeological samples are sufficiently large to permit this kind of detailed analysis, which required nearly a kilogram of material. This subject needs further study, to investigate to what extent it is a problem in archaeological samples.

Preliminary investigations of the ion exchange properties of a clay and a sherd was described in section 7.3, and although only about 15% of the activity of the uranium and thorium series in the sherd was replaceable, it was clear that this could give rise to serious uncertainties in dose rate calculations, and it was decided to incorporate this step in the detailed site by site analysis described in sections 7.4 to 7.6.

Fortunately for the work described in chapter 5, it can be concluded from section 7.4 that routine techniques are adequate for estimating the annual dose rate for well preserved sherds where there is little or no series disequilibrium or complications from ion exchange. For site P12 the routine techniques underestimated the age by only 6%, compared with that from gamma spectrometry; for site P41 this increased to 10%. The estimated total errors in the dates were similar for both methods, and easily covered the differences between the two techniques.

However, for sites where a significant proportion of activity is held on ion exchange sites, and where Ra-226 excess and Rn-222 escape is important, routine techniques may seriously underestimate the true errors on individual dates. Although the movement in the site age of Sham Wan (site 164) was only 3% (average of two sherds)

due to a fortuitous cancelling of gross errors in alpha counting and gas cell analysis (see also sections 8.1 and 8.2), gamma spectrometry showed that isotope measurement error does not fully describe the uncertainties in the annual dose rate, and that possible variation in the average activity held on ion exchange sites is an additional source of error. From a consideration of the soil exchange properties, it is concluded that the Ra-226 in these samples is probably supported, although whether by Th-230 or deposition from ground water, it is impossible to decide. In site 164 ion exchange properties increase the typical errors from 12% to about 15%, for site 214, Cheung Chan, the same problem increased the typical errors from 9% to 20%. The standard deviation in the dates from the latter site was 18% even using dose rates derived from gamma spectrometry, which is about three times what would be expected from the error in an individual date, and it is believed that this anomalous spread is firm evidence that the uncertainties arising from ion exchange properties do indeed contribute to the total errors in sherd ages. On average, for the eight sherds studied from this site, routine techniques gave rise to a systematic underestimate of the age by about 12%.

For a site with widely varying soil activities and radioisotope exchange properties, gamma spectrometry combined with ion exchange experiments has also been shown to be a useful tool for aiding the selection of material likely to produce reliable dates.

In assessing errors arising from ion exchange experiments, it has been assumed that the importance of such errors is proportional to the fraction of exchangeable activity. It is recognised that this assumption is not necessarily true. It is possible to consider a sample with a large total ion exchange capacity, but which does not have significant replaceable activity, perhaps because the ground water carries negligible concentrations of radioisotope ions. In any future work it would be desirable to monitor this total ion exchange capacity, and this can be done easily by a minor modification to the exchange experiment. If a known activity of Ba-133 was added to the $BaCl_2$ solution, then the activity absorbed by the sample would give a direct measure of the total exchange capacity, because the ratio of Ba-133 to the stable isotope would be known. The absorbed

activity would be readily determined by gamma analysis of one or more of the several gamma peaks from Ba-133. Other replacement combinations, such as Na-22 added to NaCl solution, could also be considered. Indeed, as there is a variable dependence of the total exchange capacity on the replacement ion used, the use of different ions in different exchange experiments would give a better estimate of the total exchange capacity, and also indicate whether the replacement of radioisotopes was significantly dependent on the replacement ion.

In the final section of this chapter (7.7) correlations between radon escape and such parameters as Ra-226/U-238 activity ratios, and exchangeable Ra-226 were examined. A relationship was observed between increasing fractional retention of Rn-222 and a decreasing fraction of exchangeable Ra-226. This observation permits the expansion of the conventional model of Rn-222 escape to include that escaping from Ra-226 held on hydrated clays. The average effective grain size of those intact crystals and unhydrated clay grains emanating Rn-222 was deduced from the non exchangeable Pb-210/Ra-226 activity ratio, and it appears that most of the samples studied must be intensively fractured on a microscopic scale in order to account for the typical emanating grain diameter of less than 1 μm. This conclusion supports that of earlier workers.

Comparison of individual dose rates derived from routine techniques and gamma spectrometry have revealed discrepancies of as much as 90% (in the alpha dose rate of 214b7, section 7.5). Gamma spectrometry is believed to give a much more accurate estimate of these dose rates, and it now remains to identify which of the routine techniques gives rise to these unacceptable errors. This is done in chapter 8.

C H A P T E R VIII

THE PERFORMANCE OF ROUTINE DOSIMETRY TECHNIQUES WHEN COMPARED WITH GAMMA SPECTROMETRY

INTRODUCTION

In the past it has proved difficult to demonstrate that routine dosimetry techniques do in fact reliably determine those parameters that they are intended to measure, primarily because of a lack of pottery and soil samples of well known isotope activities. In the previous chapter broad comparisons were drawn between alpha, beta and gamma dose rates derived from established techniques with those from gamma spectrometry. Here, all those routine measurements are collected together and compared with the predictions of the appropriate measured parameters derived from spectrometry analyses. The six techniques examined are thick source alpha counting, gas cell analysis, beta TL dosimetry, gamma TL dosimetry, flame photometry and Po-210 alpha spectrometry.

8.1 THICK SOURCE ALPHA COUNTING

Thick source alpha counting together with flame photometry was until recently the most common method used to estimate the alpha and beta dose rates to a buried sherd. Although this has largely been superceded by beta TLD for beta dose rate measurements (see section 8.3), alpha counting is still, in principle, an accurate method of determining the alpha dose rate, as the alpha count rate is very nearly directly proportional to the alpha dose rate, independent of the activity ratio of the two major decay chains, or of their states of equilibrium, (AITKEN, 1978a).

Figure 8.1.1 shows the alpha counting cell in use at Oxford. The 'viced' sherd, or loose soil, is placed in direct contact with a disposable fluorescent screen (manufactured from zinc sulphide on mylar as developed by HALLDEN and HARLEY (1960), and manufactured by Wm. B. Johnson and Associates, Inc., Research Park, Montville, New Jersey, N.J. 07045.)

Figure 8.1.1 The alpha counting cell

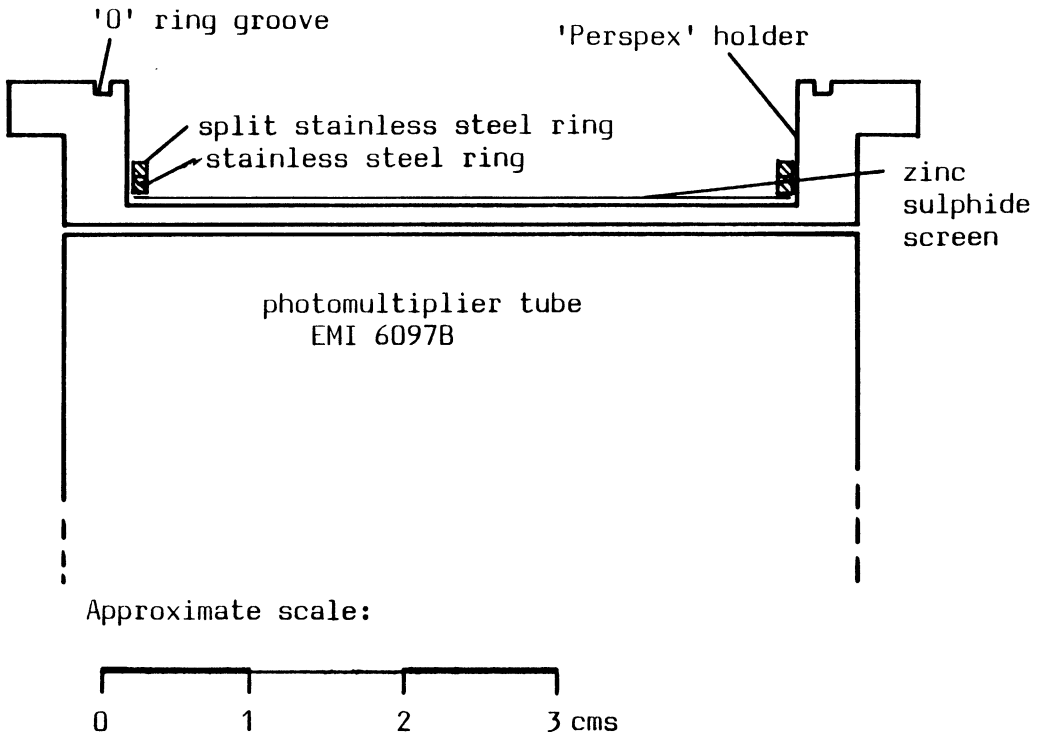

The resulting light pulses are then detected by a photomultiplier tube. The counting electronics are normally operated with a threshold that rejects pulses from noise or beta particles; this threshold position is discussed in more detail in Appendix E. Both soils and sherds are counted dry, although no special precautions are taken to exclude all moisture.

In fine grain dating, where the alpha dose rate contributes typically 30% of the total, the reliability of the unsealed alpha count rate (see also section 8.2) is of critical importance if accurate dates are expected. Surprisingly, little direct testing of this reliability has been carried out. BOWMAN (1976) confirmed that the count rate from a single nuclide source, Am-241 incorporated into a $CaCO_3$ matrix (of unstated grain size), was consistent with that expected from the known activity. Four natural samples were also examined, but the concentrations used to predict the count rate from at least one of these are almost certainly incorrect (126 ppm Th-232, 2.2 ppm U-238 for sample GSP-1, derived from neutron activation analysis. Compare these results with those in section 6.7.3, and FLANAGAN, 1969). The remaining three, two thorium rich sherds, again of unstated grain size, and a finely powdered USNBS thorium sand, overcounted by 2%, 14%, and 5% respectively, after correction for gas loss.

8.1.1 Comparison of observed and predicted count rates

Using alpha particle range data for pottery, the alpha count rate per unit activity for each of the isotope groups of section 6.1.1 were calculated, for the standard source area and threshold setting, (see Appendix E). These calculations permit the spectrometer analyses to be used to predict both sealed and unsealed alpha count rates.

A comparison of such predictions with the observed count rates is given for 24 sherds in table 8.1.1. The observed unsealed count rates are clearly discrepant, and the overcounting cannot be simply attributed to gas retention; in general they are consistently higher than even the predicted sealed count rates. It was at first thought that this overcounting was correlated with the degree of Rn-222 loss. Figure 8.1.2 gives the degree of overcounting plotted against the

Table 8.1.1

Predicted and observed alpha count rates, $ksec^{-1}$: sherds

Sample	Rn-222/Ra-226 activity ratio	Spectrometer prediction α_o	α_s	Observed α_o	$\frac{\alpha_o \text{ observed}}{\alpha_o \text{ spectrometer}}$
P12J04	1.03_{14}	9.0_{3}	8.9_{4}	10.0	1.11
P12K02	1.30_{29}	8.9_{3}	8.3_{5}	10.0	1.12
P12N02	0.96_{6}	9.1_{2}	9.2_{3}	10.3	1.13
P12Q02	1.05_{19}	8.6_{3}	8.5_{5}	10.3	1.20
P41J07	0.92_{10}	14.6_{5}	15.2_{7}	15.4	1.05
P41J10	1.07_{20}	15.9_{5}	15.6_{7}	17.9	1.13
P41J11	1.09_{14}	16.6_{5}	16.2_{8}	16.1	0.97
164m4	0.61_{4}	32.7_{11}	38.4_{13}	38.0	1.16
164m9	0.70_{4}	27.1_{10}	30.7_{12}	32.0	1.19
214b7	0.67_{9}	24.8_{6}	28.2_{8}	35.8	1.44
214b8	0.49_{3}	28.6_{7}	34.2_{9}	35.0	1.22
214b13	0.42_{2}	29.7_{8}	41.0_{10}	28.6	0.96
214b14	0.44_{2}	28.1_{12}	36.6_{14}	30.8	1.10
214b15	0.43_{2}	41.6_{19}	53.6_{21}	42.8	1.03
214b16	0.58_{4}	27.0_{7}	32.0_{10}	31.3	1.16
214b17	0.46_{2}	49.3_{20}	61.8_{21}	52.2	1.06
214b18	0.51_{3}	28.1_{10}	33.3_{12}	39.1	1.39
169j2	0.63_{5}	11.8_{5}	14.4_{7}	15.0	1.27
547b	0.81_{7}	13.6_{5}	14.7_{6}	20.7	1.52
215a2	1.86_{70}	5.4_{3}	4.6_{4}	6.9	1.28
132k17	0.78_{7}	8.1_{2}	8.9_{4}	21.1	2.6
200g17	1.04_{12}	16.2_{4}	16.0_{6}	18.4	1.14
505a5	1.04_{24}	5.0_{2}	5.0_{4}	5.7	1.14
200g18	0.85_{3}	15.8_{5}	16.4_{6}	17.4	1.10

Derived from last column: mean 1.23, median 1.14

Note:
1) errors are in the least significant figures.
2) errors of 5% are usually assumed in the observed values of the unsealed count rate.
3) α_s represents the count rate calculated assuming no gas loss.
4) all count rates are for a 13.85 cm^2 counting area with a threshold set to reject 15% of the pulses from a thick Th-232 source in equilibrium with its daughters (see Appendix E).
5) the approximately 95% confidence interval on the median lies between 1.10 and 1.22 (NAIR, 1940).

Figure 8.1.2 Overcounting of alpha particles plotted against fractional Rn-222 retention: sherds

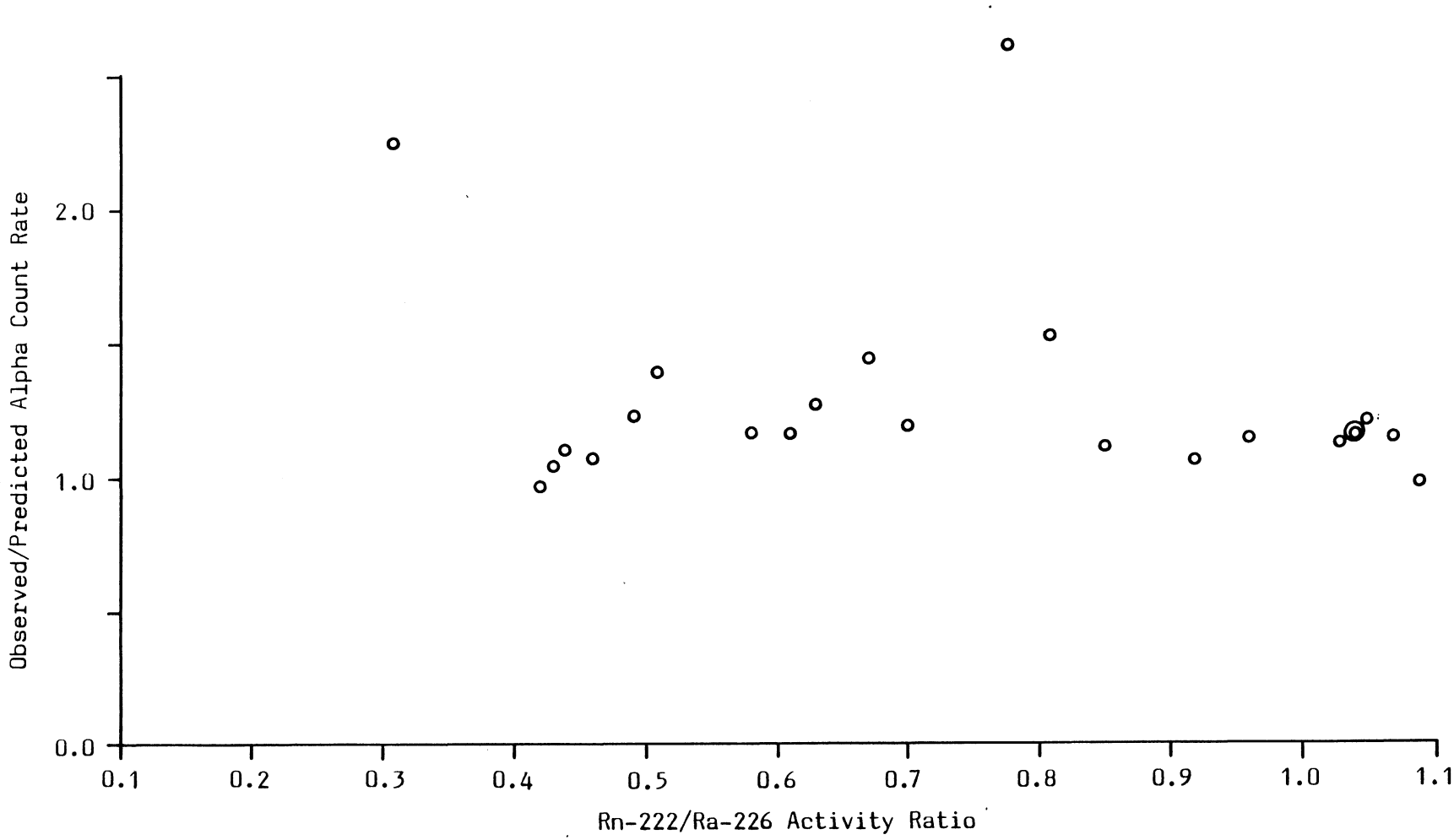

Rn-222/Ra-226 activity ratio (i.e. the degree of radon retention) for these 24 sherds and no correlation is apparent.

Table 8.1.2 gives similar information for 18 soil samples, and overcounting is again present. As can be seen from figure 8.1.3, there is no obvious correlation with radon loss.

8.1.2 Likely sources of count rate discrepancy

As gamma spectrometer analysis has been thoroughly tested with known composition samples, and comparable testing of alpha counting, mentioned in section 8.1, has been cursory, it is thought that the most likely sources of these discrepancies are:

i) Effective sample area - although BOWMAN (1976) reports experiments to determine the effective zinc sulphide screen area, no similar tests to determine effective sample area are described. As most samples are either dried soils or 'viced' sherds, inevitably there will be cavities adjacent to the screen, surrounded by the outer surfaces of sample grains. Alpha attenuation by the air in such cavities will be negligible and it is thus possible that the screen 'sees' a greater effective sample area than the simple geometric cross-section of the sample.

ii) Sample inhomogeneity between large and fine grains - it was shown in section 7.2 that the alpha activity of fine grains of pottery may be substantially (about 40%) higher than that of the bulk sample. It is possible that these fine grains fall through a 'viced' sample and fill the cavities between larger grains adjacent to the zinc sulphide screen. These would then give rise to a greater count rate than that predicted from bulk analysis. However, this explanation is thought unlikely; because of limited sample size, it is standard practice to use 'viced' material left over from fine grain extraction for alpha counting. This was certainly true of most of the Peruvian work (chapter 5), and in addition the fine grain content of many soils, for example the sandy soil P35K which overcounted by 360%, is negligible.

iii) Surface activity on grains - if a substantial proportion of the sample activity is held on the grain surfaces, perhaps deposited

Table 8.1.2

Predicted and observed alpha count rates, $ksec^{-1}$: soils

Sample	Rn-222/Ra-226 activity ratio	Spectrometer prediction α_o	α_s	Observed α_o	$\frac{\alpha_o \text{ observed}}{\alpha_o \text{ spectrometer}}$
P04J	1.09_{22}	7.6_{3}	7.4_{4}	6.8	0.89
P23A	0.84_{12}	11.4_{4}	12.0_{6}	12.4	1.09
P34	0.92_{16}	8.6_{3}	8.9_{5}	10.1	1.17
P35J	1.12_{12}	17.7_{5}	17.1_{7}	24.9	1.41
P35K	0.99_{22}	6.8_{3}	6.8_{5}	31.1	4.6
P17L	1.14_{40}	9.2_{3}	8.4_{5}	12.7	1.38
P37Q	0.52_{7}	8.4_{3}	10.5_{6}	11.6	1.38
P10K	1.11_{15}	10.0_{3}	9.7_{5}	12.9	1.29
S164p	0.95_{13}	14.1_{4}	14.3_{6}	29.1	2.06
S164m7	0.76_{12}	14.4_{5}	15.2_{8}	31.0	2.15
S214b	0.63_{5}	35.3_{9}	37.8_{8}	53.2	1.51
P12N	1.12_{20}	9.8_{3}	9.6_{5}	11.0	1.12
P41J	0.88_{10}	11.5_{3}	11.9_{5}	12.9	1.12
S222/2	0.77_{11}	9.7_{3}	10.2_{5}	11.2	1.15
S222/10	0.55_{3}	35.6_{18}	43.5_{21}	56.8	1.60
S222/23	0.29_{1}	39.7_{10}	64.9_{16}	77.3	1.95
S222/28	0.51_{11}	4.8_{2}	5.7_{5}	8.8	1.83
S222/29	0.54_{9}	5.3_{2}	6.2_{4}	7.5	1.42

Derived from last column: mean 1.62, median 1.40

Note:
1) errors are in the least significant figures.
2) errors of 5% are usually assumed in the observed values of the unsealed count rate.
3) α_s represents the count rate calculated assuming no gas loss.
4) all count rates are for a 13.85 cm^2 counting area with a threshold set to reject 15% of the pulses from a thick Th-232 source in equilibrium with its daughters (see Appendix E).
5) the approximately 95% confidence interval on the median lies between 1.15 and 1.83 (NAIR, 1940).

Figure 8.1.3 Overcounting of alpha particles plotted against fractional Rn-222 retention: soils

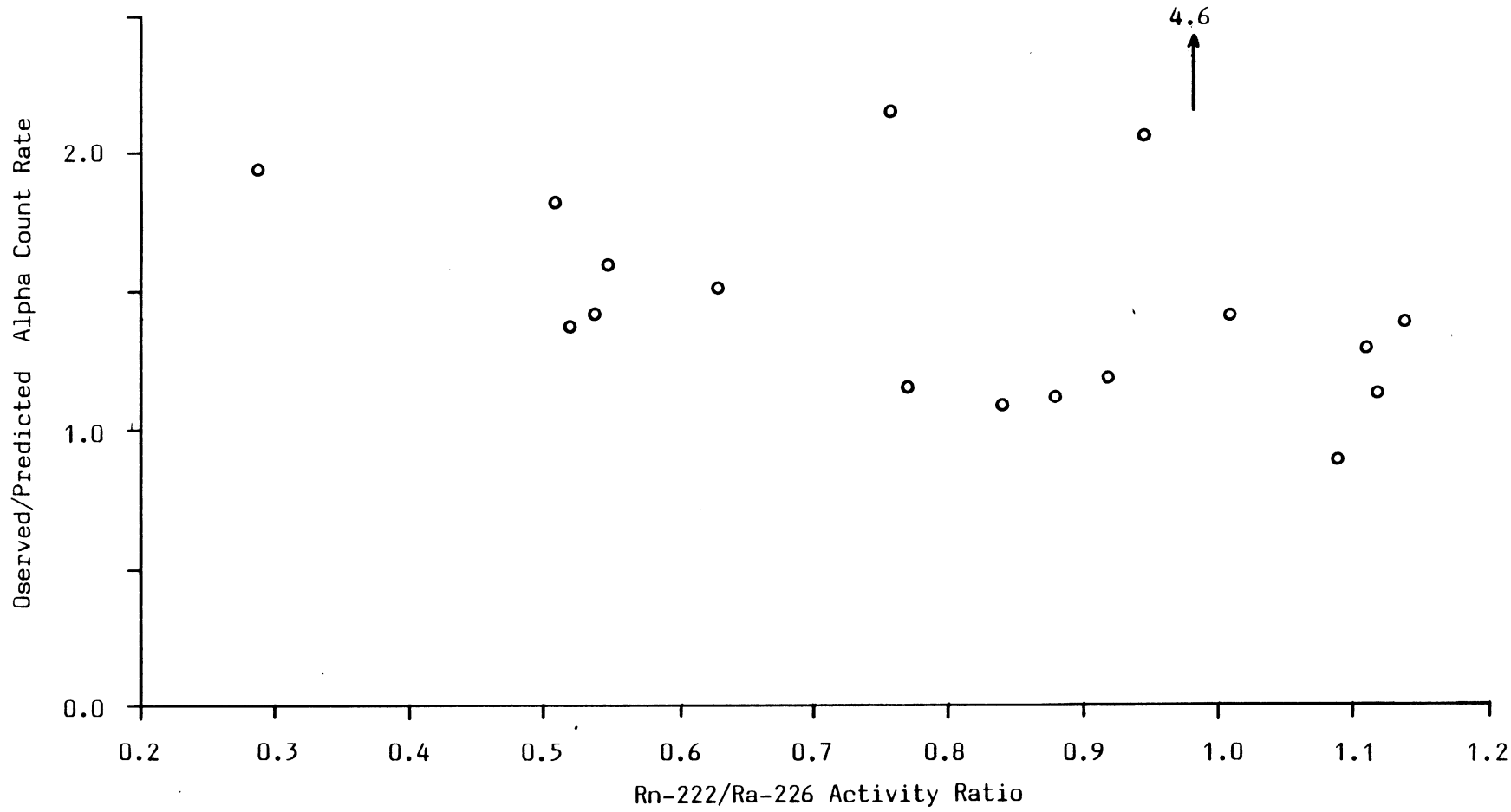

there by ground water action, then an abnormally high counting efficiency is expected which would also lead to overcounting.

It is not within the scope of this thesis to identify which, if any, of these possible sources of error actually give rise to counting discrepancies. However, it is appropriate to describe some preliminary experiments which give an indication of a means of circumventing these problems.

8.1.3 Empirical approach to the problem of overcounting of alpha activity

A variety of samples, active sands, soils and pottery, have been mixed with polyester resin (typically a 50:50 mix), and cast in moulds 42 mm in diameter. The resulting disc was removed from the mould, and lapped on a fine grade of carborundum paper until the sample grains were exposed. By filling the inter grain cavities with an absorbing medium, it was anticipated that whichever mechanism was responsible for overcounting, the effect would be considerably reduced. Repeated counting of active samples during lapping showed that once the grains were clearly exposed, further lapping did not change the observed count rate. All such samples were counted within 48 hours of casting, in order to minimize any increase in count rate due to build up of Rn-222 daughters in the now solid sample. Rn-220 daughters would be close to equilibrium at the end of such a period.

Before comparing the count rates obtained after casting in resin with those predicted, it is necessary to allow for the dilution in resin. In the data to be presented in the following paragraphs, this is done simply by normalising, by weight of components, to a pure mineral sample, i.e. in the case of a 50:50 mix, by multiplying the observed count rate by two. The approximations involved in this normalisation are discussed in the next section.

Table 8.1.3 shows the count rates predicted from gamma spectrometry compared with those observed from a loose sample, (i.e. not cast in resin) for one uranium and two thorium sands, all finely powdered. Note that although the thorium sands are those described in table 6.7.3 (section 6.7.2) the alpha activities include small amounts of U-238 not given in table 6.7.3. Two of these loose samples show significant overcounting. The count rates shown in the final

Table 8.1.3 Alpha count rate for high activity samples of known parent concentration

Sample	Parent concentration	Unsealed alpha count rate predicted $ksec^{-1}$	observed $ksec^{-1}$	cast in resin $ksec^{-1}$
NBL 74-A	1040 ppm U-238 in dunite	1580 (1630 if no gas loss)	2175	1620
NBL-80	1010 ppm Th-232 +37 ppm U-238 in dunite	560	635	560
NBL-109	104 ppm Th-232 +3.8 ppm U-238 in silica	57.4	57.2	54.8

Notes: 1) count rates are for a 13.85 cm^2 counting area with a threshold set to reject 15% of the pulses from a thick Th-232 source in equilibrium with its daughters (see Appendix E).

2) the predicted count rate from the uranium ore is calculated using the level of Rn-222 escape observed in gamma spectrometry.

3) errors in the predicted count rates are dominated by spectrometry calibration errors, typically 2%. Errors in the two sets of observed count rates are primarily statistical, i.e. $\pm$ 1.5%.

column are those obtained from the same samples after casting in resin and lapping. The improved agreement is remarkable.

Table 8.1.4 shows similar data for four soils and two sherds taken from tables 8.1.2 and 8.1.1. A similar improvement can be seen. The only sample which still shows gross disagreement is the Hong Kong soil, 214b, and it should be noted that the visible grains on the exposed surface of this disc were unusually large, up to several millimetres across. It is possible that the lapping process exposed fissures within these large grains which were not resin filled, again giving an increased detection efficiency.

8.1.4 Effect of resin on alpha ranges

The normalisation by weight procedure described in the last section is a simplification of a very complex situation which is best described by considering two extreme cases. Assume that the grain size of a sample mixed in resin is very much larger than the typical alpha ranges (e.g. 1 mm), and that the resin/sample weight ratio is 1:1. In this case, almost all the alpha particles reaching the zinc sulphide screen will have passed entirely through pottery (or soil), and very few through resin. Then the appropriate range to use in equation 1 of Appendix E is that of pottery (or soil) and the simple normalisation by weight routine predicts the correct alpha count rate. Note that this also assumes that the grain/resin geometry is such that the proportion of sample area exposed by lapping is the same as the proportion of sample by weight.

Now consider the other extreme, when the sample grain size is much less than the alpha range, (e.g. 2 μm). Then the 1:1 mixture would appear homogeneous to alpha particles, and the appropriate range to use would be that of a material of the same atomic number $\underline{Z}$ and atomic weight $\underline{A}$, as the resin/sample mixture. The average $\underline{Z}$ of polyester resin is close to that of carbon ($\underline{Z}$=6), that of pottery is about 10.5, and so the alpha ranges in oxygen ($\underline{Z}$=8) should be appropriate to such a 1:1 resin/pottery mixture. The alpha ranges in oxygen are about 13% lower than those of pottery, in the energy range of interest. Thus we can expect that the predicted alpha count rate from known activities using pottery ranges will be at most 13%

Table 8.1.4 Alpha count rates from some soils and sherds when cast in polyester resin

Sample		Predicted from gamma spectrometer $ksec^{-1}$	Observed from loose sample $ksec^{-1}$	Observed from sample cast in resin $ksec^{-1}$
S164p	soil	14.1_4	29.1	13.9
S164m7	soil	14.4_5	31.0	13.4
S214b	soil	35.3_9	53.2	44.6
P35K	soil	6.8_3	31.0	5.9
P12J04	sherd	9.0_3	10.0	7.7
P12Q02	sherd	8.6_3	10.3	8.8

Note: 1) count rates are for a 13.85 cm^2 counting area with a threshold set to reject 15% of the pulses from a thick Th-232 source in equilibrium with its daughters (see Appendix E).

2) the predicted count rates are calculated using the level of Rn-222 escape observed by gamma spectrometry.

3) statistical errors in the two sets of observed count rates are less than $\pm$ 3%.

too great when applied to pottery/resin mixtures. In practice, however, the grain sizes of the soil and pottery samples used were much closer to the larger grain size extreme discussed above, and so in general the observed count rates are closer to the predicted values than might otherwise be expected.

It is suggested that to improve the accuracy of the predicted alpha count rate for pottery/resin or soil/resin mixtures, the sample should be crushed to less than 10 μm before mixing. Then the average range of the mixture can be applied to predict the true count rate. This approach could then be applied routinely to the analysis of alpha activity of soils and sherds.

8.1.5 Count rate build up in a sealed sample

One further possibility which follows from this approach deserves mention; that is the potential for giving the degree of radon escape in the laboratory.

A sample of uranium doped concrete (see chapter 3) was crushed to less than 500 μm and analysed in the spectrometer. Another portion of this crushed sample was mixed with resin and cast directly in an alpha cell, in such a way as to completely fill the volume of the cell. The sample was allowed to cure, and lapped in the usual way. It was then sealed in the cell with a zinc sulphide screen, and the build up of count rate followed over a ten day period (i.e. 2.5 half lives of Rn-222). The observed count rates are plotted in figure 8.1.4 against an exponential time scale. The straight line is a least squares fit to the data, and the predicted count rates, sealed and unsealed, from gamma spectrometry are also shown. The eventual count rate from the least squares fit is 1% greater than that predicted from gamma spectrometry. The scatter in count rates is larger than that expected from the statistical errors shown, and it is presumed that this scatter is due to movement of radon into and out of the inevitable dead spaces around the sample. Nevertheless, this illustrates the possibility of counting a pottery/resin mixture immediately after casting and lapping, to give the unsealed count rate, and sealing the sample for, say, 20 days (five half lives of Rn-222) before recounting to obtain the sealed count rate. The difference between the two

Figure 8.1.4 Increase of count rate in sealed sample cast in resin, plotted against exp[-λt], where λ is the Rn-222 decay constant and t is the elapsed time since sealing

Note: the two levels marked 'G' are the sealed and unsealed predictions from gamma spectrometry

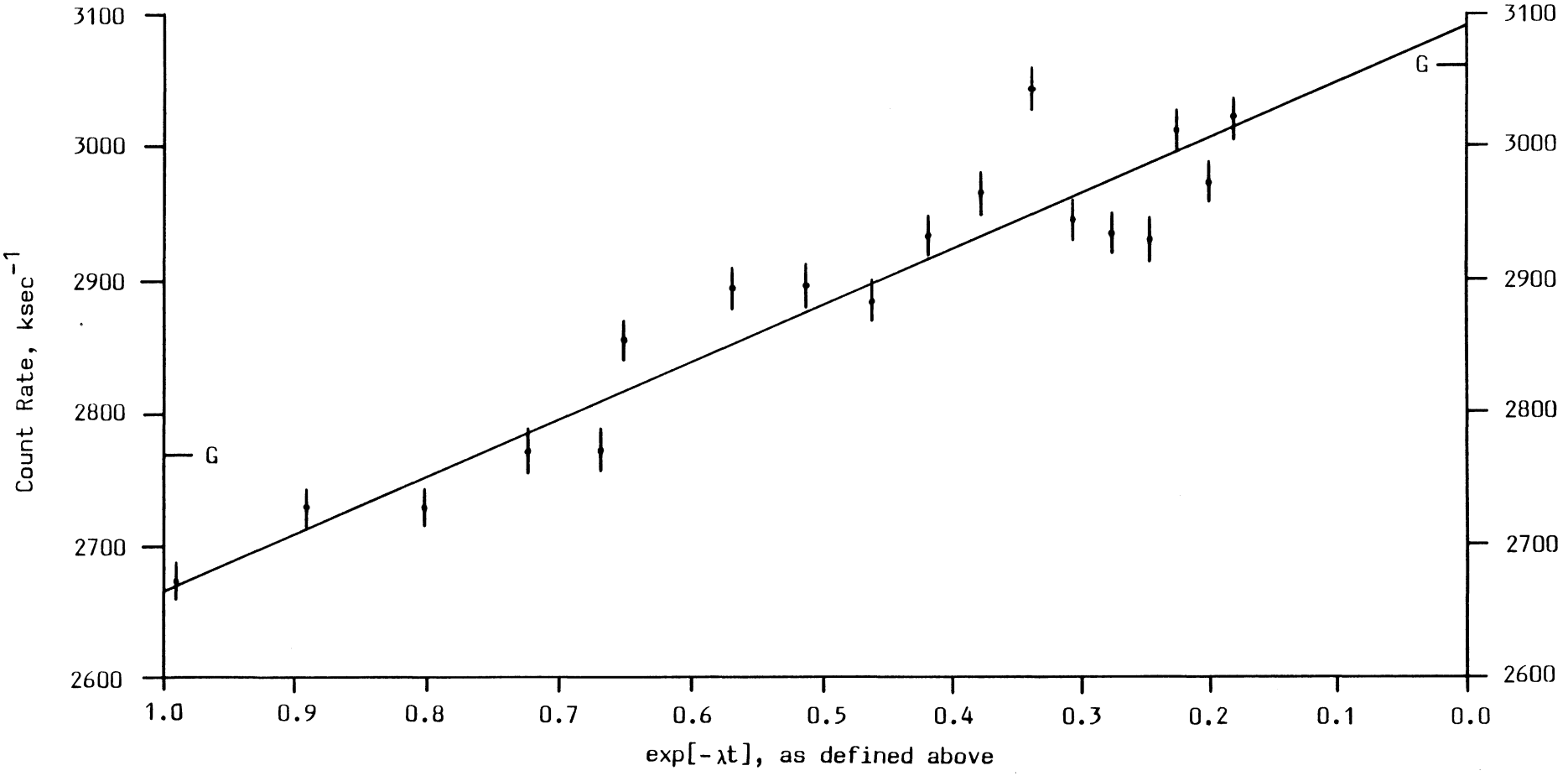

count rates is a direct measure of the degree of Rn-222 loss.

8.1.6 Conclusion

It has been shown that alpha counting as routinely employed can overestimate the alpha activity of soils by up to 360%, and of sherds by up to 160%. This is clearly unsatisfactory, and must cast serious doubt on any existing dates which were calculated using dose rates depending heavily on this technique.

However, such overcounting may be avoided if the sample is mixed with polyester resin to form a solid disc before lapping and counting. Presumably the ideal way would be to crush the mineral to less than 10 μm grain diameter before mixing, and use the average alpha ranges for the pottery/resin mixture. However, the results obtained indicate that for 'viced' pottery or soils, it is sufficient to use pottery ranges directly. It is suggested that until an approach more soundly based on theory is developed, samples should be counted both loose and in resin. If the loose count rate is greater by 10% than the resin count rate, then the latter is the more reliable. If they are similar, then the average count rate is the best estimate. In any case, it is thought unwise to associate errors of less than say, 10% with such alpha counting.

8.2 GAS CELL ANALYSIS

In routine thick source alpha counting, it is customary to determine the count rate with the cell sealed as well as unsealed. If the sealed count rate over the first 24 hours is greater than 1.1 times the unsealed count rate, then the escape of radon isotopes is significant, and analysis must include the use of a gas cell. This was developed by DESAI (1975) and provides a correction to the unsealed alpha count rate to allow for the nett change in gas escape in going from the state before excavation to that used for alpha counting. The gas cell is illustrated in figure 8.2.1, and a detailed description of the principle and operation is given by AITKEN (1978b). The important feature is that the only alpha particles detected by the zinc sulphide screen are those derived from radon isotopes (or their daughter products) which have escaped from the sample.

Figure 8.2.1 The gas cell

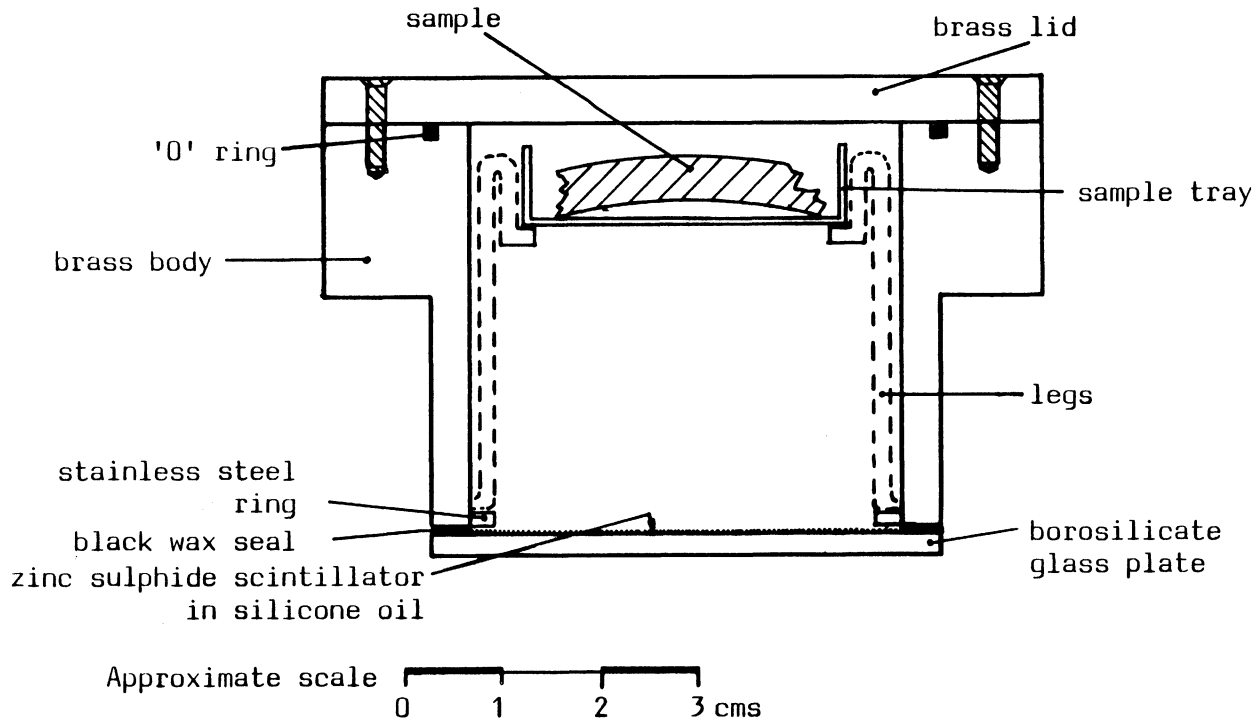

Because the gamma spectrometer cannot determine Rn-220 escape reliably, no attempt will be made to compare gas cell measurements of the escape of this isotope. However, the estimates of the degree of escape of Rn-222 will be compared. The gas cell system produces two such figures; g_{br}, which is a measure of the alpha count rate lost as a result of Rn-222 escape from the sherd in the buried state (i.e. solid and wet), and g_{cr}, the lost count rate with the sherd in the laboratory state (i.e. 'viced' and dry as for alpha counting). These measurements are independent of the thick source alpha counting technique and thus the criticisms made of that method in section 8.1 do not invalidate gas cell measurements.

Section 6.6.12 presented evidence that the build up of Rn-222 in the polypropylene sample holder used in gamma spectrometry is not significant, and so the lost Rn-222 activity determined by this technique can be converted directly into a lost alpha count rate using the data in Appendix E. This is to be compared with g_{cr}. Similarly the quantity to be compared with g_{br} is derived from the difference between Ra-226 and Pb-210 activities. This assumes that the observed Pb-210 activity reflects the Rn-222 activity before excavation. The reliability of this assumption was questioned in section 7.5 for some of the samples used here.

8.2.1 Gas cell measurements compared with spectrometer predictions

Table 8.2.1 gives the predicted 'lost' count rate from Rn-222 escape in the 'viced' state, g_{cr}, and in the 'buried' state, g_{br}, for sherds from the two sites discussed in section 7.5, based on the gamma spectrometer analyses. The count rates calculated from gas cell analysis are also shown. Of the 7 comparisons given, 4 give excellent agreement in the determination of g_{cr} but the remaining 3 are seriously discrepant. As the escape of Rn-222 is likely to be very dependent on the water content of the sample, it is presumed that some of this discrepancy arises from different moisture levels in the different portions of these samples used for the two methods of analysis, particularly as they were analysed at different times, and no attempt was made to control this water content using, say, a dessicator.

The 'lost' count rates for the samples in the 'buried' state are in much better overall agreement, although in general it seems

Table 8.2.1 Comparison of observed and predicted gas cell count rates

Sample	spectrometer g_{cr} $ksec^{-1}$	spectrometer g_{br} $ksec^{-1}$	observed g_{cr} $ksec^{-1}$	observed g_{br} $ksec^{-1}$	$\frac{\text{observed}}{\text{specrometer}}$ g_{cr}	$\frac{\text{observed}}{\text{specrometer}}$ g_{br}
214b7	2.8_5	5.9_6	9.9_4	6.1_2	3.5	1.0
214b8	5.5_5	6.5_6	5.4_4	6.0_3	1.0	0.9
214b13	10.9_7	12.9_8	17.6_2	11.2_3	1.6	0.9
214b14	8.1_7	10.5_9	8.3_2	13.3_3	1.0	1.3
214b15	11.9_8	12.6_9	12.2_3	15.6_4	1.0	1.2
164m9	5.4_8	6.8_9	2.1	8.6	0.4	1.3
164m4	3.6_7	3.6_8	3.7	5.9	1.0	1.6
				mean	1.4	1.2

Note: errors given are in the least significant figures.

that the gas cell overestimates the Rn-222 escape in the ground. This could be due to back diffusion of radon when the sherd was surrounded by soil, or it could reflect Pb-210 mobility, as discussed in section 7.5

8.2.2 Conclusion

Unfortunately the comparisons given here cannot be considered conclusive, for reasons already discussed. However, it does seem that for some samples at least the gas cell has accurately determined the amount of Rn-222 escape in the 'viced' state. It may be that stricter control of the sample moisture content in the laboratory is needed to improve the agreement between the two methods of measurement. The 'lost' count rate from the solid sherd with the water content as it was immediately after excavation is also in fair agreement with the spectrometer predictions, especially when the uncertainties arising from the mobility of Pb-210 activity and water content before excavation are taken into account.

8.3 BETA DOSE RATE ESTIMATION USING TL DOSIMETRY

The estimation of the beta dose rate to a sherd is normally undertaken using beta TLD. The system used in this work was developed by BAILIFF (1976) and described in BAILIFF and AITKEN (1980); a related approach has also been described by MEJDAHL (1978b). Figure 8.3.1 shows the assembly used to hold the sample and TL dosimeter (natural calcium fluoride). This is then stored in a lead pot, usually for more than ten days, and the dose in the phosphor evaluated in the usual way. After subtraction of background, a geometrical factor is taken into account to give the infinite matrix beta dose rate. The calibration of this system, and discussion of the errors arising from variations in the relative proportions of the U-238 chain, the Th-232 chain and K-40 are described in detail in BAILIFF (1976). The samples are normally in the 'viced' state and are unsealed.

8.3.1 Beta dose rates from TL dosimetry compared with those calculated from gamma spectrometry

Table 8.3.1 gives the beta dose rate predictions from gamma spectrometry for 17 sherds, taken from sections 7.4 and 7.5. Note

Figure 8.3.1 The beta TLD assembly

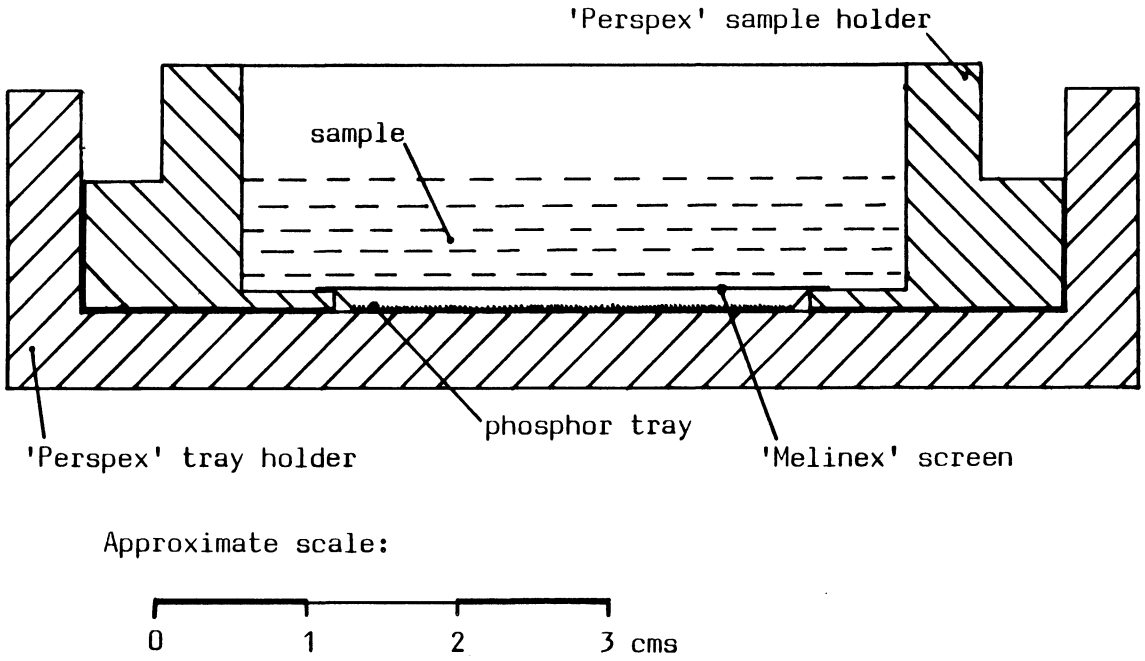

Table 8.3.1

Comparison of observed and predicted beta TLD dose rates

Sample	Predicted by spectrometer mrad yr^{-1}	Observed beta TLD mrad yr^{-1}	observed / predicted
P12J04	233_{12}	249	1.07
P12K02	241_{14}	255	1.06
P12N02	233_{8}	250	1.07
P12Q02	239_{10}	241	1.01
P41J11	472_{13}	461	0.98
P41J10	421_{14}	469	1.11
P41J07	421_{14}	460	1.09
164m4	427_{16}	421	0.99
164m9	327_{12}	326	1.00
214b7	247_{13}	248	1.01
214b8	301_{12}	256	0.85
214b13	235_{14}	207	0.88
214b14	242_{15}	266	1.10
214b15	330_{16}	301	0.91
214b16	287_{12}	266	0.93
214b17	308_{9}	285	0.93
214b18	257_{13}	259	1.01

Derived from above: median 1.01, mean 1.00
standard deviation 0.08

Note: 1) errors shown are in the least significant figures.
2) errors in the oserved data are usually assumed to be 5%.
3) the approximately 95% confidence interval on the median lies between 0.93 and 1.07 (NAIR, 1940).

that the dose rates given here are not necessarily identical with those shown earlier, which used the Pb-210 activities to give the dose rate before excavation. Beta TLD measures the dose rate in the laboratory state, and so the Rn-222 activities are used directly in calculating the dose rates for the comparisons shown here.

The agreement is excellent, and as the individual ratios group closely about the average, with no seriously discrepant results, the calculation of the standard deviation of 7.9% is meaningful. This is consistent with the combined errors of between 3% and 6% from gamma spectrometry and typically 5% from the TL dosimetry measurements, confirming that beta TLD is a reliable technique for determining the beta dose rate of the sample in the 'viced' state. This dose rate should then be modified to allow for the change in radon escape after excavation. The information available from gas cell measurements permits such adjustment.

8.4 GAMMA DOSE RATE ESTIMATION USING GAMMA TL DOSIMETRY

The use of gamma TL dosimetry to measure the annual gamma dose rate was described in chapter 3, and a comparison with scintillator measurements was given in chapter 4. This section provides comparison of the overall performance of gamma TLD with predictions based on gamma spectrometry.

8.4.1 Gamma TLD measurements compared with spectrometry predictions

Table 8.4.1 lists dose rate predictions from gamma spectrometry for a number of different soil samples. The corrected dose rates, i.e. after allowance has been made for observed site water contents and cosmic ray dose rate contributions (see chapter 4), are also shown and in the final column these are compared with the appropriate gamma TLD measurement corrected to give the infinite matrix dose rate as described in chapter 3.

The result from P35 I/J should be put aside. This level was very narrow, only a few centimetres thick, and did not approach an infinite gamma matrix. The capsule dose rate includes contributions from above and below; the lower level, P35K, was certainly less active, and much thicker.

Table 8.4.1 Comparison of predicted and observed gamma TLD dose rates

Sample	Observed water content %	Gamma TLD mrad yr^{-1}	Spectrometer uncorrected mrad yr^{-1}	Spectrometer corrected mrad yr^{-1}	$\frac{\text{gamma TLD}}{\text{predicted}}$
S164m7 / S164p	20	178	157 6	139	1.28
P40	76	102	120 6	94	1.09
P04J	4.6	129	120 6	127	1.02
P23	1.9	155	147 7	157	0.99
P34	3.1	124	108 6	117	1.06
P35I/J	0.6	178	262 9	273	(0.65)
P35K	0.6	139	108 5	120	1.16
P17l	1.8	122	123 6	134	0.91
P37Q	30	107	93 6	99	1.08
P10K	3.2	158	140 7	148	1.07
P37J	25	153	104 8	111	1.38
P45J	11	151	81 5	102	1.48
P06	8.7	148	120 6	122	1.21

Derived from last column: mean 1.14, median 1.08

Note:
1) the approximately 95% confidence interval on the median lies between 1.02 and 1.28 (NAIR, 1940)
2) cosmic ray dose rates and water content corrections were used to derive the corrected spectrometer dose rates. The cosmic ray dose rate for site 164 was 10 mrad/yr. See chapter 4 for the appropriate figures for the Peruvian sites.
3) calcium fluoride (natural) in copper capsules was used to obtain the gamma TLD results.
4) errors are in the least significant figures.
5) the result from P35I/J is omitted from the calculation of both the mean and the median.

The overall agreement between the two techniques is considered fair, especially when the sizes of the cosmic ray and water content corrections are considered. For instance the 76% water content of site P40 necessitates an attenuation factor of 0.54, reducing the terrestrial dose rate to 64 mrad yr^{-1}. The cosmic ray dose rate of $30 \pm \frac{8}{4}$ mrad yr^{-1} appropriate to a Peruvian highland site, is then added to this to give the final dose rate of 94 mrad yr^{-1} compared with the observed dose rate of 102 mrad yr^{-1}. On average there is probably a tendency for the capsule measurements to overestimate the dose rate compared with the gamma spectrometer. However, it would be unwise to place too much emphasis on this; the corrections involved in calculating the Peruvian TL dosimeter results were large (see chapter 4) and the Hong Kong result (S164) was measured in Hong Kong under non ideal conditions. It is thought that systematic errors of several percent could easily have arisen here which would not normally occur, and so this discrepancy cannot be regarded as firmly established.

8.5 FLAME PHOTOMETRY

Flame photometry has been used in conjunction with alpha counting for many years to determine the potassium concentration, and hence the beta and gamma dose rate from K-40, when beta and gamma TLD was unavailable. It is a routine analytical technique in use in many fields, and is described in detail by SUHR and INGAMELLS (1966).

8.5.1 Comparison with gamma spectrometry

Table 8.5.1 lists 26 comparisons of potassium analyses by flame photometry, converted into K-40 activities using data from Appendix E, with K-40 activities obtained from gamma spectrometry measurements. The median of the observed to predicted ratios is 0.88 and the spread in these values is large, from 0.35 to 1.64. Flame photometry uses samples of about 100 mg, gamma spectrometry of about 7 g. Clearly flame photometry is potentially much more sensitive to sample inhomogeneity, and usually about 1 g of sample is crushed to less than 200 μm and thoroughly mixed before 100 mg is selected for analysis. (HUXTABLE, private communication). Nevertheless, it is presumed that the major cause of this scatter is sampling errors.

Table 8.5.1 Comparisons of K-40 analysis by flame photometry with that by gamma spectrometry

Sample	(a) flame photometry pCi g^{-1}	(b) gamma spectrometry pCi g^{-1}	(a)/(b)
sherds:			
169j2	10.9	17.4_{9}	0.63
547b	4.4	2.8_{7}	1.6
215a2	7.5	8.4_{9}	0.9
132k17	18.7	16.7_{8}	1.12
200g17	29.7	25.6_{10}	1.16
505a5	11.3	13.6_{9}	0.83
7b	6.9	7.4_{9}	0.93
P12J04	9.2; 12.1	17.5_{11}	0.53; 0.69
164m4	8.5	21.3_{11}	0.40
164m9	12.8	14.5_{8}	0.88
214b7	6.9	8.5_{10}	0.81
214b8	11.6	12.1_{9}	0.96
214b13	5.8	5.2_{10}	1.12
214b14	7.4	6.7_{12}	1.10
214b15	6.7	7.2_{10}	0.93
214b16	8.9	10.8_{7}	0.82
214b17	1.2	<1	-
214b18	11.5	7.0_{10}	1.64
soils:			
P12N	12.4	14.6_{10}	0.85
S164m7	7.0	8.4_{9}	0.83
S214b	1.9	1.4_{5}	1.4
S222/2	6.7	19.1	0.35
S222/10	18.6	22.4	0.83
S222/23	17.0	34.0	0.50
S222/28	4.6	4.4	1.05
S222/29	5.9	7.6	0.78

Derived from last column: mean 0.92, median 0.88

Notes: 1) errors are in the least significant figures.

2) flame photometry data has been converted from % K_2O to pCi g^{-1} using data given in Appendix E.

3) the approximate 95% confidence interval on the median lies between 0.82 and 1.05 (NAIR,1940).

8.6 ALPHA SPECTROMETRY ANALYSIS OF Po-210

The analysis of Po-210 activity is the final routine technique to be examined. DESAI (1975) applied this approach to both pottery and soils, and the technique was described in detail by her. Very briefly, the mineral sample is brought into solution in hot hydrofluoric acid, and after various chemical procedures the Po-210 is plated onto one side of a silver disc. The alpha activity on the disc is then analysed using a silicon barrier detector. The efficiency of the process is monitored by the addition of a known activity of Po-208 to the sample solution. The Po-210 activity of a sample is a good measure of the Pb-210 activity, as Po-210 has a half life of 138 days, and so there is little chance of disequilibrium being set up between these two isotopes.

8.6.1 Comparisons with gamma spectrometry

Unfortunately there are only three Po-210 measurements available on the material analysed by gamma spectrometry. These are given in table 8.6.1. Beyond noting that the agreement appears excellent, no further comment will be made.

8.7 SUMMARY

Of the six routine techniques examined, only beta TLD, and Po-210 alpha spectrometry gave results consistent with the gamma spectrometer predictions. The results for gamma TLD were considered inconclusive; although the observed dose rates were probably significantly different from those predicted from gamma spectrometry, in view of large uncertainties in the gamma TLD results which would not normally be expected, this difference is not positively established. Gas cell analysis gave only moderate agreement, with occasional very discrepant analyses, and the two techniques which have now been in common use for about 15 years did not perform at all well. Flame photometry gave results that were usually 12% lower than those from gamma spectrometry, with individual results discrepant by as much as $\pm$ 65%. The error usually associated with this technique is $\pm$ 5%. It is thought that these discrepancies arise mainly from sampling errors.

Table 8.6.1

Comparison of Po-210 activities from alpha spectrometry with Pb-210 activities from gamma spectrometry

Sample	Po-210 pCi g^{-1}	Pb-210 pCi g^{-1}	Po-210/Pb-210
S164m7	1.10_{4}	1.15_{12}	0.96
164m4	2.3_{2}	2.36_{14}	0.97
164m9	2.6_{1}	2.81_{15}	0.93

Note: errors are in the least significant figures.

Thick source alpha counting gives even greater cause for concern. It has been shown that this technique overestimates the alpha activity of sherds typically by 14%, and that of soils by 40%. Individual discrepancies of 160% (sherd) and 360% (soil) have been observed. Again errors of only $\pm$ 5% have usually been assigned to measured count rates in the past. No correlation with Rn-222 escape was found for the 24 sherds or 18 soils studied. Preliminary experiments using samples mixed in polyester resin were described which avoid this overcounting, and an empirical approach to routine alpha counting based on these experiments suggested.

Fortunately the overall effect on dates already published is expected to be small (usually less than 10%). From sections 7.4 and 7.5 alpha dose rates appear to have been overestimated by 13% on average. For published dates based only on alpha counting and flame photometry, this suggests a total error in the age of -9% on average, but this does not take into account the occasional gross errors of as much as 70% that will undoubtedly have arisen as a result of alpha counting errors, (e.g. sample b7 in section 7.5.10). Those dates which incorporated beta and gamma TLD information will of course be much less sensitive to this source of error. In addition, most of the earlier dates used an incorrect calibration for fine grain dose rate, which was shown in chapter 2 to overestimate the archaeological dose by 16%. The nett error in dates due to the latter effect is about +8%, which suggests that on average the corrections to the fine grain dose rate and to alpha counting will cancel out on existing dates.

Appendix A

'SAMPO', A FORTRAN PROGRAM FOR COMPUTER ANALYSIS OF GAMMA SPECTRA FROM SOLID STATE DETECTORS

All of the reduction of gamma spectra to photon energies and count rates in the second part of this thesis has been performed using SAMPO, a FORTRAN program written by Jorma T. Routti at the Lawrence Radiation Laboratory, University of California, for the analysis of complex photopeak spectra from solid state detectors. All the computing was performed on the University of Oxford's ICL 2980. Full details of the analysis methods and the use of the program are given in ROUTTI and PRUSSIN (1969) and ROUTTI (1969).

Briefly, the purpose of the analysis is to determine the exact channel locations and areas of photopeaks, the energies and intensities of the corresponding gamma rays and the statistical and calibration uncertainties associated with these quantities. This analysis is based upon the study of photopeaks, which may be single peaks, or clusters of peaks called multiplets, on a continuum due to the Compton continua of higher energy lines and the general counting background. The exact channel location and peak areas, together with statistical uncertainties, are determined by fitting a section of the measured spectrum in the least squares sense using analytical functions to represent the peak shapes. These functions consist of a Gaussian with provisions for exponential tailing on both the low and high energy sides, and the parameters defining these functions at a particular energy are obtained by an initial least squares fit of intense well isolated lines. The sources described in Appendix B, MSP/1 and MSD/2, were used to obtain these calibration spectra. From this initial calibration fit an array of four calibration parameters defining the Gaussian centroid and width, and the distance from the centroid of the junctions with the low and high energy tailing functions, are obtained from each gamma line, and as these parameters vary smoothly with energy, interpolation provides values for any desired region of the spectrum. Routine analysis of low intensity peaks uses this calibration array as input data, rather than perform the calibration for each individual spectrum.

The first stage in routine analysis is to perform a peak search

to identify the approximate centroids of photopeaks, and to select the intervals in which up to 6 photopeaks may be analysed at a time. SAMPO performs both statistical and peak shape tests to identify these centroids. The program produces a list of all the peaks found, and also indicates which have passed the tests of acceptance. Listed but unaccepted peaks provide information on photopeaks that may have to be included in the fitting procedure for a complete analysis. (They may for instance be multiplets, which are rejected on shape grounds). The results of a peak search computation are illustrated in table A.1. Peaks may then be added or removed from the selected fitting interval before the program is instructed to perform the fitting procedure.

The peak energies are calculated from calibration data derived from the initial calibration runs. Linear interpolation was used for the work described here, although more sophisticated procedures are available.

Figures A.1, A.2, and A.3 give three examples of the results of peak fitting in three different energy regions. Note that the analysis of the regions illustrated in figures A.2 and A.3 would have been virtually impossible by hand.

Table A.1

Printout from peak search routine after analysis of spectrum from soil sample P41J

sample weight 5.68 g

count time 170 ksec

I	APPROXIMATE CHANNEL	APPROXIMATE ENERGY	SIGNIFICANCE OF PEAK	CHECK-1 SIGNIF	CHECK-2 SHAPE	ACCEPTED CHANNELS	NUMBER	ADD CHANNEL	DROP CHANNEL
1	108	19.2	62.153		REJECT				
2	144	26.0	2.337	SMALL	REJECT				
3	255	46.5	7.948		CHECK	255	1		
4	293	53.5	2.466	SMALL	REJECT				
5	347	63.3	11.649		CHECK	347	2		
6	422	77.0	28.792		REJECT				
7	478	87.2	12.169		CHECK	478	3		
8	510	93.1	12.392		REJECT				
9	544	99.3	2.694	SMALL	REJECT				
10	575	104.9	2.354	SMALL	REJECT				
11	708	129.2	3.682	SMALL	CHECK				
12	790	144.2	3.317	SMALL	REJECT				
13	844	154.1	2.042	SMALL	REJECT				
14	982	179.3	2.799	SMALL	REJECT				
15	1018	185.9	14.534			1018	4		
16	1053	192.3	2.661	SMALL	REJECT				
17	1146	209.3	4.853		CHECK	1146	5		
18	1307	238.7	38.263			1307	6		
19	1381	252.2	2.594	SMALL	REJECT				
20	1478	269.9	3.565	SMALL	CHECK				
21	1519	277.4	2.030	SMALL	CHECK				
22	1617	295.3	21.182			1617	7		
23	1696	309.7	2.613	SMALL	REJECT				
24	1852	338.2	13.062		CHECK	1852	8		
25	1927	351.9	29.096			1927	9		
26	2244	409.8	2.220	SMALL	CHECK				
27	2343	427.9	2.524	SMALL	REJECT				
28	2438	445.3	2.777	SMALL	REJECT				
29	2537	463.4	4.631		REJECT				
30	2669	487.5	2.371	SMALL	REJECT				
31	2739	500.3	2.475	SMALL	REJECT				
32	2797	510.9	11.433			2797	10		
33	2922	533.7	2.141	SMALL	CHECK				
34	3193	583.2	12.599		CHECK	3193	11		
35	3264	596.2	2.972	SMALL	REJECT				
36	3288	600.6	2.681	SMALL	REJECT				
37	3336	609.3	19.237			3336	12		
38	3697	675.3	2.277	SMALL	REJECT				
39	3981	727.2	4.774		CHECK	3981	13		
40	4207	768.5	2.756	SMALL	REJECT				
41	4301	785.6	2.114	SMALL	REJECT				
42	4349	794.4	2.239	SMALL	CHECK				
43	4717	861.7	2.097	SMALL	REJECT				
44	4927	900.0	2.465	SMALL	REJECT				
45	4990	911.6	11.222			4990	14		
46	5305	969.1	8.787		CHECK	5305	15		
47	5400	986.5	2.124	SMALL	REJECT				
48	5559	1015.6	2.400	SMALL	REJECT				
49	5610	1024.9	2.121	SMALL	REJECT				
50	5720	1045.0	2.138	SMALL	REJECT				
51	6131	1120.1	7.107		CHECK	6131	16		
52	6330	1156.5	2.867	SMALL	REJECT				
53	6398	1168.9	2.220	SMALL	REJECT				
54	6453	1179.0	2.093	SMALL	REJECT				
55	6780	1238.7	3.640	SMALL	CHECK				
56	6818	1245.7	2.096	SMALL	REJECT				
57	7205	1316.5	2.045	SMALL	REJECT				
58	7300	1333.8	2.046	SMALL	CHECK				
59	7428	1357.3	2.694	SMALL	REJECT				
60	7546	1378.5	3.672	SMALL	REJECT				
61	7580	1385.1	2.953	SMALL	REJECT				
62	7717	1410.1	2.161	SMALL	CHECK				
63	7866	1437.4	2.113	SMALL	REJECT				
64	7995	1461.0	40.427			7995	17		

$$$$$$$$$ NEXT CONTROL CARD = PEAKADD 0.220E+03 0.269E+03 0.473E+03 0.510E+03 0.496E+03 0.000E+00

Figure A.1

Printout from peakfit routine after analysis of spectrum from soil sample P41J

sample weight 5.68 g

count time 170 ksec

Peaks fitted: 63 keV Th-234

68 keV Th-230

```
FITTING INTERVAL   =   323 (   356 )   390          PEAK CHANNELS =    347    373
LINEAR LSQ PARAM.  =  CHISQUARE    CONT.CONST.  CONT.SLOPE   CONT.PARAB.  PEAK HEIGHTS
                      0.884E+02    0.111E+03  -0.111E+00    0.244E-02    0.790E+02    0.999E+01
FITTING PARAMETERS = CONT.CONST.  CONT.SLOPE   CONT.PARAB.  PEAK HEIGHT  PEAK CENTR.  PEAK HEIGHT  PEAK CENTR.
INITIAL GUESSES    =   0.111E+03  -0.111E+00    0.000E+00    0.790E+02    0.347E+03    0.999E+01    0.373E+03

DIAGONAL OF MATRIX =   0.100E+01   0.100E+01   0.000E+00    0.100E+01    0.100E+01    0.100E+01    0.100E+01

INITIAL F OR CHISQR=   0.893E+02
INITIAL GRADIENT   =  -0.109E+01  -0.276E+01  -0.765E+03   -0.490E-01   -0.632E+00   -0.180E+00    0.202E+00

FINAL F OR CHISQR  =  0.88556E+02+OR-  0.32697E-16
FINAL PARAMETERS   =   0.113E+03  -0.105E+00    0.000E+00    0.772E+02    0.347E+03    0.882E+01    0.372E+03

FINAL GRADIENT     =  -0.932E-09  -0.143E-07  -0.265E+03    0.824E-09    0.173E-08   -0.918E-09   -0.719E-09
```

```
CHAN.  DEV.  CONTINUUM  YMIN= 0.930E+02  IIIIIIIIIIIIIII SEMILOGARITHMIC SCALE IIIIIIIIIIIIII  YMAX= 0.207E+03     DATA       FIT
323.    0.5  1.16E+02                                (                                                        1.220E+02  1.162E+02
324.    1.3  1.16E+02                                (                                                        1.310E+02  1.162E+02
325.    2.2  1.16E+02                                (                                                        1.430E+02  1.162E+02
326.   -1.0  1.16E+02                                (                                                        1.060E+02  1.162E+02
327.    1.8  1.16E+02                               I+                                                        1.370E+02  1.162E+02
328.    0.4  1.16E+02                               I+                                                        1.210E+02  1.163E+02
329.   -1.4  1.15E+02                               I+                                                        1.020E+02  1.165E+02
330.   -2.5  1.15E+02                               I+                                                        9.300E+01  1.167E+02
331.   -0.5  1.15E+02                              I +                                                        1.120E+02  1.172E+02
332.   -0.3  1.15E+02                              ) +                                                        1.150E+02  1.178E+02
333.   -0.7  1.15E+02                             I  +                                                        1.110E+02  1.187E+02
334.    2.3  1.15E+02                             I   +                                                       1.480E+02  1.200E+02
335.   -0.6  1.15E+02                             )    +                                                      1.150E+02  1.219E+02
336.    0.1  1.15E+02                             I     +.                                                    1.260E+02  1.245E+02
337.   -2.5  1.15E+02                            I       +                                                   1.030E+02  1.282E+02
338.   -0.4  1.15E+02                            I        +                                                  1.290E+02  1.332E+02
339.    0.5  1.14E+02                            I          +                                                1.460E+02  1.396E+02
340.    2.2  1.14E+02                            I           +                                               1.760E+02  1.470E+02
341.   -1.4  1.14E+02                            I            +                                              1.500E+02  1.552E+02
342.    0.6  1.14E+02                            I             +                                             1.710E+02  1.638E+02
343.   -0.6  1.14E+02                            I              +                                            1.650E+02  1.722E+02
344.    0.5  1.14E+02                            I               +.                                          1.860E+02  1.796E+02
345.    1.4  1.14E+02                            I                 +                                         2.050E+02  1.856E+02
346.   -1.9  1.14E+02                            I                  +                                        1.650E+02  1.894E+02
347.    1.1  1.14E+02                           I                    +                                       2.070E+02  1.908E+02
348.   -1.0  1.13E+02                           I                     +                                      1.760E+02  1.894E+02
349.    0.5  1.13E+02                           I                      +.                                    1.930E+02  1.856E+02
350.    1.1  1.13E+02                           I                        +                                   1.950E+02  1.796E+02
351.   -1.2  1.13E+02                           I                         +                                  1.570E+02  1.720E+02
352.   -2.2  1.13E+02                           I                          +                                 1.380E+02  1.635E+02
353.    0.1  1.13E+02                           I                           +.                               1.560E+02  1.547E+02
354.    1.5  1.13E+02                           I                             +                              1.650E+02  1.463E+02
355.    0.9  1.13E+02                           I                              +                             1.500E+02  1.386E+02
356.    1.0  1.13E+02                           I                               +                            1.440E+02  1.320E+02
357.    0.4  1.13E+02                           I                                +.                          1.310E+02  1.266E+02
358.    0.7  1.12E+02                          I                                  +                          1.310E+02  1.224E+02
359.   -0.1  1.12E+02                          I                                   +.                        1.180E+02  1.193E+02
360.    0.1  1.12E+02                          I                                    +                        1.180E+02  1.172E+02
361.   -1.1  1.12E+02                         I                                     +                        1.050E+02  1.159E+02
362.   -0.8  1.12E+02                         I                                      +                       1.070E+02  1.152E+02
363.   -1.8  1.12E+02                         I                                       +                      9.700E+01  1.151E+02
364.    2.5  1.12E+02                         I                                        +                     1.460E+02  1.153E+02
365.    0.3  1.12E+02                         I                                         +.                   1.190E+02  1.157E+02
366.    0.2  1.12E+02                         I                                          +.                  1.190E+02  1.164E+02
367.    0.3  1.11E+02                         I                                           +.                 1.200E+02  1.172E+02
368.   -0.8  1.11E+02                        .I                                            +                 1.100E+02  1.180E+02
369.   -0.3  1.11E+02                        I                                             +.                1.150E+02  1.187E+02
370.   -0.2  1.11E+02                        I                                              +.               1.170E+02  1.193E+02
371.   -0.2  1.11E+02                        I                                               +.              1.180E+02  1.197E+02
372.    0.5  1.11E+02                        I                                                +              1.250E+02  1.198E+02
373.    1.8  1.11E+02                        I                                                 +             1.410E+02  1.196E+02
374.   -0.2  1.11E+02                        I                                                 +.            1.170E+02  1.191E+02
375.   -1.6  1.11E+02                        I                                                  +            1.020E+02  1.184E+02
376.    0.7  1.11E+02                        I                                                  +.           1.250E+02  1.175E+02
377.   -0.4  1.10E+02                        I.                                                  +           1.120E+02  1.164E+02
378.   -0.9  1.10E+02                      I                                                     +.          1.060E+02  1.153E+02
379.    1.3  1.10E+02                      I                                                      +          1.290E+02  1.142E+02
380.    1.1  1.10E+02                      I                                                       +         1.260E+02  1.132E+02
381.    0.3  1.10E+02                      I                                                        +.       1.160E+02  1.124E+02
382.   -1.0  1.10E+02                     I                                                         +       1.020E+02  1.116E+02
383.   -0.7  1.10E+02                     I+                                                         +      1.040E+02  1.110E+02
384.   -0.1  1.10E+02                    .I+                                                          +     1.090E+02  1.105E+02
385.   -0.8  1.10E+02                    .(                                                           +.    1.020E+02  1.101E+02
386.    0.6  1.09E+02                     (                                                            +   1.160E+02  1.098E+02
387.    0.5  1.09E+02                     (                                                             +  1.150E+02  1.096E+02
388.   -1.3  1.09E+02                    I+                                                             +  9.700E+01  1.094E+02
389.    0.4  1.09E+02                    (                                                               + 1.130E+02  1.093E+02
390.    1.6  1.09E+02                    (                                                                + 1.270E+02  1.091E+02
      SYMBOLS   I = CONTINUUM   . = DATA   + = FIT   * = .AND+   ( = IAND+   ) = IAND.   $ = IAND+AND.
SUMDATA=     0.12583E+04 SUMCALC=     0.11698E+04
```

```
   RESULTS FROM THE ABOVE FIT, BE CRITICAL WITH THE  ERROR ESTIMATES
   REJECT IF CHISQUARE =  0.88556E+02   OR  SIGMA =     1.205     IS UNACCEPTABLE, CHECK PLOT FOR MISSING PEAKS
   CHANNEL      FIT-ERR-CH  ENERGY-KEV  CAL-ERR-KEV EN-ERR-KEV   AREA-COUNTS FIT-ERR-PC  INTENS-COUNT CAL-ERR-PC INT-ERR-PC

  347.0613       0.0872      63.3214       0.0470       0.0496  0.1050E+04       5.8413  0.1050E+04       0.0000       5.8413

  372.2596       2.4110      67.9258       0.0433       0.4423  0.1200E+03      48.6263  0.1200E+03       0.0000      48.6263
```

Figure A.2 Printout from peakfit routine after analysis of spectrum from sherd P41J07

sample weight 5.0 g Peak fitted: 93 keV Th-234

count time 85 ksec + uranium and thorium X rays

```
FITTING INTERVAL     =   443 (   492 )    542          PEAK CHANNELS =    478    496    510
LINEAR LSQ PARAM.    =  CHISQUARE   CONT.CONST.  CONT.SLOPE  CONT.PARAB.  PEAK HEIGHTS
                        0.129E+03   0.603E+02  -0.318E+00  -0.330E-02   0.686E+02   0.249E+02   0.303E+02

FITTING PARAMETERS = CONT.CONST.  CONT.SLOPE  CONT.PARAB.  PEAK HEIGHT  PEAK CENTR.  PEAK HEIGHT  PEAK CENTR.
INITIAL GUESSES    =   0.603E+02  -0.318E+00  -0.330E-02   0.686E+02   0.478E+03   0.249E+02   0.496E+03
                                                           0.303E+02   0.510E+03
INITIAL F OR CHISQR=   0.129E+03
INITIAL GRADIENT   =   0.452E-12   0.373E-11   0.332E-09   0.550E-13  -0.476E+01   0.632E-13   0.318E+01
                                                           0.683E-13   0.542E+01
FINAL F OR CHISQR  =  0.11797E+03+OR-  0.52300E-14
FINAL PARAMETERS   =   0.589E+02  -0.308E+00  -0.240E-02   0.664E+02   0.478E+03   0.266E+02   0.492E+03
                                                           0.560E+02   0.509E+03
FINAL GRADIENT     =   0.229E-09   0.734E-08   0.153E-05  -0.101E-08   0.333E-08   0.809E-09   0.121E-08
                                                          -0.943E-09  -0.113E-08
```

```
CHAN.  DEV.  CONTINUUM  YMIN= 0.240E+02  IIIIIIIIIIIIII SEMILOGARITHMIC SCALE IIIIIIIIIIIIII  YMAX= 0.138E+03     DATA       FIT
443.   -1.8  6.82E+01                                                                          5.500E+01  6.821E+01
444.    1.6  6.81E+01                                                                          8.300E+01  6.813E+01
445.   -1.5  6.81E+01                                                                          5.700E+01  6.805E+01
446.   -0.1  6.80E+01                                                                          6.700E+01  6.797E+01
447.   -0.6  6.79E+01                                                                          6.300E+01  6.788E+01
448.   -0.5  6.78E+01                                                                          6.400E+01  6.779E+01
449.   -1.7  6.77E+01                                                                          5.500E+01  6.770E+01
450.    1.0  6.76E+01                                                                          7.600E+01  6.760E+01
451.   -1.7  6.75E+01                                                                          5.500E+01  6.750E+01
452.    0.2  6.74E+01                                                                          6.900E+01  6.740E+01
453.   -0.0  6.72E+01                                                                          6.700E+01  6.731E+01
454.   -1.1  6.71E+01                                                                          5.900E+01  6.721E+01
455.    0.3  6.70E+01                                                                          7.000E+01  6.712E+01
456.   -0.3  6.69E+01                                                                          6.500E+01  6.704E+01
457.    1.1  6.67E+01                                                                          7.700E+01  6.699E+01
458.    2.8  6.66E+01                                                                          9.400E+01  6.696E+01
459.    1.2  6.64E+01                                                                          7.800E+01  6.697E+01
460.    0.8  6.63E+01                                                                          7.400E+01  6.705E+01
461.    0.4  6.61E+01                                                                          7.100E+01  6.723E+01
462.    0.9  6.60E+01                                                                          7.500E+01  6.754E+01
463.    0.1  6.58E+01                                                                          6.900E+01  6.805E+01
464.    0.7  6.56E+01                                                                          7.500E+01  6.885E+01
465.    1.8  6.55E+01                                                                          8.700E+01  7.007E+01
466.   -0.1  6.53E+01                                                                          7.100E+01  7.188E+01
467.    0.2  6.51E+01                                                                          7.600E+01  7.456E+01
468.    0.4  6.49E+01                                                                          8.600E+01  7.829E+01
469.    1.4  6.47E+01                                                                          8.700E+01  8.306E+01
470.    0.1  6.45E+01                                                                          9.000E+01  8.881E+01
471.    0.3  6.43E+01                                                                          9.800E+01  9.540E+01
472.   -0.9  6.41E+01                                                                          9.400E+01  1.025E+02
473.   -0.2  6.39E+01                                                                          1.080E+02  1.098E+02
474.    0.0  6.37E+01                                                                          1.170E+02  1.167E+02
475.    1.3  6.34E+01                                                                          1.380E+02  1.227E+02
476.   -1.7  6.32E+01                                                                          1.090E+02  1.271E+02
477.   -0.2  6.30E+01                                                                          1.270E+02  1.297E+02
478.    0.2  6.27E+01                                                                          1.320E+02  1.302E+02
479.   -0.1  6.25E+01                                                                          1.270E+02  1.285E+02
480.    0.1  6.22E+01                                                                          1.260E+02  1.251E+02
481.    0.5  6.20E+01                                                                          1.260E+02  1.202E+02
482.   -0.1  6.17E+01                                                                          1.140E+02  1.146E+02
483.   -0.5  6.15E+01                                                                          1.040E+02  1.089E+02
484.    0.7  6.12E+01                                                                          1.110E+02  1.035E+02
485.    0.5  6.09E+01                                                                          1.040E+02  9.892E+01
486.    0.1  6.07E+01                                                                          9.600E+01  9.535E+01
487.    0.2  6.04E+01                                                                          9.500E+01  9.283E+01
488.    0.3  6.01E+01                                                                          9.400E+01  9.126E+01
489.   -0.3  5.98E+01                                                                          8.300E+01  9.029E+01
490.    0.0  5.95E+01                                                                          9.000E+01  8.968E+01
491.    0.3  5.92E+01                                                                          9.200E+01  8.910E+01
492.   -0.4  5.89E+01                                                                          8.500E+01  8.832E+01
493.    0.1  5.86E+01                                                                          8.800E+01  8.713E+01
494.   -0.5  5.83E+01                                                                          8.100E+01  8.550E+01
495.   -0.3  5.80E+01                                                                          8.100E+01  8.355E+01
496.    0.3  5.76E+01                                                                          8.400E+01  8.153E+01
497.    0.1  5.73E+01                                                                          8.100E+01  7.977E+01
498.    0.7  5.70E+01                                                                          8.500E+01  7.870E+01
499.   -0.5  5.66E+01                                                                          7.400E+01  7.866E+01
500.    0.2  5.63E+01                                                                          8.200E+01  7.977E+01
501.    0.6  5.59E+01                                                                          8.800E+01  8.208E+01
502.    0.5  5.56E+01                                                                          9.000E+01  8.553E+01
503.   -0.4  5.52E+01                                                                          8.600E+01  8.987E+01
504.   -0.4  5.49E+01                                                                          9.100E+01  9.473E+01
505.    0.4  5.45E+01                                                                          1.040E+02  9.961E+01
506.    1.6  5.41E+01                                                                          1.220E+02  1.040E+02
507.   -0.2  5.37E+01                                                                          1.050E+02  1.073E+02
508.   -0.0  5.34E+01                                                                          8.200E+01  1.091E+02
509.    1.6  5.30E+01                                                                          1.160E+02  1.092E+02
510.    1.1  5.26E+01                                                                          1.180E+02  1.074E+02
511.   -0.7  5.22E+01                                                                          9.700E+01  1.038E+02
512.    1.1  5.18E+01                                                                          1.100E+02  9.878E+01
513.   -0.5  5.14E+01                                                                          8.800E+01  9.274E+01
514.    2.0  5.10E+01                                                                          1.070E+02  8.614E+01
515.   -1.6  5.05E+01                                                                          6.500E+01  7.946E+01
516.    2.2  5.01E+01                                                                          9.400E+01  7.308E+01
517.   -0.7  4.97E+01                                                                          6.200E+01  6.732E+01
518.    0.1  4.93E+01                                                                          6.300E+01  6.233E+01
519.   -0.5  4.88E+01                                                                          5.600E+01  5.819E+01
520.   -0.3  4.84E+01                                                                          5.300E+01  5.487E+01
521.    0.6  4.80E+01                                                                          5.700E+01  5.228E+01
522.   -0.8  4.75E+01                                                                          4.500E+01  5.032E+01
523.    2.0  4.70E+01                                                                          6.500E+01  4.887E+01
524.   -2.0  4.66E+01                                                                          3.600E+01  4.777E+01
525.   -0.6  4.61E+01                                                                          4.300E+01  4.689E+01
526.   -2.1  4.57E+01                                                                          3.400E+01  4.615E+01
527.   -0.5  4.52E+01                                                                          4.200E+01  4.550E+01
528.   -0.9  4.47E+01                                                                          3.900E+01  4.491E+01
529.    0.5  4.42E+01                                                                          4.800E+01  4.436E+01
530.    0.0  4.37E+01                                                                          4.400E+01  4.382E+01
531.   -1.0  4.32E+01                                                                          3.700E+01  4.330E+01
532.   -3.8  4.27E+01                                                                          2.400E+01  4.278E+01
533.    0.5  4.22E+01                                                                          4.800E+01  4.226E+01
534.   -1.0  4.17E+01                                                                          3.600E+01  4.175E+01
535.    1.0  4.12E+01                                                                          4.800E+01  4.123E+01
536.    1.8  4.07E+01                                                                          5.400E+01  4.071E+01
537.    1.3  4.02E+01                                                                          4.900E+01  4.018E+01
538.   -0.1  3.97E+01                                                                          3.900E+01  3.966E+01
539.    0.9  3.91E+01                                                                          4.500E+01  3.912E+01
540.    1.5  3.86E+01                                                                          4.900E+01  3.859E+01
541.    1.9  3.80E+01                                                                          5.200E+01  3.805E+01
542.    1.3  3.75E+01                                                                          4.600E+01  3.750E+01
       SYMBOLS   I = CONTINUUM   . = DATA   + = FIT   * = .AND+   ( = IAND+   ) = IAND.   S = IAND+AND.
SUMDATA=     0.21441E+04 SUMCALC=     0.20261E+04
```

```
RESULTS FROM THE ABOVE FIT, BE CRITICAL WITH THE  ERROR ESTIMATES
REJECT IF CHISQUARE =  0.1180E+03   OR  SIGMA =     1.139     IS UNACCEPTABLE, CHECK PLOT FOR MISSING PEAKS
CHANNEL     FIT-ERR-CH  ENERGY-KEV  CAL-ERR-KEV EN-ERR-KEV   AREA-COUNTS FIT-ERR-PC  INTENS-COUNT CAL-ERR-PC INT-ERR-PC

477.6526      0.4262     87.1686      0.0280      0.0827   0.9030E+03     6.5163   0.9030E+03     0.0000     6.5163

491.9046      1.1139     89.7708      0.0259      0.2050   0.3612E+03    13.5691   0.3612E+03     0.0000    13.5691

508.7952      0.3849     92.8547      0.0234      0.0741   0.7614E+03     6.9873   0.7614E+03     0.0000     6.9873
```

Figure A.3

Printout from peakfit routine after analysis of spectrum from Th-228 source in dunite

sample weight 8.8 g

count time 80 ksec

sample activity ~ 0.23 nCi g^{-1}

Peaks fitted: 239 keV Pb-212

241 keV Ra-224

```
FITTING INTERVAL    =  1265 (  1305 )   1346          PEAK CHANNELS =   1308   1321
LINEAR LSQ PARAM.   =  CHISQUARE    CONT.CONST.  CONT.SLOPE   CONT.PARAB.  PEAK HEIGHTS
                        0.174E+04    0.721E+03   -0.104E+02  -0.738E-01    0.651E+05   0.505E+04
FITTING PARAMETERS  =  CONT.CONST.  CONT.SLOPE   CONT.PARAB.  PEAK HEIGHT  PEAK CENTR.  PEAK HEIGHT  PEAK CENTR.
INITIAL GUESSES     =    0.721E+03  -0.104E+02   -0.738E-01    0.651E+05    0.131E+04    0.505E+04    0.132E+04

INITIAL F OR CHISQR=    0.174E+04
INITIAL GRADIENT    =  -0.573E-12    0.521E-11  -0.303E-09   -0.847E-14    0.108E+05   -0.125E-13   -0.319E+02

FINAL F OR CHISQR   =  0.42776E+03+OR-  0.24812E-12
FINAL PARAMETERS    =    0.678E+03  -0.103E+02   -0.367E-01    0.647E+05    0.131E+04    0.564E+04    0.132E+04

FINAL GRADIENT      =  -0.321E-08   -0.285E-07  -0.261E-05   -0.265E-09    0.773E-05    0.322E-09   -0.459E-07

CHAN.  DEV.  CONTINUUM  YMIN= 0.193E+03  IIIIIIIIIIIIII SEMILOGARITHMIC SCALE IIIIIIIIIIIIII  YMAX= 0.664E+05     DATA       FIT
1265.  -2.0  1.03E+03                                                                          9.700E+02  1.033E+03
1266.  -3.4  1.03E+03                                                                          9.220E+02  1.026E+03
1267.  -2.8  1.02E+03                                                                          9.330E+02  1.018E+03
1268.  -2.2  1.01E+03                                                                          9.420E+02  1.010E+03
1269.  -2.2  1.00E+03                                                                          9.350E+02  1.003E+03
1270.  -1.4  9.95E+02                                                                          9.510E+02  9.951E+02
1271.  -1.5  9.87E+02                                                                          9.410E+02  9.873E+02
1272.  -1.7  9.79E+02                                                                          9.280E+02  9.794E+02
1273.  -1.0  9.71E+02                                                                          9.420E+02  9.715E+02
1274.  -2.2  9.63E+02                                                                          8.990E+02  9.635E+02
1275.   0.2  9.55E+02                                                                          9.630E+02  9.555E+02
1276.   1.8  9.47E+02                                                                          1.004E+03  9.474E+02
1277.   0.4  9.39E+02                                                                          9.520E+02  9.394E+02
1278.   3.6  9.31E+02                                                                          1.048E+03  9.313E+02
1279.   1.6  9.22E+02                                                                          9.740E+02  9.234E+02
1280.   1.4  9.14E+02                                                                          9.580E+02  9.156E+02
1281.   2.5  9.05E+02                                                                          9.660E+02  9.082E+02
1282.   2.2  8.97E+02                                                                          9.710E+02  9.013E+02
1283.   3.6  8.88E+02                                                                          1.010E+03  8.954E+02
1284.   2.1  8.79E+02                                                                          9.570E+02  8.911E+02
1285.   2.6  8.70E+02                                                                          9.690E+02  8.894E+02
1286.   1.9  8.61E+02                                                                          9.500E+02  8.917E+02
1287.   4.1  8.52E+02                                                                          1.034E+03  9.007E+02
1288.   2.7  8.43E+02                                                                          1.006E+03  9.201E+02
1289.   4.0  8.34E+02                                                                          1.089E+03  9.564E+02
1290.   2.1  8.25E+02                                                                          1.089E+03  1.019E+03
1291.   1.9  8.16E+02                                                                          1.192E+03  1.125E+03
1292.  -2.3  8.06E+02                                                                          1.218E+03  1.298E+03
1293.  -1.9  7.97E+02                                                                          1.504E+03  1.579E+03
1294.  -2.1  7.87E+02                                                                          1.937E+03  2.031E+03
1295.   0.8  7.78E+02                                                                          2.800E+03  2.756E+03
1296.   0.2  7.68E+02                                                                          3.903E+03  3.915E+03
1297.  -0.8  7.59E+02                                                                          5.706E+03  5.764E+03
1298.   0.1  7.49E+02                                                                          8.632E+03  8.619E+03
1299.  -2.5  7.39E+02                                                                          1.232E+04  1.260E+04
1300.  -2.5  7.29E+02                                                                          1.749E+04  1.782E+04
1301.  -1.8  7.19E+02                                                                          2.401E+04  2.429E+04
1302.  -2.4  7.09E+02                                                                          3.139E+04  3.181E+04
1303.  -0.2  6.99E+02                                                                          3.991E+04  3.995E+04
1304.   0.2  6.89E+02                                                                          4.814E+04  4.809E+04
1305.   1.4  6.79E+02                                                                          5.578E+04  5.544E+04
1306.   0.3  6.68E+02                                                                          6.129E+04  6.121E+04
1307.   2.2  6.57E+02                                                                          6.527E+04  6.470E+04
1308.   3.6  6.47E+02                                                                          6.643E+04  6.549E+04
1309.   2.9  6.36E+02                                                                          6.422E+04  6.349E+04
1310.   1.1  6.26E+02                                                                          5.926E+04  5.900E+04
1311.  -0.0  6.15E+02                                                                          5.263E+04  5.264E+04
1312.  -0.8  6.04E+02                                                                          4.499E+04  4.516E+04
1313.  -1.9  5.93E+02                                                                          3.703E+04  3.739E+04
1314.  -1.0  5.82E+02                                                                          2.988E+04  3.006E+04
1315.  -2.3  5.71E+02                                                                          2.332E+04  2.367E+04
1316.  -2.9  5.60E+02                                                                          1.811E+04  1.850E+04
1317.  -0.9  5.49E+02                                                                          1.447E+04  1.457E+04
1318.  -2.6  5.38E+02                                                                          1.147E+04  1.176E+04
1319.  -0.2  5.26E+02                                                                          9.791E+03  9.810E+03
1320.  -1.0  5.15E+02                                                                          8.361E+03  8.455E+03
1321.   2.0  5.03E+02                                                                          7.622E+03  7.446E+03
1322.   1.8  4.92E+02                                                                          6.752E+03  6.605E+03
1323.   1.9  4.80E+02                                                                          5.961E+03  5.817E+03
1324.   2.7  4.69E+02                                                                          5.215E+03  5.020E+03
1325.  -0.2  4.57E+02                                                                          4.201E+03  4.214E+03
1326.   2.5  4.45E+02                                                                          3.581E+03  3.432E+03
1327.   0.3  4.33E+02                                                                          2.727E+03  2.713E+03
1328.  -0.9  4.21E+02                                                                          2.052E+03  2.091E+03
1329.  -0.3  4.09E+02                                                                          1.569E+03  1.580E+03
1330.  -2.9  3.97E+02                                                                          1.088E+03  1.184E+03
1331.  -4.0  3.85E+02                                                                          7.790E+02  8.907E+02
1332.  -4.0  3.72E+02                                                                          5.870E+02  6.839E+02
1333.  -1.6  3.60E+02                                                                          5.080E+02  5.435E+02
1334.  -3.0  3.48E+02                                                                          3.920E+02  4.511E+02
1335.  -3.8  3.35E+02                                                                          3.230E+02  3.920E+02
1336.  -3.9  3.23E+02                                                                          2.880E+02  3.533E+02
1337.  -2.9  3.10E+02                                                                          2.790E+02  3.271E+02
1338.  -1.4  2.97E+02                                                                          2.830E+02  3.067E+02
1339.   0.3  2.84E+02                                                                          2.940E+02  2.896E+02
1340.  -1.5  2.72E+02                                                                          2.510E+02  2.744E+02
1341.   0.7  2.59E+02                                                                          2.710E+02  2.602E+02
1342.   0.7  2.46E+02                                                                          2.580E+02  2.465E+02
1343.   3.0  2.33E+02                                                                          2.830E+02  2.330E+02
1344.   3.7  2.19E+02                                                                          2.820E+02  2.196E+02
1345.   3.6  2.06E+02                                                                          2.650E+02  2.063E+02
1346.   4.8  1.93E+02                                                                          2.720E+02  1.929E+02
      SYMBOLS   I = CONTINUUM   . = DATA   + = FIT    * = .AND+   ( = IAND+   ) = IAND.   $ = IAND+AND.
SUMDATA=      0.84C65E+06 SUMCALC=      0.84022E+06

   RESULTS FROM THE ABOVE FIT, BE CRITICAL WITH THE  ERROR ESTIMATES
   REJECT IF CHISQUARE =  0.4278E+03   OR  SIGMA =      2.388      IS UNACCEPTABLE, CHECK PLOT FOR MISSING PEAKS
   CHANNEL      FIT-ERR-CH  ENERGY-KEV  CAL-ERR-KEV EN-ERR-KEV   AREA-COUNTS FIT-ERR-PC  INTENS-COUNT CAL-ERR-PC INT-ERR-PC

 1307.7550       0.0056     238.6396       0.0013     0.0016  0.7726E+06      0.2033  0.7726E+06       0.0000       0.2033

 1320.5453       0.0624     240.9836       0.0013     0.0115  0.6734E+05      1.0195  0.6734E+05       0.0000       1.0195
```

Appendix B

STANDARDISED RADIOACTIVE SOLUTIONS

Standardised solutions of various radioisotopes were used in the calibration of the spectrometer. All were obtained from the Radiochemical Centre, Amersham, Bucks. They fall into two groups.

(i) Artificial radionuclides used for obtaining the initial energy and absolute efficiency calibration curves described in sections 6.4.1 and 6.4.2. The sources made from these solutions were subsequently used whenever recalibration of the various line shape parameters reqired by "SAMPO" (Appendix A) was indicated.

(ii) Natural radionuclides used for calibrating the spectrometer for analysis. The solutions used were Ra-226 (section 6.6.4) and Pb-210 (section 6.6.6). Although not in solution the thorium nitrate salt is also considered here as an R.C.C. standard.

B.1 ARTIFICIAL RADIONUCLIDES

As the absolute activities of these solutions are not critical to the operation of the spectrometer they will not be described in detail. Each solution was diluted in an appropriate medium, and a mineral matrix standard prepared in the usual way (see section 6.6.1). However, after the first solution had evaporated to dryness, the second solution was added to the matrix containing the first, and so on until the mineral matrix contained seven different radioisotopes of known activities. This was done for two different matrices, dunite and pottery, and the final total activities packed into sample containers are listed in table B.1.

Section 6.6 discussed why cascade gamma emitters cannot be used for absolute efficiency measurement. Y-88, Na-24 and Co-60 are such emitters and were not used for the efficiency curve of section 6.4.2. The 1461 keV point of figure 6.4.3 was calculated from the K-40 absolute standard, described in section 6.6.9.

B.2 Ra-226 SOLUTION

The Ra-226 solution was supplied as 6.56 μCi Ra-226 in 5.0532 g of 0.5M HCl, correct on 1st December 1978. The overall uncertainty was given as $\pm$ 3.9%, with the component due to random variations

Table B1

Mixed source standards

Isotope	Half life years	Energy keV	MSD/2 nCi g^{-1}	MSP/1 nCi g^{-1}
Am-241	433 $_4$	26.4 59.6	1.19	0.480
Co-57	0.7417 $_6$	122.1 134.5	1.97	0.467
Cs-137	30.1 $_5$	32.1 36.6 661.6	2.24	0.732
Mn-54	0.8556 $_6$	834.8	1.72	0.618
Y-88	0.2919 $_6$	898.0	2.41	0.728
Co-60	5.27 $_1$	1173.2 1332.5	2.26	0.733
Na-22	2.60 $_1$	1247.5	2.41	1.529

Note: 1) MSD/2 contains 8.497 g dunite and the activities listed were correct on the 11th March 1979.

2) MSP/1 contains 5.5066 g of pottery (lab. code 69 pot 18) and the activities were correct on the 29th April 1979.

3) errors in half lives are in the least significant figures.

given to three sigma. For the purposes of this work, this overall error was reduced to ± 1.5%, as it was felt that the error margins assigned by R.C.C. were too conservative compared with those associated with the work in this thesis.

The solution was standardised by R.C.C. against solutions provided by the U.S. National Bureau of Standards, using a high pressure re-entrant ionisation chamber. The solution was further examined using a high resolution gamma detector and no impurities were detected.

B.3 Pb-210 SOLUTION

The Pb-210 solution was supplied as 5.16 μCi Pb-210 in 4.9905 g of 2M nitric acid containing 100 μg/ml of inert lead and 100 μg/ml of inert bismuth correct on the 23rd March, 1979. The overall uncertainty was given as ± 2.3%; this was reduced to ± 1% for the reasons given in the previous section.

The solution was standardised by R.C.C. using repeated 4π alpha counting over a period of 82 days. No radioactive impurities of total activity greater than 0.05% of the Pb-210 activity were detected.

B.4 THORIUM NITRATE

The thorium nitrate discussed in section 6.6.7 was refined in 1906, and thus all daughters down to Rn-220 should be in equilibrium with the parent. LAWRENCE (1978, private communication) of R.C.C., Amersham, has given an undated spectrographic analysis, listed in Table B.2. He has also stated that the thoria content (ThO_2) was determined as 47.5%. This corresponds to 41.7% thorium, as compared with 42.03% calculated from the formula $Th(NO_3)_4.4H_2O$.

Table B2

Undated impurity analysis of thorium nitrate salt from R.C.C.

	p.p.m.
barium	3
calcium	3
strontium	<3
sodium	<25
caesium	<25
rubidium	<5
potassium	<5
lithium	<5

No other impurities were detected.

Appendix C

DERIVATION OF THE MAXIMUM LIKELY Rn-222 ESCAPE FROM THE USNBS URANIUM STANDARD NBL 74-A

As was shown in section 6.7, the Pb-210/Ra-226 activity ratio in the USNBS standard NBL 74-A is 0.96 $\pm$ 0.02. This sand has been in its present form for at least 7 years (composition certified in 1972). At some time before that, when the sand was prepared from the original pitchblende, assume a new level of Rn-222 escape was set up, so that

$$I = I_{equil} + I_o e^{-\lambda t} \qquad \text{- - - - - - - - - 1}$$

where I is the total Pb-210 activity at time t after sample preparation,

I_{equil} is the new Rn-222 equilibrium activity at the time of measurement,

I_o is the initial excess (or deficit) of Pb-210 activity above (or below) I_{equil} immediately after new equilibrium conditions have been set up,

λ is the Pb-210 decay constant, 3.15×10^{-2} years^{-1}.

i.e. for t = 7 years,

$$I = I_{equil} + 0.80\ I_o \qquad \text{- - - - - - - - - 2}$$

In the extreme case, there might have been no loss of Rn-222 at all before sample preparation. Then, the initial activity of Pb-210 ($I_{equil} + I_o$) would have been the activity of Ra-226. Experimentally it is observed that, at t = 7 years,

$$I = 0.96(I_{equil} + I_o) \qquad \text{- - - - - - - - - 3}$$

Combining (2) and (3)

$$\frac{I_{equil}}{I_{equil} + I_o} = 0.80 \pm 0.10 \qquad \text{- - - - - - - - - 4}$$

i.e. the present Rn-222 escape could be as great as (20 $\pm$ 10)%. This is clearly not sufficiently close to equilibrium to be used as a standard for Rn-222 daughters.

Appendix D PERUVIAN SITE NOTES REPRODUCED FROM GUNN (1978)

PO1 = LA FLORIDA, Rimac Valley (outskirts of Lima) PV47-18-A2 Square T 1 - 5 and 10.

Idilio Santillana and Avelando Sansovini, Museo Nacional de Antropologia y Arqueologia, Pueblo Libre, Lima.

Face 1 - section

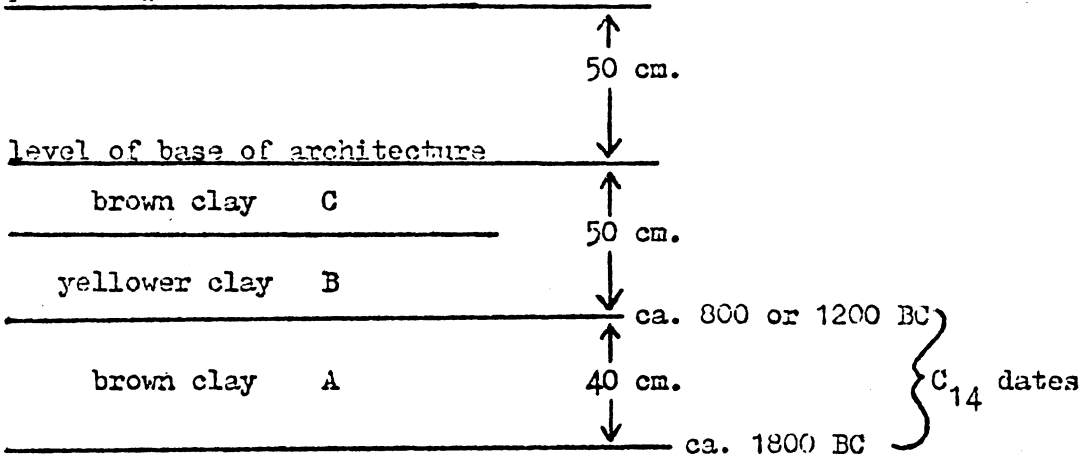

6 shards obtained from level A.

PO2 = HUACA GARAGAY, Rimac Valley (near Lima Airport) PV47-19 mound 128 pit F. U-shaped ceremonial structure, formative period. On mound 128, sunken central plaza with platforms on 3 sides; a stone-lined offering pit 1 m. diameter.

Rogger Ravines, Instituto Nacional de Cultura, Casilla 5247, Lima.

Pit F - diagram

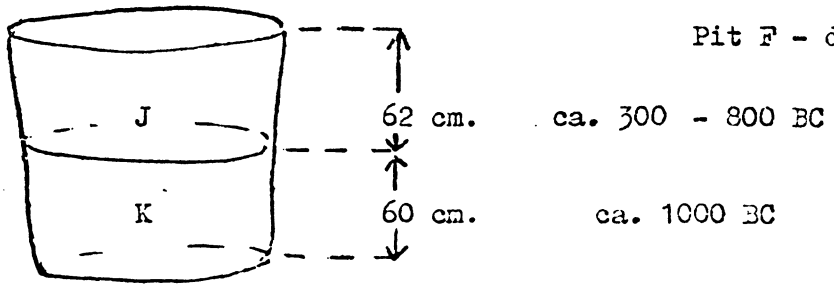

29 shards from level J; 12 shards from level K; additional material supplied by Rogger Ravines:

P02I - group of 12 shards obtained from later cemetery of cist-like graves above Huaca 128 (300 - 800 AD); P02Z - heterogeneous collection from formative period - 6 shards.

P02 ADOBE - a modern mud brick obtained from nearby factory.

P03 = LOS TRES SANTIAGOS, Rimac Valley. Huaca A, 250 metres from Huaca La Palma. Rectangular walled compound. Inca period: 3 clearly defined floor levels, all between 1470 and 1535 AD.

address see P02

P03 - section

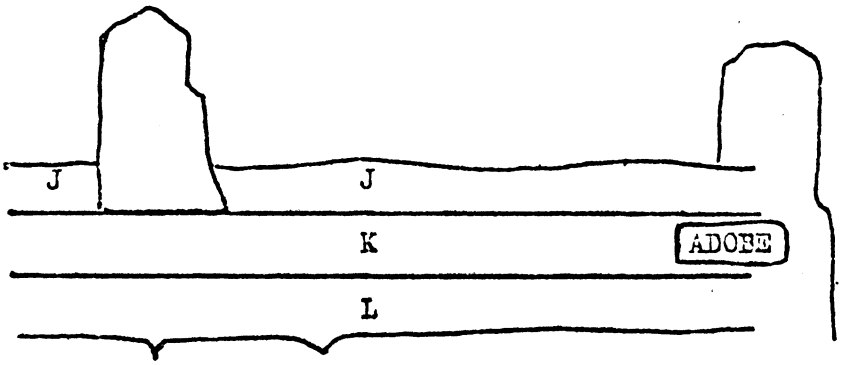

10 shards from level J; 6 from K; 2 from L. Also plaster surface and ADOBE from L; floor surface from K. P03Z01 - one large shard from earlier infill behind site ca. 800 AD.

P04 = HUACA LECHUZA, Viru Valley PV23 - 434. Occupation mound 4 m. high by 40 m. by 80 m. in Viru coastal plain; Puerto Moorian period (300 BC - 100 AD). Four phases of occupation:

(i) inhabitation of sand dune

(ii) construction of adobe walls and columns

(iii) restructuring (ash accumulates)

(iv) present top of site.

Michael West, Los Angeles County Museum of Natural History, Los Angeles. Clay Singer, Department of Anthropology, U.C.L.A., Los Angeles.

J: 7 shards from ash-fill inside large pot (phase (iii)); K: 2 oriented fragments of the large pot, 1.5 m. diameter (phase (ii) or (iii)); L: 11 shards from brown soil below base of adobe column in unit 45 (phase (i)); also 2 ADOBES, one from unit 45, one from unit 42.

P05 = Looted cemetery just NNW of Huaca Negra (P06) PV23-664. 100 - 200 graves, skeletal remains mostly of women and children; pottery now scattered at random, categorized by style.

addresses see P04.

J: Chimu blackware (1250 ± 50 AD), 3 shards; K: pressed red-ware (1150 ± 100 AD), 6 shards; L: Tomoval painted ware plus one piece of large burial pot of same period (1100 ± 50 AD), 4 shards altogether.

P06 = HUACA NEGRA DE GUAÑAPE, Viru Valley PV23-71.
Original excavation reports by Willey (1953 Bureau of American Ethnology, Bulletin 155, Washington: Prehistoric Settlement Patterns in the Viru Valley, Peru) and Strong and Evans. Occupation mound in the dune area. Strong and Evans strata cut 1, south face. Most shards from this site incompletely oxidised, poorly fired and showing signs of use as cooking vessels. Exceptions noted below.

addresses see P04.

P06 – strata cut 1, south face

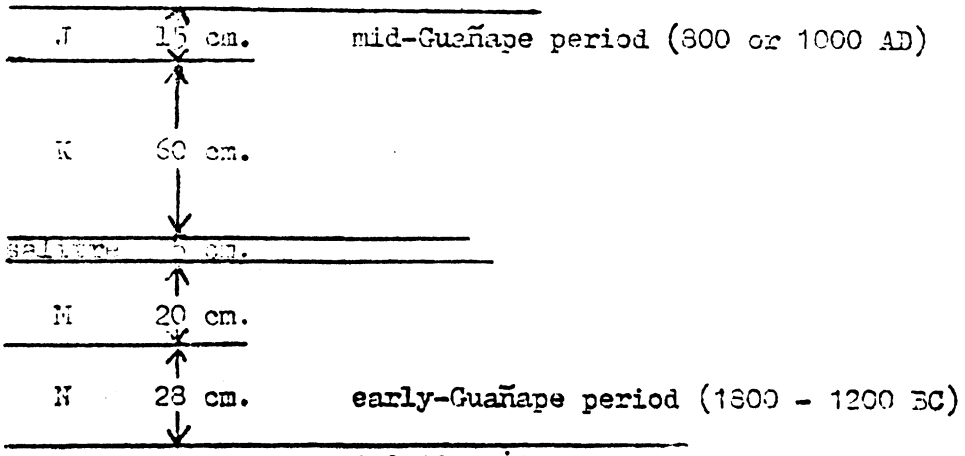

J: 3 shards, J01 is a rim-shard; K: 7 shards, K07 is diagnostic - Ancon polished ware, middle-Guañape, not a cooking vessel; M: 3 shards, M11 as K07 above; N: 7 shards, 16 (rim) and 20 have no sooting.

P07 = PV23-249, Viru Valley. Gallinazo period occupation mound cut in half by bull-dozer. On land of the Sta. Helena Cooperative.

addresses see P04.

P07 – section

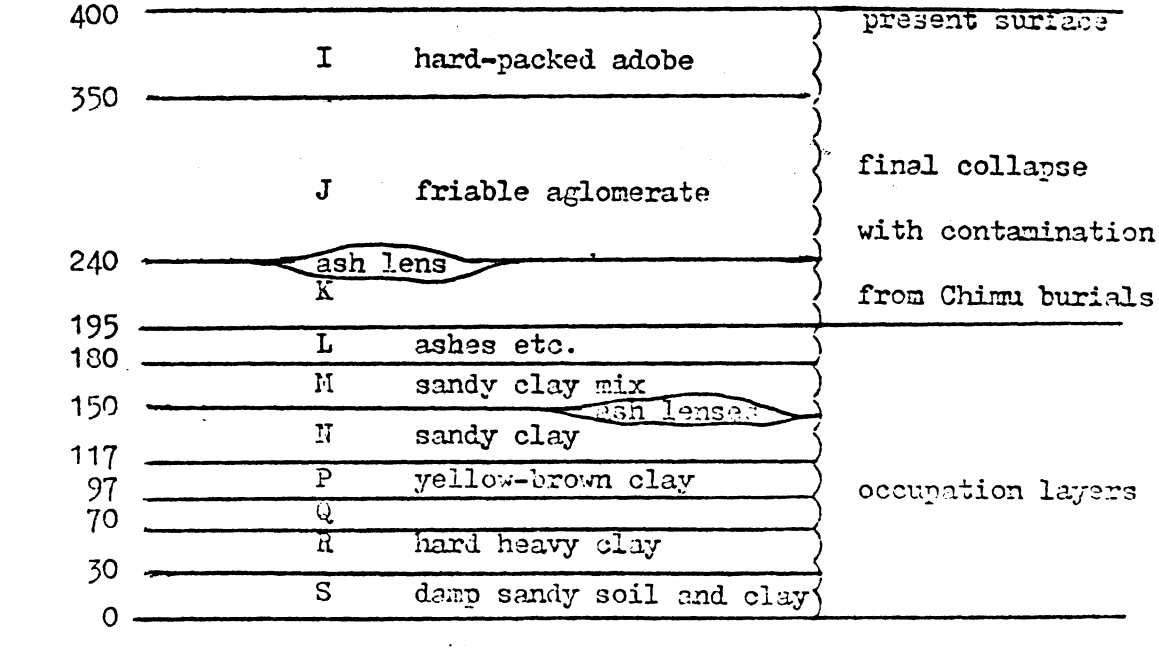

I: 4 shards; J: 8 shards, including Chimu fragment J06; K: 6 shards; L: 9 shards; M: 6 shards; N: N72 - 77, recovered from ash lens, 4 others, 9 shards altogether; P: 3 shards; Q: 9 shards and 1 burnt earth lump; R: none; S: 9 shards. Much of this material in large fragments, apparently good for archaeomagnetic work.

P08 = PV23-290, Viru Valley. Burial platform of which the base is of Puerto Moorian period, above this is artificial fill, top Moche/ Gallinazo.

addresses see P04.

J01, fragment of large Mochica or Gallinazo burial pot (300 - 900 AD). K01, fragment of Gallinazo hanging pot (300 - 700 AD). L: 6 Puerto Moorian shards from one looted pit (between 200 BC and 200 AD), plus L03 which may be younger, L05 too eroded to classify, and L10 a baked clay fragment of unknown period.

P09 = PV23-288, Viru Valley. Puerto Moorian period pyramid with Moche re-use and reconstruction.

addresses see P04.

ADOBE made in situ on Moche tapia wall. Oriented fragment removed.

P10 = PV23-632. Occupation mound near Carmelo, Viru Valley; excavation unit 01, early to middle Gallinazo period (300 - 500 AD).

addresses see P04.

P10 - section excavated by Michael West

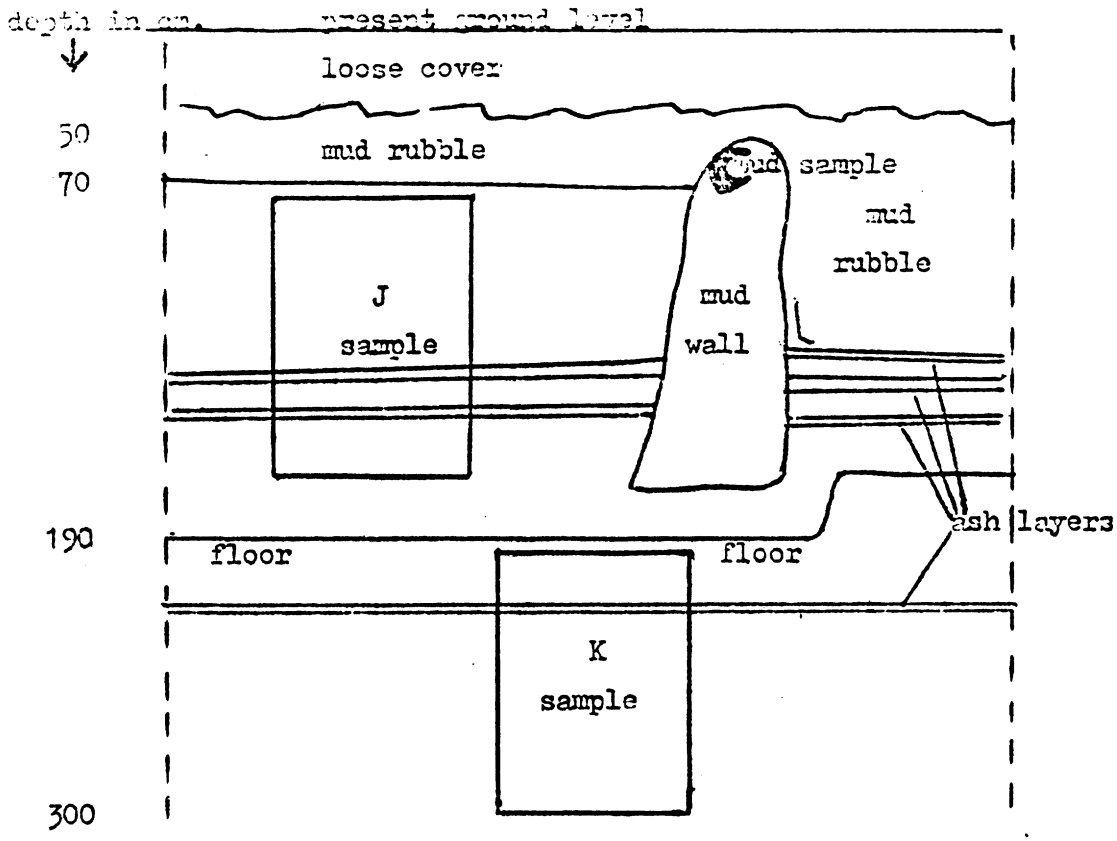

J: 11 shards; K: 5 shards, probably 50 to 100 years older than J. All of poorish quality.

P11 = PV23-504. Viru Valley. Small mound with Puerto Moorian material at base (section excavated by Mike West).

addresses see P04.

J01 - J07: small fragments of Huaca Pongo polished plain ware from volume adjacent to a large burial pot, and J08: part of the large burial pot itself (between 200 BC and 200 AD).

P12 = HUACA GALLINAZO, Viru Valley PV23-59. Excavations by Bennett (Yale University Publications In Anthropology: 43 p.30).

Pyramid dwelling; extensive site with satellite mounds. Dwelling area on west side of site designated 59A. 20 metres west of Bennett's rooms B and C is a 4 m.-square pit excavated by Chauchat and Ojeda. East face of this pit gives long section with clear stratigraphy and abundant pottery from ca. 200AD (level S) to ca. 700 AD (level J).

addresses see P04.

P12 section:— east face of Chauchat's pit

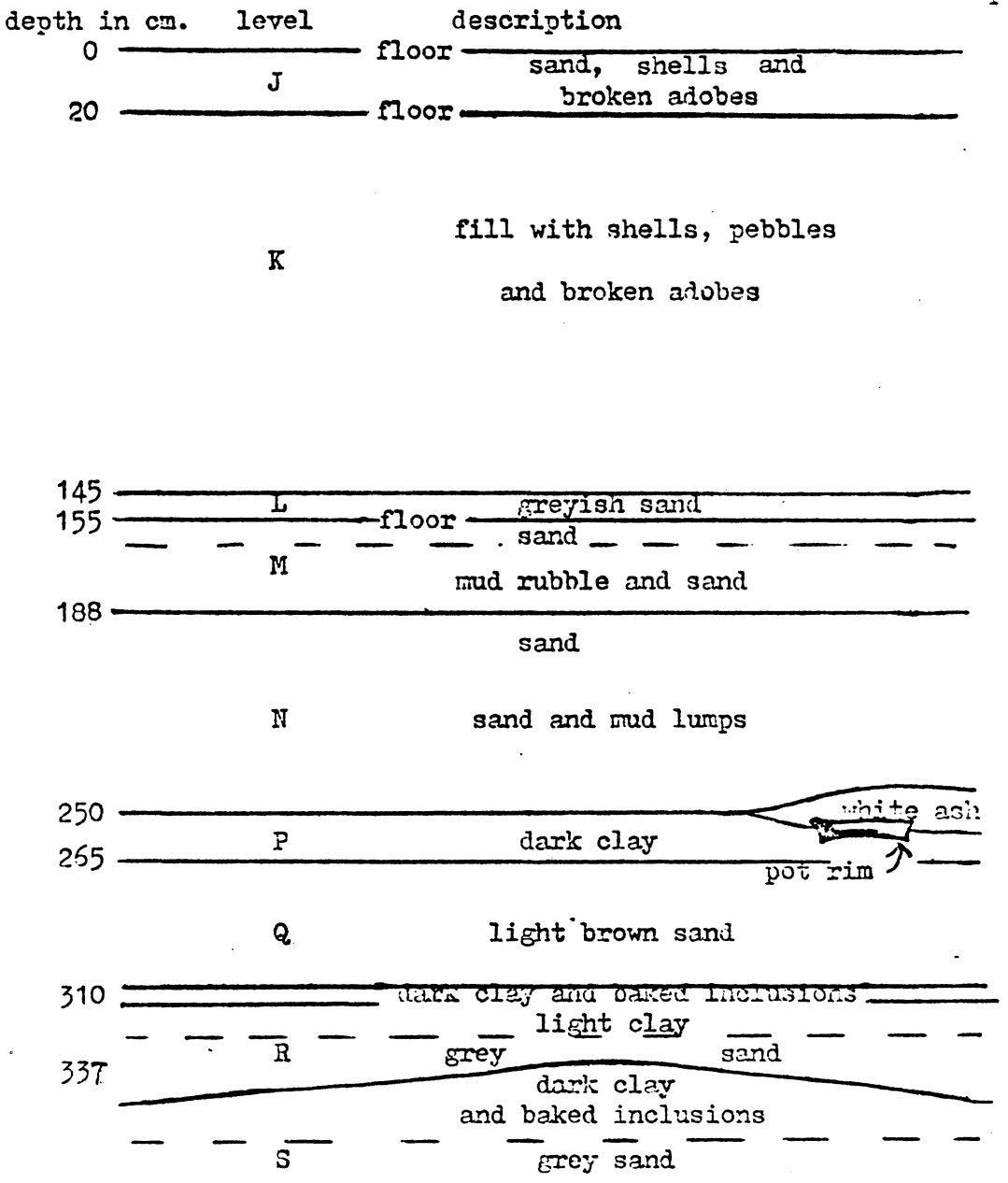

J: 8 shards; L: 6 shards (L06 is a spout); M: 6 shards; N: 11 shards; P: 10 shards plus P11, burnt earth; Q: 16 shards; R: 14 shards (but R08 to R14 probably from the same pot); S: 4 shards. Much of this material is in large pieces, well fired, and apparently good for archaeomagnetic work. Note: levels J and K sampled mainly on north face of pit, lower levels on east face (diagram).

P13 = PV23-682, Viru Valley. Mound cut through by recent irrigation canal, revealing section from late-Guañape through to Gallinazo period.

addresses see P04.

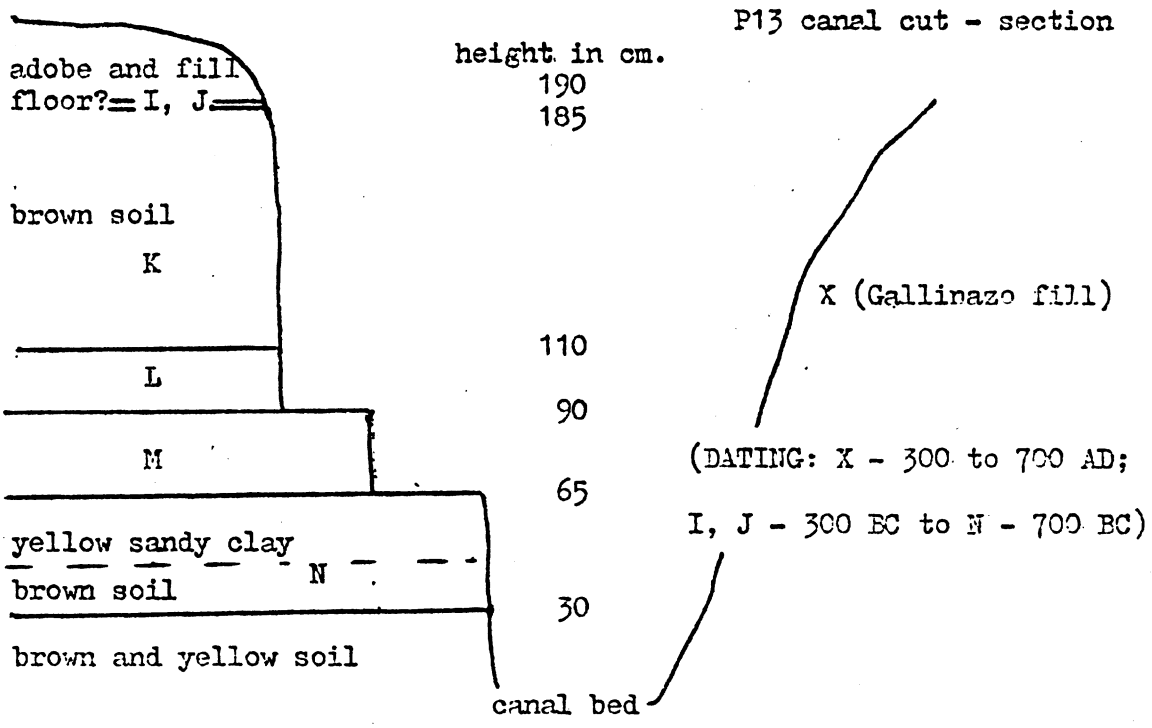

I: 5 burnished shards; J: 2 unburnished shards; K: 9 shards, K10 is burnt earth; L: 12 shards; M: 11 shards, M12 and M13 cinders; N: 5 shards, N06 to N11 cinders and burnt earth. Mostly small pieces, poor quality material.

P14 = PV23 - 88 and 89. Cemetery site WSW of Huancaco Fortress, Viru Valley; adjacent to line of large adobe wall on open sand-drift.

addresses see P04.

A: 7 coarse ware shards from area where all pottery found was of utility type; B: finer ware from obvious cemetery area recently looted, B01 to B12 painted, B13 to B25 unpainted. All material from Moche III - IV or Huancaco (700 to 900 AD).

P15 = TOMOVAL FORTRESS, Viru Valley PV23-51. (See Cultural Stratigraphy in Viru Valley, Strong and Evans, p.93) A = Strong and Evans burial site 3, due north of fortress platform. B is cleared section at west edge of Strong and Evans trench 3, Tomoval period - last occupation of site.

addresses see P04.

A: 7 shards, good material; B: 6 shards; also 2 ADOBES from fortress, 1 with face relief, 1 with cane moulding.

P16 = PV23-2; Cemetery area near Hacienda Ildefonso, Viru Valley. Strewn with wares from the Guañape and Tomoval periods (at least), sandy pampa. Surface collections only, categorized by style.

addresses see P04.

A: 7 middle or late Guañape shards (some perhaps from same pot) including A01: 2 decorated rim shards (ca.1000 BC); B01: 2 shards from a single pot - Tomoval/La Plata (ca.1200 AD); C01: large L-shaped potshard of unknown age; D: fragments of San Nicolas ware local to Viru - Tomoval period or later (1200 AD), D01: 7 pieces from one pot, D02: 3 pieces, D03: 2 pieces and D04: 4 pieces.

P17 = HUACA DEL SOL (I), Moche Valley H8000 A(1). A series of selected levels from the west face of the mound - section exposed by Mike Moseley. Moche II and III periods.

Mike Moseley, Peabody Museum, Harvard University, Cambridge, Mass.02138.

P17 - section

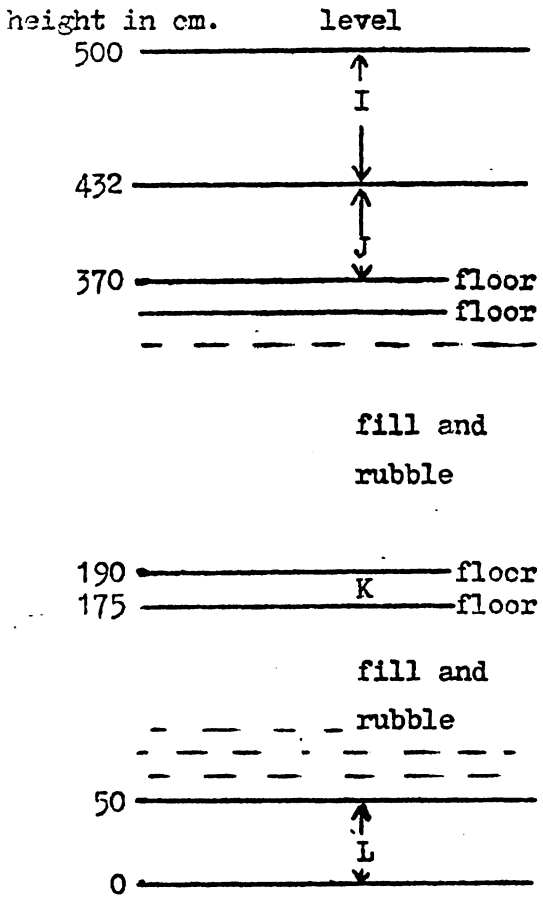

(DATING: I - ca.700 AD to L - ca.400 AD)

I: 15 shards; J: 6 shards plus 1 baked earth fragment; K: 21 shards and 2 baked earth fragments; L: 7 shards. Good samples from I, K and L. Also ADOBE brick.

P18 = HUACA DEL SOL (II), Moche Valley H8000 A(2). A series of selected points on section 2 of the east end of the mound.

address see P17.

P18 Stratigraphy:

H Middle Horizon - Chimu (1200 AD)

I Moche IV - Middle Horizon (1000 AD)

J Between two building phases, Moche III ?

K Corridor fill, Moche III ? (700 AD)

L Corner of fill left beside wall

M Moche I (ca.500 AD)

H: 21 shards; I: 12 shards; J: 13 shards; K: 3 shards; L: 5 shards; M: 11 shards. Good material.

P19 = CABALLO MUERTO, Moche Valley K4462. Chavin-type ceremonial structure. J-sample collected by Tom Povorsky from point on south flank of central mound (ca.1200 BC). K and L samples of Cupisnique ware from floors of two rooms about 20 metres north of axis of structure (ca.1100 BC).

Tom Povorsky, Routo 1, Box 212A, Edcouch, Texas 78538; and Mike Moseley, see P17.

J: 13 shards; K: 29 shards; L: 12 shards.

P20 = GALINDO, Moche Valley K4649. Moche V period inhabited area (ca.1000 AD).

address see P19.

J: 20 shards

P21 = ALTO SALAVERRY, Moche Valley. Habitation area - pre-ceramic period (ca.2500 BC ?)

address for P21 see P19.

A: baked earth (hearth) collected 13.49 local time, sun bearing 72.5°

C: baked earth (hearth) collected 14.20 local time, sun bearing 85.5°

B: burnt stones excavated from rectangular room.

Z: surface collection of burnt materials.

P22 = HUACA PRIETA, Magdalena Cao, Chicama Valley.

address see P17

J: 18 shards and 2 burnt stones from level immediately above pre-ceramic (age not established).

P23 = PAMPA GRANDE, Lambayeque Valley. Moche V period township (1000 AD). Samples collected from Unit 14, "deer house". Building was destroyed by fire, crushing contents and baking the roof-clay.

Kent Day, Office of the Chief Archaeologist, Royal Ontario Museum, Toronto, Canada.

A: 4 sets of shards from 4 whole pots found crushed on floor of the deer house, plus fragments of a grater bowl (A05) and another pot (A06) donated from laboratory collection, having been found in adjacent corridor off the deer house.

B: fragments of baked roof-clay.

C: 13 shards supplied by Kent Day from east wall, Court 1, Unit 14.

P24 = MODERN REPRODUCTION POTTERY, Cajamarca.

Alejandro Velez and Lorenzo Cabrera Abanto, Horacio H. Urtega No.144, Cajamarca, Peru.

P24 sample: shards from facsimile pots made between 1970 and 1975. Red Moche-style wares fired once to 900°C. Black Chavin-style wares fired to 800°C., then again to 500°C. under damp wood. Cooling for 12 - 15 hours before removal at 70° - 80°C.

P25 = CHAN CHAN : BURNT ROOM, Moche Valley. Large room east of Tchudi citadel, Chan Chan; site of fire hot enough to bake and then melt the inner surfaces of the adobe walls. Date of fire probably after collapse of building, colonial period ? - 16th or 17th century.

address see P17

One partially-baked brick collected at 11.55 local time, sun bearing 118.5° (from south wall of room).
One bag of burnt materials collected at random from the room.
One bag of burnt materials collected from vicinity of radiometric probe hole for TL.

P26 = CHAN CHAN : CHAIHUAC, Moche Valley. Samples taken from two levels in the Northmost of 3 pits near burial platform. Very high density of potshards present.

address see P17

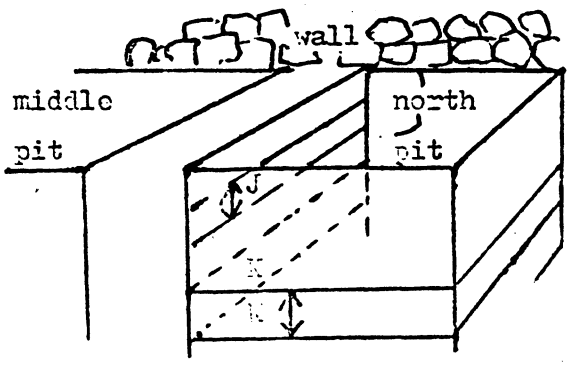

P26 - diagram

(DATING: Early Chimu, ca.900 to 1100 AD, K presumably somewhat older than J.)

J: 25 shards; K: 16 shards; one ADOBE.

P27 = CHAN CHAN : TCHUDI, Moche Valley. Excavation pit dug by J. Topic just outside south wall of Tchudi citadel. Level J is just under present ground level, for 40 cm. Level K is 225 - 280 cm. down. All ca.1250 AD.

address see P17.

J: 24 shards; K: 20 shards.

P28 = CHAN CHAN : RIVERO, Moche Valley. Excavation in innermost of three enclosure walls on the west side of Rivero citadel; once a gateway in the wall later bricked off with erect adobes. A greyish layer about 50 cm. thick begins 20 cm. below first course of erect adobes. J sample is from top 10 cm., K from bottom 10 cm. of this grey layer. All ca.1350 AD.

addresses see P17 and P23.

J: 21 shards; K: 17 shards; ADOBE containing potshard A01 and burnt clay fragment A02.

P29 = CHAN CHAN : RIVERO KITCHEN (first court in Rivero citadel), Moche Valley. Post-imperial squatter occupation, ca.1500 AD.

addresses see P17 and P23.

J: 25 shards (but J01, J02 and J03 all from same pot).

P30 = CERRO DE LA VIRGEN, Moche Valley H6368. Fishing and farming village; excavation cuts through old road-surfaces. J, top of section, ca.1400 AD; K, base of section (1 metre down) ca.1300 AD.

addresses for P30 see P17 and P19

J: 19 shards; K: 19 shards.

P31 = LLAMA CEMETERY, H105825, between Moche and Chicama valleys. Supposedly used for only a few years after the Spanish Conquest (1533 AD) possibly by the imperial family of the Chimu.

addresses see P17 and P19.

A: 13 shards collected from desert surface.

P32 = TOTORA SITE excavated by Keitinge. Colonial period midden, on the coast 2 kilometres north-west of P31. Samples from two separate excavation pits, A and B, both ca.1600 AD.

addresses see P17 and P19.

A: 20 shards; B: 13 shards.

P33 = PAI-AN POTTERY, Trujillo. Modern reproduction pottery made from Rio Moche alluvial clay.

Eduardo Calderon, Pai-An Pottery, Trujillo.

Shards from recent rejected work. Pots fired in a pit in the ground for 3 - 5 hours at about 700°C. Black wares then covered with dung smoulder for ten minutes.

R01 denotes a broken head-pot; remaining shards not numbered, but bagged as P33.

P34 = PV23-124, Viru Valley. Chimu - Chimu/Inca period rectangular enclosure of tapia and adobe, between Carmelo and

the sea (ca.1450 AD). Sample hole 6 metres from south-west wall, 3 metres from north-west wall.

addresses see P04.

A: 15 shards; K: 2 shards from wet layer in same hole; 2 ADOBES.

P35 = PACHACAMAC, Lurin Valley. Sloping strata cut above north edge of Museum car park at entrance to site; Maranga period (300 - 800 AD).

Alberto Bueno Mendoza, Calle Carlos A. Saco 180, Urb. Apolo, Lima 13.

I: 13 shards; J: 13 shards; K: 19 shards; L: 8 shards; M: 2 shards.

P36 = HUAYCAN, Lurin Valley. Upper Huaycan, town on the valley slope. A is pre-Inca stoney fill from foundations ca.1300 AD; B is an Inca midden (sample taken from straw layer) ca.1500 AD.

address see P35.

A: 22 shards, good material; B: 19 shards.

P37 = PACHAMACHAY CAVE, Ondores, Junin (altitude 4400 metres). Unit 2 west and south profiles. Stratigraphic sequence runs from pre-ceramic period to ca.1400 AD.

John W. Rick, Museum of Anthropology, University of Michigan, Ann Arbor, Michigan 48104. Ramiro Matos, Victor Criado Tejada 2896, Urb. Elio, Lima.

Correspondence between level codes and Rick's strata numbers at P37:

H	I	J	K	L	M	N	P	Q	R	S	T	U	V	W
:	:	:	:	:	:	:	:	:	:	:	:	:	:	:
1	2	3	4	5	6	7	8	9	10	11a	11b	12a	12b	13

I: 16 shards; J: 27 shards; K: 27 shards; L: 22 shards; M: 25 shards; N: 25 shards; P: 26 shards; Q: 27 shards; R: 41 shards; S: 15 shards, S16 is fired chert. Most of this material is small fragments, some poorly preserved in the damp soil.

P38 - un-allocated site number.

P39 = SAN BLAS (I), Ondores, Junin. Exposed surface due to slumping in salt mine. Refuse (including numerous potshards) several metres deep. Conjectural ages of levels: S ca.500 BC; P ca.300 AD; H ca.1300 AD.

addresses see P37.

H: 25 shards; I: 30 shards; J: 27 shards; K: 21 shards; L: 17 shards; M: 10 shards; N: 20 shards; P: 21 shards; Q: 16 shards.

P40 = SAN BLAS (II), Ondores, Junin. Danilo Mendoza's section through angled strata - side of a refuse tip. Very wet environment. The following are the depths of the base of each level at the back of the section (measured downward from top of section, in centimetres): I 90, J 140, K 220, L 280, M 340, N 385, P 435 Q 450, R 470, S 505, T 535.

addresses see P37

I: 18 shards; J: 19 shards; K: 21 shards; L: 25 shards; M: 17 shards; N: 19 shards; P: 19 shards; Q: 18 shards; R: 13 shards; S: 16 shards; T: 23 shards.

P41 = HUARI ROADCUT (I), Ayacucho. 23.8 kilometres along the road from Ayacucho to Quinua just after left hand bend; bearing of road at this point ca. 115°. Left (north-east) side of road flanked by a cutting some 4 metres high through archaeological strata. (Airphoto 181/70 No.1526)

Teresa Carrasco and Enrique Gonzales Carre, I.N.C., Postal Union 26, Ayacucho; or Universidad Nacional Mayor, San Cristobal de Huamanga, Ayacucho.

P41 - section

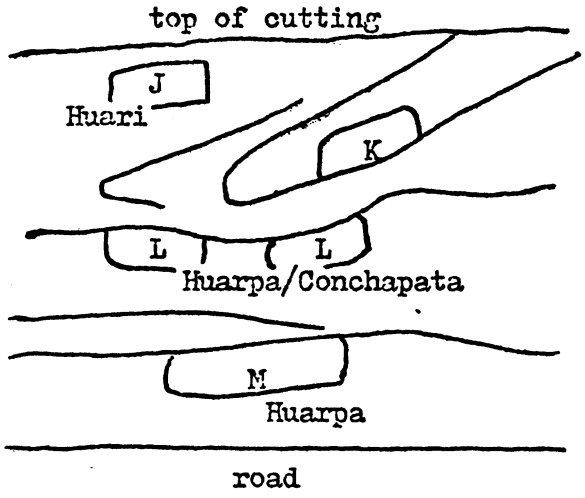

(DATE ESTIMATES:

J	800 AD	all ± 150 years)
K	700 AD	
L	500 AD	
M	400 AD	

J: 15 shards; K: 17 shards; L: 25 shards; M: 20 shards.

P42 = HUARI ROADCUT (II), Ayacucho. 24.5 kilometres from Ayacucho along the road to Quinua. Bearing of road at this point approximately 15°; 1.8 metres of archaeological strata exposed on the right hand (east) side of road.

addresses see P41.

P42 - section

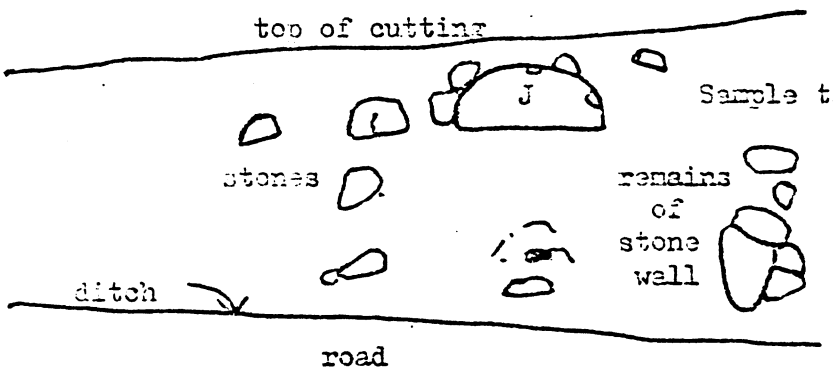

Sample taken from area J: late Huari, ca.1000 AD.

J: 26 shards.

P43 = COLONIAL AYACUCHO. 6 rooftiles all of colonial period.

addresses see P41; also: Jose Galves, I.N.C., Ayacucho.

P43A01: tile from Cancho building, estimated date 1750 - 1850 AD.

P43B01 and B02: tiles from the Moya building, estimated date 1700 - 1750 AD.

P43C01 and C02 tiles from the Chacon building, estimated date 1600 - 1700 AD: C03 also from Chacon, estimated date 1700 - 1750 AD.

P44 = HUILLCARACCAY, Cusichaca Valley, Department of Cuzco. Pre-Inca or early Inca fort above east side of Cusichaca River near its confluence with the Urubamba. Samples taken from levels associated with Chanapata occupation, around 600 BC. I and J are of the same date, H (when supplied) will be earlier.

Ann Kendall, 34 Heath Street, Stourbridge, West Midlands.

H: to be supplied by Ann Kendall. I: 10 shards; J: 13 shards.

P45 = TARAWI, Araway Hill, Cuzco. Test pit by John Rowe XVI, west profile.

John Rowe, Department of Anthropology, Berkeley University of California, San Francisco.

P45 - section

depths in cm.

present ground level

recent

J Killke — 40 / 52

K Qotacalle — 80

sterile

J: 24 shards; K: 16 shards.

P46 = PIQUILLACTA TORECHAYOC, Chillca, Urubamba Valley, Department of Cuzco. Samples taken from terrace section at junction between soil and stone base. J and K are separated horizontally, K being 15 metres NNW of J, at the top of a terrace wall between soil and slate fill as in J, exposed by a recent wall slip. J and K both date from ca.1350 AD.

address see P44.

J: 11 shards; K: 14 shards.

P47 - unallocated site number.

P48 = PUCARA, Department of Puno. Sector B, Templo Mayor, sub-sector A, north structure. Excavation unit S4 - 5 - W25 - 26, level 4 - 6 stratum B. Sample taken from between a stone floor associated with colonial and contemporary pottery and a fill (C) of the Collau period; probably B (= our K) belongs to the Collau-Inca

period ca.1400 AD.

Luis Guillermo Lumbreras, Director del Museo Nacional de Antropologia, Plaza Bolivar, Pueblo Libre, Lima.

K: 8 shards provided by Dr. Lumbreras.

P49 = OLLERIAYOC TRANCAPATA, Urubamba Valley, Department of Cuzco. Late intermediate period hill site. Samples removed from structures 1 and 2 in group 3, excavated by Ann Kendall in 1975. J from structure 1, group 3, quarter B: fill between floor and sterile rock base ca.1300 AD. K from structure 2, group 3, quarter C: compact earth under floor over sterile base, ca.1350 AD.

address see P44.

J: 10 shards; K: 15 shards.

P50 = PISCAYCUCHO, Chillca, Urubamba Valley, Department of Cuzco. Sample date estimated at 1400 AD.

address see P44.

J: 15 shards.

Appendix E

CONVERSION FROM ISOTOPE ACTIVITIES TO ALPHA COUNT RATE AND DOSE RATES

E.1 ALPHA COUNT RATE

It can be shown that the alpha count rate, α, from an alpha thick source can be described by (TURNER et al, 1958)

$$\alpha = \tfrac{1}{4} A D R \rho$$

where A is the counting area,
D is the disintegration rate,
R is the alpha range,
ρ is the sample density.

For a thick source, 42 mm in diameter, containing i isotopes, each of activity c_i pCi g^{-1}, with the 'i'th isotope emitting I_{ij} alphas whose range is R_{ij}, this expression can be written as

$$\alpha = 0.1281 \sum_{ij} c_i \; I_{ij} \; R_{ij} \; \rho$$

An alpha counting system is usually operated with a threshold set to discriminate against noise. This will reject a certain fraction of alpha counts, and effectively set a minimum range, δR, necessary to produce a count.

$$\text{i.e.} \quad \alpha = 0.1281 \sum_{ij} c_i \; I_{ij} \; (R_{ij}\rho - \delta R\rho) \quad - - - - - 1$$

It is conventional to set this threshold to reject 15% of all the alpha counts from a Th-232 source in secular equilibrium dispersed in a pottery like matrix. AITKEN and BOWMAN (1975) interpolate between neon and sodium to determine alpha ranges in pottery, using the data of NORTHCLIFFE and SCHILLING (1970) and WILLIAMSON et al (1966) and derive a value of 1.04 mg cm^{-2} for $\delta R\rho$. Using the same interpolated data, kindly supplied by the authors, and listed in tables E1a, E1b, and E1c, the expected alpha count rate per pCi g^{-1} has been calculated for each of the groups set out in chapter 6. These figures are listed in table E2. In addition, the calculated total count rates for full chain equilibrium are compared with the corresponding values from BOWMAN (1976).

Table E1a

Alpha energies and average ranges in pottery for Th-232 series

Isotope	Energy MeV	Intensity % of disintegrations	Range, R_ρ mg cm^{-2}
Th-232	4.01	77	3.82
	3.94	23	3.66
Th-228	5.43	72	5.80
	5.34	28	5.67
Ra-224	5.68	94	6.22
	5.45	5	5.85
Rn-220	6.29	100	7.28
Po-216	6.78	100	8.20
Bi-212	6.07	36	6.90
Po-212	8.74	64	12.30

Note: data kindly supplied by S.G.E. Bowman and M.J. Aitken.

Table E1b

Alpha energies and average ranges in pottery for U-238 series

Isotope	Energy MeV	Intensity % of disintegrations	Range, R_ρ mg cm^{-2}
U-238	4.195	77	3.98
	4.15	23	3.92
U-234	4.77	72	4.80
	4.72	28	4.72
Th-230	4.69	76	4.68
	4.62	24	4.56
Ra-226	4.78	94.6	4.82
	4.60	5.4	4.51
Rn-222	5.49	100	5.90
Po-218	6.00	100	6.76
Po-214	7.68	100	9.99
Po-210	5.30	100	5.60

Note: data kindly supplied by S.G.E. Bowman and M.J. Aitken.

Table E1c

Average alpha energies and ranges in pottery for U-235 series

Isotope	Energy MeV	Range, R_ρ mg cm^{-2}
U-235	4.35	4.04
Pa-231	4.73	4.69
Th-227	5.87	6.24
Ra-223	5.70	5.98
Rn-219	6.62	7.56
Po-215	7.36	9.45
Bi-211	6.56	7.60

Note: data kindly supplied by S.G.E. Bowman and M.J. Aitken.

Table E2

Ratio of thick source alpha count rate in pottery to sample activity

Group	Long lived isotope	Alpha count rate $ksec^{-1}/(pCi\ g^{-1})$
1	U-238, U-235	0.360
2	U-234	0.458
3	Th-230, Pa-231	0.450
4	Ra-226	0.461
5	Rn-222, Rn-219	2.404
6	Pb-210	0.558
7	Th-232	1.617
8	Rn-220	2.910

Uranium series total, assuming secular equilibrium: 4.691
Thorium series total, assuming secular equilibrium: 4.527

Ratio of totals to corresponding data derived from BOWMAN (1976):

U series	Th series
0.993	0.999

Note: 1) assumes counting area of 42 mm diameter, and threshold set at 85% as described in text.

2) the alpha count rate per unit activity assumes the total activity of U-238 plus U-235 is 1 $pCi\ g^{-1}$.

E.2 DOSE RATE DATA

The dose rate information presented in table E3 assumes that all of the energy emitted in a decay is absorbed within the medium of interest, and is based upon individual decay energies for the thorium and uranium series given by BOWMAN (1976), which are in good agreement with BELL (1977, 1979b). The potassium data is taken from BELL (1979b) as are the atomic decay constants, listed in table E4.

Table E3

Annual dose rates for each isotope group

Group	Long lived isotope	Alpha mrad yr^{-1}	Beta mrad yr^{-1}	Gamma mrad yr^{-1}
1	U-238, U-235	77.9	16.1	1.20
2	U-234	88.5	-	0.27
3	Th-230, Pa-231	86.5	0.2	0.21
4	Rn-226	88.7	0.06	0.11
5	Rn-222, Rn-219	356.4	17.8	31.22
6	Pb-210	98.5	7.8	0.03
7	Th-232	281.8	9.6	17.45
8	Rn-220	390.9	16.7	28.0
	K-40	-	9.72	2.92
Totals for uranium series		796.5	42.0	33.0
Totals for thorium series		672.7	26.3	45.4
Ratio of totals to data presented in BOWMAN (1976):				
Uranium series		1.001	1.002	1.001
Thorium series		1.001	0.998	1.01

Note: 1) based on data presented in BOWMAN (1976) and BELL (1979b).

2) dose rates are for isotope concentrations equivalent to those from an activity of 1 pCi g^{-1} of natural uranium in secular equilibrium with its daughters, 1 pCi g^{-1} of Th-232 similarly in equilibrium, and 1 pCi g^{-1} of K-40.

Table E4

Decay constants and derived ratios of concentration to activity

Isotope	Decay constant, sec^{-1}
U-238	4.91898×10^{-18}
U-235	3.1229×10^{-17}
Th-232	1.5688×10^{-18}
K-40	1.758×10^{-17}

U-238/U-235 atomic ratio = 137.88

K-40 isotopic abundance = 0.01167%

Derived from above:

U-235/U-238 activity ratio = 0.04605

1 ppm natural uranium = 0.3493 pCi g^{-1} total parent activity

= 0.3339 pCi g^{-1} U-238

1 ppm natural thorium = 0.1100 pCi g^{-1} Th-232

1% K_2O = 7.091 pCi g^{-1} K-40

Note: based on Bell (1979b).

Appendix F

AGE CALCULATIONS FOR SITE 164: SHAM WAN, LAMMA ISLAND, HONG KONG

F.1 SUPPORTED Ra-226 EXCESS

Consider first the simpler case of Th-230 supported Ra-226 excess. Making the assumptions detailed in section 7.5.4, the annual dose rate can be calculated as described below.

The U-238 and Ra-226 contributions are taken from the activities tabulated in table 7.5.1 with that of the Rn-222 daughters from the activity of Pb-210. The Th-232 and K-40 activities are used unchanged. The beta and gamma dose rates can then be calculated directly, using the data presented in Appendix E. Allowance must be made for the water content of the sherds and soil respectively, (see, for example, ZIMMERMAN, 1978), and finally the cosmic contribution of 10 mr yr^{-1} added to the gamma dose rate.

The alpha dose rate calculation is less straightforward. As noted by AITKEN and BOWMAN, (1975), in developing the a value system it has been experimentally observed that whereas the TL per unit absorbed energy is strongly dependent on the energy of the alpha particle, the TL per unit length of track is not. As will be seen from equation (1) of Appendix E the alpha count rate is also dependent on track length rather than energy. Hence it is convenient to express the alpha dose rate in terms of alpha count rate, because there is then no need to know the alpha energy, at least to first order. The effective alpha dose rate, D'_α, is then given by

$$D'_\alpha = 0.127\ a\ \alpha \qquad \text{- - - - - - - - - - 1}$$

where a is the a value, taken from HUXTABLE and AITKEN (1978) and given in table F.1,

α is the alpha count rate for a thick source of area 13.85 cm^2 (42 mm diameter).

The data for converting from the activity of a particular isotope to the equivalent alpha count rate is also given in Appendix E. The effective alpha dose is then reduced by the sherd water content, again as described in ZIMMERMAN (1978).

These three dose rate terms may then be used in the age equation

Table F1

Total dose and 'a' value data for Sham Wan

	164m4	164m9
ED + I	4435_{440}	3800_{500}
a	$0.12 \pm 4\%$	$0.10 \pm 3\%$

Note: 1) taken from HUXTABLE and AITKEN (1978)

2) errors in total dose are in the least significant figures.

$$\text{Age} = \frac{ED + I}{D'_\alpha + D_\beta + D_{\gamma,c}} \qquad \text{- - - - - - - - 2}$$

where $\underline{ED} + \underline{I}$, the total archaeological dose given in table F.1, is taken from HUXTABLE and AITKEN (1978).

F.2 UNSUPPORTED Ra-226 EXCESS

The situation in the case of unsupported radium excess is much more complicated. Here, that part of the total dose rate derived from unsupported Ra-226 excess will have been decreasing exponentially with time, and this time dependent effect will then appear in the denominator of the age equation.

Taking the uranium chain alone:

Let $\underline{I_U}$ be the activity of the radium parent isotopes,

$\underline{I_R}$ be the radium excess above the level of $\underline{I_U}$ at time $\underline{t}' = 0$,

then the total radium activity at time $\underline{t}'$, $\underline{I_{t'}}$, will be

$$I_{t'} = I_U + I_R e^{-\lambda t'}$$

where $\underline{\lambda}$ is the Ra-226 decay constant. Thus the total amount of decayed radium after elapsed time $\underline{t}$ will be

$$\int_o^t I_{t'}\, dt' = \int_o^t (I_U + I_R e^{-\lambda t'})\, dt'$$

or $$\bar{I}\, t = I_U t + \frac{I_R}{\lambda}(1 - e^{-\lambda t})$$

where $\underline{\bar{I}}$ is the average radium activity during time $\underline{t}$.

i.e. $$\bar{I} = I_U + \frac{I_R}{\lambda t}(1 - e^{-\lambda t}) \qquad \text{- - - - - - - - 3}$$

But we measure $\underline{I_E}$, the modern radium excess, where

$$I_E = I_R e^{-\lambda t} \qquad \text{- - - - - - - - 4}$$

Substituting into (3) from (4), we have

$$\bar{I} = I_U + \frac{I_E}{\lambda t}(e^{\lambda t} - 1) \qquad \text{- - - - - - - - 5}$$

For illustration, if $\underline{t}$ = 5000 years, $\underline{\lambda} = 4.33 \times 10^{-4}$ years^{-1}

$$\bar{I} = I_U + 3.56\, I_E$$

that is, the average radium activity is the sum of the supported

activity and 3.56 times the present excess. This could be a large correction if, as in this case, the present radium activity is about twice the uranium activity.

To describe the individual dose rate terms, a further assumption must be made about the level of Rn-222 escape from the two 'sources' of this isotope, i.e. supported and unsupported Ra-226. Here it is assumed that the fraction of escape is the same for both types.

After making the appropriate substitution for I_U and I_E, the beta dose rate D_β from the uranium series can be expressed as a function of t, and the contribution from the thorium series and potassium are then added on as constants. Thus

$$D_\beta = D_{\beta U} + \frac{D_{\beta E}}{\lambda t}(e^{\lambda t} - 1) + D_{\beta Th} + D_{\beta K} \quad ----- 6$$

where $D_{\beta U}$ is the beta dose rate from that activity in the uranium chain that includes the supported Ra-226 activity, the other terms have the corresponding meanings.

The equivalent alpha count is expressed similarly,

$$\alpha = \alpha_U + \frac{\alpha_E}{\lambda t}(e^{\lambda t} - 1) + \alpha_{Th} \quad -------- 7$$

where the meaning of the subscripts is as above.

The gamma and cosmic dose rates remain as before, of course.

Equation (7) is substituted into the usual alpha dose calculation, equation (1), and then this, with equation (6), is substituted into the age equation (2), after making the appropriate water content allowances as before. The resulting equation contains t, the age, on both sides, and cannot be solved explicitly. The ages given in chapter 7 were calculated iteratively.

Appendix G

CALCULATION OF AVERAGE EFFECTIVE SIZE OF AN EMANATING GRAIN FROM A KNOWLEDGE OF THE ACTIVITY RATIO OF FIXED Pb-210 TO FIXED Ra-226

The underlying principles of this calculation were set out in section 7.7.2. The formal derivation is detailed here, and the assumptions and approximations set out.

Consider a spherical mineral grain, radius r_T, with a homogeneously distributed total Ra-226 activity R_T. Let the total Ra-226 activity contained in a thin shell within the surface of this grain be R_s, such that the remaining radium activity, R_c, is contained in a sphere radius r_c. Then R_T is contained in a volume $\frac{4}{3}\pi r_T^3$, and R_c in a volume $\frac{4}{3}\pi r_c^3$ and

$$\frac{R_c}{R_T} = \frac{r_c^3}{r_T^3} \qquad \text{- - - - - - - - 1}$$

Now let the activity ratio of Pb-210 to Ra-226 be p. It is assumed here that all the Pb-210 originated from Ra-226 contained within the grain. Let the fraction of Ra-226 daughters (down to and including Pb-210) that escapes from the outer shell of the grain by recoil of daughter nuclei be f, so that the total Pb-210 activity retained by the grain is given by

$$R_c + (1 - f)R_s$$

$$\text{i.e.} \quad p = \frac{R_c + (1 - f)R_s}{R_T} \qquad \text{- - - - - - - - 2}$$

$$\text{Now} \quad R_s = R_T - R_c \qquad \text{- - - - - - - - 3}$$

Substituting (3) into (2) gives

$$\frac{R_c}{R_T} = \frac{p - (1 - f)}{f} \qquad \text{- - - - - - - - 4}$$

Combining (1) and (4) gives

$$r_T = \frac{r_T - r_c}{1 - \sqrt[3]{\frac{(p-1)}{f} + 1}} \qquad - - - - - - - - 5$$

QUET (1975) gives a recoil range for a radon nucleus of 20 to 70 nm. We shall use 50 nm for the value of $(r_T - r_c)$.

It now remains to discuss the value of $\underline{f}$. If a thin film of Ra-226 atoms were deposited on an infinite plane mineral surface, then, assuming that indirect recoil (see section 7.7.2) did not contribute, 50% of the Rn-222 nuclei produced would recoil away from the surface and escape. We shall also assume this to be true for any Rn-222 nuclei produced within 50 nm of the surface. However, we are interested in Pb-210 escape, and there are four alpha decays between Ra-226 and Pb-210. These additional decays will increase the loss of Ra-226 daughters to approximately 60% by the time the Pb-210 step is reached.

Now consider a spherical mineral grain. As the radius tends to infinity, $\underline{f}$, the fraction of Ra-226 daughters lost, will tend to 0.6. However, at a diameter of 50 nm, all the daughters are assumed to escape. The value of $(r_T - r_c)$ has been given the value 50 nm, and in order to maintain the validity of this substitution, we limit $\underline{r_T}$ to values greater than 50 nm. Not all the daughters will escape from a sphere of this radius, and so we place a corresponding limit on $\underline{f}$ of 0.95 at r_T = 50 nm.

The function

$$f = 0.6 + \frac{17.5}{r_T} \qquad - - - - - - - - 6$$

has these properties. In addition, when r_T = 2500, i.e. 100 times the radius at which all the daughters would escape, $\underline{f}$ is 1% greater than the value as $\underline{r_T}$ tends to infinity, which is not unreasonable.

Substituting (6) into (5) we have, for $r_T > 50$

$$r_T = \frac{50}{1 - \sqrt[3]{\frac{(p-1)}{0.6 + 17.5\, r_T^{-1}} + 1}} \qquad - - - - - - 7$$

A plot of $\underline{p}$ against $\overline{r_T}$ is shown in figure G.1. Although it is recognised that the expression for $\underline{f}$ is empirical, for the purposes of the qualitative comparisons of section 7.7, it is considered adequate. Changes in the average recoil range $(\overline{r_T} - r_c)$ simply compress or expand the $\overline{r_T}$ axis, to first order. The errors given in table 7.7.1 are derived only from uncertainties in $\underline{p}$, and do not include uncertainties in $(\overline{r_T} - r_c)$, which would systematically affect all the values given.

Figure G1 Variation of the the activity ratio Pb-210/Ra-226, p, with effective emanating grain radius, r_I

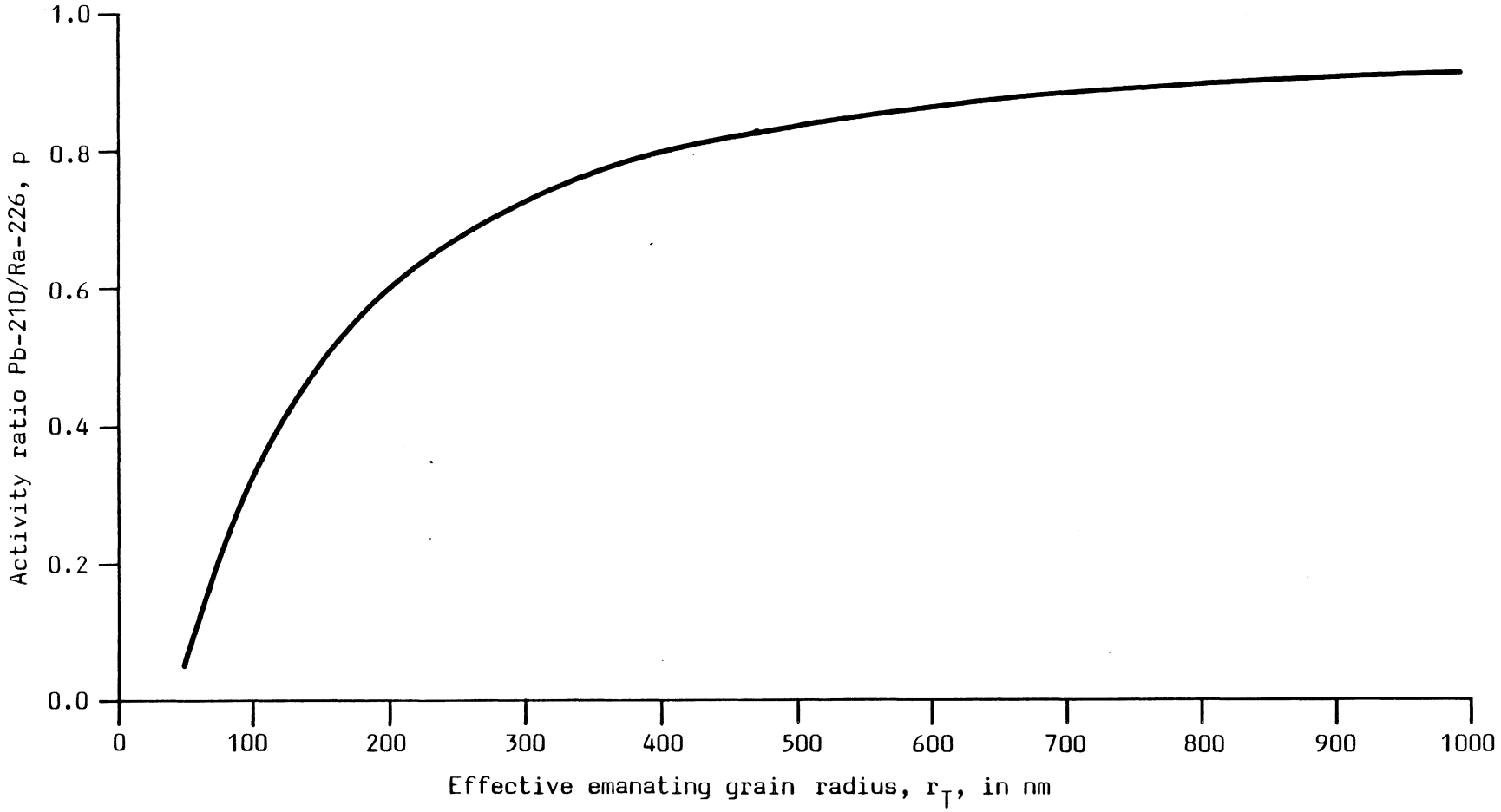

REFERENCES

Adams, F., Dams, R., 1970; Applied Gamma Ray Spectrometry, Pergamon, Oxford.

Adams, J.A.S., 1964; Laboratory gamma ray spectrometer for geochemical studies. In "The Natural Radiation Environment", Adams, J.A.S., Lowder, W.M., (eds), University of Chicago Press.

Aitken, M.J., 1968; Low-level environmental radiation measurements using natural calcium fluoride. In "2nd Int. Conf. on Lumin. Dosim.", Auxier, J.A., Becker, K., Robinson, E.M.. (eds), CONF-680920, Washington, D.C.

Aitken, M.J., 1969; Thermoluminescent dosimetry of environmental radiation on archaeological sites. Archaeometry, 11, 109-114.

Aitken, M.J., 1976; Thermoluminescent age evaluation and assessment of error limits: revised system. Archaeometry, 18, 233-238.

Aitken, M.J., 1978; Dose-rate evaluation. In "A Specialist Seminar on Thermoluminescence Dating", Oxford, PACT No. 2, Council of Europe.

Aitken, M.J., 1978; Radon loss evaluation by alpha counting. In "A Specialist Seminar on Thermoluminescence Dating", Oxford, PACT No. 2, Council of Europe.

Aitken, M.J., Alldred, J.C., 1972; The assessment of error limits in thermoluminescent dating. Archaeometry, 14, 257-267.

Aitken, M.J., Alldred, J.C., Thompson, J., 1968; A photon-ratemeter system for low-level thermoluminescence measurements. In "2nd Int. Conf. on Lumin. Dosim.", Auxier, J.A., Becker, K., Robinson, E.M., (eds), CONF-680920, Washington, D.C.

Aitken, M.J., Bowman, S.G.E., 1975; Thermoluminescent dating: assessment of alpha particle contribution. Archaeometry, 17, 132-138.

Allman, M.A., Lawrence, D.F., 1972; Geological Laboratory Techniques. Blandford Press, London.

Almond, P.R., McCray, K., Watanabe, S., 1968; The energy response of LiF, CaF_2 and $Li_2B_4O_7$: Mn from 26 keV to 22 MeV. In "2nd Int. Conf. on Lumin. Dosim.", Auxier, J.A., Becker, K., Robinson, E.M., (eds), CONF-680920, Washington, D.C.

Bailiff, I.K., 1976; Some new techniques in thermoluminescence dating. Unpublished M.Sc. thesis, Oxford University.

Bailiff, I.K., Aitken, M.J., 1980; Use of thermoluminescence dosimetry for evaluation of internal beta dose-rate in archaeological dating. Nucl. Inst. Methods, 173, 423-429.

Bell, W.T., 1976; The assessment of the radiation dose-rate for thermoluminescence dating. Archaeometry, 18, 107-110.

Bell, W.T., 1977; Thermoluminescence dating: revised dose rate data. Archaeometry, 19,99.

Bell, W.T., 1979; Attenuation factors for the absorbed radiation dose in quartz inclusions for thermoluminescence dating. Ancient TL, No. 8, 2-13.

Bell, W.T., 1979; Thermoluminescence dating: radiation dose-rate data. Archaeometry, 21, 243-245.

Bell, W.T., 1980; Beta source calibration: some problems associated with the utilisation of the gamma irradiation of quartz and other phosphors (part I). Ancient TL, No. 10, 3-9.

Bell, W.T., 1980; Beta source calibration: some problems associated with the utilisation of the gamma irradiation of quartz and other phosphors (part II). Ancient TL, No. 11, 2-6.

Bell, W.T., Mejdahl, V., 1980; Beta source calibration and its dependency on grain transparency. In "A Specialist Seminar on Thermoluminescence Dating", Oxford, in press.

Berger, M.J., Seltzer, S.M., 1964; Tables of energy losses and range of electrons and positrons. In "Studies of Penetration of Charged Particles in Matter", Publ. 1133, National Academy of Sciences - National Research Council, Washington.

Bowman, S.G.E., 1975; Dependence of supralinearity on predose: some observations. Archaeometry, 17, 129-131.

Bowman, S.G.E., 1976; Thermoluminescent dating: the evaluation of the radiation dosage. Unpublished D.Phil. thesis, Oxford University.

Buckman, H.O., Brady, N.C., 1960; The Nature and Property of Soils. Macmillan, New York.

Burlin, T.E., 1966; A general theory of cavity ionization. Brit. J. Radiol., 39, 727-734.

Burlin, T.E., Chan, F.K., 1969; The effect of the wall on the Fricke dosemeter. Int. J. App. Rad. Isotopes, 20, 767-775.

Camp, D.C., Gatrousis, C., Maynard, L.A., 1974; Low background Ge(Li) detector systems for radioenvironmental studies. Nucl. Inst. Methods, 117, 189.

Carruthers, L.T., Morgan, D.W., 1975; A commercially available Compton suppression NaI-Ge(Li) unit for low level gamma analysis of environmental samples. Health Physics, 29, 872.

Cashwell, E.D., Neergaard, J.R., Everett, C.J., Schrandt, R.G., Taylor, W.M., Turner, G.D., 1973; Monte Carlo photon codes: MCG and MCP. Los Alamos Scientific Laboratory Report LA-5157-MS.

Chiu, T.N., 1978; Sham Wan, Lamma Island. An archaeological site study. Geology. Journal Monograph III, Hong Kong Archaeological Society.

Cline, J.E., 1968; In proceedings of "11th Scintillation Semiconductor Counter Symposium", IEEE Trans. Nucl. Sci.

Cooper, J.A., 1970; Factors determining the ultimate sensitivity of Ge(Li) gamma ray spectrometers. Nucl. Inst. Methods, 82, 273-277.

Cooper, J.A., Perkins, R.W., 1971; An anti-coincidence shielded dual Ge(Li) gamma ray spectrometer for low level environmental radionuclide analysis and gamma-gamma coincidence studies. Nucl. Inst. Methods, 94, 29-38.

Cooper, J.A., Perkins, R.W., 1972; A versatile Ge(Li)-NaI(Tl) coincidence-anticoincidence gamma ray spectrometer for environmental and biological problems. Nucl. Inst. Methods, 99, 125-146.

Deans, P.N., 1964; Computer techniques in gamma spectrometry. In "The Natural Radiation Environment", Adams, J.A.S., Lowder, W.M., (eds), University of Chicago Press.

Debertin, K., Schötzig, U., 1978; Coincidence summing corrections in Ge(Li) spectrometry at low source to detector distances. Nucl. Inst. Methods, 158, 471.

Desai, V.S., 1975; Studies in radon emanation relevant to thermoluminescent dating. Unpublished M.Sc. thesis, Oxford University.

Dutreix, M.D., Bernard, M., 1966; Dosimetry at interfaces for high energy X and gamma rays. Br. J. Radiol., 39, 205-210.

Evans, R.D., 1968; The Atomic Nucleus. McGraw Hill, London.

Evans, R.D., 1968; X-ray and gamma-ray interactions. In "Radiation Dosimetry", vol. 1, Attix, F.H., Roesch, WM.C., (eds), Academic Press, London.

Fitzgerald, J.J., Brownell, G.L., Mahoney, F.J., 1967; Mathematical Theory of Radiation Dosimetry. Gordon and Breach, London.

Flanagan, F.J., 1969; U.S. geological survey standards - II. First compilation of data for the new U.S.G.S. rocks. Geochim. et Cosmochim. Acta, 33, 81-120.

Fleming, S.J., 1969; The acquisition of radiothermoluminescence by ancient ceramics. Unpublished D.Phil. thesis, University of Oxford.

Fleming, S.J., 1970; Thermoluminescence dating: refinement of the quartz inclusion method. Archaeometry, 12, 133-145.

Fleming, S.J., 1975; Supralinearity corrections in fine grain thermoluminescence dating: a reappraisal. Archaeometry, 17, 122-129.

Fleming, S.J., 1978; The quartz inclusion method. In "A Specialist Seminar on Thermoluminescence Dating", Oxford, PACT No. 2, Council of Europe.

Fleming, S.J., 1979; Pre-dose method: basic elements. In "A Specialist Seminar on Thermoluminescence Dating", Oxford, PACT No. 3, Council of Europe.

Grinberg, B., Le Gallic, Y., 1961; Charactéristiques fondamentales d'un laboratoire de mesure de très faibles activités. Int. J. App. Rad. Isotopes, 12, 104.

Grodstein, G.W., 1954; U.S. National Bureau of Standards, Report no. 1003, data reproduced in "Applied Gamma Ray Spectrometry", Adams, F., Dams, R., 1970, Pergamon, Oxford.

Gunn, N.M., 1978; Archaeomagnitude field strengths from Peru. Unpublished Ph.D. thesis, University of Liverpool.

Gunn, N.M., Murray, A.S., 1980; Geomagnetic field magnitude variations in Peru derived from archaeological ceramics dated by thermoluminescence. Geophys. J. R. astr. Soc., 62, 345-366.

Gustafson, P.F., Brar, S.S., 1964; Measurement of gamma emitting radionuclides in soil and calculation of the dose arising therefrom. In "The Natural Radiation Environment", Adams, J.A.S., Lowder, W.M., (eds), University of Chicago Press.

Hallden, N.A., Harley, J.H., 1960; An improved alpha-counting technique. Anal. Chem., 32, 1861-1862.

Hedges, R.E.M., McLellan, M., 1976; On the cation exchange capacity of fired clays and its effect on the chemical and radiometric analysis of pottery. Archaeometry, 18, 203-207.

Hennig, G.J., 1980; Unpublished Ph.D thesis, University of Köln.

Hunt, G.J., O'Riordan, M.C., Whetmath, P.J., 1978; An anti-coincidence shielded Ge(Li) gamma ray spectrometer with high sensitivity for measurement of environmental radionuclides. Nucl. Inst. Methods, 156, 573-589.

Huxtable, J., 1978; Fine grain dating. In "A Specialist Seminar on Thermoluminescence Dating", Oxford, PACT No. 2, Council of Europe.

Huxtable, J., Aitken, M.J., 1978; Thermoluminescence dating of sherds from Sham Wan. Hong Kong Archaeological Society, Journal Monograph 111, 116-124.

Huxtable, J., Murray, A.S., 1980; The reproducibility of TL data from fine grain discs. Ancient TL, No. 10, 1-2.

ICRP 24, 1977; Radiation Protection in Uranium and Other Mines. International Commission on Radiation Protection, Pergamon, Oxford.

ICRU Report 33, 1980; Radiation Quantities and Units. International Commission on Radiation Units and Measurements, Washington, D.C.

Jain, M., Evans, M.L., Close, D.A., 1979; Nondestructive assay technology for uranium resource evaluation, infinite medium calculations. LA-7713-MS, informal report, Los Alamos, University of California.

Kaye, G.W.C., Laby, T.H., 1973; Tables of Physical and Chemical Constants. 14th ed. Longman, London.

Kingery, W.D., 1974; Differential thermal analysis of archaeological ceramics. Archaeometry, 16, 109-111.

Leeper, G.W., 1964; Introduction to Soil Science. Melbourne University Press.

Lewis, S.R., Shafrir, N.H., 1971; Low level Ge(Li) gamma ray spectrometry studies in marine radioactivity studies. Nucl. Inst. Methods, 93, 317.

Løvborg, L., Kirkegaard, P., 1974; Response of 3" x 3" NaI(Tl) detectors to terrestrial gamma radiation. Nucl. Inst. Methods, 121, 239-251.

Marshall, C.E., 1977; The Physical Chemistry and Mineralogy of Soils, vol. 1 and 2. Wiley, London.

McKenzie, J.M., Donovan, P.F., Gynn, A.C., 1967; Nucl. Inst. Methods, 54, 147.

Meakins, R.L., Dickson, B.L., Kelly, J.C., 1979; Gamma ray analysis of K, U and Th for dose rate estimation in thermoluminescent dating. Archaeometry, 21, 79-88.

Mejdahl, V., 1970; Measurement of environmental radiation at archaeological excavation sites. Archaeometry, 12, 147-159.

Mejdahl, V., 1972; Dosimetry technique in thermoluminescent dating. Risø report no. 261, Research Establishment Risø, Danish Atomic Energy Authority.

Mejdahl, V., 1978; Measurement of environmental radiation at archaeological sites by means of TL dosimeters. In "A Specialist Seminar on Thermoluminescence Dating", Oxford, PACT No. 2, Council of Europe.

Mejdahl, V., 1978; Thermoluminescence dating: a thermoluminescence technique for beta-ray dosimetry. In "A Specialist Seminar on Thermoluminescence Dating", Oxford, PACT No. 2, Council of Europe.

Mejdahl, V., 1979; Thermoluminescence dating: beta dose attenuation in quartz grains. Archaeometry, 21, 61-72.

Miller, W.F., Reynolds, J., Snow, W.J., 1958; Argonne National Lab. Report ANL-5902, Tabulated in "Applied Gamma Ray Spectrometry", Adams, F., Dams, R., 1970, Pergamon, Oxford.

Mitchell, R.L., 1964; Trace elements in soil. In "Chemistry of the Soil", Bear, F.E., (ed), Reinhold Publishing Corp., New York.

Moxham, R.M., Tanner, A.B., 1977; High resolution gamma ray spectrometry in uranium exploration. Jour. Research U.S. Geol. Survey, 5.6, 783-795.

Murray, A.S., Wintle, A.G., 1979; Beta source calibration. In "A Specialist Seminar on Thermoluminescence Dating", Oxford, PACT No. 3, Council of Europe.

Nair, K.R., 1940; Sankya, 4, 551, tabulated in Campbell, R.C., 1967; Statistics for Biologists. Cambridge University Press.

Natrella, M.G., 1963; Experimental Statistics. National Bureau of Standards Handbook 91, U.S. Dept. of Commerce, Washington, D.C.

Naudet, R., 1974; Les réacteurs naturels d'Oklo. Bilan au 1er mai 1974. Commissariat à l'Energie Atomique (France), (ISSN-0007.4543), Bulletin d'Informations Scientifiques et Techniques, 193, 7-46.

NCRP 45, 1975; Natural Background Radiation in the United States. National Council on Radiation Protection and Measurements, Washington, D.C.

NCRP 50, 1976; Environmental Radiation Measurements. National Council on Radiation Protection and Measurements, Washington, D.C.

Northcliffe, L.C., Schilling, R.F., 1970; Range and stopping-power tables for heavy ions. Nuclear Data Tables, A7, 233-463, Academic Press, New York.

Ogunleye, O.T., Attix, F.H., Paliwal, B.R., 1980; Comparison of Burlin cavity theory with LiF TLD measurements for Cobalt-60 gamma rays. Phys. Med. Biol., 25, 203-213.

O'Brien, K., 1974; The cosmic ray field at ground level. In "The Natural Radiation Environment II", Adams, J.A.S., Lowder, W.M., Gessell, T.F., (eds), CONF-720805, Washington, D.C.

Paton, T.R., 1978; Formation of Soil Material. George, Allan and Unwin, London.

Pernicka, E., Wagner, G.A., 1979; Primary and interlaboratory calibration of beta sources using quartz as thermoluminescent phosphor. Ancient TL, No. 6, 2-6.

Quet, C., 1975; Recoil emanating power and specific surface area of solids labelled by radium recoil atoms. I. Theory for single solid particles. Radiochem. Radioanal. Lett., 23(5-6), 359-366.

Rado, P., 1969; An Introduction to the Technology of Pottery. Pergamon, Oxford.

Roesch, WM.C., 1958; Dose for non-electronic equilibrium conditions. Radiat. Res., 9, 390-410.

Rosholt, J.N., 1959; Natural radioactive disequilibrium of the uranium series. Geological Survey Bulletin 1084-A, Washington, D.C.

Routti, J.T., 1969; SAMPO, a FORTRAN IV program for computer analysis of gamma spectra from Ge(Li) detectors, and for other spectra with peaks. UCRL-19452, University of California, Berkeley.

Routti, J.T., Prussin, S.G., 1969; Photopeak methods for the computer analysis of gamma ray spectra from semiconductor detectors. Nucl. Inst. Methods, 72, 125-144.

Schayes, R., Lorthioir, M., Lheureux, M., 1963; Thermoluminescent dosimeter PNP 080. Revue MBLE, 6.1, Brussells.

Scott, M.R., 1968; Thorium and uranium concentrations and isotopic ratios in river sediments. Earth Planet. Sci. Lett., 4, 245-252.

Singhvi, A.K., Aitken, M.J., 1978; Americium-241 for alpha irradiations. Ancient TL, No. 3, 2-9.

Smith, A.R., Wollenberg, H.A., 1974; High-resolution gamma spectrometry for laboratory analysis of the uranium and thorium decay series. In "The Natural Radiation Environment II", Adams, J.A.S., Lowder, W.M., Gessell, T.F., (eds), CONF-720805, Washington, D.C.

Snyman, G.C., Clayton, C.G., 1963; Some observations on the scattering of beta particles by thick absorbers. Int. J. App. Rad. Isotopes, 14, 183-188.

Steiger, R.H., Jäger, E., 1977; Subcommission on geochronology: convention on the use of decay constants in geo- and cosmochronology. Earth Planet. Sci. Lett., 36, 359.

Storm, E., Israel, H.I., 1970; Nuclear Data Tables, A7, 565, Academic Press, New York.

Suhr, N.H., Ingamels, C.O., 1966; Solution technique for analysis of silicates. Anal. Chem., 38, 730-734.

Szöghy, I.M., Kish, L., 1977; Determination of radioactive disequilibrium in uranium bearing rocks. Can. J. Earth Sci., 15, 33-44.

Tanner, A.B., 1964; Radon migration in the ground: a review. In "The Natural Radiation Environment", Adams, J.A.S., Lowder, W.M., (eds), University of Chicago Press.

Tanner, A.B., 1978; Radon migration in the ground: a supplementary review. In "The Natural Radiation Environment III", Houston, Texas, CONF 780422, U.S. Dept. of Commerce, Virginia.

Taylor, R.E., (ed), 1976; Advances in Obsidian Glass Studies. Noyes Press, Park Ridge.

Thompson, J., 1970; The influence of previous irradiation on thermoluminescent sensitivity. Unpublished D.Phil. thesis, Oxford University.

Turner, R.C., Radley, J.M., Mayneord, W.V., 1958; The alpha ray activity of human tissues. Brit. J. Radiol., 31, 397-406.

Watt, D.E., Ramsden, D., 1964; High Sensitivity Counting Techniques. Pergamon, Oxford.

Williamson, C.F., Boujot, J.P., Picard, J., 1966; Tables of ranges and stopping-powers of chemical elements for charged particles of energy 0.05-500 MeV. Rapport CEA-R 3042, Centre d'Etudes Nucleaire de Saclay.

Wintle, A.G., Aitken, M.J., 1977; Absorbed dose from a beta source as shown by thermoluminescence dosimetry. Int. J. Appl. Radiat. Isotopes, 28, 625-627.

Wintle, A.G., 1973; Anomalous fading of thermoluminescence in mineral samples. Nature, 245, 143-144.

Wintle, A.G., 1978; Anomalous fading. In "A Specialist Seminar on Thermoluminescence Dating", Oxford, PACT No. 2, Council of Europe.

Wintle, A.G., 1980; Thermoluminescence dating: a review of recent applications to non-pottery materials. Archaeometry, 22, 113-122.

Wollenberg, H.A., Smith, A.R., 1964; Studies in terrestrial gamma irradiation. In "The Natural Radiation Environment", Adams, J.A.S., Lowder, W.M., (eds), University of Chicago Press.

Zimen, K.E., Mertens, P., 1971; Kernruckstoss in festen Stoffen und Knock-out-Effeckt, (Nuclear recoil in solids and the knock out effect). Z. Naturforsch., Ser. A, 26(4), 773-775.

Zimmerman, D.W., 1970; The dependence of thermoluminescence on energy and type of ionizing radiation and its significance for archaeologic age determination. Unpublished D.Phil. thesis, University of Oxford.

Zimmerman, D.W., 1971; Thermoluminescent dating using fine grains from pottery. Archaeometry, 13, 29-52.

Zimmerman, D.W., 1978; Introduction to basic procedures for sample preparation and thermoluminescence measurement of ceramics. In "A Specialist Seminar on Thermoluminescence Dating", Oxford, PACT No. 2, Council of Europe.

ERRATA

Page xi, para. 2, line 1, for "MacKintosh" read "McIntosh"

Page 6.11, para. 2, line 2, for "reaily" read "readily".